2009

Advanced materials for electrodes and electrolyte in rechargeable lithium batteries

Sau yen Chew
University of Wollongong

ADVANCED MATERIALS FOR ELECTRODES AND ELECTROLYTE IN RECHARGEABLE LITHIUM BATTERIES

A thesis submitted in fulfillment of the

requirements for the award of the degree

DOCTOR OF PHILOSOPHY

from

UNIVERSITY OF WOLLONGONG

by

SAU YEN CHEW, B. ENG. (HONS.), M. ENG.

INSTITUTE FOR SUPERCONDUCTING & ELECTRONIC MATERIALS,

AND THE

FACULTY OF ENGINEERING

2009

CERTIFICATION

I, Sau Yen Chew, declare that this thesis, submitted in fulfillment of the requirements for the award of Doctor of Philosophy, in the Institute for Superconducting & Electronic Materials, Faculty of Engineering, University of Wollongong, is wholly my own work unless otherwise referenced or acknowledged. The document has not been submitted for qualifications at any other academic institution.

Wollongong, Australia

22 May 2009

For See How, Sabine and my parents

ACKNOWLEDGEMENTS

Financial support from the ARC Center of Excellence for Electromaterials Science (ACES), and the University of Wollongong, by means of a UoW PhD Scholarship and Tuition Fee Scholarship, is gratefully acknowledged. Special thanks go to the Electrochemical Society (ECS) for funding my summer study at Paul Scherrer Institut (PSI), Switzerland via the 2008 ECS Colin Garfield Fink Summer Fellowship.

I wish to express my utmost gratitude to my thesis supervisor, *Professor Hua Kun Liu*, and co-supervisor, *Dr. Jiazhao Wang*, for their invaluable advice, encouragement, understanding, and trust during my stay at UoW.

I would like to express my deepest appreciation to *Prof. Shi Xue Dou*, Director of ISEM, for accepting me as a PhD student and providing the appropriate facilities and expertise during the course of my studies.

I am grateful to *PD Dr. Petr Novák*, Head of the Batteries Group, PSI Switzerland, for his scientific discussions and support during my appointment as a Visiting Scientist in PSI. I would also like to thank *Prof. Dr. Sotiris E. Pratsinis*, Director of the Particle Technology Laboratory (PTL), Swiss Federal Institute of Technology Zurich (ETH), Switzerland, for numerous fruitful discussions and for providing me with the facilities available in his laboratory.

I wish to thank *Mr. Timothy Patey* (PSI) and *Mr. Robert Büchel* (PTL) for their assistance in the synthesis of $LiMn_2O_4$ thin films by using flame spray deposition apparatus. During my stay at PSI, I had the pleasure of working with a number of scientists and postgraduate students such as *Dr. Jean-Francois Colin, Dr. Wolfgang Märkle, Dr. Maire Pascal, Mr. Werner Scheifele, Mr. Hermann Kaiser, Mr. Fabio La*

Mantia, Mr. Fabio Roschiano, Ms. Franziska Simmen, Mr. Patrick Ruch, and Mr. Andreas Hintennach, who have made my time in Switzerland unforgettable. Also, the administrative assistance from *Ms. Isabella Kalt* is gratefully acknowledged.

Technical assistance from people at UoW, such as *Dr. Jun Chen* (FT-IR and Raman), *Dr. Konstantin Konstantinov* (TGA, and SEM), *Dr. David Wexler* (TEM), *Dr. Zaiping Guo*, and *Assoc. Prof. Chee Too* (vacuum filtration equipment) is also gratefully acknowledged. It was also my pleasure to work with a number of local and overseas collaborators such as *Prof. Maria Forsyth* (Monash University, Australia), *Prof. Douglas R. MacFarlane* (Monash University, Australia), *Dr. Jiazeng Sun* (Monash University, Australia), *Dr. Frank Krumeich* (ETH Zurich, Switzerland), *Prof. Dayse dos Santos* (São Paulo State University, Brazil), *Prof. Chuanqi Feng* (Wuhan University, China), and *Ms. Dongyun Zhang* (Shanghai Jiao Tong University, China) during my studies in ISEM.

I also wish to thank *Dr. Wai Kong Yeoh, Dr. Jung Ho Kim, Dr. Jerry Zhao, Dr. Bernie Huang, Dr. Scott Needham, Dr. Min-Sik Park, Dr. Joe Xu, Mr. Dapeng Chen, Dr. Olga Shcherbakova, Dr. Germanas Peleckis, Dr. Marie Roussel, Dr. Jane Yao, Mr. Brad Winton, Mr. Shulei Chou, Mr. Georgin Lao, Mr. Jin-Soo Park,* and *Mr. Andrey Shcherbakov*, for creating a pleasant working environment during my studies in ISEM.

I wish to thank *Dr. Tania Silver* for the critical reading of my publications and also the proofreading of my thesis. My heartfelt thanks also go to *Mr. Ron Kinnell*, for all his technical assistance with the maintenance of equipment and scientific facilities.

I would like to thank my parents, brother, and sister for their continued support and love. Finally, I would like to thank my lovely husband, *Dr. See How (Desmond) Ng*, who gave me strength, dedication, and guidance during the high and low points of my PhD studies.

TABLE OF CONTENTS

ABSTRACT

The lithium-ion (Li-ion) battery possesses many outstanding advantages over the well known rechargeable battery systems, in particularly higher energy density and longer shelf life, as well as not suffering from the memory effect problems of Ni-MH batteries. Those advantages are making it the greatest energy source of choice for the portable electronic market. Graphite and $LiCoO_2$ are commonly used in commercial Li-ion battery. Despite their widespread utilization, the current electro-active materials have reached to a limit in terms of delivering even higher power, energy density, and longer cycle life for the new, emerging field of large-scale energy storage systems, such as in the automotive industry. Hybrid and fully electric cars need safer, cheaper, and higher performing batteries in order to offer an important alternative to combustion engines.

To overcome the shortcomings of the current Li-ion battery, improvements are needed to push the Li-ion technology to the next level. Hence, the motivation for this PhD work is to search for potential electro-active materials, by means of the synthesis of film and powder based electrodes, fine-tuning of the composition of the composite electrodes, and characterization of them for possible application in Li-ion rechargeable batteries. Among the anode candidates studied were free-standing carbon nanotube (CNT) films, tin glycolate, and polypyrrole coated silicon (Si-PPy) nanocomposite materials. Two cathode candidates were also studied: lithium manganese oxide ($LiMn_2O_4$) thin film, and polypyrrole coated lithium trivanadate (LiV_3O_8-PPy) composite. Ionic liquid based polymer electrolyte was also studied to enhance Li-ion battery safety features.

Free-standing CNT film electrodes have been synthesized by a simple vacuum filtration method. The free-standing electrodes were produced without any binder or metal current collector, which significantly reduced the total weight. The free-standing CNT film electrodes were also flexible and had good electrical conductivity with the addition of carbon black. Three different types of CNTs were used, i.e. single-wall

CNTs (SWCNTs), double-wall CNTs (DWCNTs) and multi-wall CNTs (MWCNTs). The films based on MWCNT are much better than SWCNT and DWCNT films in terms of their electrochemical performance, with stable cycling behavior of 300 mAh g^{-1} after 40 cycles. A detailed study revealed that MWCNT electrode exhibited a reversible, sharp, and intense peak at approximately 0.15 V vs. Li/Li^+ during the Li^+ de-intercalation process. A thin solid electrolyte interphase (SEI) layer was observed on the surface of MWCNTs after prolonged cycling. This proved that only multi-wall CNTs have the capability for significant Li^+ ion intercalation/de-intercalation. Novel tin glycolate particles were prepared by the polyol-mediated method. The prepared powders consist of fine tin-based particles (80 – 120 nm), encapsulated within tin glycolate shells. When applied as an anode material for Li-ion batteries, the glycolate shells buffered the volume expansion upon Li-Sn alloying, and thus the tin glycolate particles showed a high specific charge of 416 mAh g^{-1} beyond 50 cycles. Novel Si-PPy nanocomposite was prepared by coating the Si particle surfaces with PPy by the *in situ* chemical polymerization method. The cycle stability of Si-PPy nanocomposite electrodes was greatly enhanced with 50 wt. % PPy. The loading level of PPy plays a major role in determining the stability of the nanocomposite, and consequently creates a good matrix to improve the electrical conductivity, buffer the volume change during cycling, and prevent cracking and pulverization of the Si.

A new approach was developed to rapidly synthesize nanostructured $LiMn_2O_4$ thin films by flame spray deposition (FSD) and *in situ* annealing. The $LiMn_2O_4$ films on stainless steel current collector exhibited good cyclability, with two pairs of redox peaks at approximately 4.00 and 4.15 V vs. Li/Li^+. The study indicated that spinel $LiMn_2O_4$ thin films can be prepared by the fast and efficient FSD method. LiV_3O_8-PPy composites were synthesized by a low-temperature solution route followed by an *in situ* polymerization method. For LiV_3O_8 material, only 24 wt. % of PPy is needed to enhance the electrical conductivity and stability of the composite electrode, which delivered a specific charge of 183 mAh g^{-1} beyond 100 cycles.

A solution casting method was used to prepare IL-PE composite membrane. The composite membrane was then assembled with LiV_3O_8-PPy (24 wt. % PPy) composite cathode and tested as a lithium polymer battery at room temperature. The cell delivered 200 mAh g^{-1} with respect to the mass of the cathode material.

NOMENCLATURE

- **List of Symbols**

Symbol	Name	Unit
a_i	Activity of species *i*	mol dm^{-3}
β	Full width at half maximum in radians	radians
C	Concentration	M
C-rate	Rate of charge or current density	h^{-1}
C_{dl}	Double-layer capacitance	F m^{-2}
C_{irrev}	Irreversible charge	Ah kg^{-1} or mAh g^{-1}
E	Elastic modulus	GPa
E_{dc}	DC potential	V or mV
E_f	Final potential	V or mV
E_i	Initial potential	V or mV
E_s	Switching potential	V or mV
E	Potential of half-reactions	V or mV
E^0	Standard electrode potential	V or mV
$E^{0,(-)}$	Negative electrode potential	V or mV
$E^{0,(+)}$	Positive electrode potential	V or mV
ΔE^0, U^0	Cell potential	V or mV
E_{eq}	Equilibrium potential	V
ε	dielectric constant	(dimensionless)
ε_b	elongation at failure	%
f	Frequency	Hz
ΔG^0	Standard Gibbs free energy	J mol^{-1}
I	Current	A or mA
K	Shape factor of the average crystallite	(dimensionless)
L	Thickness	cm
M	Molar mass	g mol^{-1}

- **List of Symbols (con't)**

Symbol	Name	Unit
M_r	Mass of the incident ion	kg or g
m, m_i	Mass of species i	kg or g
N^0	Number of pulses	(dimensionless)
n	Number of electrons exchanged or integer	(dimensionless)
P_v	Power density	W dm^{-3}
p	Specific power	W kg^{-1}
ρ	Specific density	g cm^{-3}
Q	Charge capacity	Ah or mAh
Q_c	Coulombic efficiency	%
Q_{irrev}	Irreversible capacity loss	%
Q_{max}	Maximum theoretical specific charge	Ah kg^{-1} or mAh g^{-1}
q	Theoretical specific charge	Ah kg^{-1} or mAh g^{-1}
R_b	Bulk resistance	Ω
R_{ct}	Charge-transfer resistance	Ω
S_{BET}	BET Specific surface area	m^2 g^{-1}
T	Temperature	K or ^oC
T_m	Melting temperature	K or ^oC
t	Time	h
V_{meso}	Total pore volumes	cm^3 g^{-1}
v	Scan rate	mV s^{-1}
v_i	Stoichiometric coefficients of species i	(dimensionless)
W_V	Energy density	Wh dm^{-3}
W	Specific energy	Wh kg^{-1}
ω_{RBM}	RBM frequency	cm^{-1}
Δx	Amount of guest species	mol
λ	Wavelength of the incident X-ray beam	nm
θ	Angle of incidence	º or degrees
σ	Ionic conductivity	mS cm^{-1}
σ	Electrical conductivity	S cm^{-1}
σ_b	Ultimate tensile strength	MPa

- **List of Conversion Factors**

Value	Equivalence
1 eV	1.602×10^{-19} J
	86.5 kJ mol^{-1}
	8066 cm^{-1}
1 cm^{-1}	1.986×10^{-23} J
1 μm	10^{-6} m
1 nm	10^{-9} m
1 Å	10^{-10} m

- **List of Abbreviations**

Abbreviation	Meaning
a.u.	Arbitrary unit
ACES	ARC Center of Excellence for Electromaterials Science
ACP	Aluminum coated primer
AFM	Atomic force microscopy
BET	Brunauer Emmett Teller
CB	Carbon black
CCCC	Computer controlled cell capture
CNTs	Carbon nanotubes
CV	Cyclic voltammetry
DC	Disordered carbon
DFT	Density functional theory
DMC	Dimethyl carbonate
DWCNTs	Double-wall carbon nanotubes
EC	Ethylene carbonate
EDX	Energy dispersive spectroscopy
EG	Ethylene glycol
EIS	Electrochemical impedance spectroscopy
ETH	Swiss Federal Institute of Technology
EV	Electric vehicle

- **List of Abbreviations (con't)**

Abbreviation	Meaning
FE-SEM	Field-emission scanning electron microscopy
FSD	Flame spray deposition
FSP	Flame spray pyrolysis
FT-IR	Fourier transform infrared
FWHM	Full width at half maximum
HAB	Height above burner
HEVs	Hybrid electric vehicles
IL	Ionic liquid
IL-PE	Ionic liquid-polymer electrolyte
IPRI	Intelligent Polymer Research Institute
ISEM	Institute for Superconducting and Electronic Materials
JCPDS	Joint committee on powder diffraction standards
LIB	Li-ion battery
LiTFSA	Lithium triflouromethanesulfonate
MWCNTs	Multi-wall carbon nanotubes
Ni-Cd	Nickel-cadmium
Ni-MH	Nickel-metal hydride
NMC	Nickel manganese cobalt oxide
NMP	1-methyl-2-pyrrolidinone
OCP	Open circuit potential
P_{13}TFSA	*N*-methyl-*N*-propyl pyrrolidinium bis(trifluoromethanesulfonyl) amide
PC	Propylene carbonate
PDAs	Personal digital assistants
PPy	Polypyrrole
PSI	Paul Scherrer Institut
PTL	Particle Technology Laboratory
PTSNa	Sodium p-toluenesulfonate
PVDF	Polyvinylidene fluoride
R&D	Research and development

- **List of Abbreviations (con't)**

Abbreviation	Meaning
RBM	Radial breathing mode
RBS	Rutherford backscattering spectrometry
RIS	Reactive ion etching
RTILs	Room temperature ionic liquids
SEI	Solid-electrolyte interphase
SEM	Scanning electron microscopy
SHE	Standard hydrogen electrode
SPE	Solid polymer electrolyte
SS	Stainless steel
SSA	Specific surface area
SWCNTs	Single-wall carbon nanotubes
TEM	Transmission electron microscopy
TGA	Thermogravimetric analysis
XRD	X-ray diffraction
ZW	Zwitterion

LIST OF FIGURES

LIST OF TABLES

CHAPTER 1

INTRODUCTION

1.1 Motivation

The worldwide thirst for portable consumer electronics since the 1980s, from the clumsy portable computers and cell phones that existed then to the present convergence of multiple devices sufficiently small to fit in a pocket, has had an enormous impact on portable power sources. Lithium technology seems to be the most promising candidate to accommodate these demands. Indeed, first generation lithium batteries, which exploit the "rocking chair" concept, were proposed in the 1970s. The Li-based battery concept was then further optimized and commercialized by Sony with the so called lithium ion (Li-ion) batteries, in which Li^+ ions shuttle between an insertion anode (e.g. graphitic carbon) and a transition cathode (e.g. $LiCoO_2$). Li-ion batteries have since emerged as the important power source of choice for the high performance rechargeable battery market.

The rise of Li-ion batteries was then unstoppable; they not only replaced Ni-Cd batteries, but left the purported successor technology, nickel-metal hydride, in their wake. Li-ion batteries had clear advantages over the nickel based competition: higher capacity and higher nominal voltage, resulting in higher energy and power densities. The worldwide market for Li-ion batteries is now valued at 10 billion dollars per annum

and growing. The next important steps in Li-ion technology are to power hybrid electric vehicles, to accommodate clean and efficient energy storage, to power implantable medical applications, such as artificial hearts, and to address global warming issues with the storage of wind/solar energy.

The advanced Li-ion technology that swept the world in the last twenty years has provided us with an exceptional quality of life that could only be imagined in science fiction. Clearly, the introduction of Li-ion technology has revolutionized portable electronic devices in this century and shows many benefits, in terms of weight, size, and design flexibility, in the field of energy storage. The Li-ion field has, however, been in constant evolution since its commencement and will continue to grow in the future.

1.2 Importance of Study

Current Li-ion batteries mainly consist of $LiCoO_2$ and graphite with engineering improvements. They are now normally charged to 4.2 V vs. Li/Li^+, which is 0.1 V vs. Li/Li^+ higher than the voltage adopted in the initial stage, so that the energy density has been increased correspondingly during the last 6 years. For example, the volumetric energy density of Li-ion batteries was approximately 350 Wh dm^{-3} in 2000 [Tarascon and Armand, 2001]. Coupled with improved cell design, the volumetric energy density now exceeds 500 Wh dm^{-3} [Yoshizawa and Ohzuku, 2007], approaching a critical limit for $LiCoO_2$ and graphite materials when they are charged and discharged at high rate capability, and long cycle life together, in an abused usage. Besides, the commercialization of "cheap" batteries with poor quality starting materials in recent

years has led to a widespread of mistrust of the technology: accounts of batteries that swell, catch fire, or even explode have been widely reported.

Today's challenge for researchers in the Li-ion battery field is to search for possible electro-active materials to overcome emerging issues by the following means: identifying new classes of materials, developing new method to synthesize known electrode materials, and fine-tuning the composition of composite electrodes. To enhance Li-ion battery safety, polymer electrolytes and ionic liquids were recently introduced.

1.3 Goals of the work

The driving question behind the work of this dissertation is: how does the Li-ion battery operate when new electro-active materials are used? Once new materials are identified as potential candidates, the next question would be on how to further improve the rate capabilities, energy density, and safety of these materials by means of electrode engineering or introducing new polymer electrolytes.

Thus, this thesis will focus on solving the above-mentioned problems by first addressing the synthesis of potential electro-active materials and then testing them as electrode materials for use in Li-ion batteries, so as to understand the structural, morphological, physical, and electrochemical changes that occur when new materials are used. Secondly, the thesis will focus on the introduction of thin film electrodes and polymer electrolyte to enhance the electrode engineering and safety features of the Li-ion battery system.

Some of the scope of this research work is briefly outlined under the following topics:

I. A literature review based on current state-of-the-art lithium-ion battery technologies, which includes a brief development history of the lithium-based battery, fundamental theory, development of electrode and electrolyte materials and future prospects for Li-ion manufacturing technology (Chapter 2).

II. Synthesis of electro-active thin films by vacuum filtration (Chapter 4) and flame spray pyrolysis (Chapter 5).

III. Synthesis of novel electro-active composite powder materials by the polyol-mediated method (Chapter 6) and the *in situ* polymerization coating technique (Chapter 7 and Chapter 8).

IV. Preparation of polymer electrolyte by the solvent casting method and testing with polypyrrole (PPy) coated LiV_3O_8 electrode for use in lithium polymer batteries (Chapter 9).

V. Study of the structural, physical, and surface morphology properties of the as-synthesized materials by X-ray diffraction (XRD), Raman spectroscopy, Fourier transform infrared spectroscopy (FT-IR), thermogravimetric analysis (TGA), field emission-scanning electron microscopy (FE-SEM), transmission electron microscopy (TEM), Brunauer-Emmett-Teller (BET) specific surface area measurements, ionic conductivity measurements, and tensile testing.

VI. Characterization of the as-synthesized thin films and powder materials as electrodes for use in Li-ion batteries, via cyclic voltammetry (CV), galvanostatic charge-discharge cycling, and also the electrochemical impedance spectroscopy (EIS) technique.

VII. Summary of the doctoral work with some suggestions for further research work (Chapter 10).

CHAPTER 2

LITERATURE REVIEW

2.1 Rechargeable Lithium Batteries

The technology revolution for the past few centuries has been accommodated by fuel combustion reactions. However, this has reached a limit and comes at a price: the high level of carbon dioxide emissions generates CO_2, creating a global warming issue, while the heavy consumption of fossil fuels has led to ever increasing oil prices. For the sake of future generations, the search for clean and efficient energy storage systems is becoming very important. Rechargeable lithium batteries have revolutionized portable electronic devices. They are the technology choice for future hybrid electric vehicles, a new direction from becoming the dominant power source for consumer electronic devices (cell phones, personal digital assistants (PDAs), laptops, and implantable medical applications) in this century.

2.1.1 History of the batteries

Storing energy in the form of an electrochemical reaction has been known to man for many centuries. The first example is the Baghdad Battery, which is believed to be around 2000 years old. It was excavated in 1936 by German archaeologists near

Baghdad, Iraq [Dubpernell, 1977]. The terracotta jars with two electrodes made of iron and copper were probably immersed in an electrolyte of natural acidic origin, such as lemon juice or vinegar, making a 2 V cell (refer to Fig. 2.1(a)). The modern development of the battery came only in 1800, through the work of Alessandro Volta (1745-1827). The Italian scientist first built the "Voltaic pile" by stacking zinc and copper discs separated by cardboard soaked in brine, as shown in Fig 2.1(b). This was the first real battery, with a stable potential depending on the metals used and on the number of layers used in the stack.

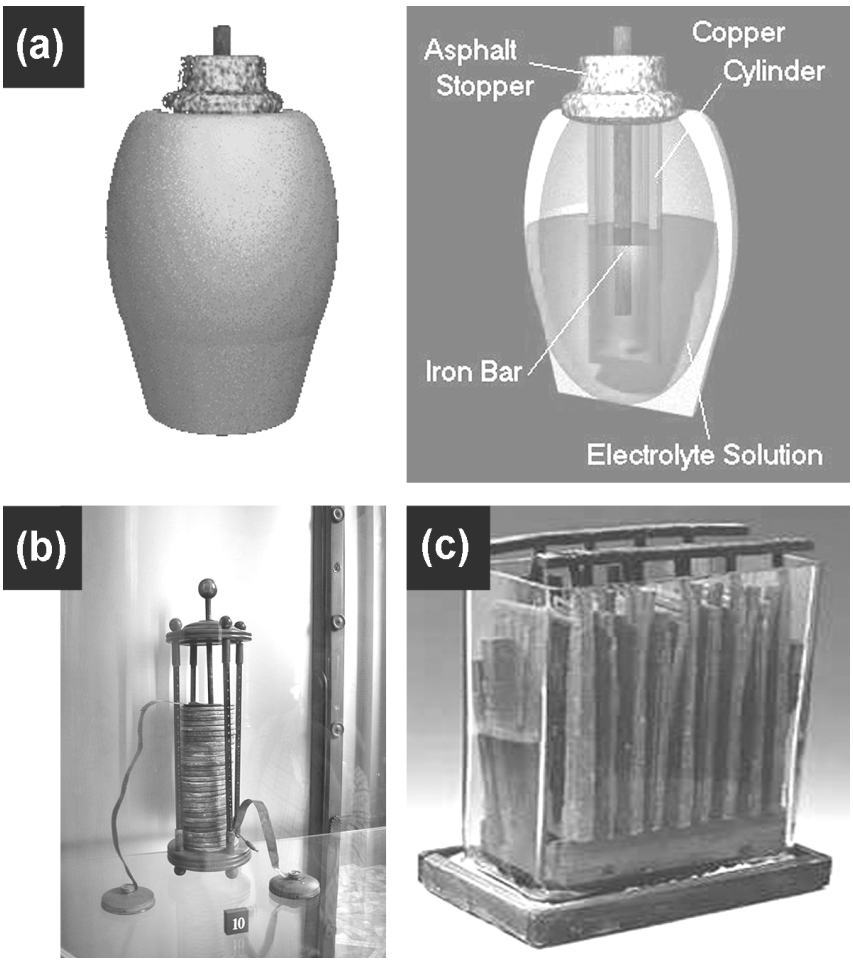

Fig. 2.1 (a) Baghdad battery and its cross-section view; (b) voltaic battery; (c) rechargeable lead-acid battery.

The Voltaic Pile was not good for delivering currents for long periods of time. This restriction was overcome in the Daniell Cell, which was developed by British researcher John Frederich Daniell in 1820. A copper plate and a zinc piece were used in a two electrolyte system. This battery could produce 1.1 V to power telegraphs, telephones, and even to ring doorbells in homes for over 100 years.

The first rechargeable lead-acid battery was then invented in 1859 by Gaston Planté (1834-1889), based on the interaction between lead sheet and an acidic electrolyte (Fig. 2.1(c)). By alternately charging and discharging this cell, its ability to supply current was increased. This concept is still in use today as the most widespread battery system in the world [Winter and Brodd, 2004].

The advantage of using lithium metal was demonstrated in the 1970s, with the assembly of a primary Li cell. The motivation to use Li metal as anode is due to the fact that Li is the most electropositive (-3.04 V vs. standard hydrogen electrode) and the lightest metal (molar mass, M = 6.94 g mol^{-1}, and specific density, ρ = 0.53 g cm^{-3}), thus facilitating the design of energy storage systems with high energy density. This means that lithium has a theoretical specific charge of 3861 mAh g^{-1}. Since then, lithium batteries have gained popularity as they became portable and useful for a variety of purposes.

As with all types of batteries, lithium batteries can be divided into two families:

I. Primary batteries, not rechargeable, such as the Li-MnO_2, Li-$SOCl_2$, and Li-FeS_2 systems
II. Secondary batteries, rechargeable, such as Li-ion or Li-polymer systems.

Primary batteries are non-rechargeable, because the electrochemical reactions are irreversible under practical conditions and therefore are single use. In secondary

batteries, the electrochemical reactions are reversible; therefore, these types of batteries are reusable. In this type of battery during discharge, the chemical energy is transformed into electrical energy. The battery can be reused again once electrical energy has been converted into chemical energy during the charging process.

2.1.2 Primary Lithium Batteries

Under the definition of primary lithium batteries it is possible to find an extremely wide array of different chemistries that employ metallic lithium at the anode and some kind of reducible compound at the cathode [Linden and Reddy, 2001]. The first lithium primary battery was the lithium–thionyl chloride battery, consisting of a $SOCl_2$ positive electrode and a lithium metal negative electrode. It was developed by the US Army for stationary applications because of the wide range of temperatures in which it can be operated (from -55 °C to +85 °C). It is built around a liquid cathode with a graphite current collector, and the electrode reactions are:

$$Li^+ + e^- \Rightarrow Li \qquad \text{(anode)}$$

$$2SOCl_2 + 4e^- + 4Li^+ \Rightarrow LiCl + SO_2 + S \qquad \text{(cathode)}$$

The discharge products (sulphur and sulphur dioxide) are soluble in the electrolyte, generally lithium aluminum chloride in thionyl chloride. This battery provides a nominal 3.5 V and an extremely long life, but has a major drawback in the constituents. Thionyl chloride is extremely toxic, and upon deep discharge, the gaseous SO_2 can build up a dangerous pressure: therefore they need to be maintained properly and are not commonly available to the public.

For general purposes, the most common primary lithium battery employs MnO_2 as cathode, and provides a nominal voltage of 3 V. Its electrode reactions can be written as:

$$Li^+ + e^- \Rightarrow Li \qquad \text{(anode)}$$

$$MnO_2 + e^- + Li^+ \Rightarrow LiMnO_2 \qquad \text{(cathode)}$$

This battery uses an organic electrolyte (propylene carbonate with $LiClO_4$) and is commonly found in wrist-watches, calculators, and all sorts of low power/low drain applications.

One last example of a primary lithium battery is the iron sulfide battery. This system is based on the following reactions:

$$Li^+ + e^- \Rightarrow Li \qquad \text{(anode)}$$

$$2FeS_2 + 4e^- + 4Li^+ \Rightarrow Fe + 2Li_2S \qquad \text{(cathode)}$$

The electrolyte in this cell is an organic solution based on propylene carbonate, dioxolane, and dimethoxyethane. These batteries are the primary lithium batteries that have been commercialized by many major manufacturers such as Energizer and provide a nominal voltage of 1.5 V. Therefore, they are suitable to replace normal alkaline batteries, while providing a lifetime up to 2.5 times as long. This battery is also called "lithium-iron" and is not to be confused with the rechargeable battery based on lithium iron phosphate. A similar chemistry can be employed for high temperature batteries for stationary applications.

2.1.3 Secondary Lithium Batteries

About the same time, several inorganic compounds were discovered to react with the alkali metals in a reversible way. This crucial finding led to the development of high energy rechargeable lithium batteries. Michael Stanley Whittingham first proposed a system with metallic lithium at the anode and titanium disulfide (TiS_2) at the cathode in 1976, when working for Exxon [Whittingam, 1976]. The mechanism of the battery was the reversible insertion of lithium ions into TiS_2, but the use of Li metal as the anode creates uneven dendrite growth, which poses great safety concerns, as it can lead to an explosion hazard.

For this reason it was proposed to use an insertion material at the anode as well. In 1981, the first workable graphite anode was patented by Bell Labs [Samar and Somerset, 1981]. Later, John Bannister Goodenough proposed Li_xMO_2 (where M is Co, Ni, or Mn), which led to the first commercial lithium-ion battery (Li-ion), manufactured by Sony in 1991. This cell was based on a graphitic anode and a lithium cobalt oxide cathode [Ozawa, 1994]. When assembled, the cell was in the discharged state, which creates another safety advantage for storage and transport.

Li-ion batteries are based on the reversible insertion (intercalation) and removal (de-intercalation) of lithium ions in and from host materials. Because of this property, they are also called “rocking chair batteries”. The electrolyte is a solution of a lithium salt in an organic solvent. A schematic diagram of the functioning principle is shown in Fig. 2.2. On the right side, the positive electrode is the original source of lithium ions, while on the left side is the negative electrode, completely without lithium metal. During charge, lithium ion (Li^+) travel from the positive to the negative electrode,

creating the compounds $Li_{1-x}CoO_2$ and Li_xC_6. When the battery is discharged, Li^+ ions are intercalated into the positive electrode, leading to the original situation.

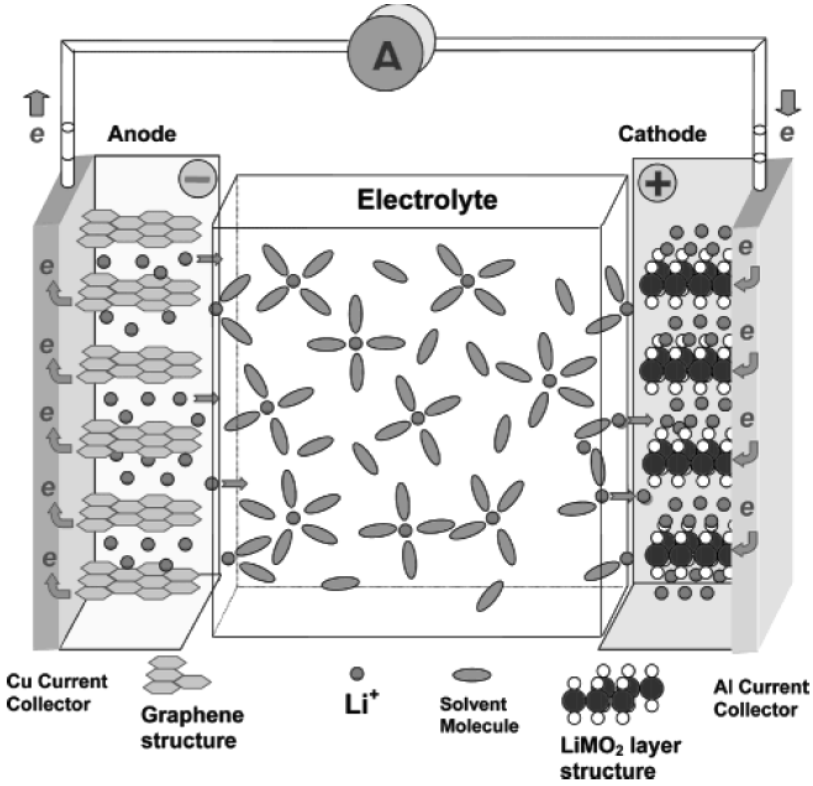

Fig 2.2 Schematic representation of a Li-ion battery shows the electrochemical intercalation process during discharge. The anode is composed of graphite, while the cathode is a layered oxide. Li^+ ions are removed from the graphene layers and simultaneously inserted into the layered oxide [Xu, 2004].

As mentioned above, when a Li-ion battery is assembled, it is in its discharged state. Li^+ ions are included in the cathodic material ($LiCoO_2$ in the example), and they need to be de-intercalated from the cathode to the anode in order to charge the battery. During the charge process the positive electrode is oxidized, and the negative electrode is reduced following the reactions below:

$$6C + xLi^+ + xe^- \Rightarrow Li_xC_6 \qquad \text{(anode)}$$

$$Li_{1-x}CoO_2 + xLi^+ + xe^- \Rightarrow LiCoO_2 \qquad \text{(cathode)}$$

In actual practice, not all ions are transported back and forth, i.e. $0 < x < 1$. In Li-ion batteries, the electrodes are separated by a polymeric membrane that is permeable to the electrolyte but ensures electrical insulation between the anode and the cathode. The vast majority of today's Li-ion batteries are still based on this simple concept.

2.1.4 Principles of Operation

When discussing the electrochemical properties in this PhD study, a "*full cell configuration*" is always applied. Basically, the electrochemistry of the overall cell reactions can be separated into the half-cell reactions of the processes, which take place at the cathode or anode. At the anode, one half-cell reaction involves the oxidation (Ox) of one species, and at the cathode, the second half-cell reaction involves the reduction (Red) of the other. When a component in a battery is oxidized, one electron leaves its bulk, travels through an external circuit doing work, and reenters the battery at the other end, reducing the material at the opposite electrode.

At the anode: $\mathrm{Re}\,d_1 \rightarrow Ox_1 + e^-$ (2.1)

At the cathode: $Ox_2 + e^- \rightarrow \mathrm{Re}\,d_2$ (2.2)

Overall reaction: $\mathrm{Re}\,d_1 + Ox_2 \rightarrow Ox_1 + \mathrm{Re}\,d_2$ (2.3)

Each of these reactions is related to a *standard electrode potential*, E^o, which can be calculated from the thermodynamic data of the reaction. Under equilibrium conditions:

$$E^0 = \frac{-\Delta G^0}{nF} \tag{2.4}$$

where, $-\Delta G^0$ = standard Gibbs free energy

n = number of electrons

F = Faraday constant (96487 C)

As it is impossible to measure individual electrode potentials in an absolute sense, they are each measured with reference to another electrode, which is used as the standard electrode. The electrode normally used for this purpose is the *standard hydrogen electrode* (SHE), where the temperature is equal to 25 ^{o}C, the pressure is equal to 1 bar, and all species are at unity activity. For non-standard conditions, the *Nernst equation* can be used to calculate the potential of the half-reactions (E) at equilibrium:

$$E = E^0 - \frac{RT}{nF}\sum \ln a_i^{v_i} \tag{2.5}$$

where, a_i = activity of relevant species

v_i = stoichiometric coefficients of relevant species

R = gas constant

T = absolute temperature

The cell voltage of an electrochemical cell is calculated from the electrode potentials (reduction potentials) of the half-reactions. The overall *theoretical cell voltage*, ΔE^0 or U^0, is obtained by subtracting the negative electrode potential, $E^{0,(-)}$, from the positive electrode potential, $E^{0,(+)}$:

$$U^0 = \Delta E^0 = E^{0,(+)} - E^{0,(-)} \tag{2.6}$$

Values of potentials for various half-cell reactions have been tabulated [Brett and Brett, 1993], and these enable theoretical cell voltages to be calculated if the two half-cell reactions are known. Some important standard potential values in battery technology are shown in Fig. 2.3. A high cell voltage is obtained by combining two electrode systems with potentials far from each other. Based on the figure, Li-ion cells have a relatively wide potential window, with a very negative potential at the anode (reduction condition) and high potential at the cathode (oxidation condition).

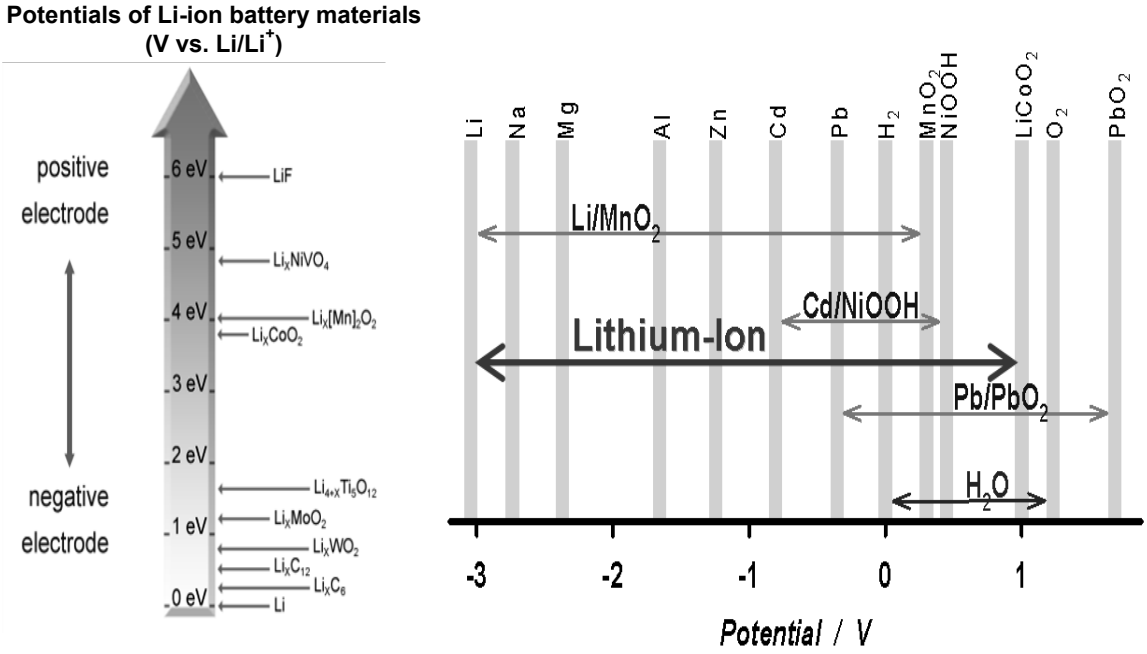

Fig. 2.3 Some standard potentials of battery electrodes [Novák, 2008].

For several of the performance criteria of electrochemical power sources, a distinction must be made between the theoretical values and the practical values. Theoretical values are calculated from the thermodynamics of the electrochemical cell reaction. Practical values are related to the total mass of the complete battery, including the mass of the electrolyte, the separators, the current collectors, the terminals, and the

cell housing [Linden and Reddy, 2002]. In this work, the specific charge (capacity) always refers to the weight of the active component only.

The maximum accessible energy is simply the free energy of the reaction, ΔG. Consequently, high energy results from the choice of electrode materials. This can be achieved by the selection of electrodes with the greatest difference of electrochemical potential, μ [Pletcher, 1991]. The cell voltage can be derived from the standard Gibbs free energy of the equivalent chemical reaction:

$$U^0 = \Delta E^0 = \frac{-\Delta G^0}{nF} \tag{2.7}$$

To evaluate the properties of electrodes in a secondary cell, some general concepts are introduced, and these are written according to the International Union of Pure and Applied Chemistry (IUPAC) Recommendation 1993 [Gritzner and Kreysa, 1993], as follows:

- **Charge capacity** Q (SI unit: mAh or C)

The charge capacity is the total amount of charge obtainable from a cell. It can be derived from Faraday's equation:

$$Q = \int_{t_1}^{t_2} I(t)dt = mnF \tag{2.8}$$

- **Specific charge** q (SI unit: mAh g^{-1} or Ah kg^{-1} or C kg^{-1})

The specific charge is the total charge obtainable under specific discharge conditions from a practical cell in one discharge cycle divided by the total mass of the cell (m_i):

$$q = \frac{nF}{\sum_i m_i} \tag{2.9}$$

The specific charge is often incorrectly called “specific capacity”. Although "specific capacity" is used by many authors for batteries and battery electrodes, according to valid IUPAC recommendations, this term is misleading because "capacity" is the property of a capacitor [Gritzner and Kreysa, 1993; Novák, 2008].

To compare the energy content or energy density content of cells, the terms *specific energy* (Wh kg^{-1}) or *energy density* (Wh dm^{-3}) are employed, whereas the rate capability is expressed either as *specific power* (W kg^{-1}) or *power density* (W dm^{-3}):

- **Specific energy** w (SI unit: Wh kg^{-1} or J kg^{-1})

The specific energy is the amount of electrical energy per unit of mass that a battery is able to deliver, and is a function of the cell potential (V) and charge capacity (Ah kg^{-1}):

$$w = \frac{nF\Delta E^0}{\sum_i m_i} \tag{2.10}$$

- **Energy density** W_V (SI unit: Wh dm^{-3} or J dm^{-3})

The energy density is the amount of electrical energy per unit of volume:

$$W_{V.} = \frac{nF\Delta E^0}{\sum_i V_i} \tag{2.11}$$

- **Specific power** p (SI unit: W kg^{-1})

The specific power is the ability of the cell to deliver power per unit mass:

$$p = \frac{I\Delta E^0}{\sum_i m_i} \tag{2.12}$$

- **Power density** P_v (SI unit: W dm^{-3})

The power density is the power divided by the volume of the cell:

$$P_v = \frac{I\Delta E^0}{\sum_i V_i} \tag{2.13}$$

- **Coulombic Efficiency** (SI unit: %)

The coulombic efficiency represents the ratio of charge released during the discharge to the charge necessary for charging the battery.

$$Coulombic\ Efficiency = \frac{n_{th} Discharge}{n_{th} Charge} x100\% \tag{2.14}$$

- **The charge-discharge rate** *C-rate* (SI unit: h^{-1})

When electrochemically cycling a cell, the term charge-discharge rate or C-rate ($C/\Delta t$) is often employed to describe the time frame for either one full charge or discharge. C denotes either the theoretical charge capacity of a cell or battery (Ah) or the nominal capacity of a cell or battery, as indicated by the manufacturer. For example, C/37 therefore means a current theoretically allowing a full discharge in 37 hours.

- **Irreversible capacity loss** (SI unit**:** %)

It is also important to define how much capacity is lost after each cycle. Irreversible capacity loss is therefore explained by the following equation:

$$Irreversible\ Capacity\ Loss = \frac{n_{th}\ Charge - n_{th}\ Discharge}{n_{th} Charge} \times 100\% \tag{2.15}$$

2.1.5 Advantages and Commercial Applications

A Ragone chart was plotted in Fig. 2.4 to express the energy and power density characteristics for different electrochemical storage systems. Different electrochemical systems have distinct characteristics. Supercapacitors or ultracapacitors, which are located at the right of the chart, provide a small amount of energy over an extremely short time and are thus suitable for fast rate of charge and discharge, i.e. the acceleration of a car at a traffic light. Fuel cells are at the top left corner of the chart. They have high energy density, with the energy delivered over longer times, so they can provide the energy necessary to cruise for a long period at a constant speed when driving on a highway. Batteries are somewhere in between these systems, providing a bridge between the two. This makes them suitable for either replacing or complementing one of the other technologies.

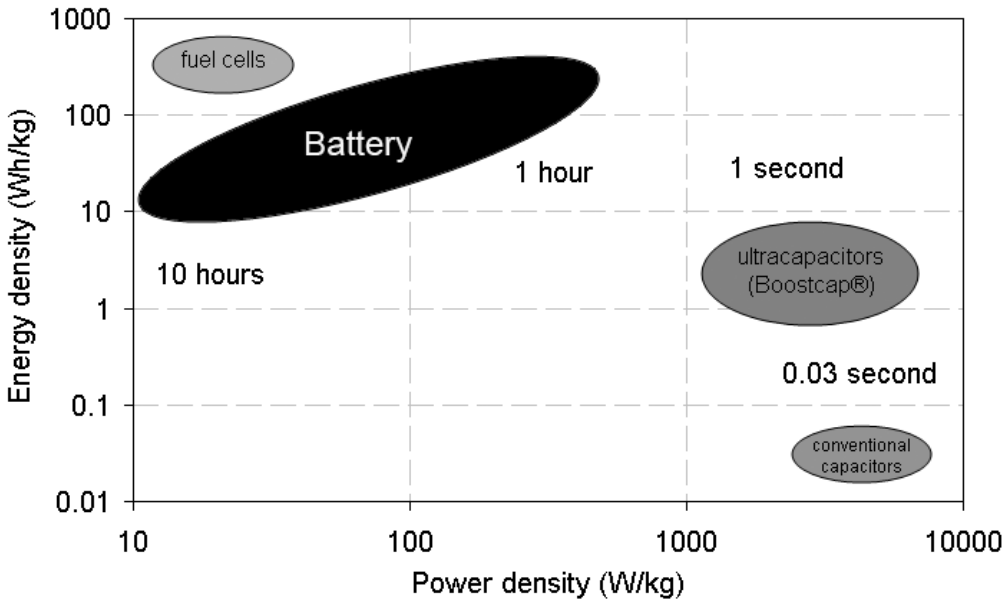

Fig. 2.4 A typical Ragone chart for different electrochemical energy storage systems. They are compared according to their gravimetric energy and power density. Source: http://en.wikipedia.org/wiki/Ragone_chart

Li-ion batteries are most commonly found in the portable market. Thanks to their high energy density, it is possible to have a light and compact energy source that can power electronic devices for several hours or even days. Fig. 2.5 shows a comparison of Li-ion with other rechargeable batteries (NiMH and NiCd).

In this plot, lithium based batteries are in the top right corner of the chart, showing higher gravimetric and volumetric power density. In comparison with other systems, Li-ion batteries show values two or three times higher. This gives the possibility of packing the same energy into half of the weight, which represents an enormous advantage when portability is required. Typical markets for the application of Li-ion batteries are in information technology (camcorder, laptop computer, and digital camera) and portable machine tools (drills, saws, and sanders). Li-ion batteries are used in stationary applications too. They are used in telecommunications to power radio stations for telephone networks when the power network is down [Dell, 2000].

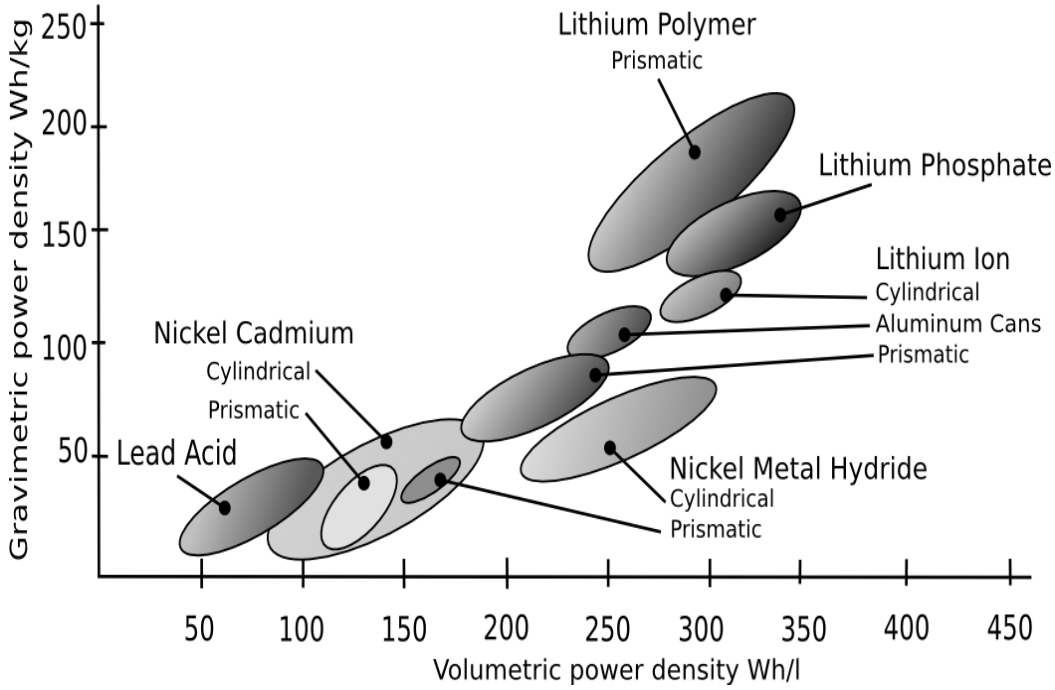

Fig. 2.5 Comparison of various types of rechargeable batteries. Source: http://en.wikipedia.org/wiki/Rechargeable_battery

From the consumer's point of view, Li-ion batteries have the following advantages [Scrosati, 1995; Owen, 1997; Winter *et al.*, 1998; Tarascon and Armand, 2001]:

I. High energy density: approximately double that of Ni-Cd batteries.
II. High output voltage: 3 times greater output power than Ni-Cd batteries.
III. One cell battery pack designs because of the high cell voltage of 3.6 V.
IV. Low maintenance battery: no memory and no scheduled cycling is required to prolong the battery's life.
V. Low self-discharge rate: around 2 % per month at 20 °C.
VI. Long life cycle: 500 recharging cycles with consistent performance.
VII. Cost saving: money is saved on disposal of waste batteries.
VIII. Cause little harm when discarded: Li-ion batteries do not contain cadmium, mercury, or other toxic heavy metals.
IX. Wide operating temperature range due to non-aqueous electrolytes.
X. Lithium has a very negative redox potential, -3.04 V vs. SHE, and also a low molar mass of approximately 7 g mol^{-1}.

According to a new and updated technical market report on lithium batteries, Markets and Materials, from BCC Research, the rechargeable secondary lithium battery market was approximately $4.6 billion in 2006 and will continue growing to more than $6.3 billion by 2012, with a compound annual growth rate of 5.6 %, as shown in Fig. 2.6. A new generation of energy-hungry electronic devices, such as digital cameras, camera phones, and high performance portable computing devices, is the main force driving the growth. Just as lithium batteries replaced nickel-based primary batteries for many applications, current Li-ion battery designs are beginning to be replaced by

advanced lithium-ion chemistries, for examples lithium phosphate, lithium iron phosphate, and especially, lithium polymer systems.

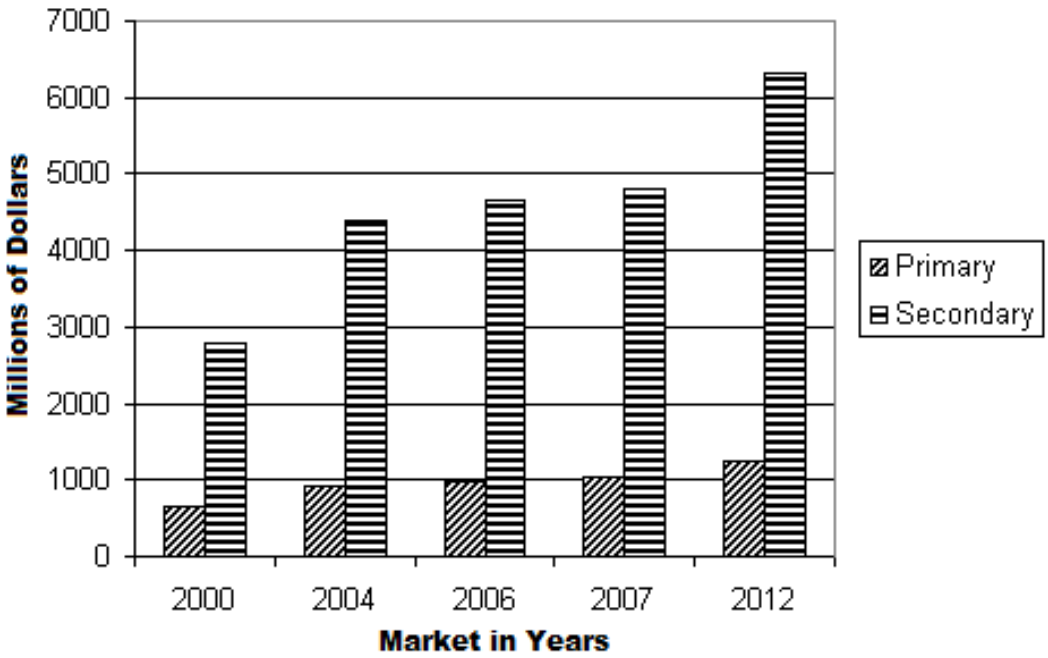

Fig 2.6 Global forecast for lithium battery sales through 2012. Source: http://www.batteriesdigest.com

For many years, nickel-cadmium was the only suitable battery system for portable equipment from wireless communications to mobile computing. Nickel-metal-hydride and Li-ion batteries emerged in the early 1990s, fighting head-to-head to gain customer acceptance. Today, Li-ion is the fastest growing and most promising battery chemistry, and Li-ion will still lead the demand in powering portable devices. Fig. 2.7 shows the distribution of the rechargeable battery market for different applications. Clearly, Li-ion batteries play a major role in PDA, digital camera, motion picture, cellular phone, and computer devices. However, large volume production of batteries for electric and hybrid electric cars has not yet been established.

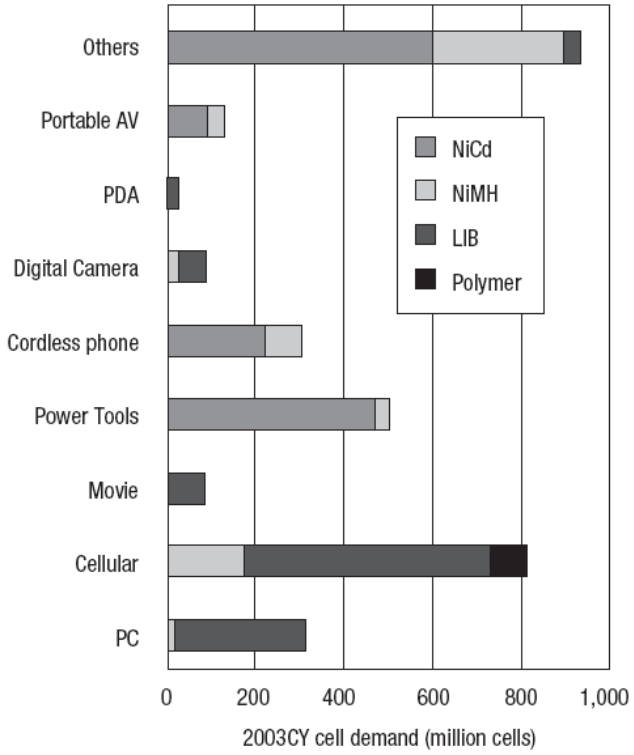

Fig 2.7 Uses for each type of rechargeable battery in the world market. Source: http://www.batteryuniversity.com

The market for rechargeable lithium batteries has been undergoing a rapid expansion. Depending on the functionality, different requirements are needed to cater for different parts of the market, for instance, in portable electronic devices as compared to hybrid electric vehicles and renewable energy storage systems (refer to Fig. 2.8). For renewable energy, batteries are needed to store the electricity for use at night or on cloudy days. The detailed requirements are listed below [Novák, 2008]:

- **Portable electronic devices**

  Operating temperature : +5 – +40 ^{o}C

  Calendar life : 3 – 5 years

  Cycle life : 500 – 1000, deep cycles

  Charge-discharge rate : 0.5 – 2 C

- **Hybrid electric vehicles**

  Operating temperature : ***-40 – +60*** ^{o}C

  Calendar life : ***10 – 15*** *years*

  Cycle life : 3000 – 7000, various cycles

  Charge-discharge rate : 1 – ***10*** *C*

- **Renewable energy storage**

  Operating temperature : ***-20 – +50*** ^{o}C

  Calendar life : ***15 – 20*** *years*

  Cycle life : 10000 – 15000, shallow cycles

  Charge-discharge rate : 0.1 – 0.5 C

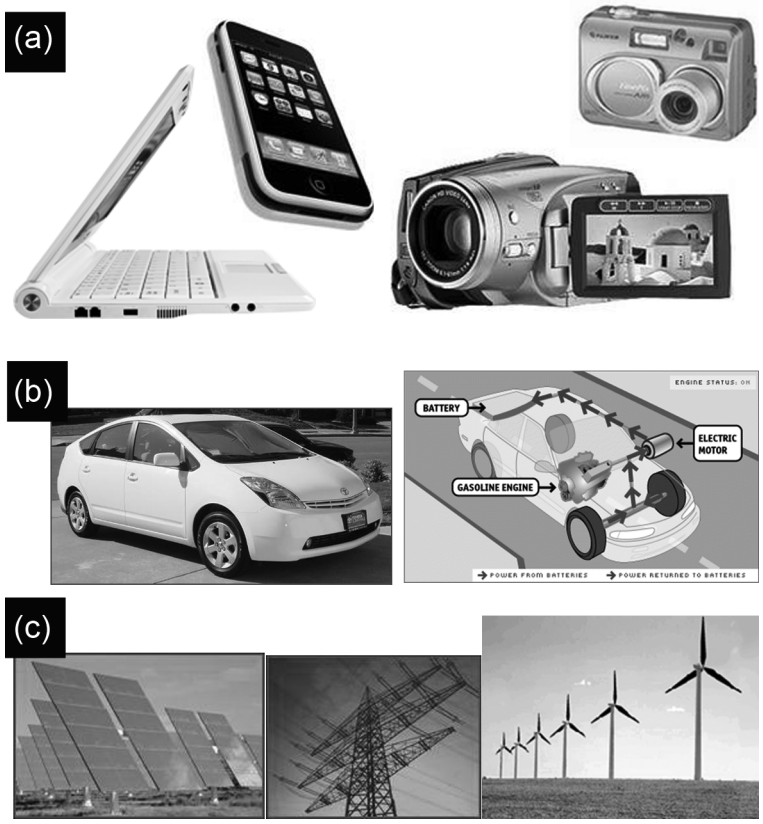

Fig 2.8 Application of Li-ion batteries in (a) portable electronic devices, and potential energy storage in (b) hybrid electric vehicles and (c) renewable energy [Novák, 2008].

Some requirements, which are highlighted in *italics,* are the targeted condition, which is now restricted by the power capability and energy storage capacity of the currently available Li-ion batteries.

2.1.6 The Challenges

Nowadays, thinner, lighter, space-effective, and shape-flexible batteries with larger autonomy are in constant demand from consumers. In addition to use in consumer electronics, Li-ion batteries are growing in popularity and represent a serious challenger in the years to come to take over the defense, automotive, and aerospace markets. Such demand generates more challenges for research and development, to search for new cell configurations and new electrochemistry for the next generation of Li-ion batteries.

2.1.6.1 Materials and Cost

Billions of Li-ion cells are produced, but this is not sustainable, as cobalt ($LiCoO_2$) must be obtained from natural resources. The price of this metal has been extremely unstable in the past few years, and the trend is rising. Additionally, the main cobalt resources are located in politically unstable countries, and this instability makes the supply even more unreliable. Moreover, cobalt is extremely toxic, and it should be properly recycled. Hence, there is an enormous interest, primarily driven by cost and environmental concern to search for alternative insertion compounds.

Regarding performance, the challenge is to enhance both power and energy density for advanced batteries, especially those for use in automotive applications. The power density can be improved by finding materials that can guarantee a higher rate of

charge and discharge, the energy density by enlarging the potential window with positive electrode materials that have an intercalation potential at 5 V vs. Li/Li^+ or more. Consequently, considerable research is being focused on identifying new cathode and anode materials by innovative synthesis and processing procedures to develop low cost materials with high performance. The high intercalation potential window is also limited by the currently available electrolytes. Electrolyte starts to oxidize around 4.5 V vs. Li/Li^+ and therefore is not stable at high potential. Hence, polymer electrolytes and room temperature ionic liquids are being investigated, leading to so-called lithium polymer batteries.

2.1.6.2 Safety

If abused by the user or not carefully designed by the manufacturer, batteries can be potentially dangerous. Li-ion batteries combine highly energetic materials in contact with a flammable electrolyte based on one or more organic solvents. They can suffer premature failure if subjected to particular conditions, such as incineration, overcharging, or external short circuiting or crushing, which can lead to fire and explosion.

Li-ion batteries are considered safe because of their lithiated carbon (Li_xC_6). It has a much higher melting point compared with that of lithium metal. However, exothermic reactions between Li_xC_6 and the electrolyte can be triggered by the application of heat. Besides this, the potential window ranges experienced in common 4 V Li-ion batteries are beyond the stability window of the electrolytes. Therefore, electrolyte decomposes upon contact with the active materials, for both anodes and cathodes. The interface between the cathode and the electrolyte is further complicated

by the dissolution of the active materials. This is a particularly serious problem at the end of charging at elevated temperatures, conditions under which electrolyte oxidation can proceed at accelerated rates.

It is clear that Li-ion batteries which have smaller size and weight will suffer a greater temperature rise than similar batteries that are larger and heavier. Thus, heat dissipation in Li-ion batteries turns out to be a major engineering challenge, especially for batteries that cater for the high power applications. However, much effort has also been made in research to improve the thermal stability by replacing the aqueous electrolytes with non-flammable electrolytes, i.e. polymer electrolytes or ionic liquids. It is hoped that with sustainable research, Li-ion batteries with desirable safety and electrochemical characteristics will emerge.

2.1.6.3 Aging

A unique drawback of the Li-ion battery is that its life span is dependent upon aging (shelf life). From the time of manufacturing, regardless of whether it was charged or the number of charge/discharge cycles, the battery will decline slowly and predictably in capacity. This means that an older battery will not last as long as a new battery, due solely to its age. This aging problem arises from the poor mechanical and chemical stability of the active materials. Aging consists of corrosion of current collectors, irreversible material phase changes, isolation of active materials, electrolyte decomposition, the loss of contact to conductive particles, etc. Again, it is important to find good electro-active candidates that will maintain their mechanical properties, chemical structure, composition, and surface characteristics based on the optimum operating conditions.

2.2 Negative Electrode Materials

Table 2.1 List of negative electrode materials for Li-ion batteries [Ohzuku *et al.*, 1995; Winter *et al.*, 1998b; La Mantia, 2008].

Reduced form	Oxidized form	E_{eq} [a] (Li/Li$^+$) / V	Q_{max} [b] / mAh g^{-1}
Graphite based compounds			
LiC_6	Graphite	0.1	372
$Li_{1/2}C_6$	Graphite	0.13	186
$Li_{1/3}C_6$	Graphite	0.22	124
Alloys			
LiAl	Al	0.35	993
$Li_{17}Sn_4$	Sn	0.42 - 0.66	790
Li_3Sb	Sb	0.9	660
$Li_{21}Si_5$	Si	0.3	4200
Titanates			
Li_xTiO_2	TiO_2	1.8	170
$Li_{4+x}Ti_5O_{12}$	$Li_4Ti_5O_{12}$	1.5	160

[a] The electrochemical activity can be observed in a range of potentials.

[b] The specific charge is relative to the weight of the pristine active material.

E_{eq} is the equilibrium potential, and Q_{max} is the maximum theoretical specific charge.

For a Li-ion battery, the anode is usually composed of lithium metal or a lithium insertion/conversion compound. Graphite is known as the most common commercially available anode material for Li-ion batteries due to its low cost, excellent cyclability, reliability, and non-toxicity [Owen, 1997; Winter *et al.*, 1998b; Tarascon and Armand, 2001]. Table 2.1 lists common alternative materials for the negative electrode in Li-ion batteries.

Most present research is moving towards replacing carbonaceous anode with non-carbonaceous anode, as well as with metal alloys and titanates. The driving force

behind this current research trend is to obtain a new generation of anode materials with higher specific capacities (> 372 mAh g^{-1}) and high power (10 C-rate), while retaining the good properties of carbonaceous materials, such as cyclability, cost, and safety features.

2.2.1 Carbonaceous Materials

The most common active material for negative electrodes in lithium-ion batteries is graphite. It is a layered compound formed by graphene sheets; and Li^+ ions are intercalated between such layers. It forms four different compounds by Li^+ intercalation at low potential, namely Li_yC_6 (refer to Table 2.1). The theoretical specific charge, obtained at y = 1, is equal to 372 mAh g^{-1}. Intercalation of lithium into graphite is highly ordered; there is one intercalated layer for each 1/y layers (stage formation) [Besenhard and Fritz, 1983]. This order is repeated in the whole crystallite. For this reason, lithium-graphite compounds have different structures and different phases. Intercalation potentials of the different phases are between 0.22 and 0.1 V vs. Li/Li^+ [Dahn, 1991]. These characteristics make graphite a good compound for negative electrode in high voltage batteries. The nature and surface of graphite also strongly influence the cycle life of the battery [Goers *et al.*, 2003].

In the potential range of Li^+ intercalation in graphite, most of the electrolytes are thermodynamically unstable. The formation of a stable passivation film at the surface of graphite particles is essential. This passivation film, also called the Solid Electrolyte Interphase (SEI), has to be electronically isolating and to allow the passage of Li^+. It is composed of organic (polymeric) and inorganic lithium salts, formed during the reduction of the electrolyte [Peled, 1979; Besenhard *et al.*, 1995; Aurbach *et al.*, 1999;

Xu, 2004]. The nature and the properties of the SEI are correlated with the surface groups in graphite, as well as with the electrolyte solvents and solutes.

For the non-graphitic carbons, also called hard carbons, lithium can be inserted not only between the graphene layers, but also into the voids of this material and onto the sides of isolated graphene layers. Such carbons show specific charge capacities of around 400 to 2000 Ah kg^{-1}, and are mainly synthesized by pyrolysis of sugars or polymers [Larcher *et al.*, 1999]. The main problem associated with these hard carbons is the high irreversibility, leading to poor cycling stability [Winter *et al.*, 1998b].

Recently, with the discovery of new crystalline carbon nanotubes (CNTs), i.e. the single-wall (SW), double-wall (DW) and multi-wall (MW) types, there appears to be a new paradigm in carbonaceous-based battery electrode materials. CNTs can be visualized as rolled sheets of graphene, which are sometimes capped at each end. They could also be either SW with diameters as small as 0.4 nm, or MW consisting of nested tubes with outer diameters ranging from 5 – 100 nm [Baughman *et al.*, 2002]. Their unique properties allow them to exhibit increased capacity as an active material and induce highly improved cyclic characteristics as an additive to the anode material [Endo *et al.*, 1995; Wu *et al.*, 1999; Lu and Chung, 2001; Frackowiak and Béguin, 2002; Ng *et al.*, 2005].

Based on the scientific report of Meunier *et al.* (2002), it is possible to charge SWCNTs up to one lithium for every three carbon atoms and higher. A significant reversible capacity has been found, up to 1000 mAh g^{-1} for SWCNTs and 780 mAh g^{-1} for MWCNTs [Gao *et al.*, 2001]. However, the large irreversible component of the capacity (coexisting with the large reversible storage capacity), the large hysteresis in voltage between charge and discharge, and the absence of a voltage plateau during lithium de-intercalation for SWCNTs and DWCNTs, currently limit energy storage

density and energy efficiency when compared with those of other competing carbonaceous materials [Frackowiak and Béguin, 2002].

2.2.2 Lithium-Metal Alloys

Lithium alloys, which can be reversibly formed and decomposed electrochemically in non-aqueous electrolyte solutions, are natural alternative candidates to Li anodes in rechargeable Li batteries. Indeed, there are many reports on binary and ternary Li alloys that have been tested as Li battery anodes [Dahn, 1998; Liu *et al.*, 1998; Mohamedi *et al.*, 2001].

Of special importance in this respect are the Li-Sn compounds, because lithium can be inserted into tin to form alloys of high Li content up to $Li_{17}Sn_4$, corresponding to a theoretical capacity of 790 mAh g^{-1} [Winter and Besenhard, 1999]. Since it has the highest known theoretical capacity (4200 mAh g^{-1}), silicon would seem to be a superior anode material for high energy-density Li-ion batteries [Tarascon and Armand, 2001]. The equilibrium potential of such alloys in electrolytes containing Li^+ ranges between 1.0 – 0.3 V vs. Li/Li^+. Compared with lithium-graphite, the equilibrium potential of the lithium alloys is more anodic, thus the specific charge loss in alloys due to the reduction of the solvents in the electrolyte is smaller with respect to the graphites.

It appears that the insertion of lithium in many alloys, including Li-Sn and Li-Si compounds, is accompanied by pronounced volume changes (> 300 %). This lead to an intrinsic instability of the lithiated alloys in solutions: cracking, loss of passivation, intensive reduction of solution species by the lithiated alloy's surface, and electrical disconnection of active mass due to the formation of surface films [Huggins, 1998]. As a result, serious fading is always observed after several cycles. In attempts to improve

the capacity retention of lithium alloy anodes, several methods have been proposed. It is essential to disperse Si and Sn in a highly ductile matrix with a large plastic deformation region. The matrix should also have high electronic conductivity for effective charge transfer reactions to take place. When the inactive metal matrix is replaced by soft carbon [Ng *et al.*, 2006; Park *et al.*, 2008] and polypyrrole [Guo *et al.*, 2005b; Yuan *et al.*, 2006], a significant improvement in capacity retention has been observed. This is due to the compliant nature of the carbon and polymer matrix, which maintains contact during the volume changes.

It is also found that small particles (nanosized) could perform better as anode materials for rechargeable batteries in terms of stability during discharge-charge (lithiation-delithiation) cycling [Winter *et al.*, 1998b; Ng *et al.*, 2006]. Large absolute volume changes can be avoided when the size of the metallic host particles is kept small. In this case, even large volume expansion of the particles does not crack them, as their absolute changes in dimensions are small enough.

The cycle life of the lithium alloys has also been improved by the use of electrochemically reducing compounds based on the alloying metal. During the first cycle, the real active material has to be formed by reduction of the compounds. SnO is a typical example of this class of compounds [Idota *et al.*, 1997; Courtney and Dahn, 1997a]. In both cases a high amount of irreversible specific charge was obtained in the first cycle, due to the electrochemical formation of Sn from the starting compounds, and the formation of Li-SnO matrixes seemed to stabilize the repeated formation of the lithiated alloys.

The commercialized Sony Nexelion cells use tin-based amorphous alloy anode [Miyaki, 2005], with 92 % capacity retention after 100 cycles. This high performance was attributed to the inclusion of multiple metallic elements in the anode, which

minimize dimensional change. These results appear to indicate that alloy-based Si anodes may show potential for commercial Li-ion secondary cells.

2.2.3 Titanium Compounds

Titanium containing compounds, such as the anatase form of titanium dioxide (TiO_2) [Sudant *et al.*, 2005] and titanium spinel ($Li_4Ti_5O_{12}$) [Strobel *et al.*, 1996], are included in the list of negative intercalation electrodes for lithium-ion batteries, even if it is possible to use them as positive electrode. The equilibrium potential of titanium oxide is 1.78 V vs. Li/Li^+, while lithium titanate has an equilibrium potential of 1.56 V vs. Li/Li^+ [Ohzuku *et al.*, 1995; Thackeray, 1999].

Li-ion batteries using such negative electrodes show low voltage (~ 2.0 V) with respect to standard batteries (~ 3.7 V). The maximum theoretical capacity of TiO_2 is around 170 mAh g^{-1}. These characteristics make TiO_2 suitable for low energy Li-ion batteries. Both titanium compounds form two phase systems during Li^+ intercalation, thus showing a very well defined equilibrium potential [Hardwick *et al.*, 2007].

The advantage of using such electrodes is related to the more anodic equilibrium potential of the intercalated compound. In this potential region, no thermodynamic reduction of the electrolyte and no possibility of lithium electroplating occur, allowing the usage of much higher current density, which is favorable for high power and fast charge/discharge. This is not the case for the negative electrodes based on graphite particles, where the equilibrium potential of the Li compound is around 0.1 V vs. Li/Li^+.

2.3 Positive Electrode Materials

Table 2.2: List of alternative cathode materials for Li-ion batteries [Whittingham, 2004; La Mantia, 2008].

Reduced form	Oxidized form	E_{eq}[a] (Li/Li$^+$) / V	Q_{max}[b] / mAh g^{-1}
Layered transition metal oxides			
$LiCoO_2$	Li_xCoO_2	3.5 - 4.2	274
$LiNiO_2$	Li_xNiO_2	3.5 - 4.2	274
$LiMnO_2$	Li_xMnO_2	3.5 - 4.2	285
$Li(NiMnCo)O_2$	$Li_x(NiMnCo)O_2$	3.0 - 4.5[c]	274[c]
Spinel			
$LiMn_2O_4$	$Li_xMn_2O_4$	3 - 4	213
Olivine			
$LiFePO_4$	$FePO_4$	3.4	170
Vanadates			
$Li_{3.6}V_6O_{13}$	$Li_xV_6O_{13}$	2.8	179
LiV_2O_5	$Li_xV_2O_5$	2.3	142

[a] The electrochemical activity can be observed in a range of potentials.

[b] The specific charge is relative to the weight of the pristine active material.

[c] The mixed oxides could show varying behavior depending on the exact composition.

E_{eq} is the equilibrium potential, and Q_{max} is the maximum theoretical specific charge.

In general, the active materials for positive electrodes are compounds based on transition metals which can release lithium ions from the structure by oxidation of the transition metal cations [Whittingham, 2004]. It is a Li^+ host material with a more positive redox potential. To obtain high rate capability and high reversibility, it is important that during intercalation the structure of the active material remains unchanged. Most of the active materials for the positive electrode of lithium-ion batteries have a layered structure, with transition metal ions ordered in one layer (slab)

and lithium ions in the following layer (interslab). The disorder in the structure can be quantified from the amount of transition metals which are in the interslab region. Li^+ ions can diffuse rapidly in the structure only if the material is highly ordered [Winter *et al.*, 1998b; Whittingham, 2004]. Moreover, to obtain high enough specific energy density, it is necessary that at least one Li^+ ion per transition metal atom can be removed from (or accommodated in) the structure. Also, the electronic conductivity of the compounds is important. If it is too low, some conductive additives (mainly carbonaceous) have to be added into the electrode composition. To hold the electrode together, a binder is needed, and thus most electrodes are complex porous composites.

Table 2.2 displays the alternative cathode materials and their corresponding characteristics. The compounds for positive electrodes are generally divided into four major categories: the layered transition metal oxides, the spinel oxides, the olivines, and the vanadates. The crystal structures of layered and spinel oxides and of olivines are illustrated in Fig. 2.9 below based on Wadsley's method. [Ohzuku and Brodd, 2007].

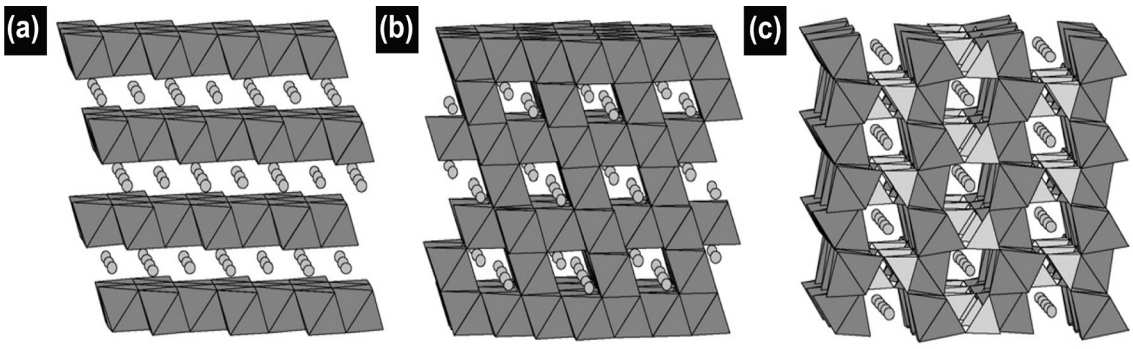

Fig. 2.9 Schematic illustration of (a) layered structure $LiCoO_2$; (b) spinel structure $LiMn_2O_4$; (c) olivine structure $LiFePO_4$, with MO_6-octahedra (M: transition metal) and PO_4-tetrahedra [Ohzuku and Brodd, 2007].

2.3.1 Layered Transition Metal Oxides

Lithium cobalt oxide ($LiCoO_2$) was the first active material for positive electrode that was commercialized on a large scale (by Sony in 1990). $LiCoO_2$ has a layered structure, which means that the Li^+ could be removed or inserted electrochemically. It shows a flat operating voltage of 3.9 V vs. Li/Li^+. However, the actual specific charge of $LiCoO_2$ is only ~ 135 mAh g^{-1}. This is because only 50 % of the Li^+ ions can be removed from the structure. The complete removal of the Li^+ ions from the interslab will result in structural changes and phase transitions. The oxygen layers rearrange themselves to form CoO_2 [Whittingham, 2004]. This CoO_2 is electrochemically inactive with respect to Li^+ ions intercalation. As a result, $LiCoO_2$ is not the perfect cathode material, and there are particular concerns related to the safety of the battery, pollution, health issues, and the cost of the cobalt.

Lithium nickel oxide ($LiNiO_2$) is isostructural with $LiCoO_2$, with Ni having a low cost advantage compared to Co. It has a higher specific charge compared with $LiCoO_2$, but a lower operating voltage, with a sloping charge-discharge profile. This nickel compound has shown too many shortcomings for practical usage. Studies on this compound suggest that its synthesis is difficult due to lithium volatility, and the resulting compound is often highly disordered, since both lithium and nickel have similar atomic radii [Winter *et al.*, 1998b]. Moreover, the de-intercalated compound seems to be unstable and therefore dangerous in contact with organic liquids [Whittingham, 2004]. There have been many attempts to replace part of the nickel with Co or Al [Saadoune and Delmas, 1998; Nakai *et al.*, 1998]. The purpose is to reduce the interslab disorder and thus increase the stability of the structure, especially at low

lithium content. However, due to the lower operating voltage, the composite materials show poor performance in terms of energy density.

Layered lithium manganese oxide ($LiMnO_2$) has a similar structure to $LiCoO_2$, with space group *Pmmn* in an orthorhombic structure [Winter *et al.*, 1998b]. However, the structural stability is hard to retain, as due to the mobile Mn^+ ions, $LiMnO_2$ tends to form a spinel structure. Dahn and his colleagues systematically investigated this layered material and successfully stabilized the structure with titanium and manganese ions in tetravalent states [Paulsen *et al.*, 1999]. The material shows a specific charge of 155 mAh g^{-1} with a sloping charge-discharge characteristic ranging from 2.5 – 3.8 V vs. Li/Li^+. As reported by Ohzuku and Brodd (2007), it is possible to improve the capacity and operating voltage of layered $LiMnO_2$.

In 2001, the fully symmetric compound lithium nickel manganese cobalt oxide, $Li(Ni_yMn_zCo_{1-y-z})O_2$ was proposed [Ohzuku and Makimura, 2001; Whittingham, 2004]. $Li(Ni_yMn_zCo_{1-y-z})O_2$, the so called NMC compounds, represents the third generation of active materials for the positive electrode of lithium-ion batteries. The most studied compounds are the ones with z = y, in particular the z = y = 1/3 compound. As a general rule, manganese and cobalt are present in the structure as Mn^{4+} and Co^{3+}, respectively, while nickel is observed as a combination of Ni^{2+} and Ni^{3+}. Manganese seems to be needed for structure stabilization, nickel offers most of the electrochemical activity, cobalt tends to help the rate capability, and excess lithium increases the capacity [Whittingham, 2004]. It has been shown that upon lithium removal, the unit cell volume change in $Li(Ni_{1/3}Mn_{1/3}Co_{1/3})O_2$ is less than 2% [Kim and Chung, 2004], which is one of the factors that might explain the high cyclability of this material. The NMC compounds can reach a high specific charge (~ 170 mAh g^{-1}) with long cycle life. An over-lithiated form of the NMC, with the general formula $Li_{1+x}(Ni_yMn_zCo_{1-y-z})_{1-x}O_2$, does exist. NMC

encompasses a range of materials that are regarded as promising substitutes for today's industry standard $LiCoO_2$ because of their improved electrochemical performance and thermal stability in the charged state. Nonetheless, their behavior at high potentials (positive to 4.5 V vs. Li/Li^+) and their different long term performance for different values of the lithiation parameter *x* is still opened for debate.

2.3.2 Spinel Oxide

Lithium manganese oxide spinel compound ($LiMn_2O_4$) is a popular positive electrode in Li-ion batteries due to the high abundance of the raw materials, low cost, favorable charge density, rather high electronic conductivity, and suitable electrode potential. The oxide, λ-MnO_2 ($[Mn_2]O_4$), represents the host spinel framework [Winter *et al.*, 1998b]. $LiMn_2O_4$ has a cubic spinel structure, as shown in Fig. 2.9(b), which can be described as a cubic close-packed oxygen array, with the oxygen anions on the 32*e* sites of the *Fd3m* space group. The manganese cations occupy half of the octahedral interstitial sites, 16*d*, and the lithium cations occupy one eighth of the tetrahedral sites, 8*a* [Thackeray *et al.*, 1983].

This spinel oxide was originally proposed by Thackeray *et al*. and has been extensively explored by Bellcore Laboratories [Tarascon *et al.*, 1991; Tarascon and Guyomard, 1993]. It has three equilibrium potentials for lithium ion intercalation: two are in the 4 V potential region (4.0 and 4.1 V vs. Li/Li^+), and these are represented as peaks '2' and '3' in Fig. 2.10; another one is in the 3 V potential region (3.1 V vs. Li/Li^+) and is represented by peak '1' in Fig. 2.10. Usually, only the lithium intercalation peak in the 4 V potential region is used, so that the cell is constructed in the discharged state [Whittingham, 2004]. The average oxidation state of the manganese

is critical to obtain an effective cycle life. When the oxidized state of the manganese experiences the 3 V potential region (normally below 3.50 V vs. Li/Li^+), dissolution of the manganese takes place, and the Jahn-Teller distortion associated with Mn^{3+} ions is produced. This effect transforms the cubic crystal symmetry of the spinel into tetragonal symmetry. A volume expansion of about 6.4 % occurs associated with this phase transition, which results in poor cycling performance [Tarascon *et al.*, 1991].

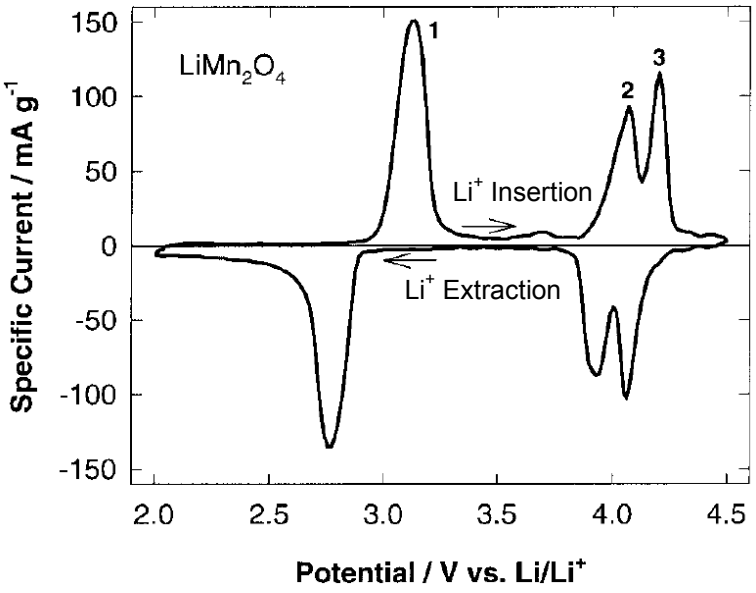

Fig. 2.10 Cyclic voltammogram of $LiMn_2O_4$ spinel [Winter *et al.*, 1998b].

The electrochemical performance in the 4 V potential region of $LiMn_2O_4$ spinel is strongly dependent on the preparation method. $LiMn_2O_4$ compound is traditionally made by sintering the corresponding carbonates in the approximate temperature range between 700 ^oC and 900 ^oC, by the conventional solid-state method [Lanz *et al.*, 2000]. However, this has several disadvantages, such as difficulty in controlling particle sizes, high operating cost, inhomogeneous product with irregular morphology, and poor control of stoichiometry.

A solution-based method has been proposed, with the sol-gel method selected to prepare nanoparticles of $LiMn_2O_4$ spinel, using lithium acetate, manganese acetate, and citric acid as the chelating agent [Bach *et al.*, 1990; Tsumura *et al.*, 1993; Pereira-Ramos, 1995; Ernst *et al.*, 2007]. Nanoparticles of $LiMn_2O_4$ synthesized by a one-step intermediate-temperature solid-state reaction [Guo *et al.*, 2004] demonstrated much higher initial capacity (130 mAh g^{-1}) than that of the commercial material (110 mAh g^{-1}) produced by the conventional solid-state reaction. However, this material will show slight fading on long term cycling. This is attributed to the instability of organic based electrolyte at the very high voltage when charging the cell, where the formation of $Li_{1+x}Mn_2O_4$ phase will lead to the formation of Mn^{2+} because the structure is disproportionate: $2Mn^{3+} = Mn^{2+} + Mn^{4+}$ [Winter *et al.*, 1998b]. Mn^{2+} is soluble in the electrolyte, and so every attempt has to be made to minimize its formation.

This spinel is still attracting much interest as the positive electrode of a high-power Li-ion battery for hybrid electric vehicles, even though at high charge rates this material only has a specific charge of 80 mAh g^{-1} [Whittingham, 2004].

2.3.3 Olivine

$LiFePO_4$ is the first positive material which is low cost, environmentally benign, and can be charged reversibly up to 1 Li per Fe [Padhi *et al.*, 1997]. The compound is an olivine that is electrochemically active to Li^+ intercalation. During de-intercalation, it forms a two phase system: $LiFePO_4$ is in equilibrium with $FePO_4$. The equilibrium potential of such a system in an electrolyte containing Li^+ is equal to 3.4 V vs. Li/Li^+. The theoretical specific charge of the $LiFePO_4$ compound is equal to 170 mAh g^{-1}. The low electronic conductivity of such compounds (10^{-9} S cm^{-1}) does not permit us to use

them "as they are" in positive electrodes [Yamada *et al.*, 2001]. They have to be mixed with carbonaceous compounds. Alternatively, doping with some parts per million of Nb increases the conductivity by 8 orders of magnitude [Chung *et al.*, 2002]. Carbon coating was also used to enhance the electronic conductivity [Huang *et al.*, 2001].

2.3.4 Vanadates

Vanadium oxide, V_2O_5, was one of the first layered oxides to be studied [Whittingham, 1976b]. It has a complex intercalation behavior, involving several phases in relation to the lithium content. After the first full charge, the lithiated compound shows a sloppy behavior during galvanostatic cycling. This effect makes V_2O_5 an unpromising material for practical applications. Other vanadium oxide compounds were also studied, such as V_6O_{13} [Murphy *et al.*, 1979], which can intercalate up to 1 Li per V, and LiV_3O_8 [Besenhard and Schöllhorn, 1976], the structure of which can be expanded to accommodate more lithium ions (Fig. 2.11).

Lithium trivanadate, $Li_{1+\alpha}V_3O_8$ is a non-stoichiometric bronze obtained for α close to 0.1 – 0.2 [Pistoia *et al.*, 1984]. It is an attractive starting material for practical applications in the positive electrode of a rechargeable lithium battery, in the voltage range of 2.0 – 3.7 V vs. Li/Li^+. A normally prepared sample could reversibly insert more than 3 Li atoms per formula unit [West *et al.*, 1987; Dubarry *et al.*, 2004]. $Li_{1+\alpha}V_3O_8$ also has a layered structure, with the stacking of V_3O_8 anionic layers held together by Li^+ ions residing at the octahedral sites, as shown in Fig. 2.11. The V_3O_8 layer is formed by a chain of VO_6 octahedra and VO_5 square pyramids connected to each other by corner/edge sharing [Picciotto *et al.*, 1993].

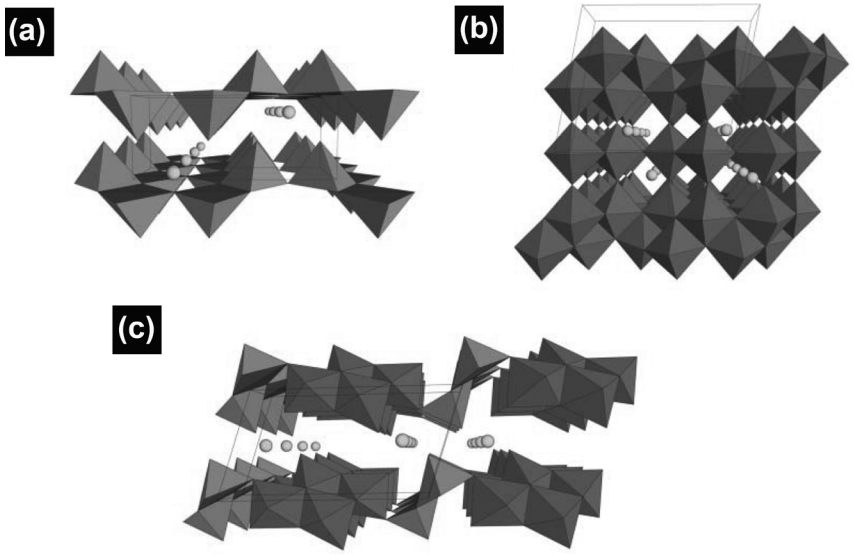

Fig. 2.11 Structures of (a) layered LiV_2O_5 with VO_5 square pyramids; (b) double sheet $Li_xV_6O_{13}$ with VO_6 octahedra; and (c) LiV_3O_8, with both VO_5 square pyramids and VO_6 octahedra. The lithium atoms are round in shape [Adapted from Whittingham *et al.*, 2005].

Previous XRD experiments have shown that the electrochemical insertion of Li^+ occurs into two phases of $Li_{1+x}V_3O_8$: from $x \approx \alpha$ to $x \approx 1.9$, Li^+ is inserted into single phase $Li_{1+\alpha}V_3O_8$ (potential range 3.70 – 2.65 V vs. Li/Li^+); and from $x \approx 3$ to $x \approx 4$, Li^+ is inserted into single phase $Li_4V_3O_8$ (potential range 2.5 – 2.0 V vs. Li/Li^+). In between, the mechanism is a two phase process with the transformation approximately taking place from $Li_{2.9}V_3O_8$ to $Li_4V_3O_8$ [Picciotto *et al.*, 1993; Kawakita *et al.*, 1999].

According to Nassau and Murphy (1981), the electrochemical performance, such as the specific charge, rate capability, and cyclability of LiV_3O_8 are strongly influenced by the preparation method. Many routes have been applied to fabricate LiV_3O_8 particles, which mainly consist of the sol-gel method [Pistoia *et al.*, 1984; Dubarry *et al.*, 2004], rapid cooling [Liu *et al.*, 2002], efficient grinding [Pistoia *et al.*, 1990], hydrothermal synthesis [Xu *et al.*, 2004], the dehydration method using aqueous lithium vanadate gel

[West *et al.*, 1987], microwave-assisted synthesis [Yang *et al.*, 2005], and ultrasonic treatment [Kumagai and Yu, 1997]. Chemical lithiation leading to the composition $Li_{3.8}V_3O_8$ [Chaloner-Gill *et al.*, 2000; Ng *et al.*, 2008] allows the use of these positive electrode materials as the lithium source in cells containing a carbon negative electrode.

2.4 Electrolytes

The electrolyte in electrochemical systems serves as a medium to transfer electrons, as ions, inside the cell between the anode and the cathode. In addition, a separator is placed in between the electrodes to isolate the electronic charge flow.

The electrolyte used in lithium-ion batteries is a combination of linear (ethylene carbonate, EC) and cyclic carbonates (dimethyl carbonate, DMC) as solvents, and lithium hexafluorophosphate ($LiPF_6$) as the salt. A 1M $LiPF_6$ solution of EC:DMC in a 1:1 (wt.) ratio has a conductivity of about 10.7 mS cm^{-1}, and it is usable in the temperature range from -20 to 50 °C. The exact formulation of the electrolyte is very important for the cycle life of the battery [Peled, 1979; Xu, 2004].

Although the conductivity is very high for this non-aqueous electrolyte, it is nevertheless still too low to avoid non-homogeneous usage of thick electrodes when high power is required. Because of the use of the higher oxidation potential (above 4.5 V vs. Li/Li^+) of the cathode, the non-aqueous electrolyte will also suffer from the decomposition reaction. Therefore, the replacement of the liquid electrolyte with thin polymer membrane would be highly desirable. Polymer electrolytes and ionic liquids are believed to be the right candidate electrolytes for the next generation of Li-ion batteries [Meyer, 1998; Buzzeo *et al.*, 2004; Xu, 2004].

2.4.1 Polymer Electrolytes

Polymer electrolytes combine the advantages of solid-state electrochemistry with the ease of processing inherent to plastic materials. The motivation and advantages of using polymer electrolyte in Li-ion batteries are listed in Table 2.3.

Table 2.3 Advantages of polymer electrolyte in Li-ion batteries [Meyer, 2004].

	Advantages	Description
1.	Suppression of dendrite growth	The use of polymer electrolyte provides less free pathways for the formation and growth of lithium dendrite during charging periods, which in turn maximizes the cycling efficiency and reduces the internal short-circuiting of the cells.
2.	Enhanced endurance to varying electrode volume during cycling	Polymer electrolyte is more compliant than conventional inorganic ceramic electrolytes. This feature enables the polymer to adapt to the volume changes of both electrodes that occur during charge-discharge cycling.
3.	Reduced reactivity	Polymer electrolyte, due to its solid-like nature and much lower liquid content, is expected to be less reactive than liquid electrolyte.
4.	Improved safety	Solid-state construction of a polymer electrolyte battery is more tolerant to shock, vibration and mechanical deformation. Cells can be packaged in an evacuated flat "plastic bag" which is prone to corrosion.
5.	Better shape flexibility	A rectangular battery is preferable since it occupies space more efficiently in consumer electronics.

Following the direction proposed by Wright (1998) and Armand (1994), studies by several researchers have led to an understanding of the basic requirements on the polymers to be used as the ideal host, as listed below:-

I. Electrochemically stable in wider voltage windows (0 – 5 V vs. Li/Li^+) to overcome the overcharge/discharge reaction.

II. Sufficient conductivity, above 0.1 – 1 mS cm^{-1} at room temperature to minimize internal resistance.

III. Chemically and electrochemically compatible with electrode materials and other components in the battery.

IV. Good thermal stability (up to 70 ^oC), especially in contact with lithium electrode.

V. High cation mobility to limit concentration polarization.

Poly(ethylene oxide), PEO, is the most widely studied polymer because it has an ability to solvate a wide range of salts, is compatible with a wide range of plasticizers and other polymeric materials, and is also soluble in a number of common organic solvents at room temperature. PEO is a linear polymer with a helical structure (refer to Fig. 2.12(a)). This open structure provides the flexibility of the PEO chains.

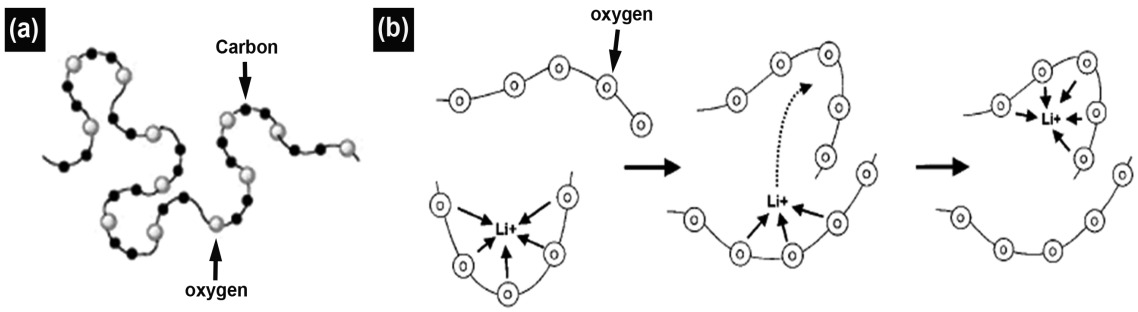

Fig 2.12 (a) PEO with a linear helix structure, (b) schematic of the segmental motion assisted diffusion of Li^+ in the PEO matrix [Meyer, 1998].

PEO can form a double helix structure through the coordination interactions between the ether O of PEO and Li^+, and then Li^+ can be transported in this helical channel through jumps between adjacent coordinate sites (c.f. Fig. 2.12(b)). General

mechanisms for the transport of Li^+ in PEO-based polymer electrolytes are coupled with the local relaxation and segmental motion of PEO chains, but the conditions for this can only be obtained when PEO is in its amorphous state.

Unfortunately, due to its particular structure, PEO often shows much higher crystalline ratios at room temperature, resulting in a very low room temperature ionic conductivity. Besides this, the low melting temperature (T_m) also results in poor dimensional stability. Moreover, batteries must operate at 80°C at least to reach a sufficient ionic conductivity.

In 1994, Bellcore [Tarascon *et al.*, 1996] developed a plasticized electrolyte, which can be considered as midway between a liquid and a dry polymer electrolyte, because it consists of a liquid electrolyte embedded in a polymer matrix mainly based upon poly(vinylidene fluoride-co-hexafluoropropylene), PVdF-HFP. Such a membrane system combines the merits of both technologies, that is to say, good ionic conductivity together with the ability to prepare flexible flat configuration membranes, which prevent liquid electrolyte leakage. However, due to the presence of fluorine atoms, this separator cannot be used in rechargeable lithium cells because of severe chemically-driven interfacial issues that lead to the deterioration of the electrochemical performance of the batteries [Xu, 2004].

To bypass these issues, within this work we have tried to combine the advantages of liquid electrolyte solvated PEO, which ensures a good interface with the lithium, and poly(vinylidene fluoride) PVdF, which enables the fabrication of freestanding liquid electrolyte loaded separators. PVdF has been identified as a potential host for lithium polymer batteries. This PVdF itself has a dielectric constant, ε, of 8.4, which assists in greater ionization of salt and thus provides a higher level of charge

carriers. This polymer host is expected to be more anodically stable because of the strong electron-withdrawing functional group [Manuel Stephan and Nahm, 2006].

In connection with this, a blending technique for composite polymer electrolytes has been considered. Blending can be more useful because of the ease of preparation and the control of the properties of polymer electrolytes allowed by changing the composition of the blended polymer matrix [Xu, 2004]. True polymer batteries may still be some way off, but in the meantime, we will see more attempts to use ionic liquids as either solvents for lithium salts or plasticizers for polyether based electrolytes.

2.4.2 Ionic Liquids

Classical solutions of electrolytes are obtained by dissolution of salts in molecular solvents. On the other hand, a salt may be melted down, or in other words 'liquified', by providing heat to the system to counterbalance the salt lattice energy. Such a system, called molten salts or ionic liquid (IL), consists of ions and their combinations and is free of any molecular solvent. Salts having a low melting point are liquid at room temperature, or even below, and form a new class of liquids usually called room temperature ionic liquids (RTILs) [MacFarlane *et al.*, 2007].

All RTILs share the general structural of a large, poorly coordinated inorganic anion combined with an asymmetrical organic cation. So far, some of the most popular types of these compounds employed in electrochemical studies have incorporated the 1-alkyl-3-methylimidazolium, *N*-methyl-*N*-alkylpyrrolidinium, and tetraalkylammonium cations. On the anionic side, tetrafluoroborate (BF_4^-), hexafluorophosphate (PF_6^-), and bis(trifluoromethylsulfonyl)imide [bistriflimide, $N(Tf)_2^-$] have been most prevalent. The structures of these ions and an explanation of the notation adopted to describe the

various cations are given in Fig. 2.13 [Buzzeo *et al.*, 2004]. The conductivity of RTILs is within a broad range of 0.1 – 18 mS cm^{-1}. The self diffusion coefficients of ionic liquid ions are of the order of 10^{-10} – 10^{-12} m^2 s^{-1}. These relatively low values are due to the high IL viscosity. Basically, the stability windows of ILs are reported to be in a broad range from 2 – 6 V vs. Li/Li^+ [Galiński *et al.*, 2006].

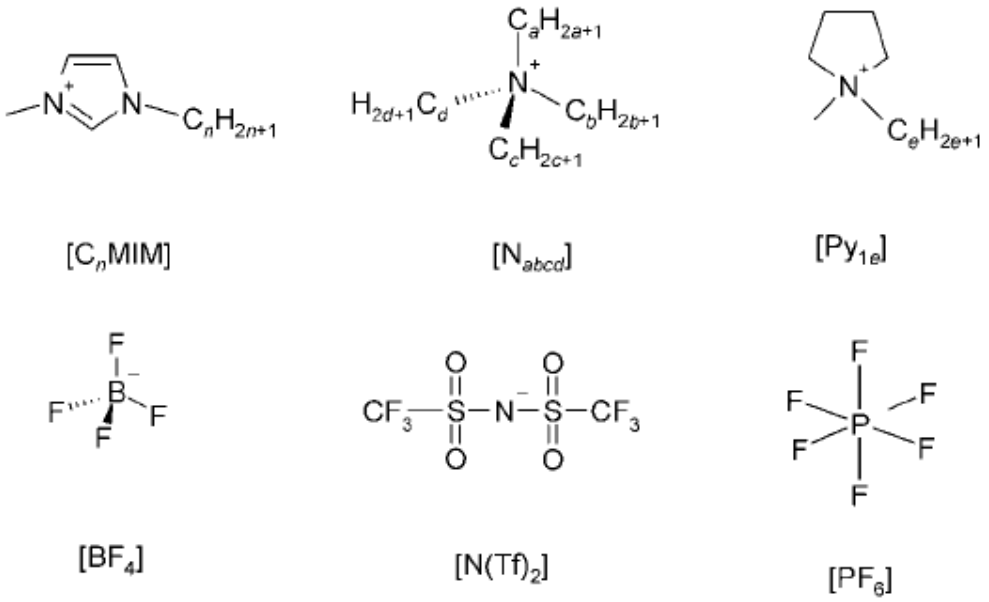

Fig. 2.13 Molecular structures of cations and anions commonly employed in the synthesis of RTILs [Buzzeo *et al.*, 2004].

There have been some attempts to use RTILs as electrolytes in lithium batteries, by dissolving a lithium salt in an ionic liquid. The resulting electrolyte was an IL consisting of three to four ions. The electrolyte was tested in the $Li/LiCoO_2$ system with a lithium foil anode. The *N*-methyl-*N*-propylpiperidinium and bis(triflouromethanesulfonyl)imide electrolyte showed the best properties in the battery: the charge/discharge coulombic efficiency was close to 100 % at a voltage from 3.2 – 4.2 V vs. Li/Li^+ [Sakaebe and Matsumoto, 2003].

RTILs have excessively low vapor pressures, are non-flammable, and have high conductivities, making them serious candidates for safer batteries. But the question remains as to whether they can be produced cheaply, at the desired purity, with sufficient conductivity at low temperature.

2.5 Current Manufacturing Technology and Future Prospects

Typical Li-ion cell constructions are shown in Fig. 2.14. Normally these cells are built in cylindrical, prismatic, or coin-type cell configurations. The basic cell chemistry and design are the same for all types of Li-ion cells. For example, in Fig. 2.14(a), thin layers of cathode, separator, and anode are rolled up on a central mandrel and inserted into a cylindrical can. The gaps are filled with liquid electrolyte. The basic design remains unchanged on substitution of one electrode material for another, although the layer thickness might change.

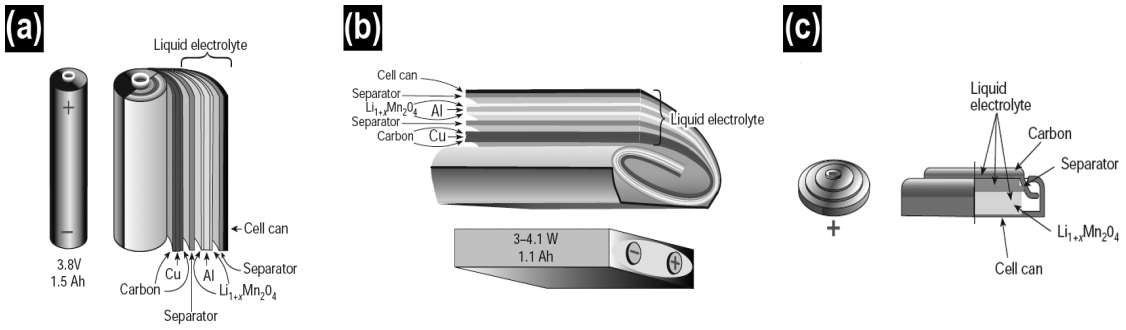

Fig. 2.14 Schematic drawing showing the shapes and components of various Li-ion battery configurations: (a) cylindrical, (b) prismatic, and (c) coin [Tarascon and Armand, 2001].

With the aim of combining the commercial success of liquid Li-ion batteries with the advantages of polymer manufacturing, Bellcore researchers introduced the first

plastic Li-ion, which is based on thin-film battery technology with plasticized polymer electrolyte [Tarascon *et al.*, 1996]. Such batteries have been developed commercially since 1999 and have many potential advantages in the continuing trend towards electronic miniaturization. A schematic drawing of a thin and flat, plastic Li-ion battery is shown in Fig. 2.15.

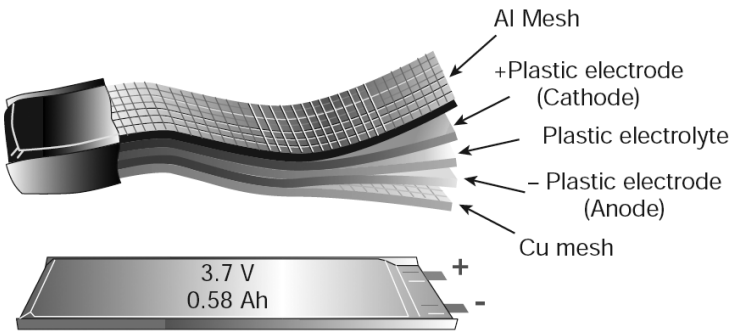

Fig. 2.15 Construction of thin and flat plastic Li-ion battery [Tarascon and Armand, 2001].

Apparently, the next important step in Li-ion battery technology is to replace the liquid electrolyte with a polymer electrolyte, because the all solid-state thin film battery is recognized as the most attractive technology for rechargeable electronic sources, since it combines higher safety and energy density with better formability than is observed in a conventional battery using organic solvent.

Since the polymer- and liquid-electrolyte based battery systems have the same chemistry, both can be expected to give essentially the same energy storage capability. In practice, the Li-ion polymer cells or thin film batteries have a slightly higher internal resistance, which restricts their high-rate capability. The real advantage of the polymer cell construction lies in the internal bonding of the polymer electrolytes to the surface of the anode and cathode. Since the polymer electrolyte films adhere strongly to the

surface of the electrodes, self-supporting cell constructions are possible. This permits the use of a flexible plastic-metal laminate for the cell enclosure, which gives an advantage in weight over the metal can constructions. The internal bonding characteristic also permits large footprint constructions. This is in contrast with the constructions shown in Fig. 2.14, where stack pressure on the electrodes is applied by the metal cans [Brodd *et al.*, 2004]. The thin film Li-ion batteries show good resistance to mechanical and electrical abuse conditions. They can easily pass the crush tests without incident and when overcharged/discharged did not cause a problem.

Much recent work has been focused on flat, two-dimensional configurations, but these are limited in term of energy output. The need for greater performance with less space has recently led to the exploration of three-dimensional (3D) batteries. Notten *et al.* (2006) from Philips Research Laboratories proposed a new all-solid-state 3D-integrated battery concept. The basic principles of this concept are schematically represented in Fig. 2.16 [Notten *et al.*, 2007]. Starting with a thin-film current collector (a) covering a highly doped, well conducting, Si-substrate (b), a large surface area is obtained by anisotropic etching of the Si-substrate. Subsequently, the active battery layers are coherently deposited inside this highly structured substrate, starting with an effective barrier layer (c), preferably TiN or TaN, to protect the substrate from Li penetration, followed by a 50 nm Si thin film anode (d), a solid-state electrolyte, e.g. Li_3PO_4-based, (e) and a thin film, transition metal oxide cathode material, in this example, 1 μm $LiCoO_2$ (f). Deposition of a second current collector (g) completes the 3-D integrated battery. During charging, lithium ions are withdrawn from the $LiCoO_2$ electrode and transported via the solid-state electrolyte to the silicon anode, where they are intercalated.

Similarly, adding a 3D concept opens the ways to a larger variety of configurations (such as the assembly of positive-negative electrodes and electrolyte) while maintaining a short diffusion length for electrodes and ions, which is essential if a battery is to have the required power. Although the benefits of 3D batteries have been clearly demonstrated, the main difficulties lie in finding simple and low cost assembly processes.

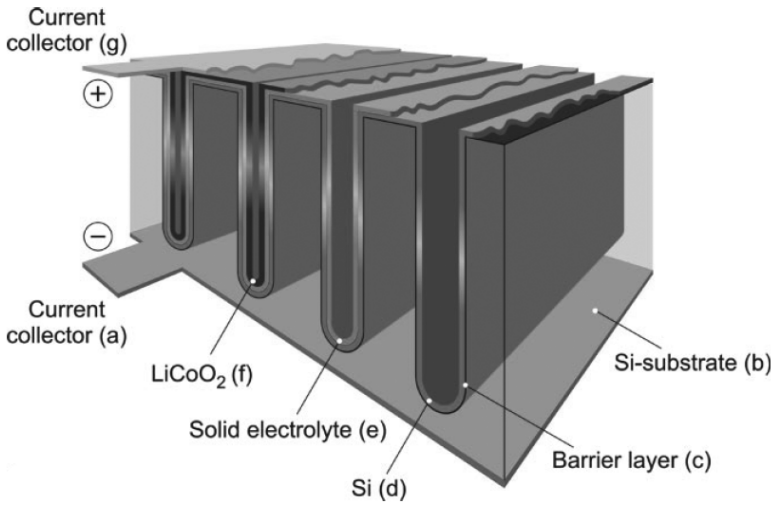

Fig 2.16 3D integrated all-solid-state Li-ion battery for which surface enlargement has been accomplished by electrochemical or reactive ion etching (RIE) of a silicon substrate [Notten *et al.*, 2007].

CHAPTER 3

EXPERIMENTAL DETAILS

3.1 Overview

This research work consists of two main parts: the first part covers the fabrication and characterization of the electrochemically active materials; while the second part involves the application of these electrochemically active materials as electrodes for use in lithium rechargeable batteries.

Various anodes, cathodes, and electrolytes were prepared by using different synthesis routes. They are mainly categorized into 2 forms: powder and thin film materials. Powder based electro-active materials were prepared by the polyol mediated method (tin glycolate), the sol-gel method (LiV_3O_8), and the chemical polymerization method (Si-PPy, LiV_3O_8-PPy). Thin film electrode materials were synthesized by a vacuum filtration technique (CNT films) and a flame spray deposition technique ($LiMn_2O_4$ film). For solid polymer electrolyte (SPE), IL-SPE membrane was prepared by the solvent casting method.

Fig. 3.1 illustrates the overall flowchart of the experimental methodology used in this study.

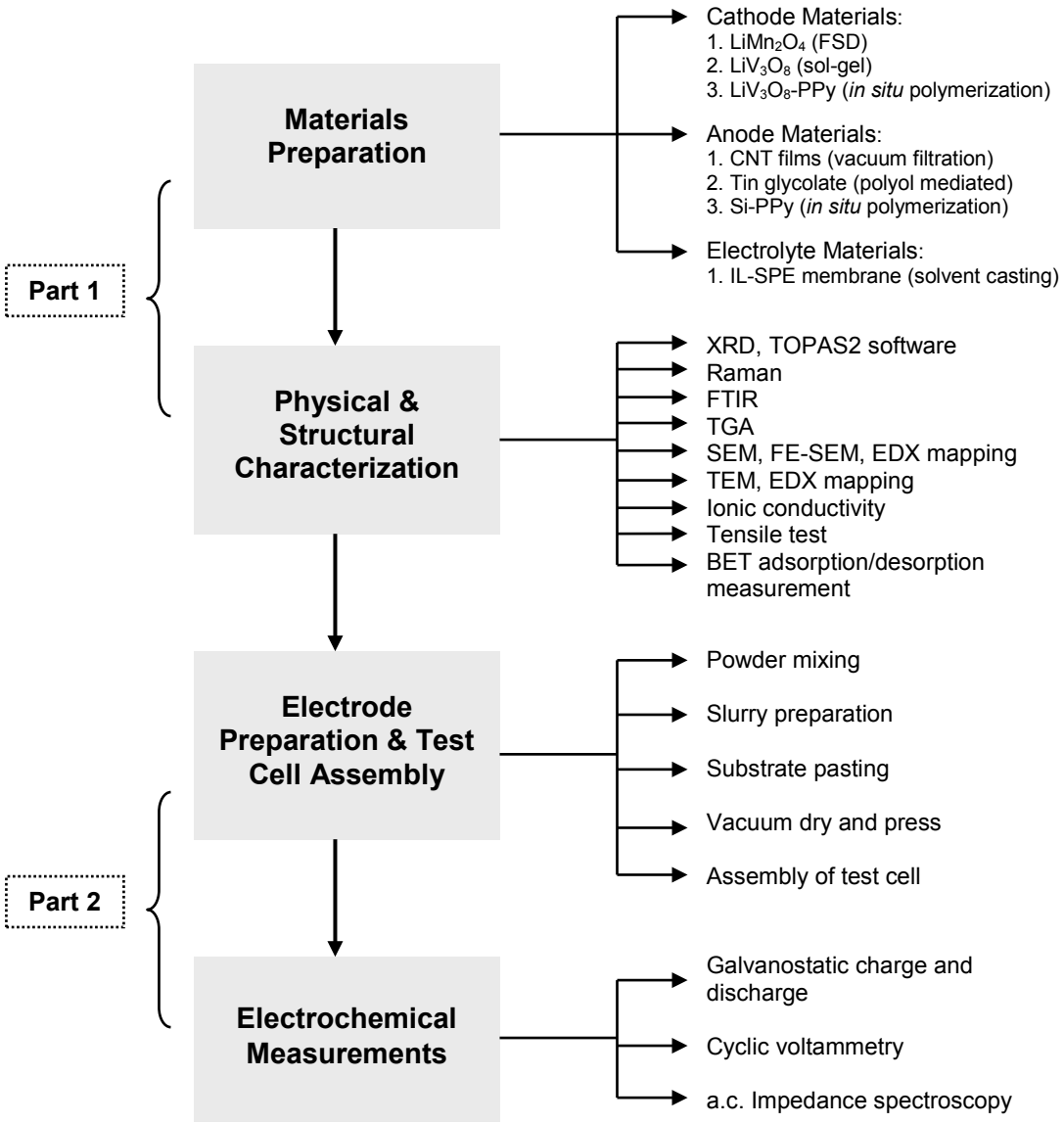

Fig. 3.1 The overall flowchart gives a simplified view of the experimental techniques and procedures.

3.2 List of Materials

The list of materials and chemicals used for the synthesis, characterization, and electrochemical testing is summarized in Table 3.1. The details of the suppliers are also provided for better reference.

Table 3.1: Description of materials and chemicals used throughout the studies. Chemicals are listed in alphabetical order.

Materials/Chemicals	Formula	Purity (%)	Name of Supplier
1,4 butane sulfone	$C_4H_8O_3S$	98	Sigma-Aldrich
1-butylimidazole	$C_7H_{12}N_2$	98	Aldrich
1-methyl pyrrolidine	$C_5D_3H_8N$	98	Aldrich
1-methyl-2-pyrrolidinone (NMP)	C_5H_9NO	99.5	Sigma Aldrich
2-ethylhexanoic acid	$CH_3(CH_2)_3CH(C_2H_5)CO_2H$	99	Riedel-de Haën
Acetone	CH_3COCH_3	99	Chem-Supply
Acetonitrile	CH_3CN	99.5	Sigma Aldrich
Aluminium foil	Al	-	China
Aluminium coated primer foil	ACP	-	GAIA
Carbon black Super P Ensaco 350	C		Timcal
Citric acid anhydrous	$C_6H_8O_7$	99	Sigma Aldrich
Copper foil	Cu	-	China
CR2032 coin-type cells	-	-	Hohsen
Double-wall CNT powder	C	98	Carbon Nanotechnologies Incorporated
Ethanol	C_2H_5OH	Reagent	Sigma Aldrich
Electrolyte	1 M $LiPF_6$ in a 50:50 (w/w) mixture of ethylene carbonate (EC) and dimethyl carbonate (DMC)	-	1. MERCK KgaA, Germany (ISEM) 2. Ferro Corp., USA (PSI)
Ethylene glycol	$HOCH_2CH_2OH$	99.8	Aldrich
Glass fiber separator	-	-	Paul Scherrer Institute (PSI)
Iodopropane	$CH_3CH_2CH_2I$	99	Aldrich
Iron (III) chloride anhydrous	$FeCl_3$	99.99+	Aldrich
Lithium acetylacetonate	$CH_3COCH=C(OLi)CH_3$	97	Aldrich
Lithium hydroxide	LiOH	98	Sigma Aldrich
Lithium metal	-	99.9	Aldrich
Lithium triflouromethanesulfonate	$LiCF_3SO_3$ or LiTFSA	99.995	3M
Manganese (III) acetylacetonate	$Mn(C_5H_7O_2)_3$	-	Aldrich
Methanol	CH_3OH	Reagent	Sigma Aldrich
Milli-Q Water	H_2O	5 ppb (TOC)	Millipore

Table 3.1 (cont.): Description of materials and chemicals used.

Materials/Chemicals	Formula	Purity (%)	Name of Supplier
Multi-wall CNT powder	C	95	Nanostructured & Amorphous Materials Inc
N,N-dimethyl formamide	$HCON(^{13}CH_3)_2$	99 %	Aldrich
Petroleum spirit	-	-	Aldrich
Polypropylene separator	$(C_3H_6)_n$	Celgard 2500	Hoechst Celanese Corporation
Poly(ethylene oxide)	$(-CH_2CH_2O-)_n$	-	Aldrich
Poly(vinylidene fluoride)	$(CH_2CF_2)_n$	-	Fluka
Polyvinylidene fluoride (PVDF) membrane	$(CH_2CF_2)_n$	0.22 μm thick	Millipore
Polyvinylidene fluoride (PVDF) powder	$(CH_2CF_2)_n$	-	Sigma Aldrich
Pyrrole	C_4H_5N	98	Aldrich
Silicon oil	$[-Si(CH_3)_2O-]_n$	-	Aldrich
Silicon powder	Si	325 mesh, 40 nm	Nanostructured & Amorphous Materials Inc
Single-wall CNT powder	C	95 (5 % Fe)	Carbon Nanotechnologies Incorporated
Sodium p-toluenesulfonate (PTSNa)	$CH_3C_6H_4SO_3Na$	95	Aldrich
Stainless steel foil	SS	-	Brütsch-Rüegger
Tin(II) oxalate	$SnC_2O_4.2H_2O$	98	Aldrich
Triton X-100	$(C_2H_4O)_n.C_{14}H_{22}O$	100	Sigma Aldrich
Vanadium pentoxide	V_2O_5	99	Aldrich
Whatman glass fiber filter		257 mm Diameter	Aldrich
Xylene	$C_6H_4(CH_3)_2$	97	Fluka

3.3 Method of Synthesis

The anode, cathode and electrolyte materials used in this study were prepared via either physical or chemical methods. In this section, the synthesis methods and procedures are elaborated in details.

3.3.1 Vacuum Filtration Technique

A vacuum filtration method was adopted and modified for the preparation of free-standing carbon nanotube (CNT) films [Ng *et al.*, 2005]. A typical filtration set-up is presented in Fig 3.2.

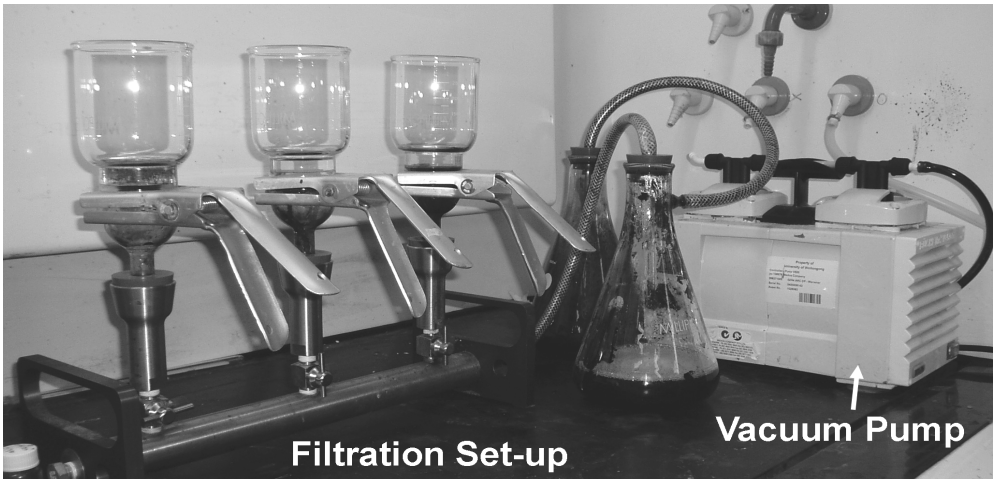

Fig. 3.2 The filtration setup for the fabrication of CNT film.

Three different types of CNTs were used, i.e., single-wall, double-wall, and multi-wall. All CNT powders were used as-received without further purification. In a typical procedure, 30 mg of CNTs and 10 wt % carbon black were dispersed into 1 wt % of Triton X-100 surfactant in 60 mL of distilled water. This suspension was then ultrasonically agitated using a probe sonicator for 2 h with 0.5 s on, 0.5 s off and power output of less than 16 W. These setting can minimize breakage of the CNT bundle and retain the CNT structure [Ng *et al.*, 2005].

To make a uniform film, the as-prepared suspension was filtered through a porous poly(vinylidene fluoride) (PVDF) membrane. As the solvent went through the pores, the CNTs were trapped on the membrane surface, forming a dark layer of entangled CNT mat. The resultant CNT mat was then washed twice with 200 mL of

distilled water, followed by another 100 mL of methanol to remove any remaining surfactant residue. Subsequently, the entangled CNT mat was allowed to dry overnight in a vacuum oven at room temperature. The CNT mat was then peeled off from the PVDF membrane and a free-standing CNT film was obtained.

3.3.2 Flame Spray Deposition

Flame spray pyrolysis (FSP) is a heterogeneous process, where the liquid precursor droplets are sprayed and combusted in the flame [Stark and Pratsinis, 2002]. FSP is capable of producing mixed metal oxide powders with particle sizes ranging from 1 to 200 nm, using low-cost precursors and production rates up to 250 g h^{-1} [Mädler et al., 2006]. Product $LiMn_2O_4$ particles made by FSP were directly deposited onto the current collector, and this process is then called flame spray deposition (FSD); while the rest were collected on a glass fiber filter (Whatmann GF/D, 257 mm in diameter).

All the FSD experiments in this study were conducted in the laboratory of Prof. Pratsinis, also known as the Particle Technology Laboratory (PTL), Institute of Process Engineering, Swiss Federal Institute of Technology (ETH), Zurich, Switzerland. The FSD set-up used in this study is shown in Fig. 3.3.

The spray apparatus consists of an external-mixing gas-assisted nozzle that is made from a capillary tube with an outer diameter of 0.91 mm (inner diameter 0.6 mm) that lies in an opening 1.2 mm in diameter, creating an annular gap with a maximum area of 0.48 mm^2. Precursor and fuel flow through the capillary tube, while the dispersion gas passes through the annular gap. The capillary ends 0.5 mm above the opening to give a constant spray angle at all liquid flow rates.

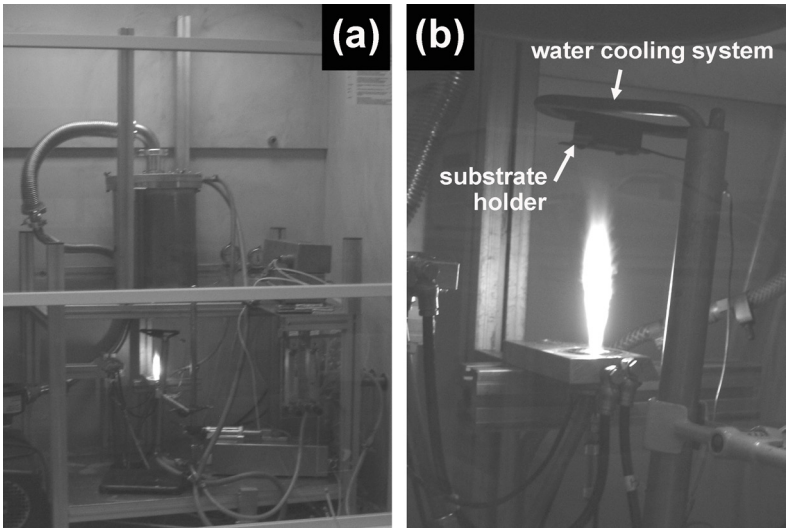

Fig. 3.3 (a) Flame spray pyrolysis experimental set-up inside a fume hood; (b) a close-up of the flame spray deposition process.

The precursor solution was prepared by dissolving lithium acetylacetonate and manganese (III) acetylacetonate in a solution, a mixture of acetonitrile and 2-ethylhexanoic acid [Ernst *et al.*, 2007]. The Li:Mn molar ratio was adjusted to 1:2, and the total metal concentration of the precursor solution was 0.4 M. The precursor solution was fed into the reactor nozzle (Table 1) by a syringe pump (Inotech R232). The liquid spray was ignited and maintained by a premixed methane/oxygen flame ring surrounding the nozzle exit. The $LiMn_2O_4$ nanoparticles were directly deposited onto stainless steel or aluminum-coated primer (ACP) current collectors, which were mounted on a water-cooled copper block [Mädler *et al.*, 2006].

After deposition for 5 min, this film was annealed *in situ* by a pure xylene spray flame [Tricoli *et al.*, 2008]. The SS current collectors were first cleaned with acetone and rinsed three times with distilled water, whereas the ACP current collectors were used as received. The growth or synthesis conditions for the $LiMn_2O_4$ thin films are shown in detail in Table 3.2.

Table 3.2 Growth conditions for $LiMn_2O_4$ thin films.

Current collector	SS and ACP
Precursor solution	$CH_3COCH=C(OLi)CH_3$ and $Mn(C_5H_7O_2)_3$ were dissolved in acetonitrile and 2-ethylhexanoic acid, total metal concentration 0.4 mol L^{-1}
Premixed CH_4/O_2 flame feed rate	1.13 L min^{-1} CH_4 and 2.40 L min^{-1} O_2
O_2 sheath feed rate	5.00 L min^{-1} O_2
Pressure drop at the nozzle tip	1.5 bar
Syringe pump	5 mL min^{-1}
Current collector temperature	120 ^oC
Height above burner (HAB)	150 mm
Deposition time	5 min
In situ flame annealing	5 mL min^{-1} of xylene were introduced for 5 min to the FSP unit

For comparison purposes, the as-synthesized $LiMn_2O_4$ thin films were further annealed via *ex situ* furnace sintering for 2 h at 200 ^oC, 400 ^oC, 600 ^oC, and 800 ^oC, respectively, in air.

3.3.3 Polyol-Mediated Synthetic Method

In a typical procedure, 0.5 g tin (II) oxalate, $SnC_2O_4.2H_2O$, was added into 50 mL of ethylene glycol (EG) in a round bottomed flask and refluxed at 195 ^oC under ambient pressure. A typical layout of the polyol-mediated system is presented in Fig. 3.4.

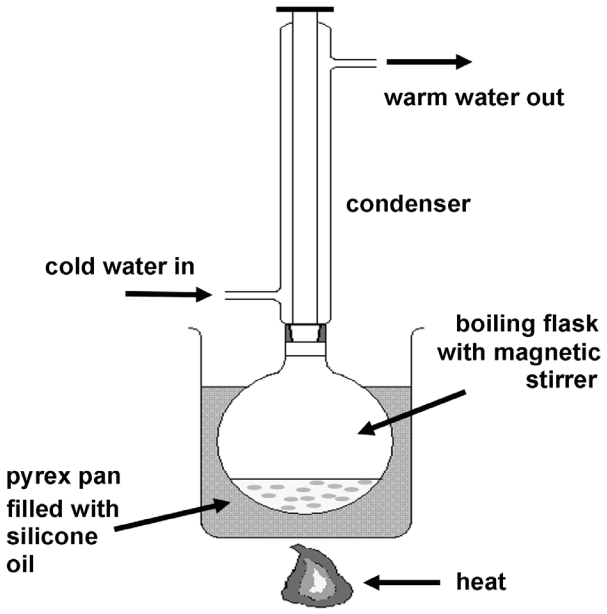

Fig. 3.4 Schematic diagram of polyol-mediated synthetic method.

The reaction can be easily followed through its distinctive color changes. During the first 45 min, the cloudy mixture turned into a clear solution. After the solution had been refluxed under constant stirring for 5 h, white precipitates began to appear in the light yellowish solution, indicating the formation of the tin glycolate crystals. After the reaction had been stopped by cooling down the solution to room temperature, the white precipitates were collected by centrifugation at 4400 rpm, followed by washing with ethanol and acetone to remove physically adsorbed EG. Finally, the as-synthesized tin glycolate powders were dried for 30 min at 80 ^{o}C in a vacuum oven.

In order to compare the electrochemical properties of the as-synthesized tin glycolate crystals with standard tin oxides, a series of tin oxide powders were produced by calcining the as-synthesized tin glycolate crystals in air for 2 h at 600 ^{o}C, 700 ^{o}C, and 800 ^{o}C, respectively.

3.3.4 Sol-Gel Method

Lithium trivanadate, LiV_3O_8, was prepared by a low temperature, rheological phase reaction sol gel method [Liu *et al.*, 2002]. The starting materials were analytically pure lithium hydroxide (LiOH), vanadium pentoxide (V_2O_5), and citric acid ($C_6H_8O_7$). First, stoichiometrically weighed amounts of LiOH, V_2O_5, and citric acid (1:1.5:4.8) were prepared. LiOH and V_2O_5 were mechanically mixed in an agate mortar. Citric acid and a limited amount of distilled water were then added slowly into the ground mixture to form a solid-liquid rheological phase. The mixture was then maintained at 80 ^oC for 12 h in a vacuum oven to evaporate the water, and a dark green precursor was obtained. Subsequently, the precursor was transferred to a porcelain crucible and sintered at 450 ^oC for 4 h, followed by 480 ^oC for 12 h, whereupon a dark brown material was obtained.

3.3.5 *In Situ* Oxidative Chemical Polymerization Method

3.3.5.1 Preparation of Si-PPy

Silicon-polypyrrole (Si-PPy) nanocomposites were prepared by the *in situ* oxidative chemical polymerization method with sodium p-toluenesulfonate (PTSNa) as the dopant and $FeCl_3$ as the oxidant. The molar ratio of monomer pyrrole to dopant was 3:1, and the molar ratio of pyrrole to oxidant was 1:3. Nanocrystalline Si powder (average size: 40 nm) was dispersed in a solution of PTSNa and pyrrole in 100 mL distilled water. The mixture was stirred while the oxidation agent, a $FeCl_3$ solution in 50 mL distilled water, was slowly added to the previous aqueous solution. The reaction

mixtures were then kept under the same conditions for 20 h. The total black mass was centrifuged, and then the mass was washed thoroughly with distilled water until free of $FeCl_3$. Finally, the black mass was dried at 50 ^oC for 4 h under vacuum.

Adding appropriate weights of the pyrrole monomer to 100 mg of Si nanopowder could vary the polypyrrole content in the composites. Before polymerization, the monomer was distilled and guarded against exposure to light to prevent residual polymerization.

Table 3.3 Formulation of Si-PPy nanocomposite.

Chemical		33 wt. %	50 wt. %	66 wt. %
Si	(mg)	100	100	100
PTSNa	(μg)	1.03	2.57	5.66
Pyrrole	(mg)	40	100	230
$FeCl_3$	(mg)	0.01	0.03	0.06

3.3.5.2 Preparation of LiV_3O_8-PPy

For 24 wt. % PPy coated onto LiV_3O_8, 1.0 g of LiV_3O_8 was dispersed into 100 mL distilled water containing 0.013 mol dm^{-3} sodium p-toluenesulfonate (PTSNa) and 0.038 mol dm^{-3} pyrrole. The mixture was magnetically stirred while 50 mL of 0.24 mol dm^{-3} iron (III) chloride anhydrous ($FeCl_3$) solution was slowly injected into the aqueous solution. It was observed after injecting $FeCl_3$ that the color of the mixture changed from dark brown to black, indicating the deposition of PPy on the surfaces of the oxide particles. Stirring of the reaction mixture was maintained for 20 h. The LiV_3O_8-PPy particles were separated from the mixture via centrifugation at 4400 rpm

for 1 hr, then washed several times with distilled water and finally dried under vacuum at 60 ^{o}C for 4h.

Table 3.4 Formulation of *in situ* chemically prepared LiV_3O_8-PPy nanocomposite.

Chemical		10 wt. %	24 wt. %
LiV_3O_8	(g)	1.00	1.00
PTSNa	(g)	0.15	0.25
Pyrrole	(g)	0.15	0.25
$FeCl_3$	(g)	1.13	1.86

For comparison purposes, mechanically prepared LiV_3O_8-PPy composite was made by high energy ball milling. The conductive PPy was prepared via oxidative chemical polymerization. The liquid pyrrole monomer, PTSNa, was dispersed in distilled water. The solution was then magnetically stirred at room temperature for 6 h to complete the polymerization reaction.

The mechanically prepared composite powder of LiV_3O_8-PPy was synthesized as follows: A measured amount of as-prepared polypyrrole powder was first dispersed in ethanol, followed by the addition of as-prepared LiV_3O_8 powder. The mixture was packed into a hardened steel vial containing steel balls, and the vial was sealed inside an argon filled glove box in order to avoid oxidation. A Retsch MM301 high-energy mechanical mill was used. After ball-milling for 24 h, the composite powder was dried at 80 °C for 12 h.

3.3.6 Preparation of Ionic Liquid-Polymer Electrolyte (IL-PE) Composite Membrane

The IL-PE composite membrane was prepared by a well-known solvent casting technique, using poly(ethylene oxide), PEO (M_W =300,000), and poly(vinylidene fluoride), PVDF (M_W = 130 000), as the polymer host.

Synthesis of all the electrolytes synthesized in this work was conducted at the Department of Materials Engineering, Monash University, Australia with the kind collaboration of Dr. Jiazeng Sun.

In this work, electrolytes were prepared by adding 0.5 mol kg^{-1} lithium triflouromethanesulfonate (LiTFSA) to P_{13}TFSA. This was then followed by adding 0.15 mol kg^{-1} of zwitterion (ZW) into the electrolytes. Both the P_{13}TFSA and the ZW were prepared in the laboratory, and the detailed synthesis routes are listed below. Stoichiometric quantities of the polymer, LiTFSA, P_{13}TFSA, and ZW were dissolved in *N,N*-dimethyl formamide (DMF) and acetonitrile, followed by continuous stirring for 24 h (refer to Table 3.5).

Table 3.5 Composition of IL-PE composite membrane.

PEO	=	24.7 wt. %
PVDF	=	16.5 wt. %
LiTFSA	=	8.1 wt. %
P_{13}LiTFSA	=	48.2 wt. %
ZW	=	2.5 wt. %

The polymer electrolyte solution was treated in an ultrasonic bath at room temperature for 2 h to form a homogeneous mixture before casting. The solvent was

allowed to evaporate at room temperature, and then the film was further vacuum dried at 60 ^{o}C to form a free-standing film with a thickness in the range of ~ 200 μm. A typical image of the IL-PE membrane is shown in Fig. 3.5.

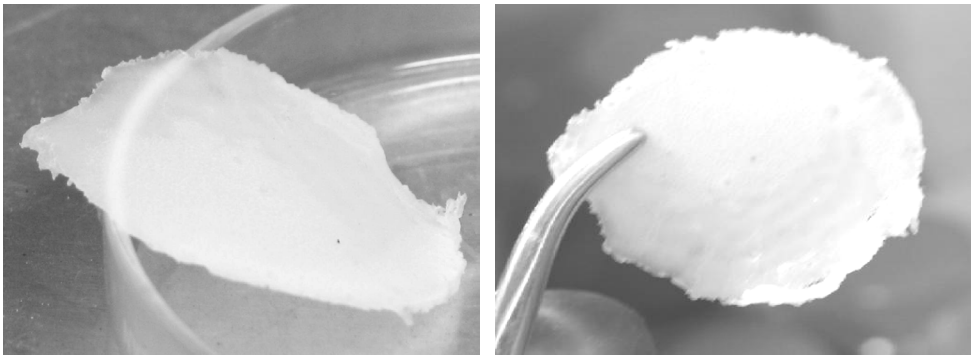

Fig 3.5 As-prepared IL-PE membrane.

3.3.6.1 Synthesis of Room Temperature Ionic Liquid (RTIL), *N*-methyl-*N*-propyl pyrrolidinium bis(trifluoromethanesulfonyl) amide [P_{13}TFSA]

Firstly, *N*-methyl-*N*-propyl pyrrolidinium iodide (P_{13}-I) was synthesized by adding 6.30 g (0.069 mol) 1-methyl pyrrolidine mixed with 15.00 g acetonitrile; 12.08 g (0.085 mol) iodopropane was added dropwise into the pyrrolidine solution, and N_2 bubbling was used. The mixture was stirred at ~ 60 ^{o}C (oil bath) overnight. The solvent was removed by distillation, and the solid product was washed with petroleum spirit three times. The final product was dried under vacuum at room temperature for more than 48 h, and 15.00 g of the product was obtained.

For P_{13}TFSA, 1.60 g (0.0056 mol) LiTFSA salt was dissolved in 2.00 g distilled water. P_{13}-I was also dissolved in 2.00 g distilled water. The two aqueous solutions were mixed together and then stirred at room temperature for 3 h. The product (organic phase) was separated from the aqueous phase by a separating funnel and washed with

distilled water twice to remove any water-soluble impurities. The final product was dried under vacuum at room temperature, and 1.79 g of the product was obtained.

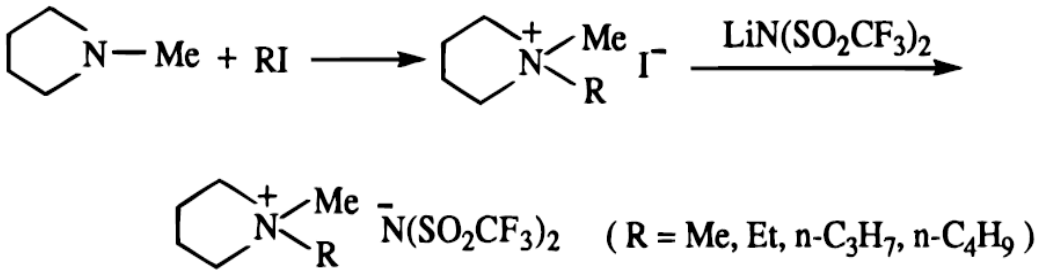

Fig. 3.6 Synthesis route of RTIL, P_{13}TFSA.

3.3.6.2 Synthesis of zwitterionic compound (ZW), 1-butylimidazolium-3-(n-butanesulfonate)

1-butylimidazole (15 g, 0.1208 mol) was added to a solution of 1,4 butane sultone (12.36 ml, 0.1208 mol) in acetone (50 ml) and the solution was stirred under N_2 for 6 days at room temperature, where the product slowly formed as a white precipitate. It was then removed by filtration under N_2. The product was washed three times with acetone and dried under vacuum. The product obtained was a hygroscopic white powder with the structure shown in Fig. 3.7.

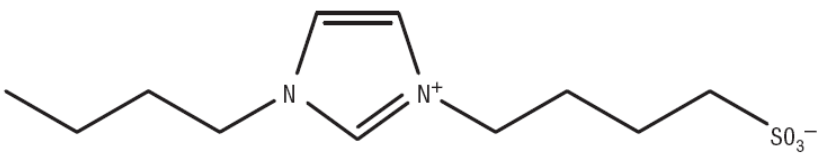

Fig. 3.7 The structure of the ZW compound, 1-butylimidazolium-3-(n-butanesulfonate).

3.4 Physical and Structural Characterization

Physical and structural characterizations of the as-synthesized materials were based on techniques described in detail in the following section. Most of the equipment for these characterization techniques was available in our Institute, with the exception of a few pieces of equipment used at the Paul Scherrer Institute (PSI), Switzerland and Monash University, Australia.

3.4.1 X-Ray Diffraction (XRD)

X-ray scattering techniques are a family of non-destructive analytical techniques which reveal information about the crystallographic structure, chemical composition, and physical properties of materials and thin films. These techniques are based on observing the scattered intensity of an X-ray beam hitting a sample as a function of incident and scattering angle, polarization, and wavelength or energy.

Bragg diffraction occurs when electromagnetic radiation or subatomic particle waves with wavelength comparable to the atomic spacings are incident upon a crystalline sample, scattered by the atoms in the system, and undergo constructive interference in accordance with Bragg's law. For a crystalline solid, the waves are scattered from lattice planes separated by the inter-planar distance d. Where the scattered waves interfere constructively, they remain in phase, since the path length of each wave is equal to an integer multiple of the wavelength. The path difference between two waves undergoing constructive interference is given by $2d \sin \theta$, where θ is the scattering angle. This leads to Bragg's law which describes the condition for

constructive interference from successive crystallographic planes (h,k,l) [Bragg and Bragg, 1913] of the crystalline lattice:

$$n\lambda = 2d\sin\theta \tag{3.1}$$

A diffraction pattern is obtained by measuring the intensity of scattered waves as a function of scattering angle. Very strong intensities known as Bragg peaks are obtained in the diffraction pattern when scattered waves satisfy the Bragg condition. Fig. 3.8 illustrates the interference between waves scattered from two adjacent planes of atoms in a crystal.

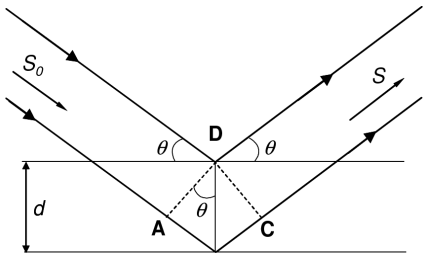

Fig. 3.8 Reflection of X-rays from lattice planes according to Bragg's law [Giacovazzo, 2002].

In addition to identifying crystalline phases, X-ray diffraction can also be used to determine the crystal size. This can be obtained from the broadening of the peaks according to the Scherrer formulae (Eq. 3.2):

$$L = \frac{K\lambda}{\beta\cos\theta} \tag{3.2}$$

where L is the crystal size, λ is the X-ray wavelength used, K is the shape factor of the average crystallite (with a typical shape factor in the neighborhood of 0.9), β is the full width at half maximum (FWHM) in radians, and θ is the peak position.

The phase purity and crystal structure of all prepared samples were collected in a 2θ configuration using a Philips PW 1730 diffractometer (Cu K_α radiation, λ = 1.5418 Å) using a scan rate of 2° min^{-1}. All XRD patterns were analyzed using the Difftech Traces v6 software package and cross-matched with the International Centre for Diffraction Data (ICDD) database (2003). For the $LiMn_2O_4$ thin film prepared in Switzerland, a Bruker AXS D8 Advance device operated at 40 kV and 40 mA with Cu Kα radiation (λ = 1.5405 Å) was used at PTL, ETH Zurich, and the data was analyzed with the TOPAS2 software package.

3.4.2 Raman Spectroscopy

Laser Raman spectroscopy is a spectroscopic technique used in condensed matter physics and chemistry to study vibrational, rotational, and other low-frequency modes in a system [Belin and Epron, 2005]. It gives information about the vibration of atoms in crystals and molecules and can be used as a complementary tool to XRD. Raman spectroscopy was used in this study to characterize the different forms of carbon for CNT films and also to identify the PPy content in Si nanocomposite. A JOBIN YVON HR800 Confocal Raman system with 632.8 nm diode laser excitation on a 300 lines mm^{-1} grating at room temperature was used. The spectroscopy was performed with the kind collaboration of Dr. Jun Chen from IPRI.

3.4.3 Fourier Transform Infrared (FT-IR) Spectroscopy

Fourier Transform Infrared (FT-IR) spectroscopy is a chemically-specific analysis technique. FT-IR is an absorption technique. When a quantum of infrared light

interacts with a molecule, the molecule may absorb the energy and vibrate faster. FT-IR spectra were acquired for tin glycolate based materials in this study to identify chemical compounds and substituent groups under ambient conditions using a Nicolet Avatar 360 Fourier Transform Infrared Spectrophotometer with a resolution of 0.5 cm^{-1}.

3.4.4 Thermogravimetric Analysis (TGA)

Thermogravimetric Analysis (TGA) is a type of testing that is performed on samples to determine changes in weight in relation to changes in temperature. Such analysis relies on a high degree of precision in three measurements: weight, temperature, and temperature change. As many weight loss curves look similar, the weight loss curve may require transformation before results can be interpreted. A derivative weight loss curve can be used to tell the point at which weight loss is most apparent. Again, interpretation is limited without further modifications, and deconvolution of the overlapping peaks may be required.

TGA is also commonly employed in research and testing to determine characteristics of materials such as polymers, to determine degradation temperatures, absorbed moisture content of materials, the level of inorganic and organic components in materials, decomposition points of explosives, and solvent residues.

Precise PPy contents in the Si and LiV_3O_8 composites were determined by TGA. In addition, the compositional and structural changes associated with the calcination process were also followed using TGA. Here, TA Instruments Q500 (U.S.A.) equipment with a heating rate of 10 $^oC\ min^{-1}$ under a flow of oxygen gas was used. The equipment offers high sensitivity, with very low baseline drift over the temperature range from

ambient to 1000 °C. Sample pan loading and furnace movement are totally automated. Normally, a sample mass of approximately 0.10 mg is required.

3.4.5 Scanning Electron Microscopy (SEM)

Scanning electron microscopy (SEM) is used primarily to observe an electrode's surface topography or the morphology of powder samples. During the SEM measurements, the sample is bombarded with a scanning beam of electrons. The electrons interact with the atoms that make up the sample, producing signals that contain information about the sample's surface topography, composition, and other properties such as electrical conductivity. Electrodes before and after electrochemical cycling were analyzed by SEM. Cycled electrode were first washed with a solvent (DMC) to remove the electrolyte and subsequently dried in argon atmosphere before the SEM experiment.

Powder morphologies were investigated using a JEOL JSM 6460A scanning electron microscope (SEM) in ISEM. Energy dispersive X-ray spectroscopy (EDX) was conducted for the elemental analysis or chemical characterization of the sample. Some of the higher resolution SEM images in this research work were obtained by using a field emission scanning electron microscope (FE-SEM; Leo 1530 Gemini), which was functioning at an accelerating voltage of 1 kV and uses an in-lens detector to obtain the secondary electron images. All FE-SEM measurements were carried out with the kind collaboration of Dr. Frank Krumeich from the Laboratory of Inorganic Chemistry, ETH Zurich, Switzerland.

3.4.6 Transmission Electron Microscopy (TEM)

In Transmission Electron Microscopy (TEM), the sample is again bombarded with a beam of electrons, and the intensity of diffraction of these electrons depends on the orientation of the planes of atoms in the crystal relative to the electron beam. At certain angles the electron beam is diffracted strongly, sending electrons away from the axis of the incoming beam, while at other angles the beam is largely transmitted. The sample can be tilted with respect to the electron beam in order to obtain specific diffraction conditions. A high contrast image can be created by blocking electrons deflected away from the optical axis of the microscope by placing the aperture so as to allow only non-scattered electrons through. This allows a resolution on the order of Angstroms, which allows the imaging of individual atoms in a crystal.

TEM investigations were performed using a Philips CM200 transmission electron microscope (TEM) operating at 200 kV. Chemical analysis was performed using an energy dispersive X-ray spectroscopy (EDX) system interfaced to the TEM. TEM samples were prepared by deposition of ground particles onto lacey carbon support films. The TEM measurements for Si-PPy nanocomposite research work were performed with the kind collaboration of Prof. Paul Munroe from the Electron Microscopy Unit, University of New South Wales, Australia.

3.4.7 Brunauer Emmett Teller (BET) Adsorption/Desorption Measurement

Brunauer Emmett Teller (BET) theory is a well-known rule for the physical adsorption of gas molecules on a solid surface, which is the basis for an important analysis technique for the measurement of the specific surface area (SSA) of a material.

Porosity of powders can be conveniently characterized by gas adsorption studies. Normally, pores with diameters in the range of 20 - 500 Å are called 'mesopores'. Two common techniques for describing porosity depend on the determination of the total pore volume and the pore size distribution, respectively. Generally, the desorption isotherm is more appropriate than the adsorption isotherm for evaluating the pore size distribution of the absorbent (e.g. CNTs). Here, the Density Functional Theory (DFT)/Monte-Carlo method was applied for pore size analysis because it provide much more accurate microscopic theories for the description of the filling of micropores and even narrow pores.

Measurements of the BET SSA and the mesopore volume of the CNT powders and films were conducted at PSI, Switzerland through a nitrogen adsorption/desorption isotherm at 77 K using Autosorb-1 equipment from Quantachrome Instruments. Prior to the adsorption process, the samples were outgassed (10^{-6} mbar) at 300 °C for 24 h. The total pore volumes (V_{meso}) were determined with the DFT/Monte-Carlo method from the amount of nitrogen absorbed at $p/p_0 \approx 0.99$. Typically, a sample mass of approximately 40 mg is required for CNT materials, depending on the sample density.

For $LiMn_2O_4$ nanopowders, the BET SSA of the powder before and after *in situ* annealing, collected from the glass fiber, was determined by the five-point nitrogen adsorption isotherm at 77 K, using a Micromeritics Tristar 3000 at PTL, ETH Zurich. All samples were degassed in N_2 at 150 °C for 1 h prior to analysis.

3.4.8 Ionic Conductivity Measurement

Conductance measurements for the IL-PE membranes were carried out in a locally designed conductance cell, consisting of two steel disk electrodes. This work

was carried out with the kind collaboration of Dr Jiazeng Sun from Monash University, Australia. The IL-PE membrane samples were placed between the two steel disks, and then this assembly was sealed tightly in the cell container under nitrogen atmosphere. The cell constant in each measurement was determined by measuring the thickness and radii of the samples. The conductance of the samples was obtained by measurements on the cell between 20 Hz and 1 MHz, using a HP4284A Impedance Meter, and determined from the first real axis touchdown point in the Nyquist plot of the impedance data. The temperature was maintained at a set temperature with a Shimaden digital temperature controller. A type T measurement thermocouple probe was located in the cell container close to the sample.

Conductance was also measured for the solution of P_{13}LiTFSA-LiTFSA-ZW by the same method described above, but using a locally designed multi-sample conductance cell, consisting of a block of stainless steel, into which were machined six sample compartments. The conductance path is formed between the wall of the compartment and a central electrode. The cell constant of each of the cells was determined by calibration with a 0.01 M KCl-water solution at 25°C before and after each sample measurement. The conductance cell was sealed in an airtight container under nitrogen atmosphere.

With conductance and cell constant data obtained, conductivity of the samples was calculated from the measured resistance, area, and thickness of the electrolyte based on the method described in the following reference [Adamson, 1973], using Eq. 3.3 as shown below:-

$$\sigma = \frac{L}{R_b A} \tag{3.3}$$

where L is the thickness (cm) of the electrolyte, A is the area of the blocking electrode (cm^2), and R_b is the bulk resistance of the electrolyte. All samples were dried under vacuum at 60 ^oC for at least 2 days before the conductance measurements.

3.4.9 Tensile Strength Measurement

Tensile strength is the stress at which a material breaks or permanently deforms. The tensile strength, along with the elastic modulus, is an important parameter of engineering materials that are used in structures and mechanical devices. Ultimate tensile strength (σ_b) is the maximum stress that a material can withstand when subjected to tension, compression, or shearing. It is the maximum stress on the stress-strain curve (Fig 3.9). Elastic modulus (E) is the mathematical description of an object or substance's tendency to be deformed elastically (i.e., non-permanently) when a force is applied to it. The elastic modulus of an object is defined as the slope of its stress-strain curve.

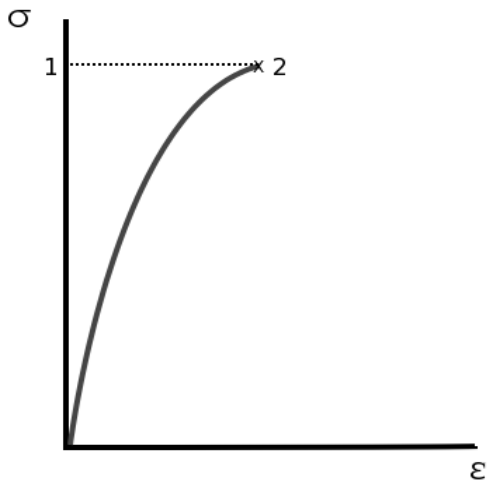

Fig 3.9 Stress vs. strain curve of a brittle material with (1) ultimate strength; (2) tensile strength.

To measure the tensile strength of the CNT films, they were cut into strips 3 mm wide and 18 mm long, and then tested under tension with TA Instruments DMA Q800 equipment. The samples were mounted for mechanical testing in air. A simple tensile test at the strain rate of 0.008 % s^{-1} was performed.

3.5 Electrode Preparation and Test Cell Assembly

3.5.1 Electrode Preparation

The working electrodes were prepared by mixing, using a mortar and pestle, electrochemically active materials with carbon black, which acts as the electrical conductor, and polyvinylidene fluoride (PVDF), which acts as the binder, in N-methyl-2-pyrrolidinone (NMP), which acts as the solvent, to form a homogeneous slurry. The exact composition of each material is stated in the details in the electrochemical characterizations section of the subsequent chapter. The slurry was then spread onto either copper (anode) or aluminium (cathode) foil, which served as the current collectors.

The typical active mass loading of the electrodes was 2 - 4 mg cm^{-2}, depending on the density of the electrochemically active samples. Subsequently, the coated electrodes (average thickness of ~ 50 μm) were dried in a vacuum oven at 110 ^{o}C for 12 h and then compressed at a pressure of 150 kg cm^{-2} to enhance the contact between the electrochemically active materials and the conductive carbon black with respect to the current collector.

For CNT anode and $LiMn_2O_4$ cathode thin films, the samples that were thus produced were first dried at 120 °C in a vacuum chamber for 12 h and then used directly as the working electrode.

If not otherwise specified, all measurements were performed using metallic lithium as the counter electrode. Because the potential of metallic lithium is nearly constant at moderate or low current densities, the counter electrode also acts as the reference electrode. These working electrodes were used for electrochemical cell assemblies for further electrochemical testing.

3.5.2 Test Cell Assembly

In order to perform electrochemical measurements and investigations, test cells were assembled. Two types of electrochemical cells were used throughout the study. For the testing conducted in ISEM, CR2032 coin cells were used. However, a homemade titanium-based electrochemical cell was assembled during the stay at PSI, Switzerland.

For the fabrication of coin cells, the cells were assembled in an Mbraun (Unilab, Germany) argon-filled glove box with O_2 and H_2O levels less than 1 ppm, by stacking a porous separator containing liquid electrolyte between the working electrode and a lithium metal counter electrode. The electrolyte used was 1 M $LiPF_6$ in a 50:50 (w/w) mixture of ethylene carbonate (EC) and dimethyl carbonate (DMC), provided by MERCK KgaA, Germany.

A schematic diagram of the CR2032 coin cell is shown in Fig. 3.10. The separator used for the coin cells was porous polypropylene membrane (Celgard 2500) with a thickness of 25 μm.

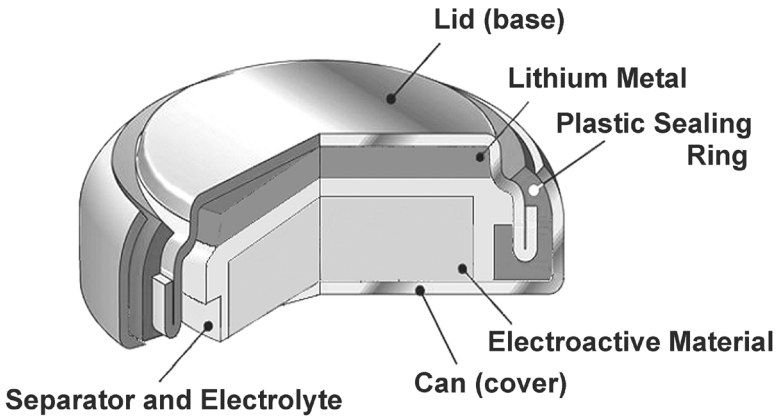

Fig. 3.10 Cross-sectional schematic diagram of the CR2032 coin cell used in ISEM.

During my visiting fellowship appointment at the PSI, a titanium homemade cell was used (Fig. 3.11). The counter electrode was placed on a titanium cylinder (8) and pressed with a spring (5) against the working electrode, which formed a coating on a copper (anode) / aluminium (cathode) current collector (10). The electrodes were separated by a 1 mm thick glass-fiber separator saturated with 500 μL of electrolyte solution, 1 M $LiPF_6$ in EC:DMC in 1:1 mass ratio (purchased from Ferro Corp., USA). The cells were assembled in a homemade argon-filled glove box with less than 1 ppm of oxygen, water, or nitrogen content.

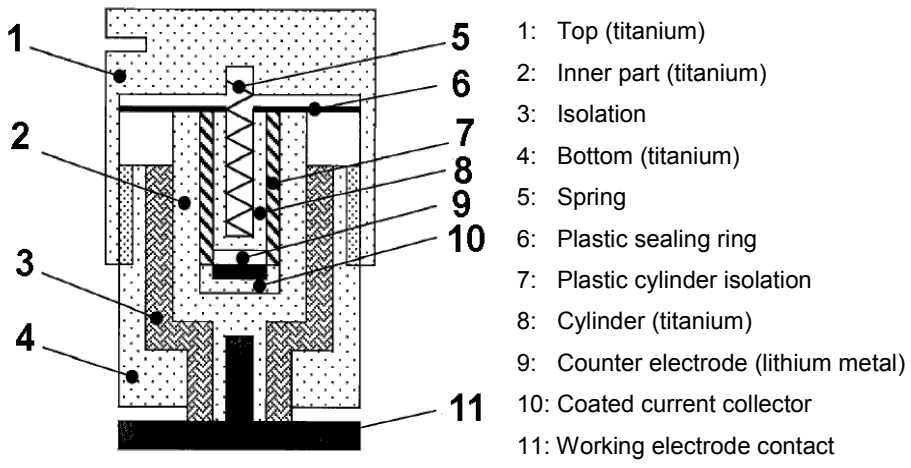

Fig. 3.11 Schematic diagram of the homemade test cell used in PSI (Coluccia, 2000).

3.6 Electrochemical Characterization

If an electrochemical system is subjected to the passage of current between the two electrodes, it is out of equilibrium. Usually we are interested in investigating the electrode process of one electrode, which is the *working electrode*. Such investigations are carried out by either controlling the cell potential (potentiostatic control) or the current that passes through the cell (galvanostatic control). The other electrode, the *counter electrode*, is used to complete the external circuit. Occasionally a third electrode is employed, the *reference electrode*. When this is the case, the electrode potential is monitored with respect to the reference electrode.

3.6.1 Cyclic Voltammetry (CV)

Cyclic voltammetry is a widely used method for studying electrode processes, especially for the determination of the thermodynamics and kinetics of electron transfer at the electrode-electrolyte interface. It is often employed as the first method to characterize new systems. The cell is cycled in a potential window, where the potential applied on the working electrode is continuously changed at a constant rate. Essentially, the potential is swept through the potential range where an electrode reaction occurs before the direction of scan is reversed, in order to define whether (a) the product of electron transfer is stable or (b) reaction intermediates or the final products are electroactive. The change of potential as a function of time is called the scan rate. The potential sweep can be described by its initial (E_i), switching (E_s), and final (E_f) potentials, and also by the scan rate, ν. The potential as a function of time (t) is:

$$E = E_i + vt \quad \text{(forward sweep)} \tag{3.4}$$

$$E = E_s - vt \quad \text{(reverse sweep)} \tag{3.5}$$

with the scan rate (in mV s^{-1}) defined as:

$$v = \frac{\Delta E}{\Delta t} \tag{3.6}$$

Other important parameters are the maximum and minimum potential ranges, which define the potential window. The choice of this potential window must take into account the stability range of the chosen electrolyte to avoid its decomposition. A positive sweep rate causes the oxidation of the working electrode, and the resulting current has a positive sign. With a negative sweep rate, the reduction of the working electrode causes a negative current.

For the cells tested at PSI, CV measurements were conducted by a Computer Controlled Cell Capture device (CCCC, Astrol Electronics AG, Oberrohrdorf, Switzerland) in a closed container with the temperature maintained at 25 ^{o}C. For the CV measurements conducted in ISEM, a CHI 660 electrochemical workstation (CH Instrument, Cordova, TN) was used for testing at room temperature.

3.6.2 Galvanostatic Cycling Measurements

In a galvanostatic measurement a constant current is applied between the working and counter electrodes. The current is applied until the set upper or lower potential limits are reached. For the working electrode a negative current would cause reduction and a positive current oxidation. The examination of the variation of potential

with time is also called chronopotentiometry. This method has an important advantage over cyclic voltammetry, because the current or current density is kept constant, so the electrode process is investigated under real battery working conditions.

For an insertion/extraction process into a compound *M*:

$$Li_xM + \Delta xLi^+ + \Delta xe^- \leftrightarrow Li_{x+\Delta x}M \qquad (3.7)$$

The amount of the guest species (Δx) can be calculated as follows:

$$\Delta x = \frac{I\Delta tM_r}{nFm} \qquad (3.8)$$

where, I is the applied current in A, Δt is the time interval in s, M_r is the molecular mass of the compound in g mol^{-1}, m is the active mass loading in g, F is the Faraday constant (9.649 x 10^4 C mol^{-1}), and n is the number of electrons exchanged.

The cells were galvanostatically charged and discharged at constant current density via a Neware battery tester (China) in ISEM at room temperature. However, a Computer Controlled Cell Capture device (CCCC, Astrol Electronics AG, Oberrohrdorf, Switzerland) was used in PSI, Switzerland to perform the testing in a closed container with constant temperature, controlled at 25 ^oC.

3.6.3 Electrochemical Impedance Spectroscopy (EIS)

The a.c. impedance spectroscopy technique involves the application of a small potential perturbation (E) at various frequencies (f) at a given dc potential (E_{dc}). The current response is monitored, and as a result, the variation of resistance with frequency for the material can be examined. A common type of impedance spectrum (Fig. 3.12)

consists of a low-frequency semicircle and a high-frequency tail. The semicircle is the result of the kinetic processes involved in the interaction between the resistor (R_{ct}) and the capacitor (C_{dl}) elements. The tail, on the other hand, results from diffusion processes and is represented in the model by a *Warburg* element.

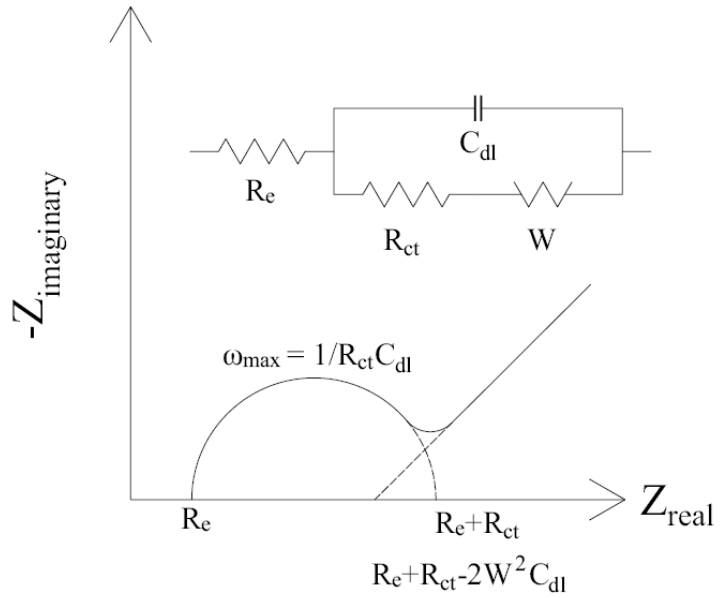

Fig. 3.12 A common impedance spectrum and the corresponding equivalent circuit for such spectra [Lindsay, 2004].

The ac impedance spectroscopy measurements were carried out using a CHI 660A electrochemical workstation system (CH Instrument, Cordova, TN) by applying a sine wave of 5 mV amplitude over a frequency range of 100.00 kHz to 0.01 Hz. All impedance measurements were carried out in the de-lithiated state (state of charge).

In the following chapter, all terms related to electrochemical reduction and oxidation processes are defined based on the standard Li-ion full cell configuration [Gritzner and Kreysa, 1993].

CHAPTER 4

FREE-STANDING CARBON NANOTUBE FILMS AS ANODES FOR LI-ION BATTERIES

4.1 Introduction

Since they were first imaged by Iijima in 1991, carbon nanotubes (CNTs) have generated interest among scientists and engineers that surpasses their interest in almost any other material known to humans. Industry enthusiasts also believe that CNTs will radically improve the performance of batteries, because of their high surface-to-volume ratio and the relatively short diffusion length in the nanosized diameter tubes, which could especially enhance the kinetic properties of the batteries [Endo *et al.*, 1995; Wu *et al.*, 1999; Frackowiak and Béguin, 2002].

The lithium storage of CNTs, in particular the single-wall carbon nanotubes (SWCNTs), has been determined experimentally to be significantly higher than that of intercalated graphite, namely > 2000 mAh g^{-1} [Lu and Chung, 2001; Shimoda *et al.*, 2002; Claye *et al.*, 2000; Kim *et al.*, 2006]. However, these impressive data were determined for the first cycle only, in a potential window ranging from 0.0 to 2.0 V or even to 3.0 V vs. Li/Li^+. Therefore, it is important to collect and publish data relevant to

the envisaged industry applications, to allow for serious comparison with current standard electrode materials.

In general, an electrode preparation technique based on mixing the CNT powders with a polymeric binder is applied [Wu *et al.*, 1999; Frackowiak and Béguin, 2002; Lin *et al.*, 2006]. However, this technique reduces the effective surface area of the active material (i.e., the surface area in contact with the electrolyte) and often limits the working temperature range due to the limited thermal stability of the binder. Therefore, in order to preserve the benefits of electrochemistry at the nanoscale, alternative electrode configurations based on super-fine and nanostructured materials were investigated.

Here, a simple filtration technique is introduced to prepare free-standing CNT films, which can be applied directly as an electrode material in the test cell. In this study, the properties of SWCNTs, double-wall carbon nanotubes (DWCNTs), and multi-wall carbon nanotubes (MWCNTs), all as free-standing films, are compared. The investigated films possess the functions both of charge storage and of a current collector when used as the anode in a cell.

4.2 Preparation of CNT Films

A vacuum filtration method was adopted (refer to Fig 4.1(a)), and this technique was modified in our group [Ng *et al.*, 2005] for the preparation of free-standing CNT films. Fig. 4.1(b) shows an optical photograph of round piece of dried CNT paper with a diameter of 380 mm. Based on previous experience [Ng *et al.*, 2005], carbon black (10 wt %) was added in order to improve the flexibility and conductivity of the film. Free-standing CNT films are attractive for basic electrochemical characterization due to

their ease of handling, favorable mechanical properties and most importantly, the absence of the polymeric binder.

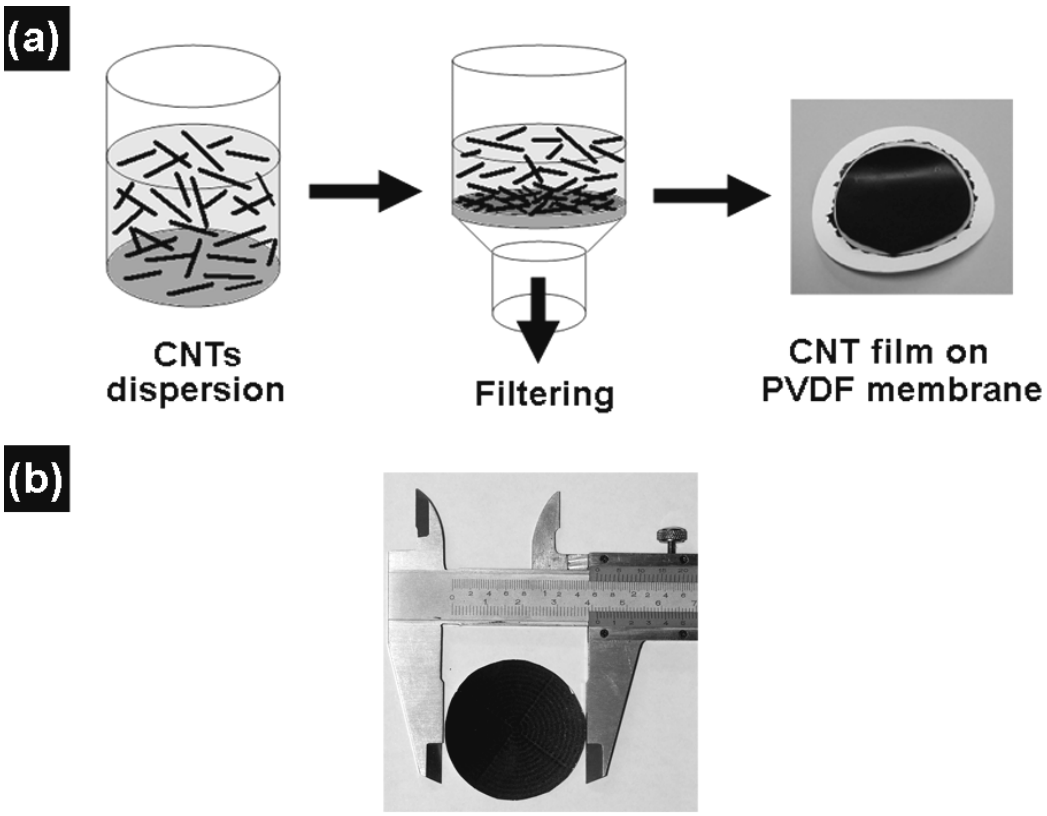

Fig. 4.1 (a) A schematic representation of the CNT film-making process. (b) A photograph of a round and black CNT film.

4.3 Electrochemical Measurements

The electrochemical measurement were conducted with equipment available in the Paul Scherrer Institut, Switzerland. Electrodes from the obtained free-standing CNT films were punched out with a diameter of 11 mm each. They were then dried at 120 °C in a vacuum chamber overnight. Test cells similar to coin-type cells [Novák *et al.*, 1995] were assembled using free-standing CNT films as the working electrode and Li metal as the counter and reference electrode. The electrodes were

separated by a 1 mm thick glass-fiber separator saturated with 500 μL of electrolyte solution, 1 M $LiPF_6$ in EC : DMC in a 1 : 1 mass ratio (Ferro GmbH). The cells were assembled in a homemade argon-filled glove box with oxygen, water, and nitrogen contents less than 1 ppm..

Both the galvanostatic and cyclic voltammetry (CV) measurements were performed using standard electrochemical instrumentation (Astrol Electronic AG, Oberrohfdorf, Switzerland). The cells were galvanostatically charged and discharged in the range of 0.01 - 2.00 V vs. Li/Li^+ at a constant specific current of 25 mA g^{-1}, inside a container with temperature controlled at 25 ^oC. In order to promote complete charge-discharge at the respective potential limits, a potentiostatic step was included until the current was 10 % of the current used in the galvanostatic step. CV measurements were performed in the range of 0.01 - 2.00 V vs. Li/Li^+ at a scanning rate of 0.05 mV s^{-1}.

4.4 Physical and Structural Characterizations

The crystallography phase purity of the CNT powder samples was determined by X-ray diffraction (XRD), and the obtained diffraction patterns are shown in Fig. 4.2. Typical CNT peaks of the (002) and (101) reflections are observed for the SWCNT, DWCNT, and MWCNT powder samples. As expected, the line shape of the (002) peak for the SWCNT powder is weaker and broader when compared with the other CNT powder samples. The intensity and width of the (002) peak are related to the variation of the interlayer spacing and the CNT orientation to the X-ray incident beam [Cao *et al.*, 2001]. Based on Bragg's equation, it is confirmed that our DWCNT powder sample has an interlayer spacing of approximately 0.3401 nm, while the SWCNT powder sample has a smaller

interlayer spacing of approximately 0.3395 nm. The interlayer spacing for the MWCNT powder sample is also similar to that of the DWCNT powder sample, namely $d_{002} \approx 0.3401$ nm.

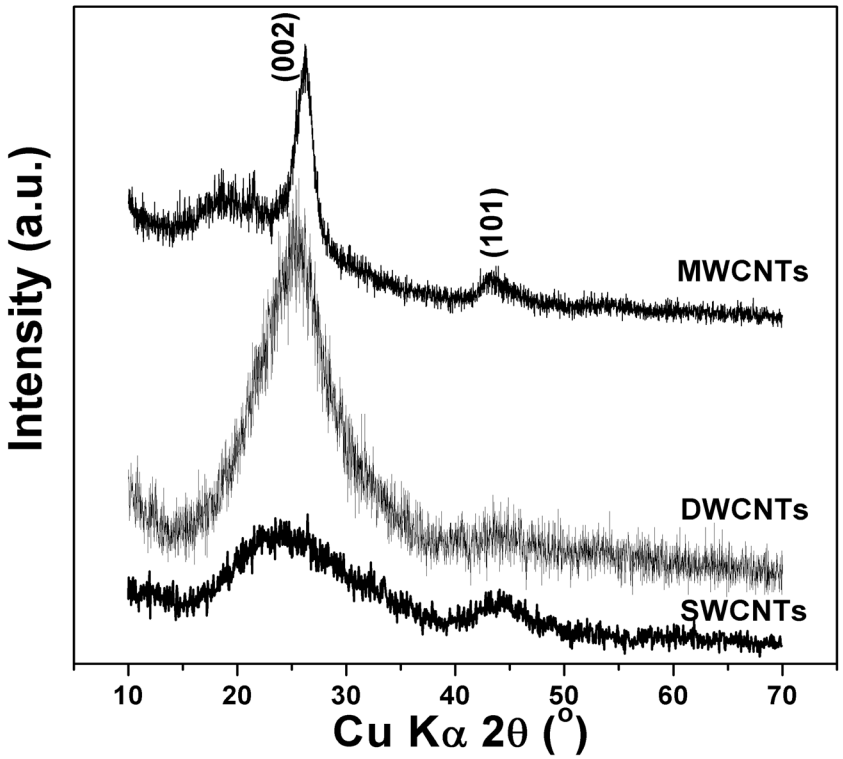

Fig. 4.2 XRD patterns of SWCNT, DWCNT, and MWCNT powders.

Fig. 4.3 shows Raman spectra of SWCNT, DWCNT, and MWCNT free-standing films. The SWCNT film exhibits a typical Raman spectrum of the SWCNT powder with three main features, which are assigned as the radial breathing mode (below 400 cm^{-1}), the D-band (1300-1350 cm^{-1}), and the G-band (1500-1600 cm^{-1}), respectively. The extra peak at 1565 cm^{-1}, appearing at the left of the G band, is a typical characteristic of a SWCNT Raman spectrum [Kim *et al.*, 2006]. The Raman spectrum of the DWCNT film is very similar to that of the SWCNT film due to their small tube diameters [Ren *et al.*, 2002]. However, the spectrum of the MWCNT film displays great differences from those of the SWCNT and DWCNT films by showing

broad D- and G-bands with maxima at 1342 and 1590 cm^{-1}, respectively, which are characteristics of disordered carbonaceous structures. This is clearly seen from the comparison with the spectrum of carbon black, shown in Fig. 4.3(d). The G-band represents the E_{2g} mode of graphite and is due to the vibration of sp^2-bonded carbon atoms in the hexagonal graphitic plane. The D-band corresponds to the A_{1g} mode, which is attributed to the vibration of carbon atoms with dangling bonds at the edges and defects of the graphitic lattice [Frackowiak and Béguin, 2002; Lin *et al.*, 2006]. In our case, the peak intensity of the D-band is higher than that of the G-band, indicating thus a high ratio of disordered carbon to graphitic carbon in the MWCNT film. Also, note that although 10 wt % of carbon black powders are present in our CNT films, the spectroscopic contribution of the carbon black is almost negligible.

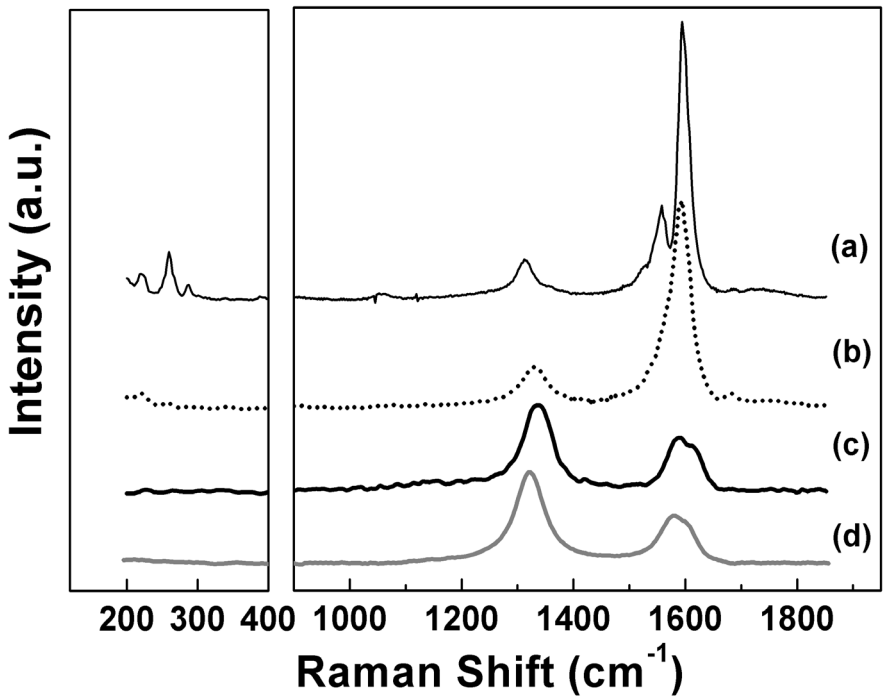

Fig. 4.3 Raman spectra of (a) SWCNT film, (b) DWCNT film, (c) MWCNT film, and (d) carbon black powder (Super P, Timcal).

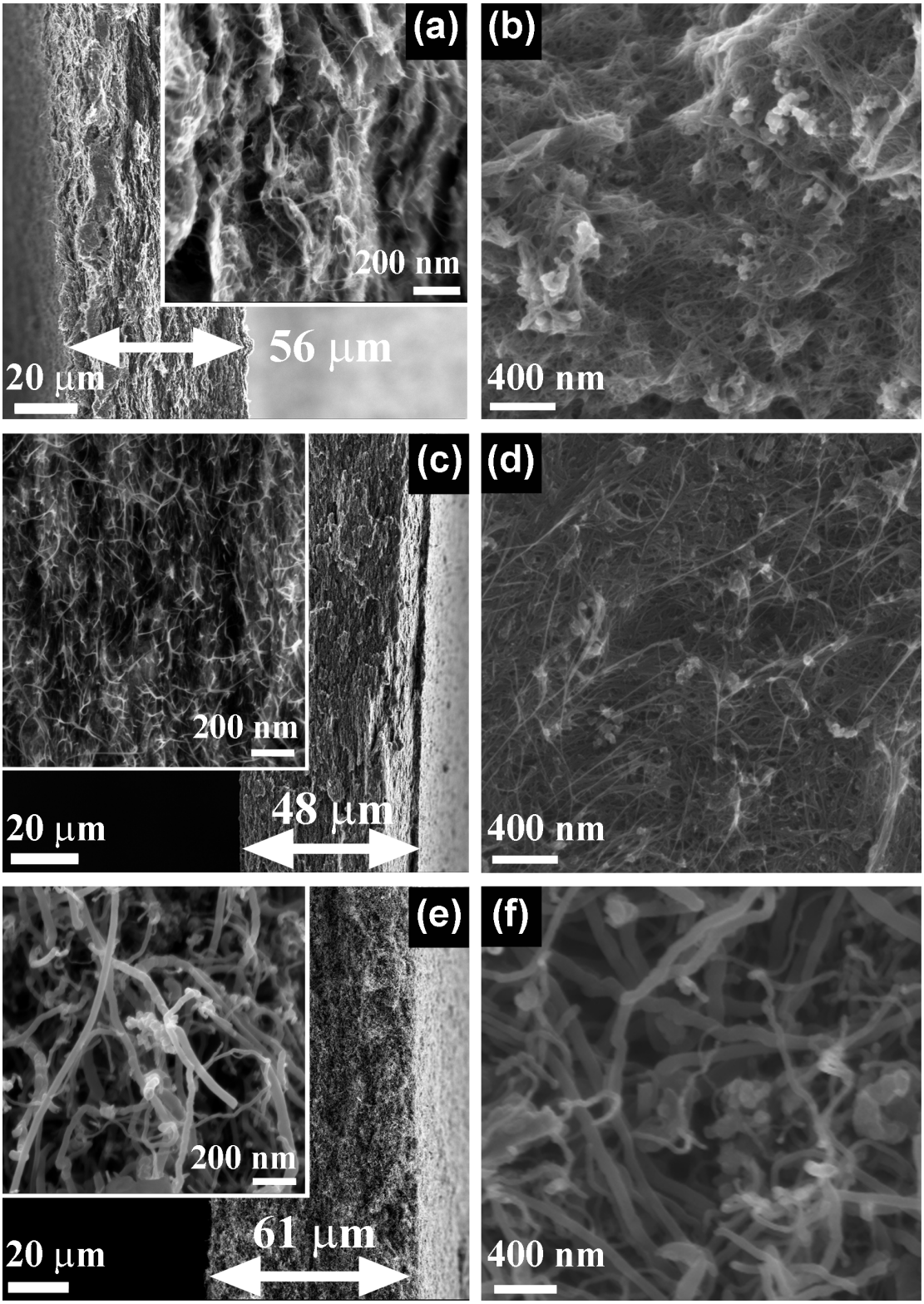

Fig. 4.4 FE-SEM cross-sectional images of CNT films with 10 wt % carbon black: (a) SWCNT film, (c) DWCNT film, and (e) MWCNT film, with insets at higher magnification, and top views of (b) SWCNT film, (d) DWCNT film, and (f) MWCNT film.

Field emission SEM (FE-SEM) images of the cross-sections and surfaces of the SWCNT, DWCNT, and MWCNT films are shown in Fig. 4.4 at different magnification levels. From the nanostructural and microtextural characterizations, all CNT films appear as webs of curved nanotubes forming strong intertwined entanglements. In Fig. 4.4(e)-(f), owing to the biggest tube diameter, MWCNTs formed the thickest film, ~ 61 μm in thickness. This film also had a loosely packed character. In contrast, the SWCNT and DWCNT films contained CNTs that had a narrower average tube diameter and were densely packed together. Basically, the intrinsic properties of the CNTs with small tube diameters and extremely long lengths enable them to be easily assembled into an entangled mat via the vacuum filtration technique.

Each of the as-prepared CNT films has a different appearance, even to the naked eye. The SWCNT film is black and not reflective; DWCNT film is black and glossy; whereas the MWCNT film is black and dull. Depending on the type of CNTs, SWCNT and MWCNT films exhibit brittle failure under tension, with elongation at failure (ε_b) ranging from 0.2 to 1.9 %. However, the DWCNT film shows ductile behaviour, with elongation at failure ranging from 0.9 to 2.5 % (Fig. 4.5). Failure of the samples is most likely caused by the propagation of pre-existing pores with concentrated stress among the CNT bundles [Whitten *et al.*, 2005].

The mechanical properties of the CNT films are noticeably diversified, depending on the different types of CNTs (Table 4.1). The DWCNT film shows the highest ultimate tensile strength (σ_b) and elastic modulus (E), followed by the SWCNT and the MWCNT film. For the CNT films, the structural component is fixed during the vacuum filtration process. For materials with long range connectivity in one dimension, the entanglement of the components becomes

effective after some deformation has taken place [Nissan and Batten, 1997]. Hence, the CNTs entanglement influence ultimate tensile strength, elongation at failure, and elastic modulus. The favourable mechanical properties of the DWCNT film are correlated well with the FE-SEM image in Fig 4.4(c), where the DWCNT film, which is the thinnest (~48 μm) and has the highest packing, exhibits better tension and stiffness compared with the SWCNT and MWCNT films.

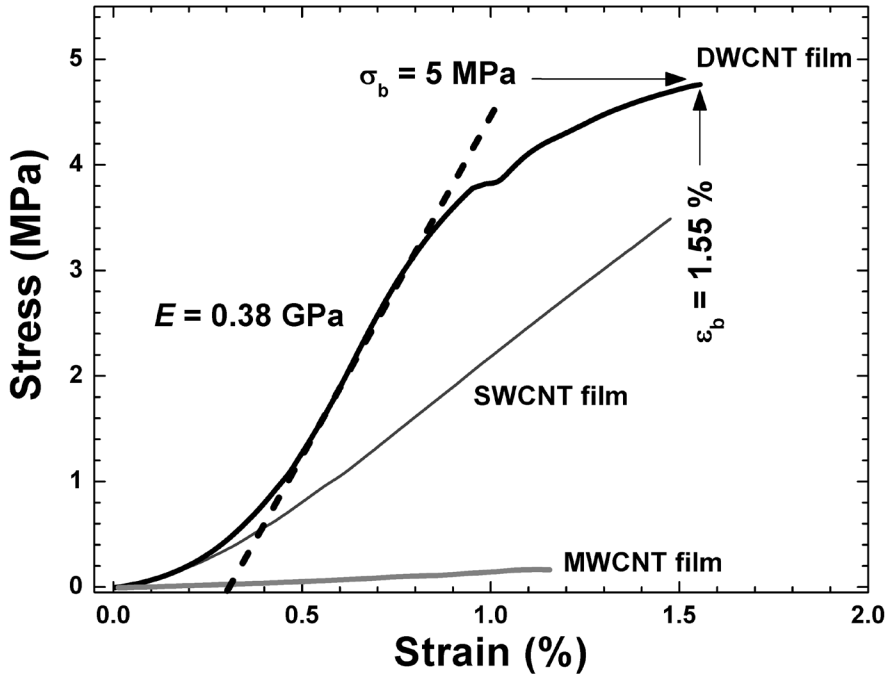

Fig 4.5 Tensile test result for SWCNT, DWCNT, and MWCNT films.

Table 4.1 Mechanical properties for different types of CNT films.

	Ultimate Tensile Strength (MPa)[a]			Elastic Modulus (GPa)[a]		
	Min	Max	Ave	Min	Max	Ave
SWCNT film	1.2	5.8	3.8	0.22	0.57	0.39
DWCNT film	4.8	16.0	11.7	0.38	1.90	1.01
MWCNT film	0.1	0.3	0.2	0.01	0.08	0.04

[a] where Min means minimum, Max means maximum, and Ave means average.

4.5 Electrochemical Performance

The electrochemical Li^+ storage properties of the three different types of CNT films were systematically investigated. Obviously, different CNT films show different electrochemical behavior. For the first reduction cycle (see Fig 4.6(a)), both SWCNT (2390 mAh g^{-1}) and DWCNT (2110 mAh g^{-1}) films exhibit much higher specific charge compared to the MWCNT film (750 mAh g^{-1}). However, most of this charge can be attributed to irreversible processes, which include the reduction of surface functional groups, formation of the solid electrolyte interphase (SEI) layer, and eventually, further side reactions [Fong *et al*., 1990; Wu *et al.*, 1999; Lu and Chung, 2001; Frackowiak and Béguin, 2002].

The electrochemical performance of these free-standing CNT electrodes in the subsequent cycles are plotted in Fig. 4.6(b). The MWCNT film exhibits a reversible charge of approximately 300 mAh g^{-1} with stable cycling behavior, whereas, the SWCNT and DWCNT films show strong fading. The coloumbic efficiency of the MWCNT film is 80 % in the 2^{nd} cycle, much higher than those of the SWCNT film (59 %) and the DWCNT film (55 %).

Cyclic voltammograms of the respective CNT electrodes are shown in Fig. 4.7. Basically, the reduction (charge or Li^+ insertion) process of the CNT films can be divided into two main regions, negative and positive to ~ 0.5 V vs. Li/Li^+. In the low potential part (negative to 0.5 V vs. Li/Li^+), Li^+ ions are intercalated into the graphitic-type layers. Positive to 0.5 V vs. Li/Li^+, the sharp negative peak at 0.6 - 0.7 V vs. Li/Li^+ can be attributed to the formation of the SEI layer [Winter *et al.*, 1998]. The SWCNT film exhibits a broader peak, while the DWCNT film exhibits a sharper, more intense peak. This strong hint indicates that the kinetics of the SEI

formation is faster in the DWCNT film. An extra peak at ~ 1.2 V vs. Li/Li^+ is clearly observed for the SWCNT film. Based on the argument of Lu and Chung (2001), this process is attributed to the reduction of surface species containing oxygen.

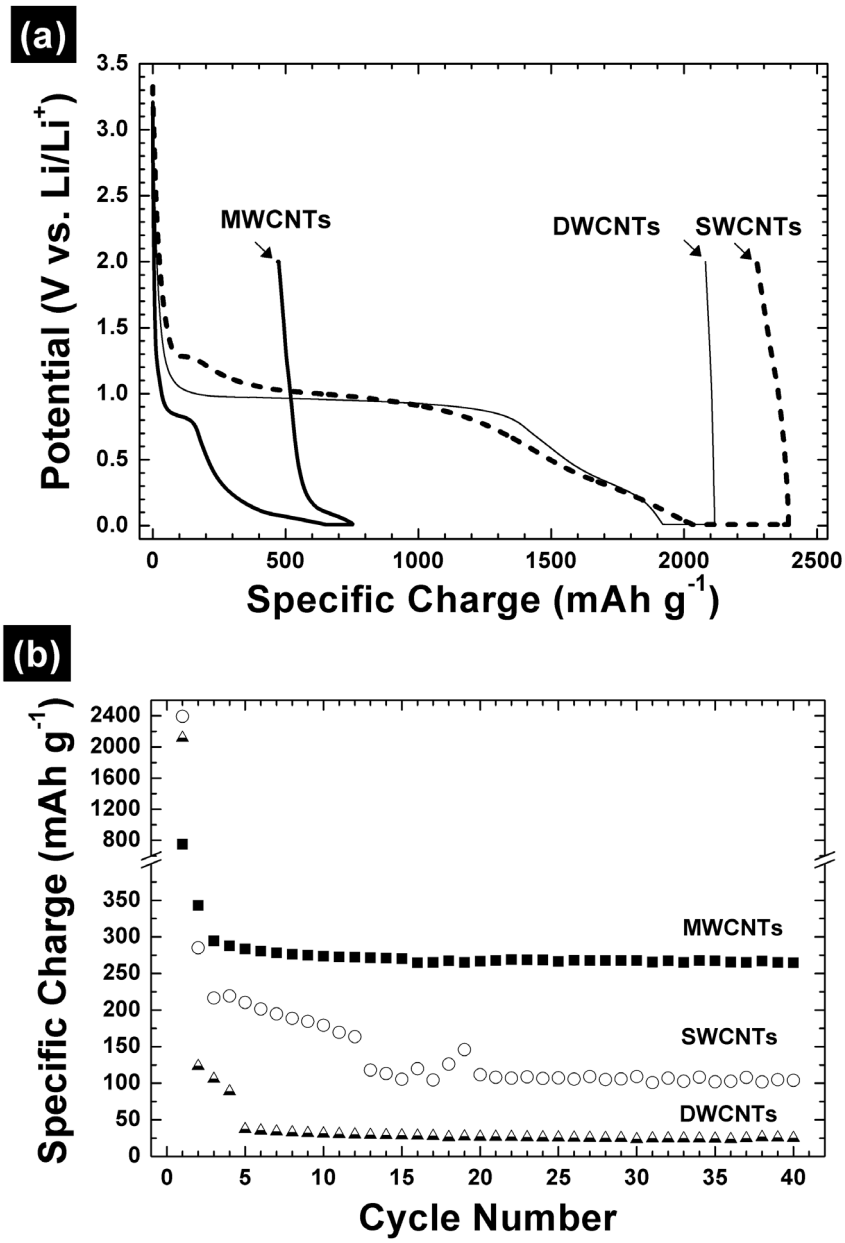

Fig. 4.6 The electrochemical performance of the free-standing CNT films: (a) galvanostatic charge-discharge profiles in the 1st cycle, and (b) cycling behavior between 0.01 and 2.00 V vs. Li/Li^+ at a specific current of 25 mA g^{-1}.

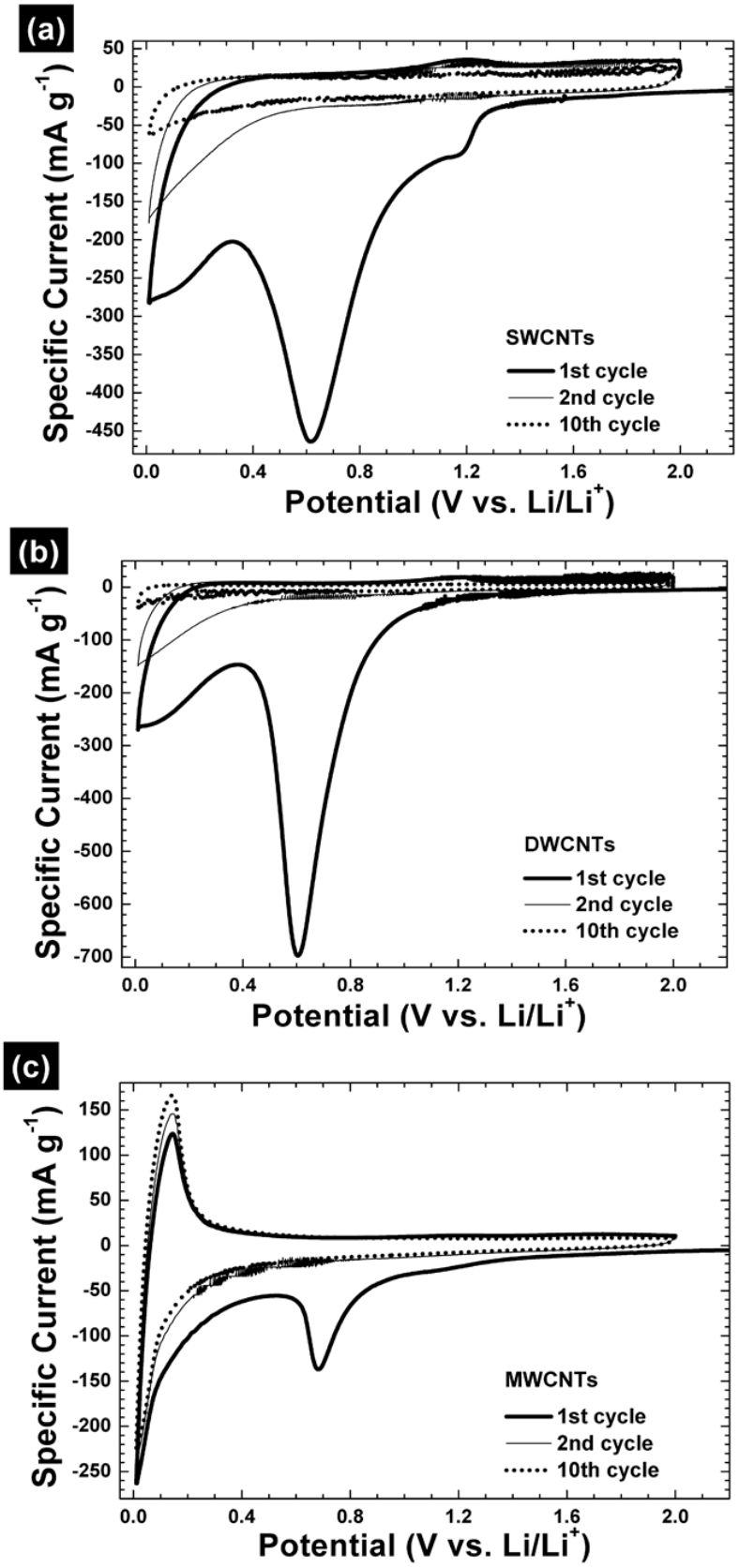

Fig. 4.7 Cyclic voltammograms at the 1st, 2nd, and 10th cycles for the free-standing CNT electrodes: (a) SWCNT film, (b) DWCNT film, and (c) MWCNT film.

As for the oxidation (discharge or Li^+ extraction) process, the MWCNT electrode exhibits a reversible, sharp, and intense peak at approximately 0.15 V vs. Li/Li^+. For graphitic materials, this peak is related to the de-intercalation of the Li^+ ions from the graphite [Spahr *et al.*, 2004], which is obviously the case here. MWCNTs have larger hollow cores of 10 - 20 nm [Lin *et al.*, 2006]. This could facilitate Li^+ ion diffusion into the internal hollow cores of the graphitic sheets of the MWCNTs and result in low overpotential for Li^+ ion insertion and extraction. In contrast, the absence of any well defined oxidation peak for SWCNT and DWCNT electrodes clearly indicates that the kinetics and/or the mechanism of the reactions are entirely different to what occurs in standard graphitic carbon materials. Only a broad peak at approximately 1.2 V vs. Li/Li^+ is observed for both SWCNT and DWCNT electrodes during the oxidation. According to Frackowiak and Béguin (2002), this behavior may partly be attributed to the quasi-reversible interaction between the lithium and the surface-oxygenated functional groups, i.e., COO^-Li^+. Lu and Chung (2001) reported that Li^+ ions can bind in the vicinity of H atoms in hydrogen-containing carbons, enabling further reaction between the lithium and the electrolyte solution. The reversible charge obtained in the cycling of SWCNTs and DWCNTs is obviously related to such doping/de-doping processes, where Li^+ ions are adsorbed on the outer surface of the CNTs. The surface available for the adsorption is mainly located in the interstitial space between the adjacent tubes and the empty spaces between highly entangled CNT bundles [Wu *et al.*, 1999; Shimoda *et al.*, 2002; Kim *et al.*, 2006].

Electrochemical reactions intrinsically occur at the interface between the solid electrode and the liquid electrolyte. Thus, the porous structure and the surface properties of the CNT films are of great interest. The specific surface area (S_{BET}) is estimated using the Brunauer-Emmett-Teller (BET) method. The relevant data are

summarized in Table 4.2, where we arbitrarily assign the irreversible charge (C_{irr}) in the potential window from 2.0 to 1.0 V vs. Li/Li^+ to the reduction of the surface functional groups, and from 1.0 to 0.3 V vs. Li/Li^+ to the SEI formation.

The values of the S_{BET} and mesopore volume (V_{meso}) are highly dependent on the type of the CNTs. After making the free-standing films, both S_{BET} and V_{meso} are reduced. For carbonaceous materials, there is a fairly good relationship between the irreversible charge with respect to the specific surface area [Winter *et al.*, 1998] and the mesopore volume [Frackowiak and Béguin, 2002]. The higher the specific surface area and mesopore volume, the higher the total irreversible charge of the electrode. Our measurements are consistent with this relationship, as shown in Table 4.2 below.

Table 4.2 Physico-chemical characteristics of the CNT samples obtained from the BET and the density functional theory (DFT)/Monte-Carlo method, and the irreversible charge (C_{irr}) of the free-standing CNT electrodes during the initial reduction process.

	CNT Powders			CNT Films		
	SW	DW	MW	SW	DW	MW
S_{BET} (m^2 g^{-1})	657	583	55	435	473	50
V_{meso} (cm^3 g^{-1})	0.95	1.10	0.15	0.75	0.93	0.13
C_{irr} by surface functional groups, 1.0 – 2.0 V vs Li/Li^+ (mAh g^{-1})	-	-	-	600	147	29
C_{irr} by SEI formation, 0.3 – 1.0 V vs. Li/Li^+ (mAh g^{-1})	-	-	-	1091	1583	233
Total C_{irr}, 0.3 – 2.0 V vs Li/Li^+ (mAh g^{-1})	-	-	-	1691	1730	262

Interestingly, the BET surface area of the SWCNT powder was reduced much more than that of the DWCNT powder during the film preparation process. For SWCNT and DWCNT films, it is hypothesis that the higher the BET surface area of the film, i.e. S_{BET} DWCNT film > S_{BET} SWCNT film, the higher the SEI formation of the electrode (1583 mAh g^{-1}). Nevertheless, having a low S_{BET} value and low V_{meso} is beneficial for the electrochemical performance, as proved by the MWCNT electrode here [Winter *et al.*, 1998; Lu and Chung, 2001].

Fig. 4.8 demonstrates the cycling behaviour of the MWCNT electrode, with a coulombic efficiency of 99% after 40 cycles, suggesting high reversibility in the Li^+ insertion and extraction processes. This MWCNT electrode shows a moderate fading behaviour in the first 5 cycles, followed by a relatively flat and smooth cycleability for the next 40 cycles.

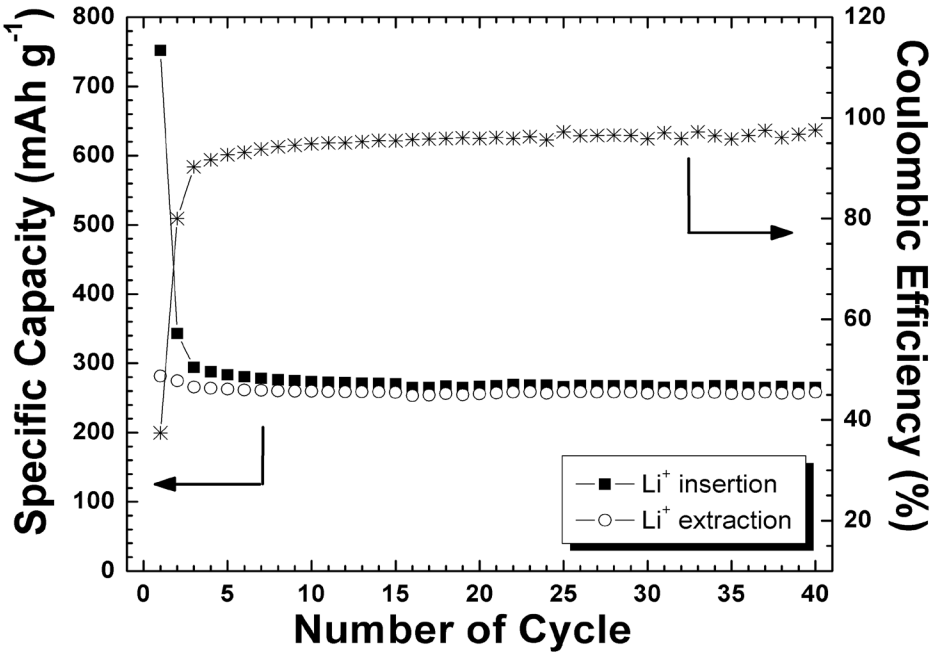

Fig 4.8 Li^+ insertion (charge) and extraction (discharge) capacity, and the corresponding coulombic efficiency profiles of MWCNT electrode cycled at a specific current density of 25 mA g^{-1}.

The high rate capability of the binder-free MWCNT film upon cycling is also plotted in Fig 4.9. Please note that the 1 C-rate is equivalent to 300 mA g^{-1}. The correlation of the current density with the "galvanostatic Li^+ extraction" and the "total Li^+ extraction" is presented. Here, "galvanostatic Li^+ extraction" is the specific charge extracted in the galvanostatic part of the half-cycle, while "total Li^+ extraction" is the total specific charge extracted in the half-cycle, including the potentiostatic part associated with the current drop. Figure 4.9 shows that the MWCNT electrode is very stable when cycled up to the 10 C-rate. However, a slightly drop of charge retention (to 105 mAh g^{-1}) was observed when the cell was cycled at the 20 C-rate over 135 cycles. In another word, the MWCNT electrode has a relatively low specific energy density when a very high current density (20 C-rate) is applied.

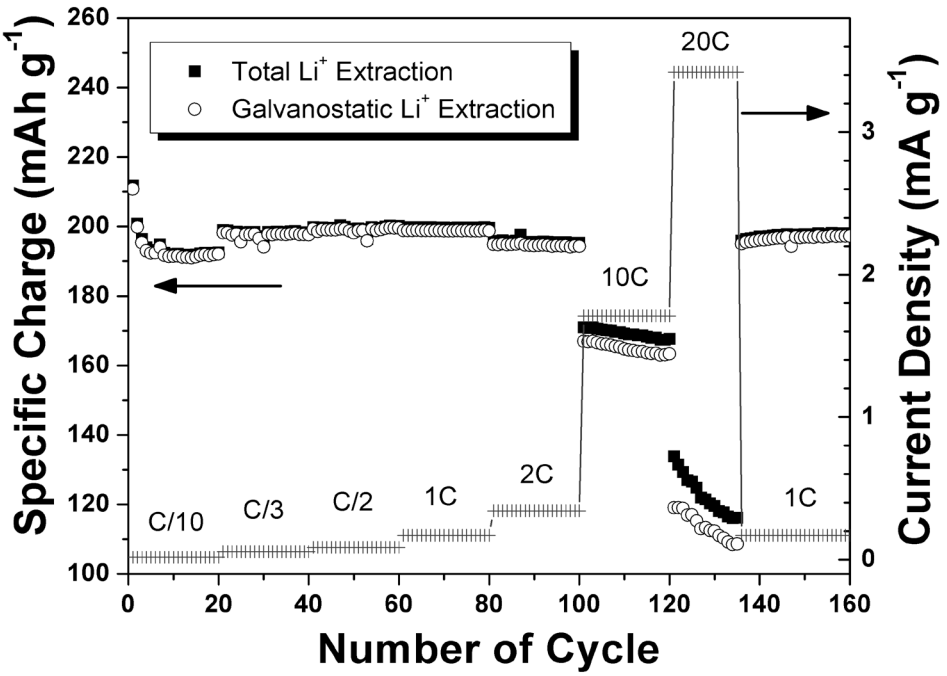

Fig 4.9 Rate capability of the MWCNT electrode. The galvanostatic and total Li^+ extraction capacity are measured at different current densities. A 1 C-rate is assumed to be 300 mA g^{-1}.

The specific charge for Li^+ extraction from Fig. 4.9 is further evaluated. The galvanostatic Li^+ extraction is given as a percentage of the total Li^+ extraction versus the C-rate, and the data is presented in Fig. 4.10. The MWCNT electrode retains a high rate capability, with over 97 % for Li^+ extraction at the 10 C-rate and 92 % at the 20 C-rate. This means that more than 93 % of the specific charge could be extracted in less than 3 min. For application in hybrid electric vehicle (HEVs), such a high rate capability is of interest in order to achieve high specific power in the lithium-ion batteries.

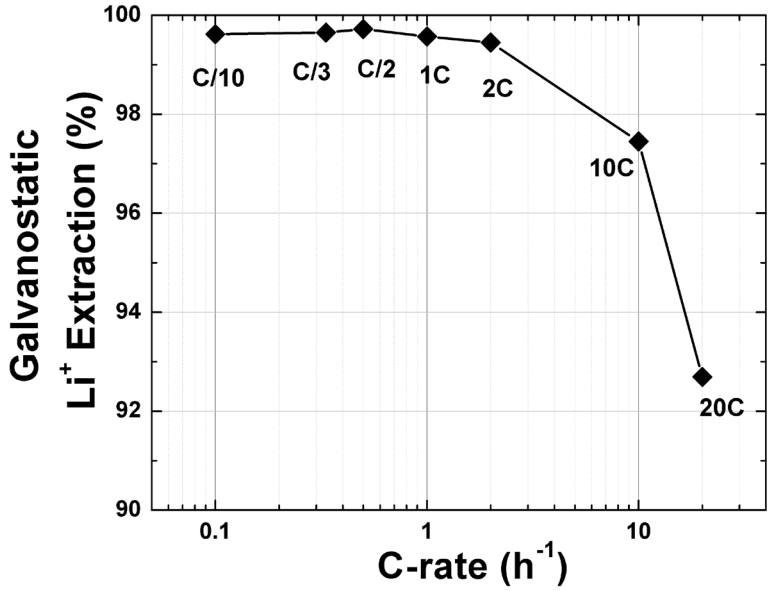

Fig 4.10 Rate capability of the MWCNT electrode. The galvanostatic Li^+ extraction, given as a percentage of the total Li^+ extraction, including the potentiostatic step, is plotted versus different C-rates.

The morphology of the CNT electrodes after prolonged cycling was examined by FE-SEM at 1 kV. Fig. 4.11 shows the images of the fresh free-standing MWCNT electrode (Fig. 4.11(a)) and the three different CNT electrodes after 100

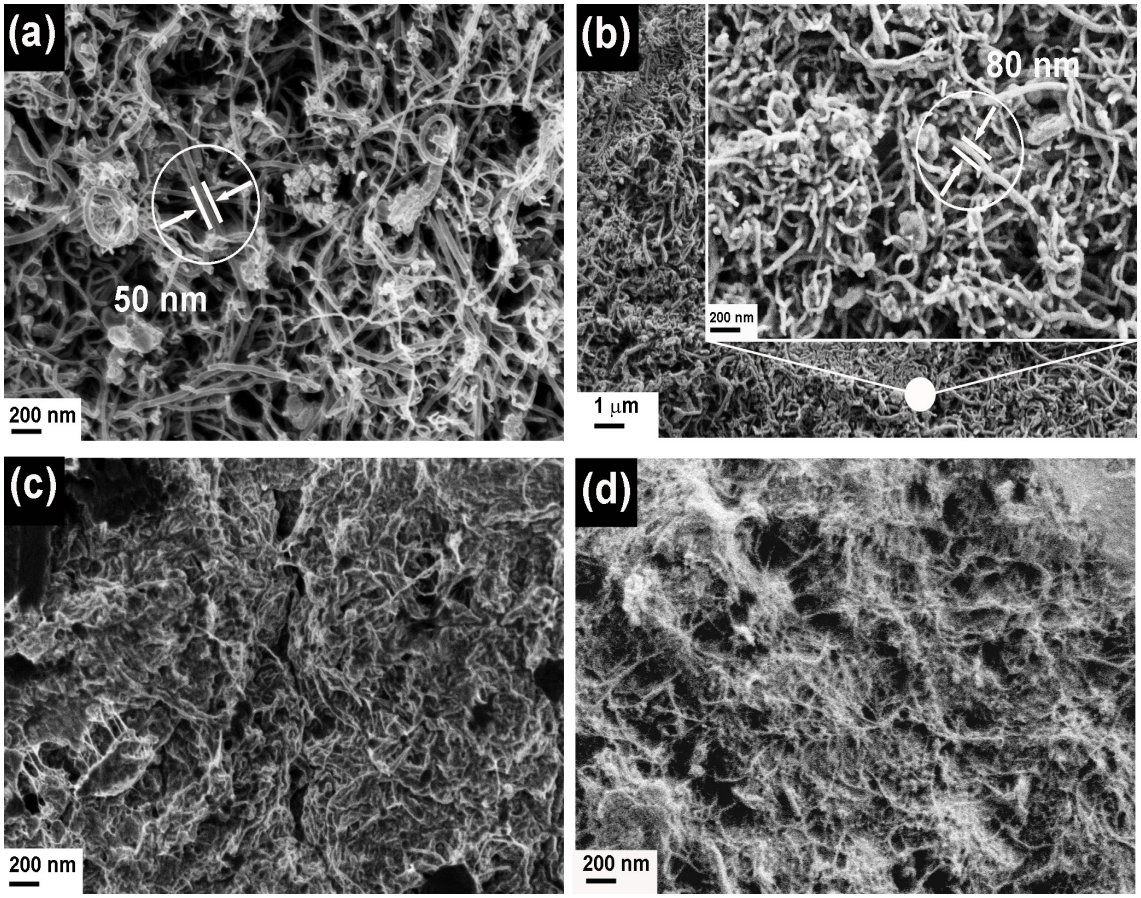

Fig. 4.11 FE-SEM images of the CNT electrodes: (a) before cycling for the MWCNT electrode; and after 100 cycles for (b) the MWCNT electrode, with the inset showing a magnification of the indicated area, (c) the SWCNT electrode, and (d) the DWCNT electrode.

electrochemical lithiation/de-lithiation cycles (Fig. 4.11(b)-(d)). For the MWCNT electrode, the shape and the mechanical integrity are still retained, a proof of its good mechanical stability after cycling. In addition, a slight increase of the average tube diameter in the MWCNT film is noticeable after prolonged cycling (cf. Fig. 4.11(a) and 4.11(b)).

FE-SEM is a powerful tool to identify the SEI layer of a cycled electrode [Würsig *et al.*, 2005]. Based on the electron microscope image, an SEI layer was deposited onto the surface of each nanotube. This is likely to be the reason for the

observed expansion of the nanotube diameter, which is increased from approximately 50 nm to approximately 80 nm after cycling, as highlighted in the figure.

For the SWCNT and DWCNT electrodes, a thick and dense layer of SEI together with other electrolyte decomposition products is observed, not only on the surface of the CNTs, but also in the spaces between the entangled CNTs. There is higher penetration of the electrolyte into the porous film structure, due to the high BET surface area (> 400 m^2 g^{-1}) and large mesopore volume (> 0.7 cm^3 g^{-1}) for both SWCNTs and DWCNTs, thus creating much more dead volume for the CNT electrode materials.

At the end of this comparative study of different CNT films, we wish to stress that although the MWCNT film shows the best electrochemical performance, neither the irreversible nor the specific charge are satisfactory for practical application in the present state. Despite that, our results illustrate the feasibility of the free-standing MWCNT film as a model electrode for studies of electrochemical interface reactions, without the influence of the binder and current collector, as well as studies to develop a potential anode material for high specific power applications. The mechanical properties (based on tensile testing) of the CNTs have no influence on the electrochemical performance of the cells. Clearly, this study indicates that only MWCNTs have the capability for significant Li^+ intercalation/de-intercalation.

4.6 Conclusions

Taking into account the low price of the feedstock, the straightforward preparation process, and the useful electrochemical performance, free-standing

MWCNT films are suggested as a model electrode for studying surface reactions in Li-ion batteries. The rational low surface area and the mesopore volume are good for the development of a mechanically stable and ionically conducting SEI layer. The typical structure of MWNTs with multiple rolled up sheets of sp^2 bonded graphite enable Li^+ ions to be intercalated/de-intercalated between such graphitic layers. Hence, MWCNT film exhibited a highly reversible and stable cycling performance with rather high rate capability.

CHAPTER 5

NANOSTRUCTURED $LiMn_2O_4$ THIN FILM CATHODE BY THE FLAME SPRAY DEPOSITION METHOD

5.1 Introduction

In Li-ion batteries, lithium manganese oxide spinel ($LiMn_2O_4$) is an attractive positive electrode alternative to the Co and Ni oxides currently used because of its lower cost and toxicity, and its higher electrochemical potential vs. graphite [Tarascon and Guyomard, 1993; Winter *et al.*, 1998].

Nevertheless, capacity fading at elevated temperatures and during overcharge has slowed the application of $LiMn_2O_4$ in commercial Li-ion cells. Many studies have been dedicated to the understanding and resolution of the performance degradation. However, precise measurements of the kinetics of Li-ion intercalation under conditions leading to degradation are difficult with powder-based electrodes, since the addition of conductive carbon and binder may influence the electrochemical characterization [Simmen *et al.*, 2008], where degradation often leads to disconnection. Studies of rate processes within powder-based electrodes also suffer from the additional complication of solid-phase and solution-phase resistances [Chen *et al.*, 1997].

A thin film oxide electrode is a useful model system for the study of electrochemical properties without the above limitations. Advantages of thin film oxide electrodes over powder-based electrodes include: 1) improved understanding of the lithium insertion process and the electrode/electrolyte interface reactions with pure $LiMn_2O_4$, and 2) improved quantification of the effects of morphology [Striebel *et al.*, 1999; Simmen *et al.*, 2008]. Since model electrode materials are fabricated as films that are only few microns thick, they normally add only a few ohms to the total internal resistance of the electrochemical cell [Vinod and Bahnemann, 2002].

For some applications, such as in industry for miniaturization of electronic devices and for implantation in "smart" credit cards, thin film lithium batteries are also required. Therefore, thin film fabrication techniques are important in this field. The preparation of good quality thin films for batteries has been accomplished by chemical vapor deposition [Kim *et al.*, 2003], pulsed laser deposition [Singh *et al.*, 2001], and sputtering [Xie *et al.*, 2008]. However, most of these methods need expensive apparatus or make it difficult to give the as-deposited thin film accurate stoichiometry.

Among them, spray pyrolysis [Fragnaud *et al.*, 1995] is the most versatile technique for the deposition of active material onto current collectors due to its low cost and simplicity. Recently, it has been shown that $LiMn_2O_4$ nanoparticles could be easily prepared by flame spray pyrolysis (FSP), by combustion of appropriate precursor solutions for nanoparticles synthesis [Ernst *et al.*, 2007]. There are examples in the literature where nanostructured sensing films were made by FSP and direct deposition of SnO_2 nanoparticles onto sensor substrates [Mädler *et al.*, 2006] and *in situ* annealing [Tricoli *et al.*, 2008], leading to stable, transparent, and highly sensitive gas microsensors.

The opportunity to produce $LiMn_2O_4$ thin films is obvious when considering

these examples from the literature. The electrochemical performance of further annealed thin films on different current collectors is also investigated.

5.2 Synthesis Method

Here, flame spray deposition (FSD) was employed to rapidly deposit the $LiMn_2O_4$ nanoparticles onto current collectors to make thin cathode films. This method does not require the usage of any binder or conductive carbon black. Fig. 5.1 contains a schematic diagram of the FSP setup. The axial temperature profile of the spray flame was measured, with a maximum of 500 °C at 150 mm above the burner. The temperature of the current collector was reduced to approximately 120 °C, as it was attached to the water-cooled copper block during the deposition [Tricoli *et al.*, 2008].

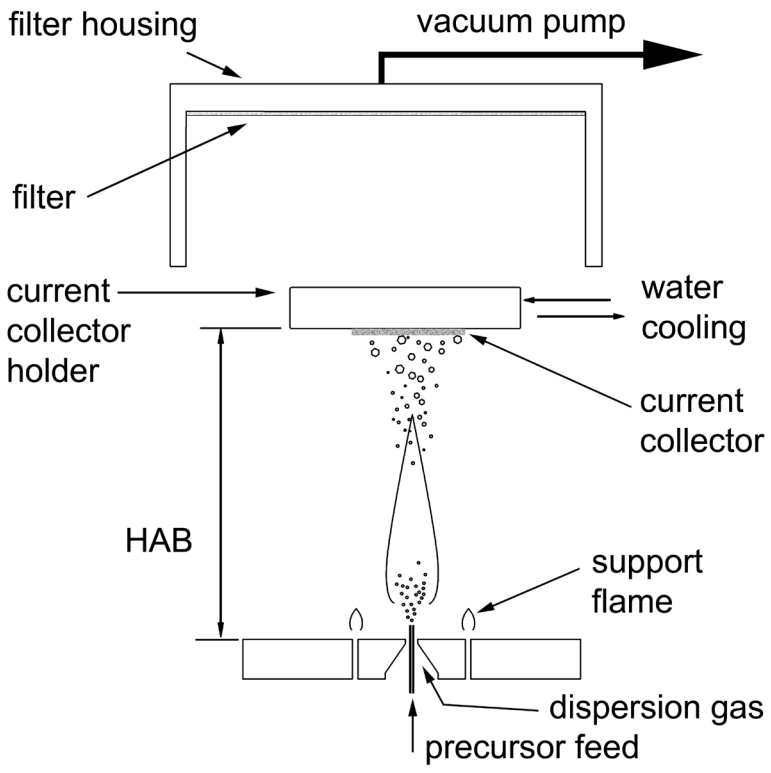

Fig. 5.1 Schematic diagram of $LiMn_2O_4$ FSD onto a water-cooled current collector.

These films were further annealed either by *in situ* flame or *ex situ* furnace calcination. Two different types of current collector, i.e. stainless steel (SS) foil and aluminium coated primer (ACP) foil, were used for electrochemical characterization.

5.3 Electrochemical Measurements

The electrochemical experiments were completed using the facilities provided in the Electrochemistry Laboratory, PSI Switzerland. The $LiMn_2O_4$ nanoparticle films on the current collector were cut into 1.0 cm^2 squares, dried at 120 ^oC in vacuum for 12 h, and used directly as electrodes. Electrochemical test cells similar to coin-type cells [Novák *et al.*, 1995] were assembled using the $LiMn_2O_4$ thin films as the working electrode and Li metal (Aldrich, 99.9 %) as both the counter and reference electrode. Both electrodes were separated by a 1 mm thick glass-fiber separator saturated with 500 µL of electrolyte solution, 1 M $LiPF_6$ in EC : DMC in a 1 : 1 mass ratio (Ferro GmbH). The cells were assembled in an argon-filled glove box with less than 1 ppm of oxygen, nitrogen, or water content.

Cyclic voltammetry (CV) and galvanostatic charge (Li^+ extraction) and discharge (Li^+ insertion) measurements were performed by a Computer-Controlled Celldata Capture (CCCC) system (Astrol Electronic AG, Oberrohrdorf, Switzerland). The CV measurements were performed in the range of 3.50 - 4.30 V vs. Li/Li^+ at the scanning rate of 0.02 mV s^{-1}. Other cells were galvanostatically charged and discharged in the same potential range at a constant specific current of 40 mA g^{-1}. All cells were tested inside a container with the temperature controlled at 25 ^oC. In order to promote complete discharge-charge at the respective potential limits, a potentiostatic step was included until the specific current was 10 % of the current used in the galvanostatic step.

All terms related to electrochemical reduction and oxidation processes are defined based on the standard Li-ion full cell configuration [Gritzner and Kreysa, 1993].

5.4 Physical and Structural Characterizations of $LiMn_2O_4$ Thin Film

The crystallinity and purity of the films deposited on SS and ACP current collector were determined by XRD. Fig. 5.2 shows the XRD diffractograms of such films on SS current collector, and Fig. 5.3 shows $LiMn_2O_4$ nanoparticles on ACP current collectors. The as-prepared $LiMn_2O_4$ on both current collectors is consistent with conventionally- and FSP-made $LiMn_2O_4$ nanoparticles [Ernst *et al.*, 2007]. The XRD patterns appeared to be in good agreement with the known spinel phases with space group Fd3m that are described in the literature (JCPDS 35-0782). Two major peaks corresponding to the (111) and (311) planes of spinel $LiMn_2O_4$ are clearly observed. The (400) peak at 44.1^o for both thin film samples overlaps with the peak from the ACP current collector. There is no notable intensity variation induced by a secondary phase or any impurities for either sample after *in situ* flame annealing.

The XRD crystal size for the samples was calculated with TOPAS2 software. It is about 10 nm for the material on both current collectors before annealing. After *in situ* flame annealing of the films on the ACP current collector, no discernible change was observed in the XRD crystal size. In contrast, the XRD crystal size of the films on the SS current collector increased by 30 % to 13 nm after *in situ* flame annealing, indicating significant crystal growth by sintering.

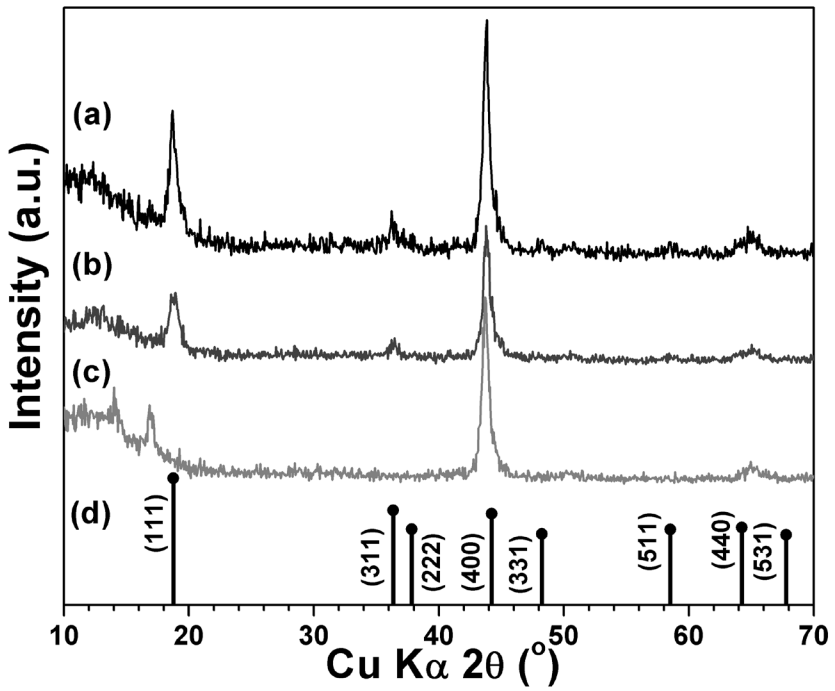

Fig. 5.2 XRD spectra of (a) *in situ* flame annealed $LiMn_2O_4$ film on SS current collector; (b) as-prepared $LiMn_2O_4$ film on SS current collector; (c) SS current collector; and (d) standard $LiMn_2O_4$ powder from JCPDS Card No. 35-0782.

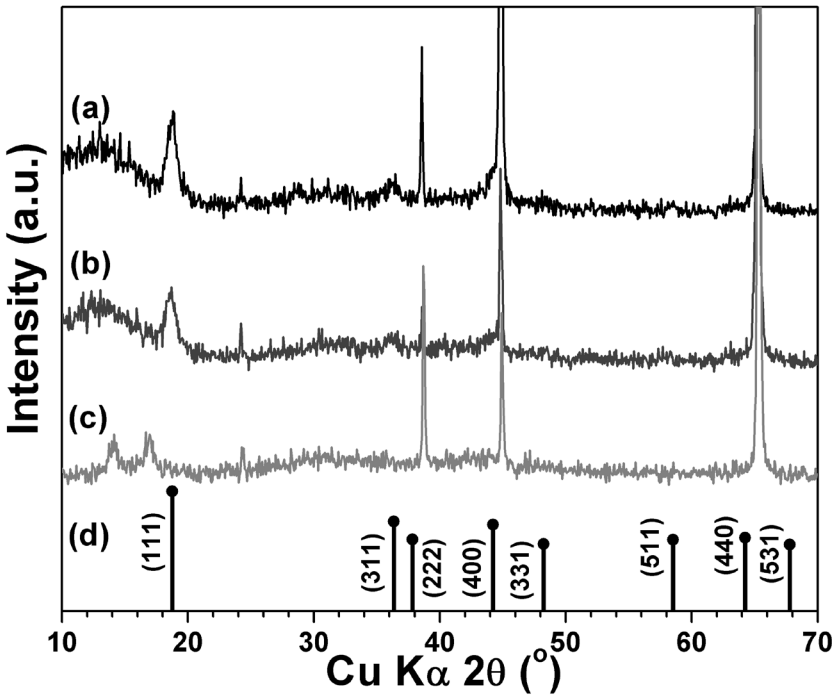

Fig. 5.3 XRD spectra of (a) *in situ* flame annealed $LiMn_2O_4$ film on ACP current collector; (b) as-prepared $LiMn_2O_4$ film on ACP current collector; (c) ACP current collector; and (d) standard $LiMn_2O_4$ powder from JCPDS Card No. 35-0782.

Table 5.1 XRD crystal size before and after *in situ* flame annealing.

Before annealing	SS current collector	=	10.4 nm
	ACP current collector	=	9.9 nm
After *in situ* flame annealing	SS current collector	=	**13.1 nm**
	ACP current collector	=	10.1 nm

FE-SEM analysis was conducted on the $LiMn_2O_4$ thin films to analyse the surface morphology. Fig. 5.4 summarizes the nanostructures of $LiMn_2O_4$ particles deposited onto SS and ACP current collectors, with and without annealing. Fig. 5.4(a) shows the surface of the thin film after direct deposition for 5 min on a SS current collector without annealing. It is clear that a homogeneous film with a thickness of approximately 7 μm was formed. The film is highly porous (98% porosity), as expected [Mädler *et al.*, 2006], with a lace-like structure composed of homogeneous nanograins with a similar size to those in SnO_2 sensor film deposited by this method [Mädler *et al.*, 2006; Tricoli *et al.*, 2008]. The corresponding films on the ACP current collector have similar morphology (Fig. 5.4(b)). Essentially, there are no detectable cracks or variation in the film structure, as no solvent evaporation takes place by this technique, in contrast to wet-deposition of slurries or pastes [Mädler *et al.*, 2006].

When these films undergo *in situ* flame annealing on the SS current collector (Fig. 5.4(c)), most of the nanoparticles are rather densely packed together, forming cauliflower-like structures [Tricoli *et al.*, 2008]. This is quite different from the corresponding ACP films (Fig. 5.4(d)), which have remained virtually unchanged after *in situ* flame annealing. It should be noted that the ACP current collector (with polymer primer coated onto the aluminum foil) is not stable after *in situ* flame annealing. The adhesion between the nanoparticles and the ACP surface is poorer than for SS, the film

on which is quite similar to the lace-like film structures of reported for micropatterned sensors [Tricoli *et al.*, 2008].

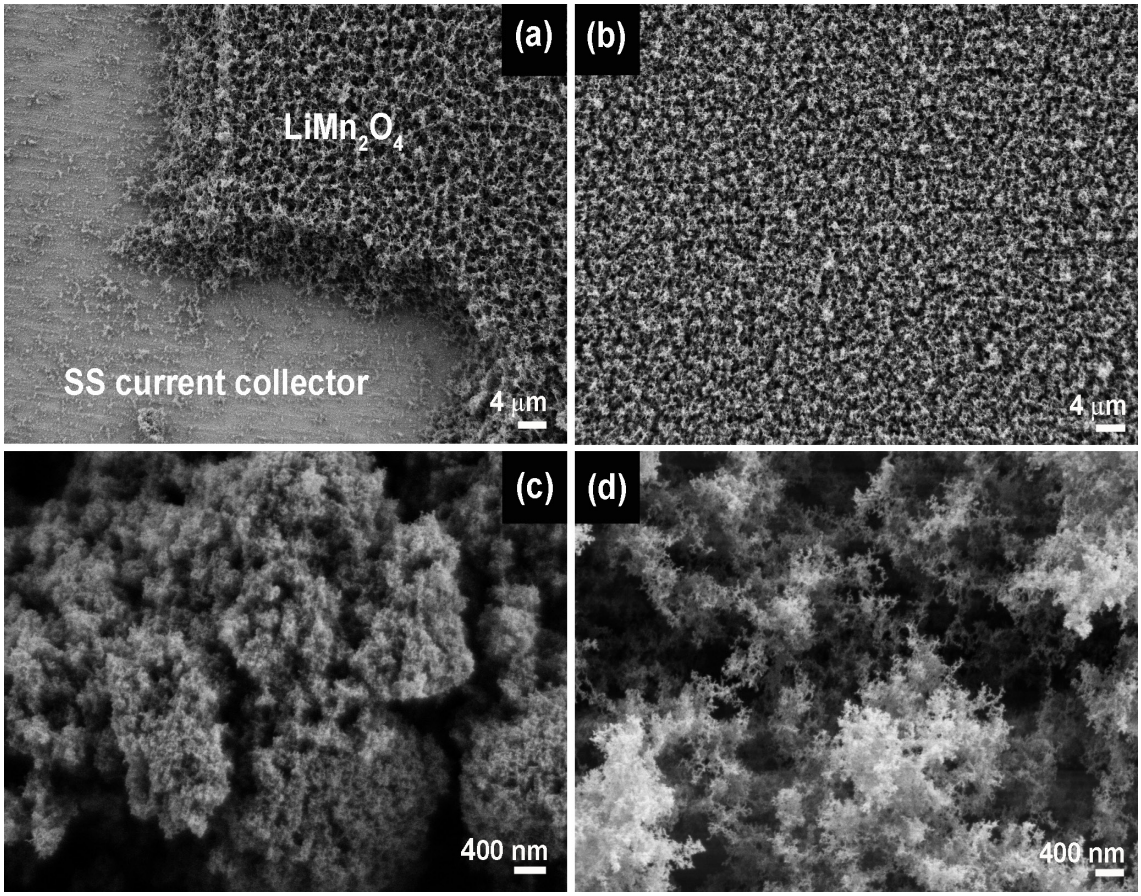

Fig. 5.4 The morphology of FSP-made $LiMn_2O_4$ nanoparticles as-deposited onto (a) SS and (b) ACP current collectors; and after *in situ* flame annealing onto the (c) SS and (d) ACP current collectors.

These results are consistent with the above XRD crystal size data, which indicated that crystal growth by *in situ* flame annealing took place on the SS current collector, but not the ACP current collector. Consistent with the above trend, though not directly comparable (because of the differences in the high temperature residence time distribution for the particles deposited on the current collectors), the specific surface area of the nanoparticles collected on the filter paper is approximately 134 m^2 g^{-1} before

annealing, while after *in situ* flame annealing the specific surface area is reduced to about 124 m^2 g^{-1}. BET measurements of the particles deposited onto the current collectors were not possible because of the small mass of the film (less than 1 mg), which is insufficient to meet the instrumental requirement of probing at least 2 m^2 per sample. Note that the specific surface area for $LiMn_2O_4$ is 134 m^2 g^{-1}.

5.5 Electrochemical Performance of *in situ* Flame Annealed $LiMn_2O_4$ Thin Films

The electrochemical performance for all the $LiMn_2O_4$ nanoparticles deposited onto different current collectors, i.e. SS and ACP foils, was tested. In an earlier stage of the experiments, aluminum foils were also tested as the current collector. However, $LiMn_2O_4$ thin film deposited onto aluminum current collector shows neither electrochemical redox peaks nor cyclability throughout the whole experiment, neither before nor after flame annealing (data not shown). As a result, further testing was focused on the SS and ACP current collectors.

A slow scan CV for the $LiMn_2O_4$ thin films before and after *in situ* flame annealing is shown in Fig. 5.5 for the initial cycle. The as-prepared FSD $LiMn_2O_4$ thin films, without further annealing for both the SS and the ACP current collectors, have no obvious redox peaks, as shown in Fig 5.5(a). Thus the *in situ* flame annealing, a direct and fast sintering step for FSP, was applied to improve the crystallinity of the thin films and to enhance their conductivity and/or contact with the current collector.

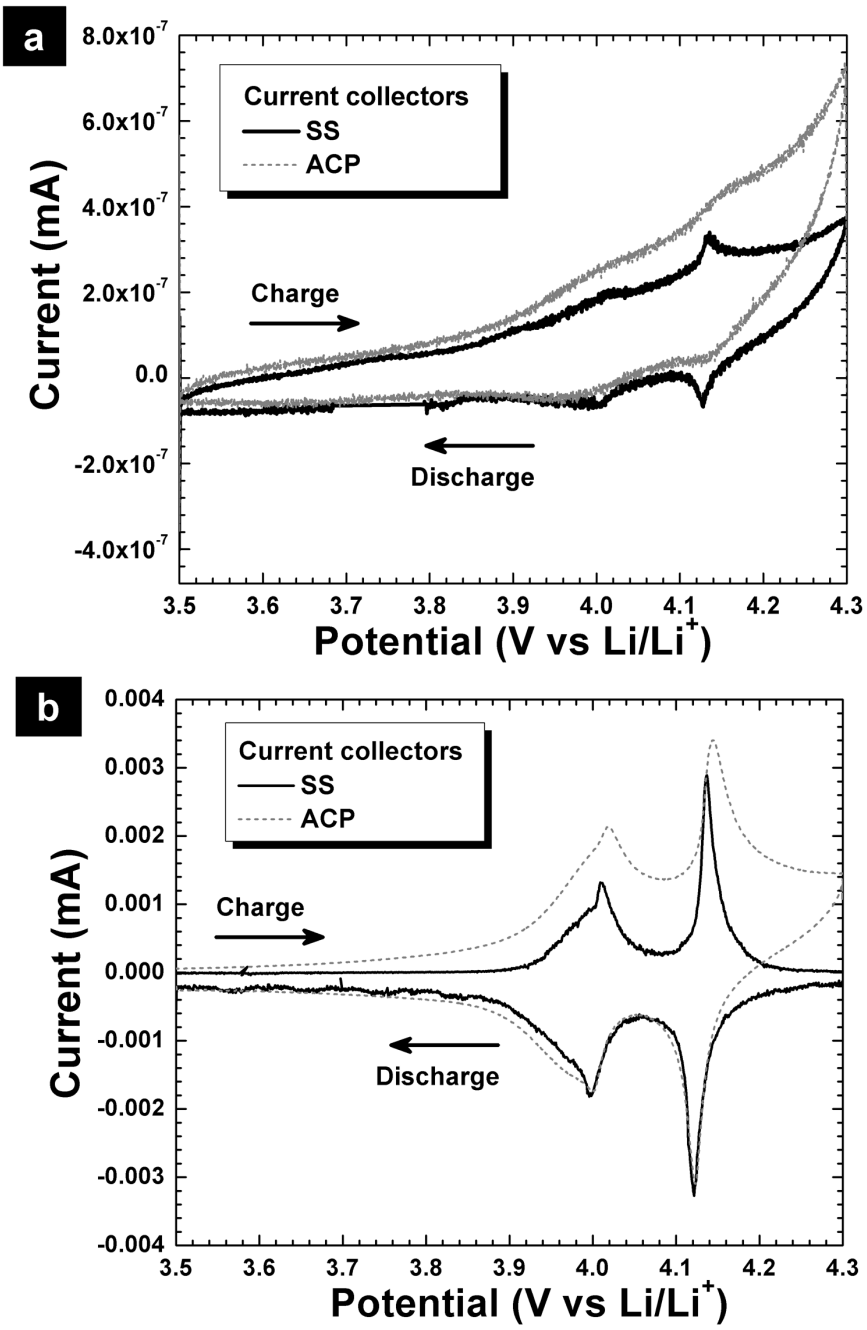

Fig. 5.5 Cyclic voltammograms of $LiMn_2O_4$ thin film electrodes on SS and ACP current collectors: (a) before annealing, and (b) after *in situ* flame annealing, with a scan rate of 0.02 mV s^{-1} for the 1st cycle.

According to Fig. 5.5, the *in situ* flame annealed $LiMn_2O_4$ thin films are electrochemically active in the applied potential range. Two pairs of redox peaks at approximately 4.00 and 4.15 V vs. Li/Li^+ are clearly observed, indicating two stages of

Li-ion extraction and insertion [Tarascon and Guyomard, 1993; Winter *et al.*, 1998]. This is a typical characteristic of the Li^+ intercalation/de-intercalation process in 8*a* tetrahedral sites of $LiMn_2O_4$ spinel during the electrochemical reaction [Tarascon and Guyomard, 1993]. The redox peaks for both *in situ* flame annealed $LiMn_2O_4$ thin films are sharp with well-defined splitting. In particular, the peaks for the thin film grown on the SS current collector are more symmetric with narrower peaks, thus suggesting better suitability of films on SS current collectors for model electrochemical experiments.

Fig. 5.6 shows the reversible charge (Li^+ extraction) of the electrodes prepared with the *in situ* flame annealed $LiMn_2O_4$ thin film on the SS and ACP current collectors upon cycling. Fading is observed after several oxidation/reduction cycles in all cases, but the decay of the specific charge for *in situ* annealed $LiMn_2O_4$ nanoparticles deposited onto the SS current collector is much slower than for those on the ACP current collector. The former electrode has an average of 0.87 % capacity loss per cycle in 30 cycles. The ratio for the charge respective to the two peaks in the film grown on the SS current collector is close to unity, as shown in Fig. 5.5(b), and therefore, the better reversibility of the cell on SS current collector is confirmed. The improved performance of the SS collector is also attributed to the better adhesion of the cauliflower-like aggregations of particles in the $LiMn_2O_4$ thin film on its surface.

The results in Fig. 5.5 and 5.6 indicate that the electrochemical response of the prepared $LiMn_2O_4$ thin films depends on the dynamics of particle or crystal growth, the adhesion, and the type of current collector. The mechanical properties of these cathode films are still poor due to the porous and fractal-like surface morphology [Chen and Schoonman, 2004; Tricoli *et al.*, 2008]. According to Fragnaud *et al.* (1995), the current collector temperature during spray pyrolysis substantially modifies the morphology and

adhesion of the films. Hence, further efforts towards improvement were continued by preparing dense and tough $LiMn_2O_4$ films by an *ex situ* annealing method.

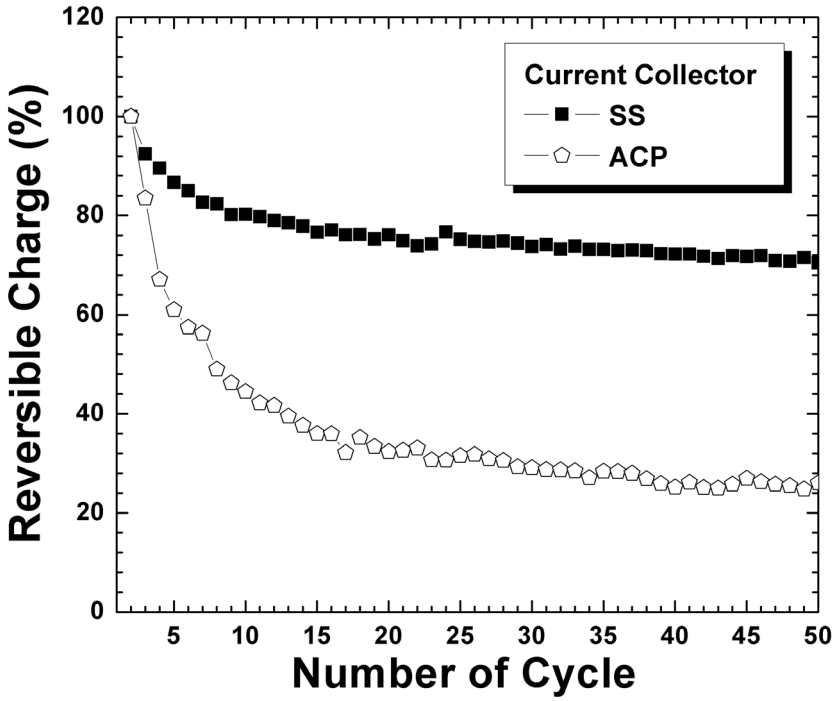

Fig. 5.6 Reversible charge as a function of cycle number from the galvanostatic experiments on the *in situ* flame annealed $LiMn_2O_4$ thin film electrodes on the SS and ACP current collectors.

5.6 Electrochemical Performance of *ex situ* Annealed $LiMn_2O_4$ Thin Films

The as-prepared $LiMn_2O_4$ thin films on SS current collectors (by FSD) were further sintered in air for 2 hrs using a furnace in the temperature range from 200 - 800 ^oC. Above 800 ^oC, the current collectors were deformed, and therefore the work was continued only up to 600 ^oC to produce a series of *ex situ* annealed $LiMn_2O_4$ thin films.

Fig. 5.7 shows the CV of the thin films annealed at 200, 400, and 600 ^oC, respectively. As can be seen from all the CVs, all samples exhibit strong and broad

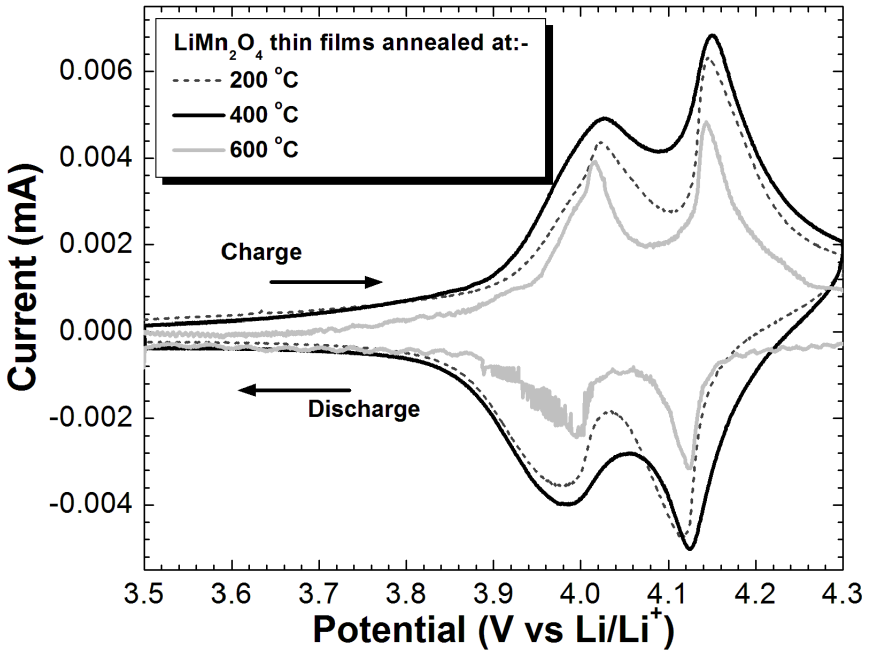

Fig. 5.7 CV of the first cycle for *ex situ* annealed $LiMn_2O_4$ thin film electrodes on SS current collectors, with annealing taking place at different temperatures. The scan rate is 0.02 mV s^{-1}.

redox peaks during electrochemical reaction in the potential region, in a similar way to Fig. 5.5(b). However, during the oxidation and reduction process, it was found that the $LiMn_2O_4$ thin film annealed at 400 ^oC showed higher peak current, which indicates stronger kinetic rates for the Li^+ insertion and extraction processes. According to Winter *et al.* (1998), the first oxidation peak (charge or Li^+ extraction) at 4.00 V vs. Li/Li^+ is attributed to the removal of Li^+ from one half of the tetrahedral 8*a* sites, as shown below:

$$LiMn_2O_4 \Leftrightarrow Li_{0.5}Mn_2O_4 + \frac{1}{2}Li^+ + \frac{1}{2}e^- \qquad (5.1)$$

The second oxidation peak at 4.15 V vs. Li/Li+ represents the removal of Li^+ from the remaining tetrahedral 8*a* sites to λ-MnO_2, which is described below:

$$Li_{0.5}Mn_2O_4 \Leftrightarrow 2\lambda - MnO_2 + \frac{1}{2}Li^+ + \frac{1}{2}e^- \qquad (5.2)$$

Fig. 5.8 shows the charge (Li^+ extraction) and discharge (Li^+ insertion) profile of the first cycle for the $LiMn_2O_4$ thin film annealed at 400 ^oC. The open circuit potential of this freshly prepared cell was 3.47 V vs. Li/Li^+, a value similar to that of the spinel $LiMn_2O_4$ phase. The Li^+ extraction and insertion curves show two plateaus around 4.00 and 4.15 V vs. Li/Li^+, and this is consistent with the two-stage behavior observed in the CV. During the reduction process in the first plateau region, Li^+ ions occupy every other available site until half of the sites are filled. At this point, the phase transformation of λ-MnO_2 to $Li_{0.5}Mn_2O_4$ is completed, producing single-phase $Li_{0.5}Mn_2O_4$. In the second plateau region, Li^+ ions will fill the remaining empty 8*a* sites. This arrangement increases the repulsion between the Li^+ ions, resulting in the small increase in the free energy drop, 100 mV [Liu *et al.*, 1996]. This is the origin of the difference in potential between the two plateaus.

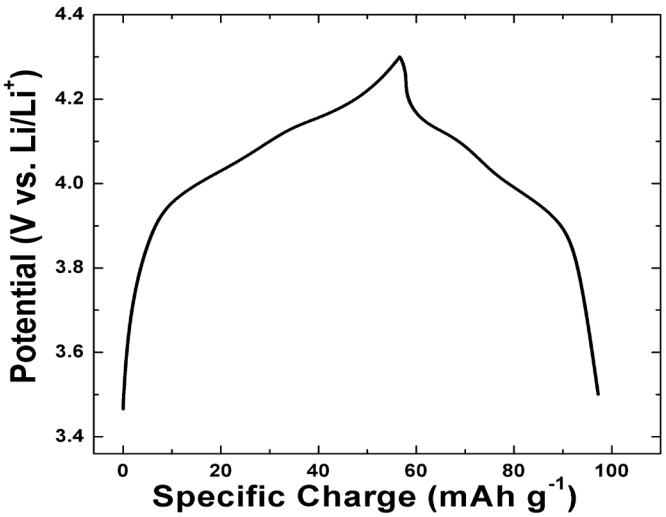

Fig. 5.8 Li^+ extraction/insertion profile for the first cycle for $LiMn_2O_4$ thin film annealed at 400 ^oC in air.

Fig. 5.9 shows the effect of the annealing temperature on the specific charge (Li^+ extraction) of $LiMn_2O_4$ vs. cycle number. The entire *in situ* flame and *ex situ* furnace annealed $LiMn_2O_4$ thin films show stable cycle life after 80 cycles. The good rechargeability and cycling stability of the $LiMn_2O_4$ thin film can be attributed to the fact that the annealed thin films, with no conductive carbon black, could suppress the Mn^{3+} dissolution, resulting in stable cyclability [Vinod and Bahnenmann, 2002].

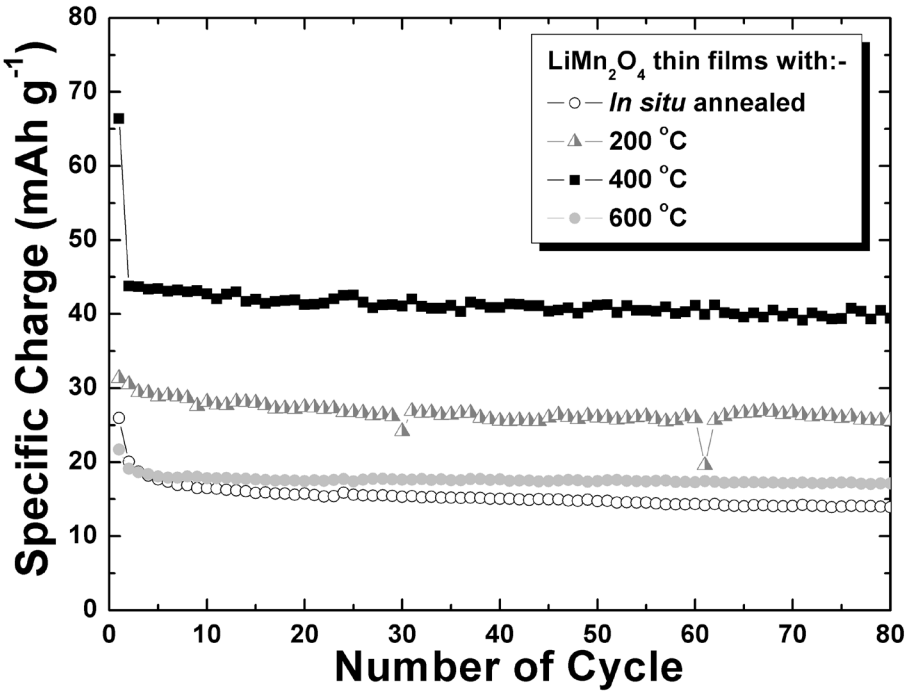

Fig. 5.9 Specific charge as a function of cycle number for *in situ* flame annealed and *ex situ* calcined $LiMn_2O_4$ thin film on SS current collector. The cell was cycled between 3.5 V and 4.3 V at a specific current density of 40 mA g^{-1}.

Many research groups [Amatucci *et al.*, 2001; Xia *et al.*, 2001] have reported that powder based $LiMn_2O_4$ electrode exhibits poor cycling behavior because of its slow dissolution into the electrolyte according to the dissolution of Mn^{3+} by the disproportionate reaction shown below:

$$2Mn^{3+} \rightarrow Mn^{4+} + Mn^{2+} \quad (5.3)$$

Such fading is linked to the dissolution of the Mn^{3+} from the high reactivity of solvent molecules that are electrochemically oxidized on the carbon surface, i.e. conductive carbon black. However, if the thin film does not contain any conductive carbon black, there is no Mn^{3+} dissolution, which is obviously the case here.

Besides this, when the cell is cycled in the applied 4 V potential range, the cubic symmetry of the $LiMn_2O_4$ structure is maintained without any severe lattice parameter change [Winter *et al.*, 1998]. Hence, Li^+ is extracted from the cubic structure with minimal contraction and expansion in an isotropic manner, resulting in good cycling stability.

It is clearly observed in Fig. 5.9 that *ex situ* furnace annealed $LiMn_2O_4$ thin film shows better initial charge retention compared with *in situ* flame annealed $LiMn_2O_4$ thin film, when both are deposited on SS current collector. Such good cycling performance of *ex situ* furnace calcined samples demonstrates that sintering in air is much more efficient than *in situ* flame annealing. In particular, $LiMn_2O_4$ thin film annealed at 400 ^oC exhibits higher specific charge after 80 cycles (~ 40 mAh g^{-1}) compared with films annealed at 200 ^oC (~ 25 mAh g^{-1}) and 600 ^oC (~ 17 mAh g^{-1}), respectively. The higher the crystallization temperature, the better the initial specific charge of the film. However, at 600 ^oC, the SS current collector was partially destroyed, as it became slightly hardened and some yellowish spots were observed on the back of the current collector, which resulted in this sample having the lowest charge retention compared with the others. This is also confirmed by an extra broad peak at 3.94 V vs. Li/Li^+, as seen in Fig. 5.7, where the CV curve was not stable when recorded, which suggests the decomposition/degradation of the SS current collector at high temperature.

5.7 Conclusions

The present studies indicate that spinel $LiMn_2O_4$ thin films can be prepared by a novel flame spray deposition method. This simple, fast and efficient method has never been applied for the preparation of any electrode thin film. After annealing, two pairs of electrochemically active redox peaks are clearly observed. For SS current collector, $LiMn_2O_4$ thin films show stable capacity retention after further heat treatment. In particular, spinel $LiMn_2O_4$ thin films annealed *ex situ* in air at 400 ^oC exhibit high initial charge capacity with good retention over 80 cycles. With $LiMn_2O_4$ thin films, Mn^{3+} originating from the conductor could be suppressed. The structure and surface morphology based on the annealing effect is also an important factor for the electrochemical cycle stability. These results indicate that annealed $LiMn_2O_4$ spinel thin films on SS current collector could be used as model electrodes to study their electrochemical behavior in lithium-ion batteries. For rechargeable microbatteries, the proposed electrode is suggested to be a potential thin film cathode due to its reasonable charge retention and cycling stability.

CHAPTER 6

HEXAGONAL-SHAPED TIN GLYCOLATE PARTICLES: A PRELIMINARY STUDY OF THEIR SUITABILITY AS LI-ION INSERTION ANODES

6.1 Introduction

There are many reports on binary and ternary Li alloys that have been tested as Li battery anodes [Dahn and Courtney, 1998; Liu *et al.*, 1998]. Of special importance are the Li-Sn compounds. It has been suggested that tin oxides (SnO, SnO_2) could be used as precursors for Li-Sn alloys. The lithiated tin alloys are formed while embedded in a Li_2O matrix [Brousse *et al.*, 1998; Chouvin *et al.*, 1999]. The use of tin oxides as precursors obviously adds a considerable irreversible capacity, which is required for the formation of Li_2O, and the formation of a Li-SnO matrix seems to stabilize the repeated formation of the lithiated alloys [Idota *et al.*, 1997; Courtney and Dahn, 1997a].

The morphological control of thermodynamically stable SnO_2 has also been widely studied. Many forms of SnO_2, such as tubes [Liu and Liu, 2005], rods [Guo *et al.*, 2004], spheres [Han *et al.*, 2005], and plates [Ohgi *et al.*, 2005], have been prepared by chemical vapour deposition [Liu and Liu, 2005; Duan *et al.*, 2005], as well as by sol-

gel [Shoyama and Hashimoto, 2003], hydrothermal [Yang and Zeng, 2004; Sun *et al.*, 2006], and non-aqueous methods [Pinna *et al.*, 2004; Ba *et al.*, 2005]. Previously, our group has demonstrated the possibility of fabricating SnO_2 nanoparticles by spray pyrolysis [Yuan *et al.*, 2006] and also SnO_2 nanowires by a self-catalyzed ball-milling process [Park *et al.*, 2007].

Recently, ultra-fine (< 5 nm) SnO_2 nanoparticles synthesized by a polyol-mediated synthesis were reported [Ng *et al.*, 2007]. Although the ultra-fine SnO_2 nanoparticles exhibited good cyclability, the extremely high first cycle irreversible charge loss of 72 % could hinder practical usage of this material. The high irreversible charge loss was mainly due to the high specific surface area of the nanoparticles, which resulted in an increase in surface decomposition products due to reaction with the electrolyte. Therefore, nanosized tin oxide particles will have to be protected from direct contact with the electrolyte, which acts as the main motivation for the study contained in this chapter.

6.2 Synthesis method

Tin oxalate precursor was used to synthesize the hexagonal-shaped and micro-sized tin glycolate particles as part of the polyol-mediated process in air. The as-synthesized tin glycolate particles were further calcined in air for 2 h at 600 – 800 ^{o}C to produce a series of tin oxides for comparison purposes.

6.3 Electrochemical Measurements

The anode was prepared by mixing as-synthesized tin glycolate or calcined tin glycolate powders (at 600, 700, and 800 ^{o}C, respectively) as active materials with 20 wt. % carbon black and 10 wt. % PVDF binders in NMP solvent to form a homogeneous slurry, which was then spread onto copper foil. Electrochemical measurements were carried out using coin-type cells. The electrolyte used was provided by MERCK KgaA, Germany. The cells were galvanostatically charged (Li^+ insertion) and discharged (Li^+ extraction) in the range of 0.01–1.50 V vs. Li/Li^+ at a constant current density of 50 mA g^{-1}, using a Neware battery tester. Cyclic voltammetry (CV) measurements were performed at a scanning rate of 0.1 mV s^{-1} using a CHI 660C electrochemical workstation system (CH Instrument, Cordova TN). All terms related to the electrochemical reduction and oxidation processes are defined based on the standard Li-ion full cell configuration [Gritzner and Kreysa, 1993].

6.4 Physical and Structural Characterizations

The phase and purity of the powder samples were determined by X-ray diffraction (XRD). Fig. 6.1 reveals products comprising tin glycolate crystallites (Fig. 6.1(a)) and nanocrystalline SnO_2 (Fig. 6.1(b-d)). For the as-synthesized tin glycolate particles, the emergence of diffraction peaks located at low angles (< 20^{o}) is characteristic of the glycolate compounds [Wang *et al.*, 2003; Scott *et al.*, 2003; Jiang *et al.*, 2004]. These peaks are attributed to the packing of building blocks associated with the glycolate polymer structure. All of the other peaks for the calcined samples can be

readily indexed to the tetragonal phase of SnO_2 (JCPDS Card No. 41-1445), with lattice constants of a = 4.738 Å and c = 3.187 Å, which are well matched with the XRD pattern of the standard (Fig. 6.1(e)). However, tin glycolate powders that were calcined in air for 2 hrs at 600 ^oC (Fig. 6.1(b)) and 700 ^oC (Fig. 6.1(c)) also show peaks corresponding to the orthorhombic phase of SnO_2 (JCPDS Card No. 29-1484). As the calcination temperature increases (Fig. 6.1(b-d)), the intensity of the tetragonal SnO_2 phase increases significantly, while the intensity of the orthorhombic SnO_2 phase is reduced. Tin glycolate powders calcined in air for 2 hrs at 800 ^oC (Fig. 6.1(d)) revealed only peaks corresponding to the tetragonal SnO_2 phase, with no impurities detected. The well-known Debye-Scherrer formula was used to estimate the average crystal size for the tin oxides, using crystalline silicon as the reference material. The estimated average crystal size was increased from 28 nm to 120 nm when the calcination temperature was increased from 600 to 800 ^oC.

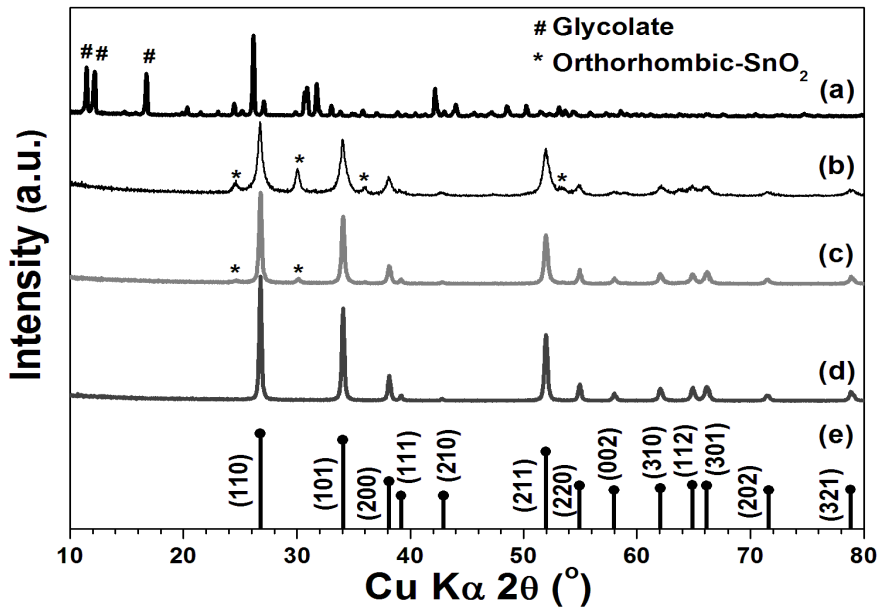

Fig. 6.1 XRD patterns of the obtained samples: (a) as-synthesized tin glycolate; and tin glycolate after being calcined for 2 hrs in air at (b) 600 ^oC, (c) 700 ^oC, (d) 800 ^oC; and (e) the JCPDS standard for SnO_2 (No. 41-1445).

The compositional and structural changes associated with the calcination process were also followed using TGA and FT-IR spectroscopy methods. Fig. 6.2(a) shows the TGA curve recorded under a flow of oxygen gas, indicating a two-step pattern of weight loss in the temperature ranges from 25 – 100 ^{o}C and 250 – 320 ^{o}C, respectively.

The first weight loss is attributed to the desorption of physically adsorbed water and ethylene glycol molecules, and the second one may be ascribed to the removal of ethylene glycol units chemically bonded to the tin element in the glycolate crystals [Wang *et al.*, 2003; Scott *et al.*, 2003; Jiang *et al.*, 2004]. A weight loss of 3.0 % is observed for the first step, and 13.0 % for the second step. In addition, the annealed sample did not show any weight loss above 800 ^{o}C. This confirms that the annealed sample consists of only SnO_2 crystallites.

Fig. 6.2(b) shows FT-IR spectra recorded from the tin oxalate precursor powder, from the as-synthesized tin glycolate particles, and also from the sample calcined at 800 ^{o}C. After the polyol-mediated process, O–C=O vibrational bands from the oxalate group at 785 cm^{-1} disappear, and CH_2– and C–OH bonds from the ethylene glycol unit at 2900 cm^{-1} and 1050 cm^{-1}, respectively, are present. The peaks corresponding to physically absorbed water or ethylene glycol units (the O–H stretching mode at 3310 cm^{-1} and the C–OH bending mode at 1050 cm^{-1}) have disappeared after calcination. Only the Sn–O stretching band still remains at 610 cm^{-1}, indicating the formation of nanocrystalline SnO_2 [Zhu *et al.*, 2000; Aurbach *et al.*, 2002; Zhao *et al.*, 2006]. These observations are consistent with previous studies, where conventional alkoxides were used as sol-gel precursors to prepare various phases of tin oxides [Scott *et al.*, 2003].

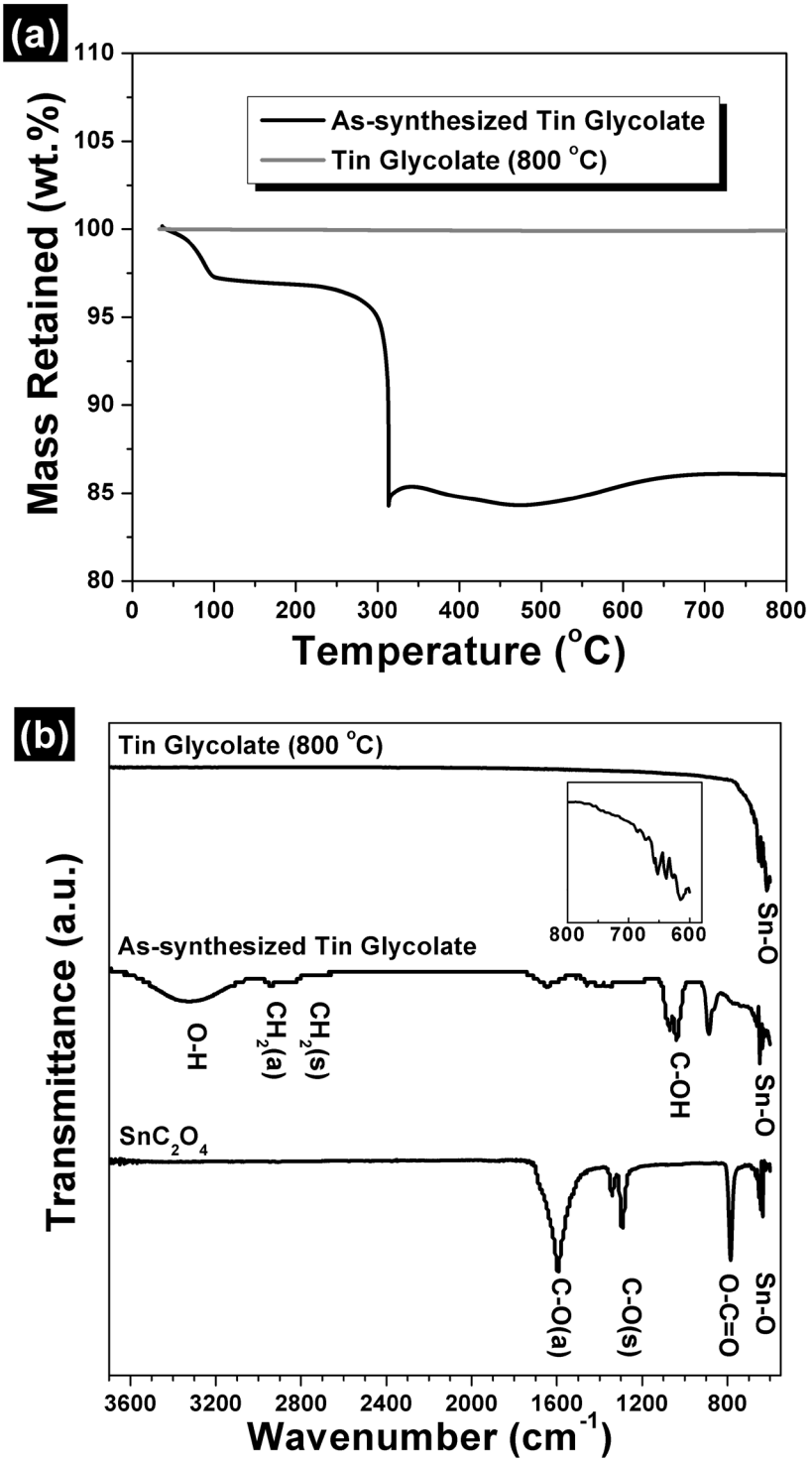

Fig. 6.2 (a) TGA curves of the as-synthesized tin glycolate and the tin glycolate after calcination at 800 ^{o}C for 2 h in air, and (b) FT-IR spectra for the tin oxalate precursor powder, the as-synthesized tin glycolate, and the tin glycolate after undergoing calcination at 800 ^{o}C for 2 h in air. For the sample calcined at 800 ^{o}C, a magnified view (inset) of the region corresponding to the Sn-O stretching band is also given.

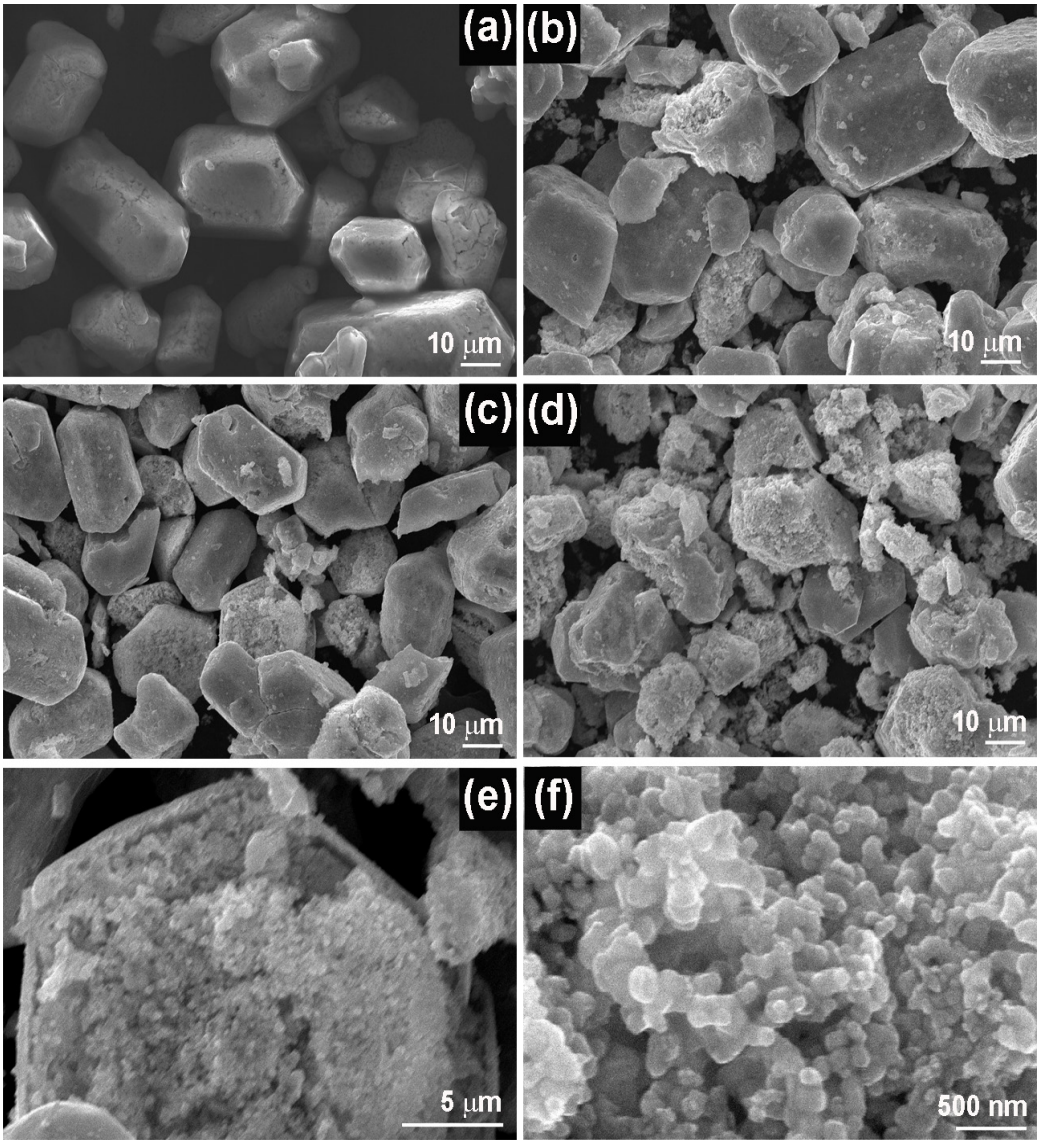

Fig. 6.3 SEM images of the obtained samples: (a) as-synthesized tin glycolate, and tin glycolate after undergoing calcination for 2 h in air at (b) 600 ^{o}C, (c) 700 ^{o}C, (d) 800 ^{o}C; (e) corresponding higher magnification image of (c), revealing encapsulation of tin oxide nanoparticles inside the hexagonal-shaped tin glycolate shell, and (f) corresponding higher magnification image of (e), confirming the nanosized nature of the tin oxide particles.

SEM images of the as-synthesized tin glycolate particles and the corresponding calcined products are shown in Fig. 6.3. As can be seen from Fig. 6.3(a), the as-

synthesized tin glycolate particles consist of hexagonal-shaped microstructures, with particle sizes up to 50 μm. However, after the as-synthesized powders were calcined in air (Fig. 6.3(b)-(d)), the hexagonal-shaped microstructures were destroyed, revealing nanosized particles encapsulated within the hexagonal-shaped glycolate shells (Fig. 6.3(e)). The destruction of the encapsulation becomes worsen as the calcination temperature increases. The average particle sizes observed in Fig. 6.3(f) are between 80-120 nm, which matches well with the previous XRD measurements.

The closely-packed nature of the nanoparticles supports the formation of a 2-dimensional aggregation of the nanoparticles into hexagonal-shaped tin glycolate microstructures, as illustrated in Fig. 6.4. At the initial stage of refluxing, oxalate groups from SnC_2O_4 are replaced by ethylene glycol units, which is supported by FT-IR measurements (Fig. 6.2(b)) due to the appearance of CH_2– and C–OH bands and the disappearance of O–C=O vibrational bands. Further refluxing results in further reactions of tin glycolate, and it eventually forms relatively large polymer-like particles, which are then self-assembled into hexagonal-shaped microstructures through a 2-dimensional aggregation of the nanostructures. The key step is the polymerization of the tin glycolate, a process that has been discussed in a number of publications for the same or similar metal alkoxides [Wang *et al.*, 2003; Scott *et al.*, 2003; Jiang *et al.*, 2004].

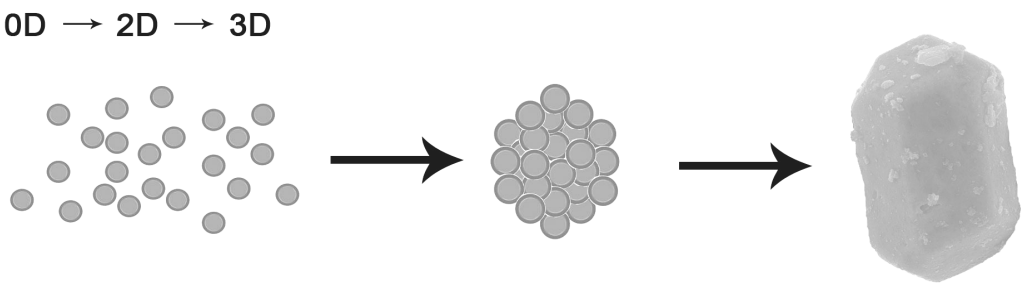

Fig. 6.4 A plausible organizing scheme for the self-construction of complex geometrical structures (e.g. polyhedra) by oriented attachment of nanostructures.

6.5 Electrochemical Performance

The electrochemical Li^+ storage properties of the as-synthesized tin glycolate and the corresponding calcined product, tin oxide nanoparticles, were systematically investigated. Generally, SnO_2 reacts with lithium in a two-step process as follows [Dahn *et al.*, 1998; Han *et al.*, 2005; Park *et al.*, 2007]:

$$SnO_2 + 4Li^+ + 4e^- \Rightarrow Sn + 2Li_2O \quad (6.1)$$

$$Sn + xLi^+ + xe^- \Leftrightarrow Li_xSn, (0 \le x \le 4.4) \quad (6.2)$$

The first process is an irreversible reaction (Eq. 6.1) where SnO_2 is reduced into tin with the formation of a Li_2O matrix. This reaction normally occurs at a potential below 0.9 V vs. Li/Li^+ [Ng *et al.*, 2007]. This reaction can contribute an irreversible specific charge as high as 710 mAh g^{-1}, while the second reaction (Eq. 6.2) corresponds to the reversible formation of Li_xSn alloys ($0 \le x \le 4.4$). The theoretical reversible specific charge from this reaction is 790 mAh g^{-1}. The Li-Sn alloying process normally occurs at a potential below 0.6 V vs. Li/Li^+ [Ng *et al.*, 2007]. Therefore, the total specific charge for Li^+ insertion in the first cycle can be as high as 1500 mAh g^{-1}.

Cyclic voltammograms (CVs) in the potential range of 0.01–1.50 V vs. Li/Li^+ were used to analyze the electrochemical Li^+ insertion properties of all the samples (Fig. 6.5). As can be seen from the CVs, a strong and broad reduction peak occurs at a potential above 0.6 V vs. Li/Li^+, which corresponds to the formation of Sn metal in a Li_2O matrix. There is a distinct contrast between the as-synthesized tin glycolate electrode (Fig. 6.5(a)) and the other calcined products, the tin oxide electrodes (Fig. 6.5(b-d)). For the as-synthesized tin glycolate electrode, a higher reduction peak (~1.2 V

vs. Li/Li^+) is observed due to the lower valence state (+2) for the tin in the compound and also the contribution from the glycolate part in the surface film formation process [Idota *et al.*, 1997; Winter and Besenhard, 1999; Zhu *et al.*, 2007]. However, the annealed products show a broad cathodic peak at 0.8 V vs. Li/Li^+.

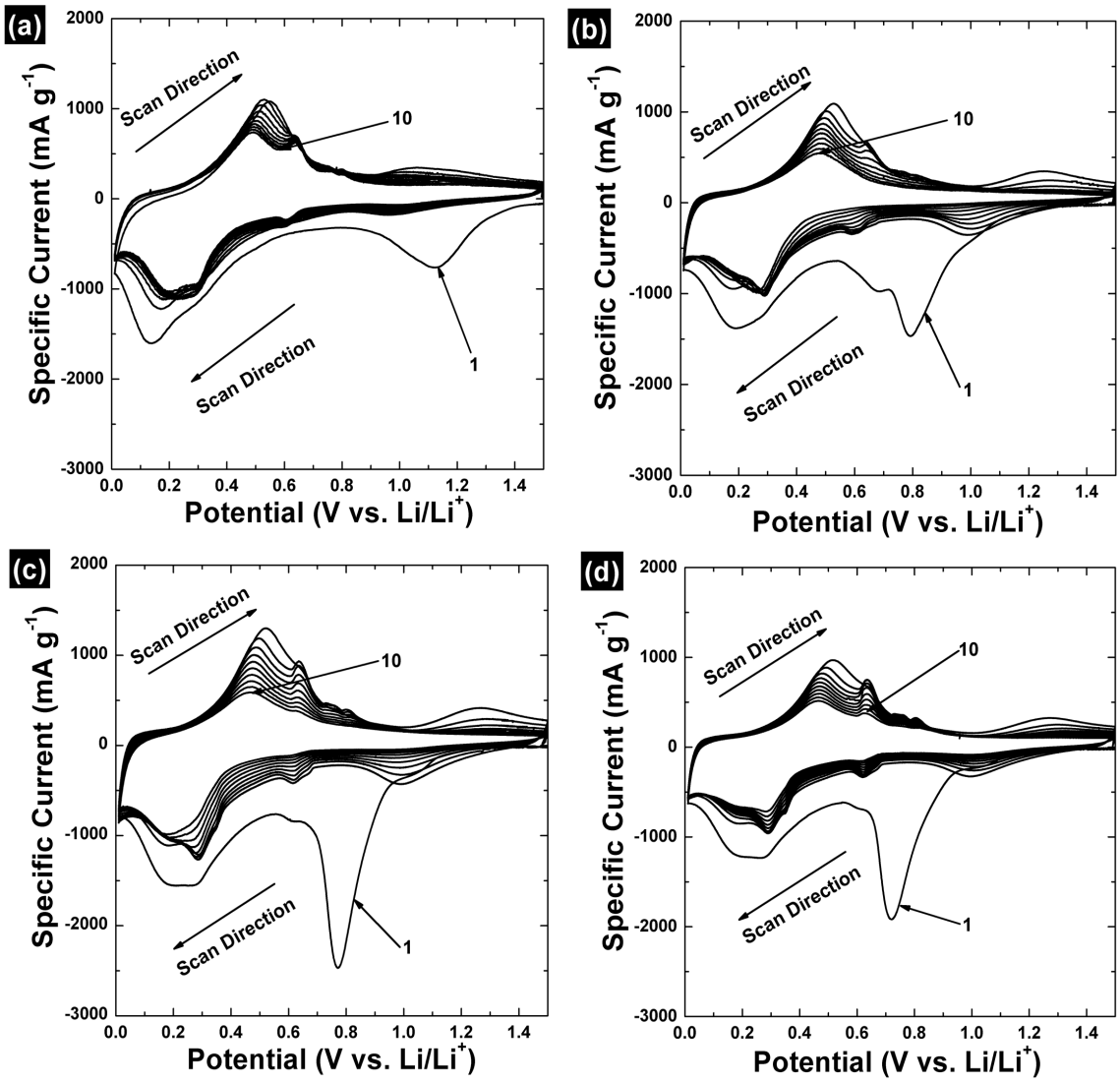

Fig. 6.5 Cyclic voltammograms of the first 10 cycles for all the obtained samples: (a) as-synthesized tin glycolate; and tin glycolate after undergoing calcination for 2 hrs in air at (b) 600 ^oC, (c) 700 ^oC, and (d) 800 ^oC (with the numbers indicating the cycle number). Cycling took at a scan rate of 0.1 mV s^{-1}.

Moreover, tin glycolate samples calcined in air at 600 ^{o}C and 700 ^{o}C (Fig. 6.5(b-c)) also show a small cathodic peak at 0.68 V vs. Li/Li^{+}, which was due to the presence of traces of orthorhombic SnO_2, as confirmed by the XRD measurements. Further cycling led to well-defined and almost identical reduction and oxidation peaks at 0.2 and 0.5 V vs. Li/Li^{+} for all the electrodes. In addition, the cycling kinetics for the as-synthesized tin glycolate electrode seems to be fairly stable over the first 10 cycles, whereas, the calcined products, the tin oxide electrodes, suffer rapid decay in the redox kinetics.

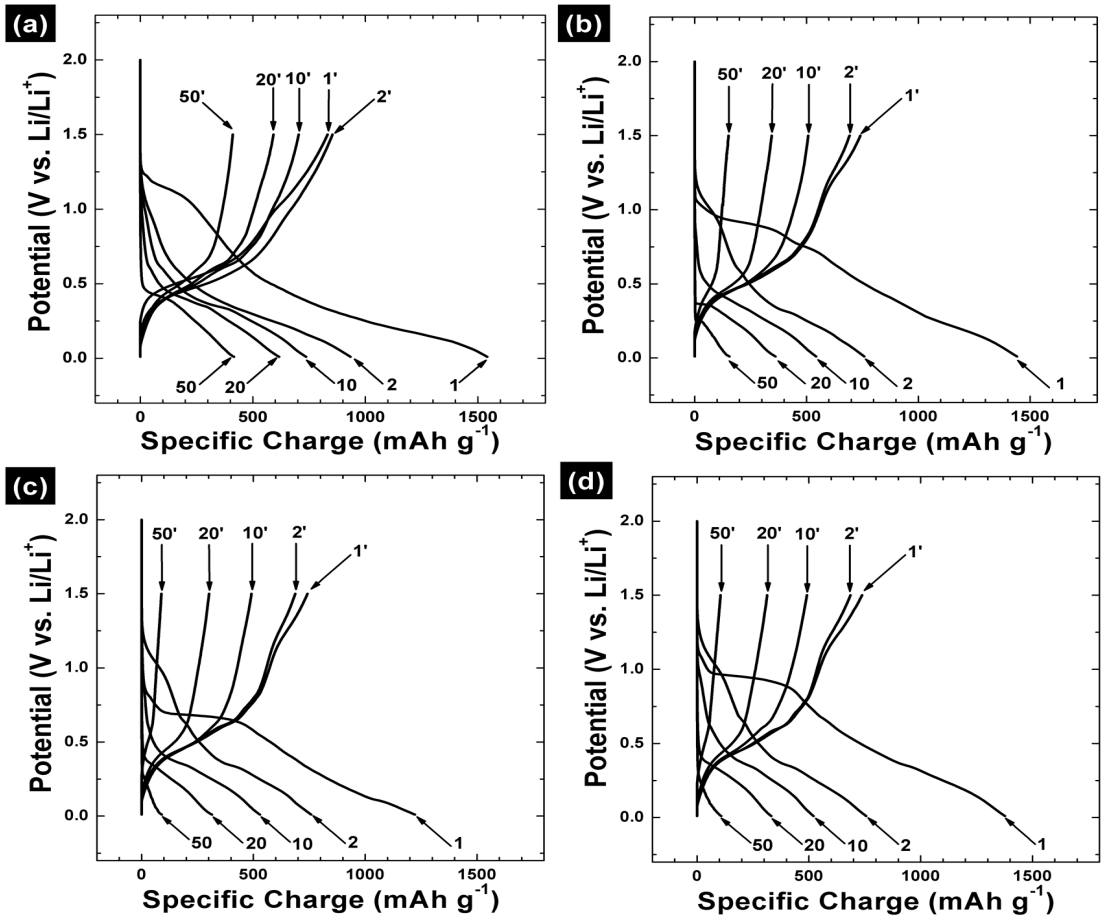

Fig. 6.6 Li^{+} insertion/extraction profiles of all the obtained samples: (a) as-synthesized tin glycolate; and tin glycolate after calcination for 2 hrs in air at (b) 600 ^{o}C, (c) 700 ^{o}C, and (d) 800 ^{o}C (with the numbers indicating the cycle number). The cells were tested at a current density of 50 mA g^{-1}.

Fig. 6.6 summarizes the 1st, 2nd, 10th, 20th, and 50th cycle electrochemical lithiation /de-lithiation data for the as-synthesized tin glycolate electrode (Fig. 6.6(a)) and the calcined tin oxide electrodes (Fig. 6.6(b)-(d)). The calculated specific charges are solely based on the active materials. The first cycle specific charges for Li^+ insertion are 1541, 1441, 1223, and 1377 mAh g^{-1} for the as-synthesized tin glycolate electrodes and the electrodes made from tin glycolate powders calcined in air at 600, 700, and 800 ^oC, respectively, with the corresponding first cycle specific charges of Li^+ extraction, 832, 741, 742, and 738 mAh g^{-1}, respectively. Therefore, the first cycle coulombic efficiencies were 54, 51, 61, and 54 % for the as-synthesized tin glycolate electrode and the electrodes made from tin glycolate powders calcined in air at 600, 700, and 800 ^oC, respectively.

The large irreversible charge loss could be attributed to the formation of Li_2O and also the irreversible trapping of lithium by the solid electrolyte interface (SEI) passivation layer. All electrodes show fading behaviour upon prolonged cycling. However, the as-synthesized tin glycolate electrode still maintained fairly high Li^+ insertion/de-insertion capacity even after 50 cycles, when compared with the other tin oxide electrodes.

Fig. 6.7 shows the cycling behaviour of the as-synthesized tin glycolate electrode and the corresponding calcined tin oxide electrodes. Using a non-restricted cycling procedure at a cycling rate of 50 mA g^{-1}, the initial reversible specific charges (2nd Li^+ insertion) are 934, 758, 758, and 756 mAh g^{-1} for the electrodes composed of the as-synthesized tin glycolate and of tin glycolate powders calcined in air at 600, 700 and 800 ^oC, respectively. Subsequently, the reversible specific charge beyond 50 cycles is maintained at 416, 155, 90, and 108 mAh g^{-1} for the as-synthesized tin glycolate electrode and the electrodes of tin glycolate powders calcined in air at 600, 700, and 800

^{o}C, respectively, corresponding to the ratios of the specific charges retained after 50 cycles to the first Li^{+} insertion, which are 44, 20, 12, and 14 %, respectively.

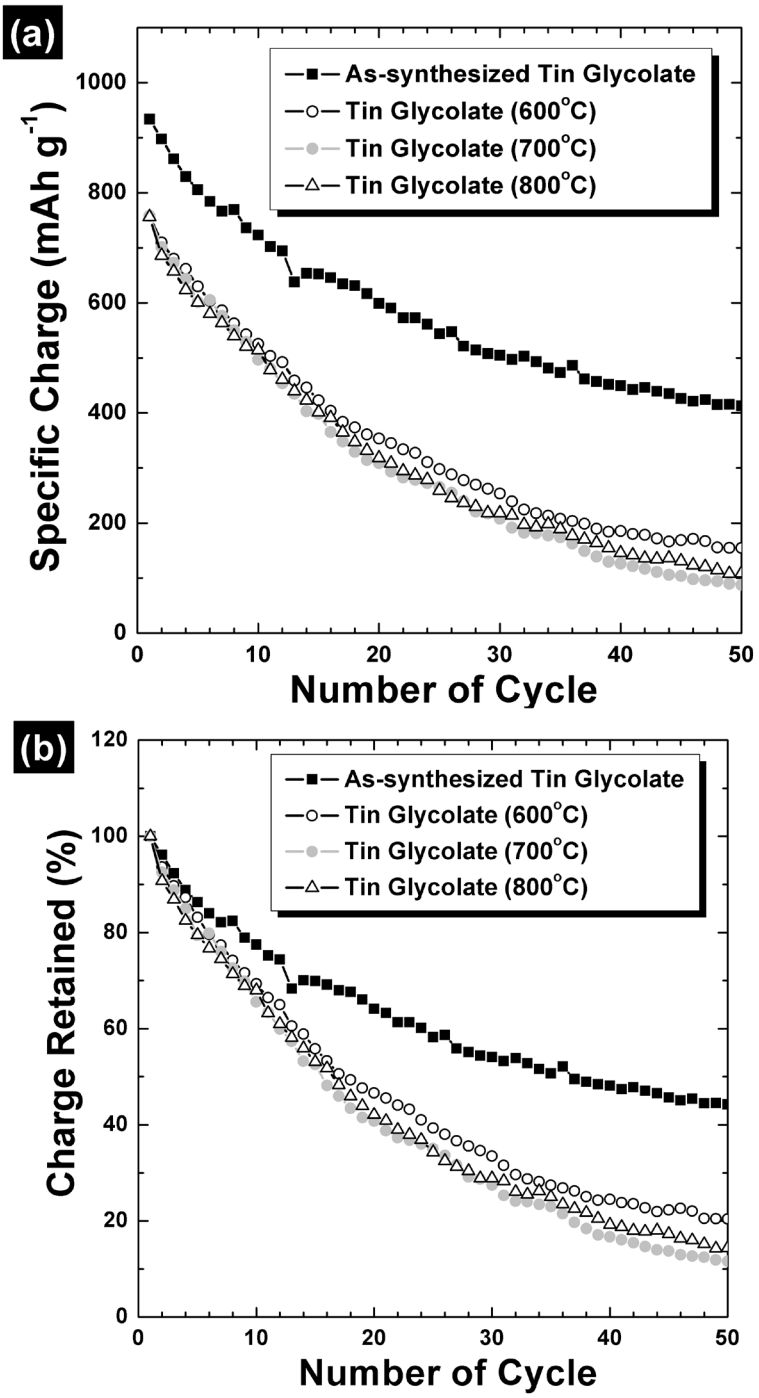

Fig. 6.7 Cycling behaviour of electrodes for all the obtained samples: (a) reversible charge as a function of cycle number, and (b) the corresponding percentage of reversible charge retained as a function of cycle number.

The superior charge retention of the as-synthesized tin glycolate electrode compared to the other tin oxide electrodes suggests the beneficial effect of the encapsulation by the glycolate microstructures in buffering the volume expansion during the alloying reactions.

Fig. 6.8 shows the cycling behaviour of the as-synthesized tin glycolate electrode. This electrode shows an irreversible charge loss (Q_{irrev}) of less than 1.2 % per cycle. However, the specific charges for the first ten cycles (> 800 mAh g^{-1}) are far beyond our expectations. SnO_2 has a theoretical specific charge of 790 mAh g^{-1}. According to the thermogravimetric analysis (TGA) results shown earlier in Fig. 2(a), SnO_2 is 84 wt % in the tin glycolate compound. This means that the specific charge from SnO_2 should not exceed 664 mAh g^{-1}. So, where does the excess charge storage come from?

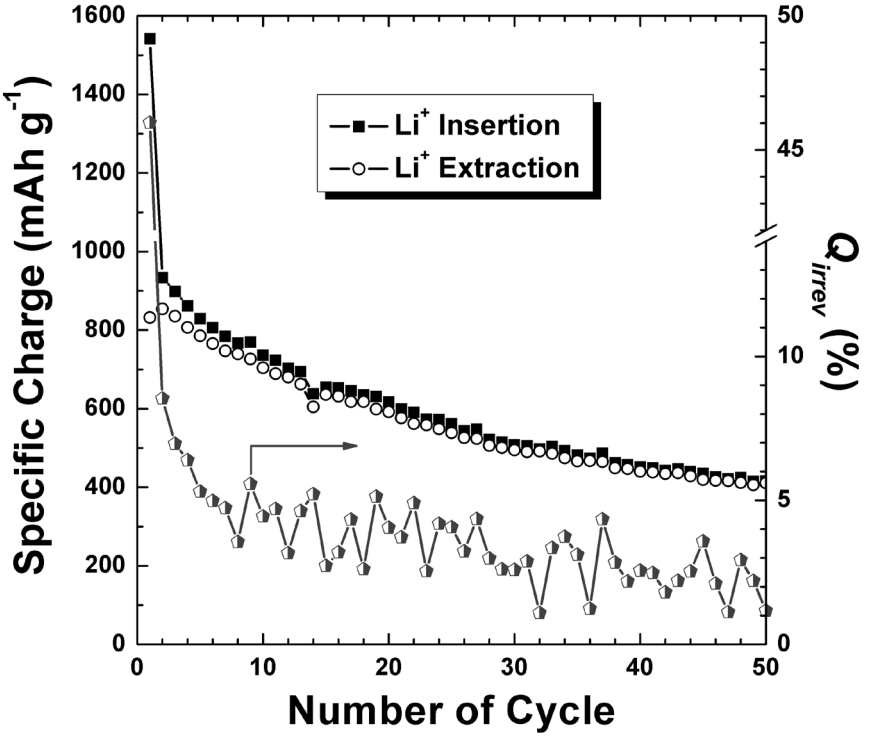

Fig. 6.8 Cycling behaviour for electrode made from the as-synthesized tin glycolate. Q_{irrev} % = percentage of irreversible capacity loss.

It has been reported in the literature that transition metal oxides show reversible Li^+ storage behaviour [Poizot *et al.*, 2000]. In these cases, a transition metal can react with Li_2O upon Li^+ extraction. This means that the reaction in Eq. 6.1 is reversible, which contributes to a very high reversible specific charge. Up to now, no experimental evidence has shown whether the reaction in Eq. 6.1 for Sn-based oxides is completely irreversible or not. However, Courtney and Dahn (1997b) have reported that Li-O bonds are not stable when the charging potential is above 1.3 V vs. Li/Li^+. Recently, Li *et al.* (2004) also indicated that the reaction in Eq. 6.1 is reversible for most metal compounds in view of their thermodynamics. The reversibility of the reaction (Eq. 6.1) from Li_2O and Sn back to Sn-O compounds is mainly influenced by the intrinsic conductivity of the compound, the grain sizes of the Li_2O and the Sn, the separation distance between the Li_2O and the Sn, and the electronic contact with the conductive additive [Li *et al.*, 2004].

For the as-synthesized tin glycolate microstructures, the Sn-based nanoparticles are embedded in a glycolate capsule, which ensures that the Li_2O and elemental Sn that are formed are in good contact, without any distinct separation. This provides a kinetic advantage for the reversible reaction in Eq. 6.1. This reaction is at least partially reversible for the first few cycles, obviously the case here, which contributes to the high reversible charge.

The morphologies of the electrodes after prolonged cycling were examined. Fig. 9 shows SEM images for the as-synthesized tin glycolate electrode (Fig. 9(a)-(b)) and the electrode composed of tin glycolate powder calcined in air for 2 h at 800 ^oC (Fig. 9(c)-(d)), after 50 cycles. Huge cracks are observed in the calcined sample, with the crack width estimated to be approximately 3 μm (Fig. 9(d)). The reason for the

cracks' creation is the pronounced volume changes of the host material under alloying/de-alloying processes [Zhu *et al.*, 2000].

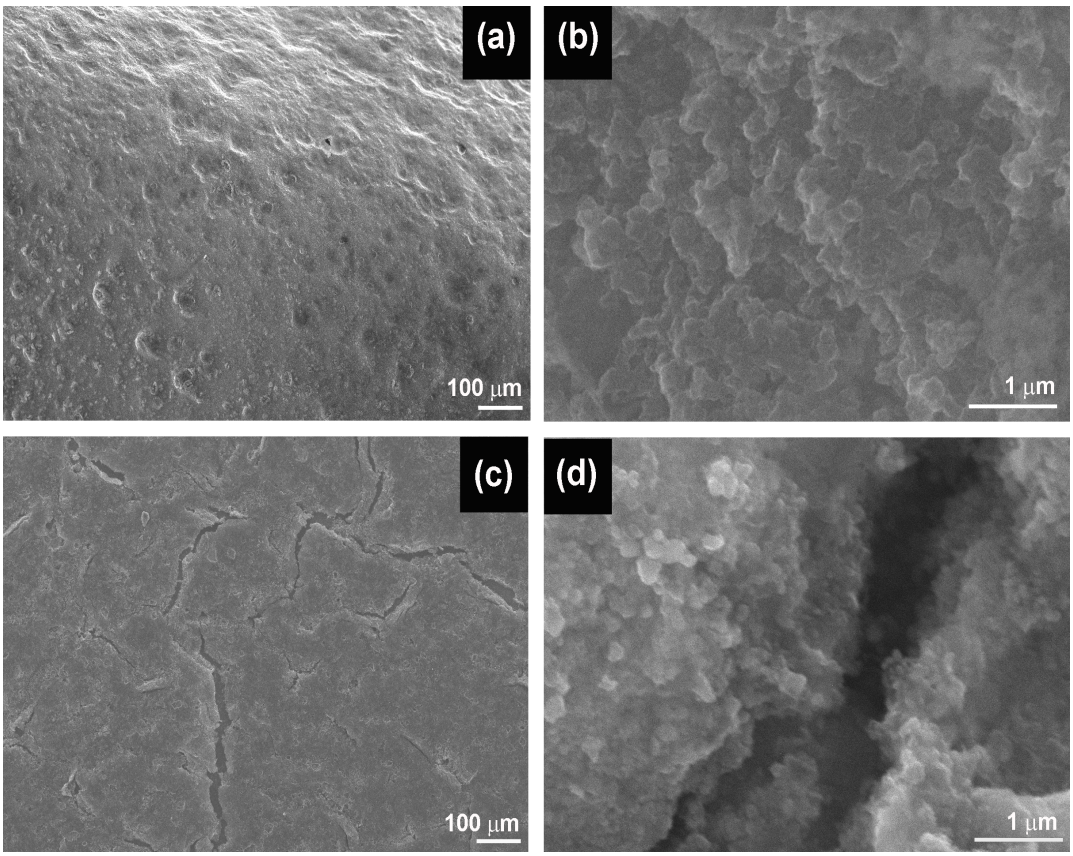

Fig. 6.9 SEM images of the electrodes after 50 cycles: for the as-synthesized tin glycolate: (a) low magnification image and (b) the corresponding high magnification image; and for tin glycolate after calcination at 800 ^{o}C for 2 hrs in air: (c) low magnification image and (d) the corresponding high magnification image.

These cracking phenomena upon cycling indicate problems associated with the integrity of the active mass. Cracking causes obvious problems related to the passivation of these electrodes by stable surface films. It is very likely that part of the active mass becomes isolated by surface films formed on the fresh active surface that the cracks expose, by reactions of Li-Sn compounds and solution components. Thereby, the electrodes fade rapidly during cycling. However, the as-synthesized tin glycolate

electrodes still maintained integrity and good contacts between particles. This suggests that the encapsulation of the Sn-based nanoparticles in the glycolate microstructures played an important role in maintaining the integrity of the electrode upon prolonged cycling.

The cyclic performance of the as-synthesized tin glycolate crystals is still not satisfactory and may benefit from further optimization. Despite that, these results illustrate the good prospect that the charge storage of glycolate anodes may be significantly enhanced by an optimized microstructure. Moreover, because many tin-based compounds have been demonstrated as promising high charge storage anode materials for use in lithium-ion batteries [Zhu *et al.*, 2000; Han *et al.*, 2005; Sun *et al.*, 2006; Ng *et al.*, 2007], plenty of room still exists for the improvement of tin glycolate structures with respect to their Li storage properties.

6.6 Conclusions

In summary, micron-sized, hexagonal-shaped tin glycolate with encapsulation of electrochemically active tin-based nanoparticles has been successfully prepared by using a one-step polyol-mediated synthesis route. The synthesis is based on the two-dimensional aggregation of the organo-tin nanocrystallites, giving an overall quasi-hexagonal microstructure in the presence of ethylene glycol after continuous refluxing in air at 195 ^{o}C for 5 hrs. This synthetic procedure is straightforward and inexpensive, and consequently can be readily adopted to produce large quantities of uniform, hexagonal-shaped tin glycolate particles. When applied as an anode material for Li-ion batteries, the as-synthesized tin glycolate displays promising Li^{+} storage capability.

CHAPTER 7

NOVEL SILICON-POLYPYRROLE NANOCOMPOSITES FOR LITHIUM-ION BATTERY ANODE

7.1 Introduction

There is great interest in developing new anode materials to overcome the limited charge storage of graphite (372 mAh g^{-1}) for rechargeable Li-ion battery [Idota *et al.*, 1997; Li *et al.*, 2001; Pereira *et al.*, 2003]. Aside from Li-Sn compound, another binary lithium alloys, Li-silicon (Li-Si) has also been widely investigated due to their low Li^+ insertion and extraction potential and the known highest theoretical charge storage of 4200 mAh g^{-1} [Guo *et al.*, 2005].

However, there is one severe problem with these Li-Si alloy anodes, i.e., the large volume change of 400 % upon Li^+ intercalation/deintercalation, which inevitably pulverizes the alloy particles. The resulting loss of connectivity with the conducting additive carbon black particles causes poor cyclability in practice [Wilson and Dahn, 1995; Gao *et al.*, 2001; Kim *et al.*, 2003; Eom *et al.*, 2006]. In order to improve the cycling characteristics of this material, it is necessary to relieve such morphological changes.

One possible solution to overcome this problem is by using composite materials, where Si is homogeneously distributed within an inactive (TiC, TiN, SiC, etc.) or less active matrix (carbon) [Kim *et al.*, 2000; Guo *et al.*, 2005; Ng *et al.*, 2006]. The relatively inert matrix with regard to electrochemical activity towards Li^+ would accommodate the mechanical stresses/strains experienced by the active phase and maintain the structural integrity of the composite electrode during the alloying/de-alloying processes.

Carbon coating with high electronic conductivity not only buffered the great volume changes during the cycling process, but also avoided possible agglomeration of the uniformly distributed silicon particles [Ng *et al.*, 2006]. It can be imagined that if there is a conductive polymer matrix, i.e. polypyrrole (PPy) in which Si is embedded, the cyclability of the Si anode could be greatly improved. The soft polymer matrix could efficiently absorb the volume changes during Li^+ insertion and extraction.

Previously, our group has demonstrated that Si-PPy composites prepared by high energy ball milling could deliver a reversible specific charge of 500 mAh g^{-1} [Guo *et al.*, 2005]. However, their cycling performance as Li-ion battery anode is not satisfactory. Due to the apparent viscosity of PPy, it is very difficult to coat PPy onto the Si powder uniformly by mechanical ball milling method.

To further increase the efficiency of the PPy as a host matrix, *in situ* polymerization method was applied to coat PPy onto nanocrystalline Si powder. A series of Si-PPy nanocomposites were prepared and the electrochemical properties of the nanocomposites were systematically evaluated.

7.2 Preparation of Si-PPy nanocomposites

Si-PPy nanocomposites were prepared by coating PPy with *in situ* oxidative chemical polymerization method onto Si nanoparticles. Adding appropriate weights of the pyrrole monomer to 1.0 g of nanocrystalline Si powder could vary the PPy content in the composites.

7.3 Electrochemical Measurement

CR2032 coin cells were assembled to test the electrochemical performance of nanocomposite anodes. The Si-PPy or Si electrodes were prepared by dispersing 85% active materials, 5% carbon black, and 10% PVDF binder in NMP solvent to form homogeneous slurry. The slurry was spread onto pieces of copper foil. The cells were assembled in an argon filled glove-box (Mbraun, Unilab Germany). The electrolyte was provided by MERCK KgaA, Germany. The cells were galvanostatically charged (Li^+ insertion) and discharged (Li^+ extraction) at a constant current density of 100 mA g^{-1} over the potential range of 0.02 - 1.20 V vs. Li/Li^+ at room temperature, using a Neware battery tester. All terms related to electrochemical reduction and oxidation processes were defined based on the standard Li-ion full cell configuration [Gritzner and Kreysa, 1993].

7.4 Physical and Structural Characterizations

Raman spectroscopy was carried out to verify the presence of PPy in the nanocomposite. A typical Raman spectrum for the Si-PPy nanocomposite is shown in

Fig. 7.1, where the Raman spectrum of nanocrystalline Si powder is also plotted for comparison. The peaks at approximately 1085, 1375, and 1599 cm^{-1} are attributed to the N-H in-plane deformation, the ring stretching, and the backbone stretching of the C=C bonds of PPy, respectively [Liu *et al.*, 2000]. This is clear evidence that PPy is present in the nanocomposite. In addition, the Raman peak of the Si-PPy nanocomposite at approximately 510 cm^{-1}, which is assigned to Si, has been downshifted and broadened when compared to that of nanocrystalline Si. It is believed that these characteristics are induced by the presence of PPy in the nanocomposites.

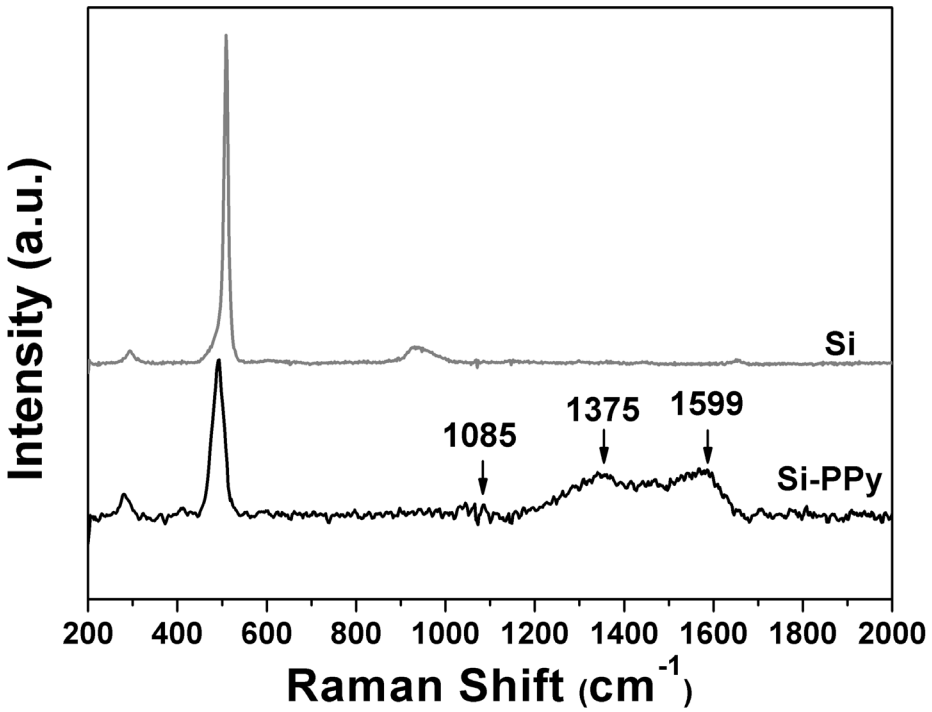

Fig. 7.1 Raman spectra of the Si and Si-PPy nanocomposites.

Thermogravimetric analysis (TGA) was carried out to quantify the amount of PPy in the nanocomposite. Fig. 7.2 shows the TGA analysis of the nanocomposites along with nanocrystalline Si and PPy powders when heated from 25 ^{o}C to 700 ^{o}C. Pure PPy powder burns off at 600 ^{o}C, while the nanocrystalline Si powder starts to oxidize

slowly in air above 700 ^{o}C. As the nanocrystalline Si powder remains stable in this temperature range, therefore the change in weight before and after the burning of PPy directly translates into the amount of PPy in the nanocomposite. Using this method, it is found that the amounts of PPy present in the nanocomposites are 33, 50 and 66 wt. %, respectively.

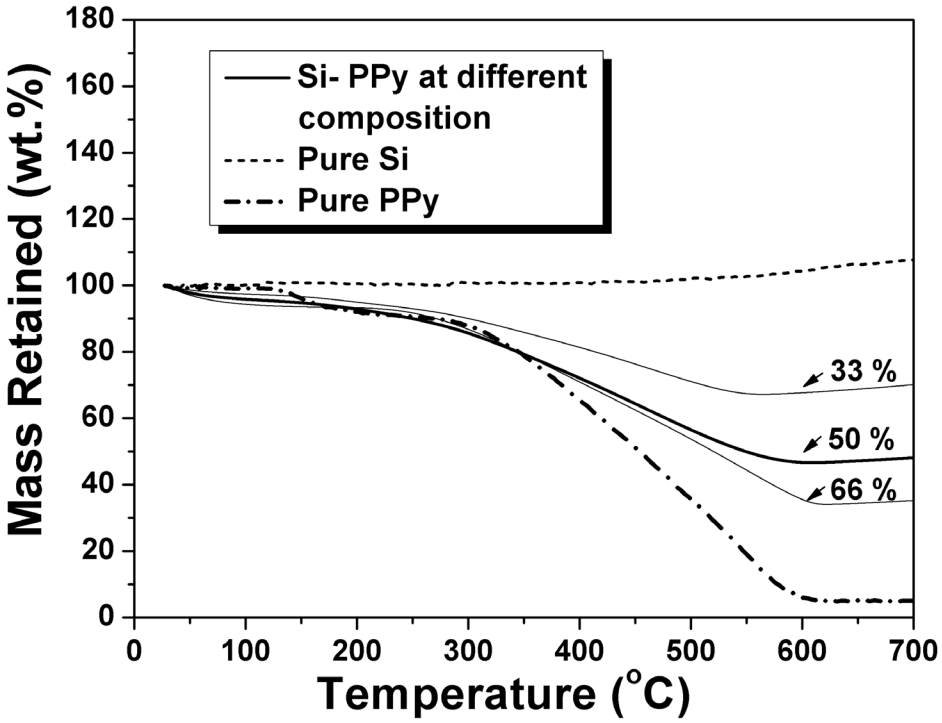

Fig. 7.2 TGA curves of Si-based nanocomposites at different PPy loading level.

TEM images of both the nanocrystalline Si powders and the Si-PPy nanocomposites with 50 wt. % PPy are shown in Fig. 7.3. It can be seen that the particles of Si are near-spherical, with a particle size of approximately 40 nm (Fig. 7.3a). Fig. 7.3b shows the surface morphology of the Si-PPy nanopowders, where it can be seen that two different structure of particles exist. Based on TEM analysis, the particles which appear smooth and round are Si, while the particles often slightly smaller and uneven in appearance belong to PPy.

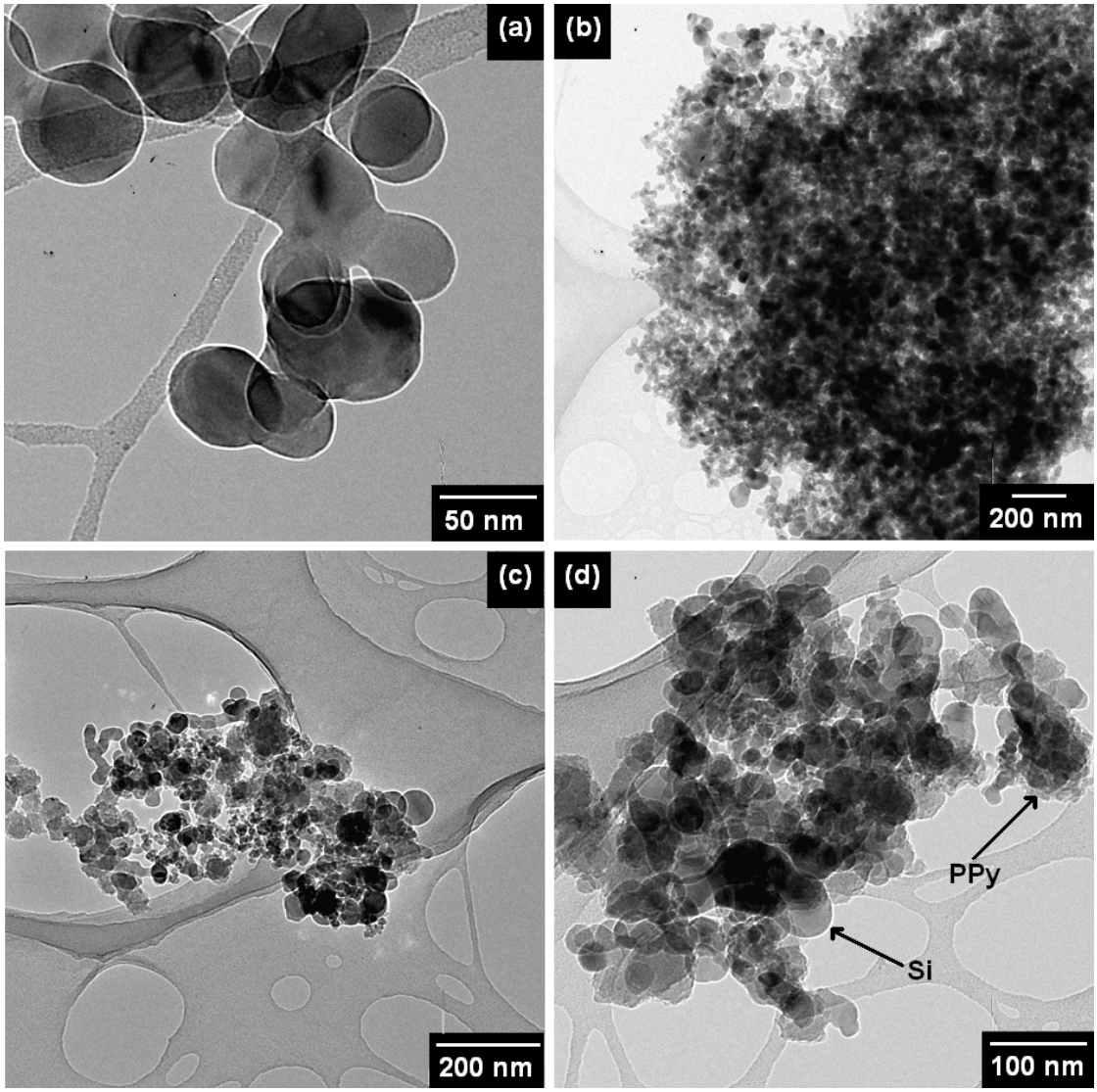

Fig. 7.3 TEM images of (a) the nanocrystalline Si powder and (b), (c), and (d) Si-PPy nanocomposite with 50 wt. % PPy at different magnifications.

TEM energy dispersive X-ray (EDX) mapping for different elements was also conducted. The white dots in Fig. 7.4b-d correspond to the presence of the elements of silicon, carbon, and oxygen, respectively, in which the carbon and oxygen are the PPy elements. From the images, the nanocrystalline Si particles are uniformly distributed among the PPy matrix.

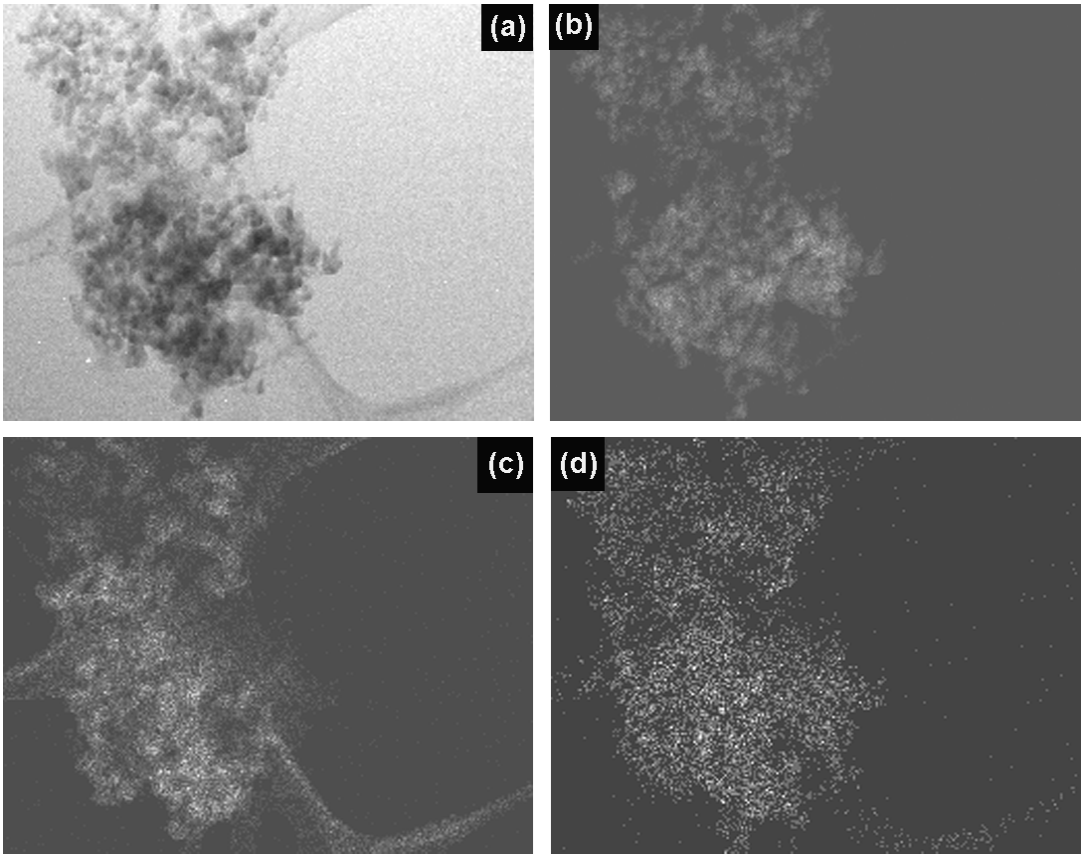

Fig. 7.4 EDX mapping of Si-PPy nanocomposite (a) original images, (b) silicon mapping, (c) carbon mapping, and (d) oxygen mapping.

7.5 Electrochemical Performance

The cycle stability is the best when the PPy loading level is 50 wt. % by TGA analysis. Fig. 7.5 shows the differential charge storage curves, and Li^+ insertion and extraction profiles (inset) of the nanocrystalline Si and Si-PPy nanocomposite with 50 wt. % PPy electrodes. The calculated specific charge is solely based on either Si or Si-PPy with 50 wt. % PPy nanocomposite in the electrode. Even though the charge storage of the first Li^+ insertion and extraction of the nanocrystalline Si electrode (Fig. 7.5a) are 3500 mAh g^{-1} and 2012 mAh g^{-1}, respectively, a strong decline after 10^{th} cycle, with specific charge of 99 mAh g^{-1} is clearly observed; with the fading rate of 9.46 % per

cycle (Fig 7.5a). This result indicates that particle size reduction cannot prevent micrometer-scale Si aggregation [Ng *et al.*, 2006].

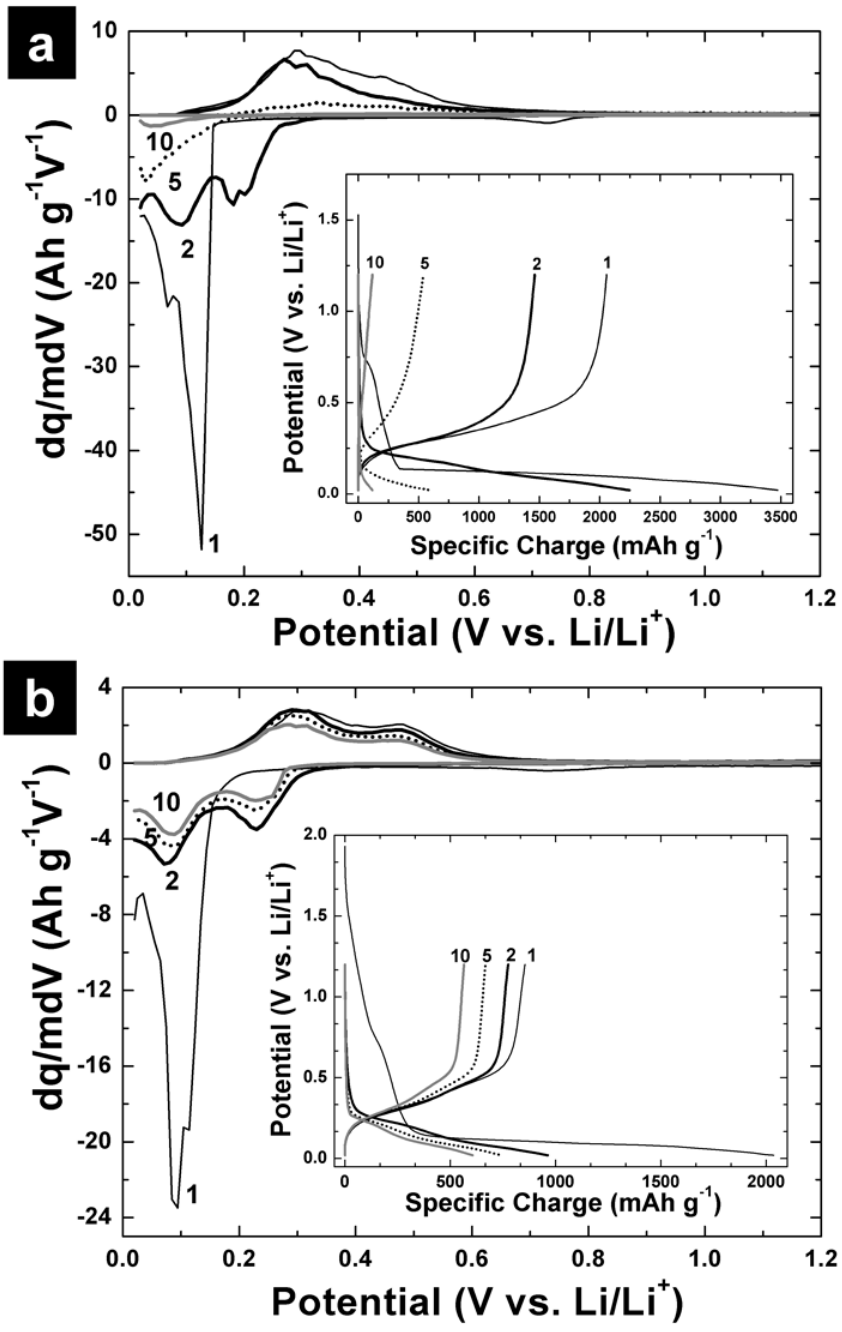

Fig. 7.5 Differential charge storage plots for (a) the Si and (b) the Si-PPy (50 wt. % PPy) nanocomposite electrodes (with the numbers indicating the cycle number). q = charge storage, V = cell potential, dq/mdV = differential charge storage. The insets show corresponding Li^+ insertion and extraction profile.

In contrast, the reversible specific charge of the Si-PPy nanocomposite with 50 wt. % PPy electrode (Fig. 7.5b) after 10 cycles is retained at 568 mAh g^{-1}. The fading rate is approximately 3.25 % per cycle, decreasing by 6.21 % per cycle compared with the nanocrystalline Si electrode. The differential charge storage curves of the Si-PPy nanocomposite with 50 wt. % PPy electrode exhibits essentially the same peak features as the nanocrystalline Si electrode. However, the first Li^+ insertion peak is shifted from 0.132 V vs. Li/Li^+ for nanocrystalline Si to 0.095 V vs. Li/Li^+ for Si-PPy nanocomposite with 50 wt. % PPy electrode. The solid electrolyte interface is different for both cases, i.e., Si | electrolyte and Si-PPy | electrolyte, respectively. Therefore, the surface kinetics is different; resulting in the shifted peaks that are observed in the differential charge storage curves [Dimov *et al.*, 2003].

Fig. 7.6a shows the comparison of the cycling performances of the Si-based nanocomposite electrodes. Si-PPy nanocomposite with 33 wt. % PPy electrode offers the highest specific charge at the first cycle compared to that of 50 and 66 wt. % PPy. However, it is followed by a drastic decay at the subsequent 20 cycles. This unstable cycling behavior may due to the fact that the low loading level of PPy is incompetent to stabilize the cycling performance of Si-based nanocomposite. When the PPy loading level is in excess, which is 66 wt. % for the case here, there is no improvement for the electrochemical performance of the nanocomposite electrode. Based on the argument of Novák *et al.* (1997), PPy does not have specific charge at potential negative to 1.5 V vs. Li/Li^+. Apparently, the excess of PPy loading level would reduce the total specific charge of the Si-based nanocomposite. Hence, for the prepared Si-PPy nanocomposite electrodes, PPy with 50 wt. % show the optimum loading level in order to compensate for the reduction of total galvanostatic charge storage while retain the stable electrochemical performance.

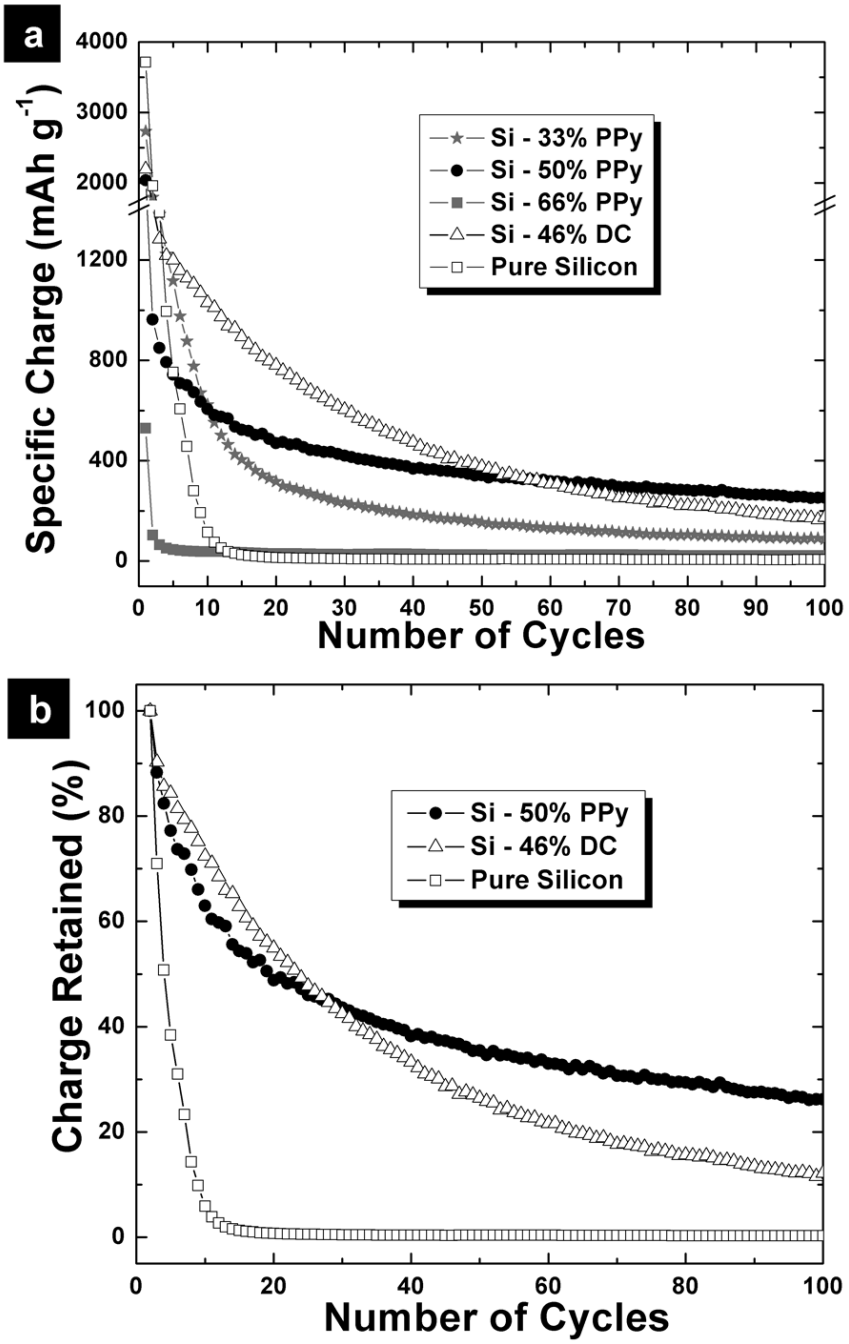

Fig. 7.6 Cycling behavior of the Si-PPy nanocomposite electrodes at different PPy loading level, compared with those of the bare Si and the Si-DC electrodes. (a) Specific charge as a function of cycle number, and (b) Charge retention versus cycle number.

For comparison, the cycling behavior of silicon-disordered carbon (Si-DC) nanocomposites is also presented in Fig. 7.6. The Si-DC nanocomposites were prepared by spray-pyrolyzing the suspensions of citric acid and ethanol, together with the same

batch of nanocrystalline Si that used in the study, in a spray pyrolysis reactor at 400 ^{o}C [Ng *et al.*, 2006]. The charge retention curves of Si-50PPy, Si-DC and Si are plotted in Fig. 7.6b. It can be clearly seen that although the initial charge storage of the Si-PPy nanocomposite with 50 wt. % PPy electrode is lower than that of the Si-DC electrode, its performance is superior than Si-DC electrode after 30 cycles, with high reversibility after prolonged cycling.

Undoubtedly, the PPy with appropriate loading level plays an important role to achieve the enhanced electrochemical performance. The improved performance could be attributed to:

1. PPy in the nanocomposite is a conductive polymer, which could increase the conductivity of the sample.
2. PPy can act as a binder, to increase the contact between particles; therefore the particle-to-particle resistance will be decreased, thus reduce the irreversible reactions with the electrolyte.
3. PPy is an effective component that buffers the huge volume changes during the Li^{+} insertion/extraction process.
4. PPy could also act as an efficient host matrix to prevent cracking and pulverization of the Si electrode due to phase transitions, thus improve the cyclability of the Si electrode.

These concepts have been verified by subsequent morphological studies. SEM images of the electrode after cycling were taken and Fig. 7.7 reveals that the cracks in the bare Si electrode are much larger and serious than in the Si-based nanocomposite with 50 wt. % PPy electrode.

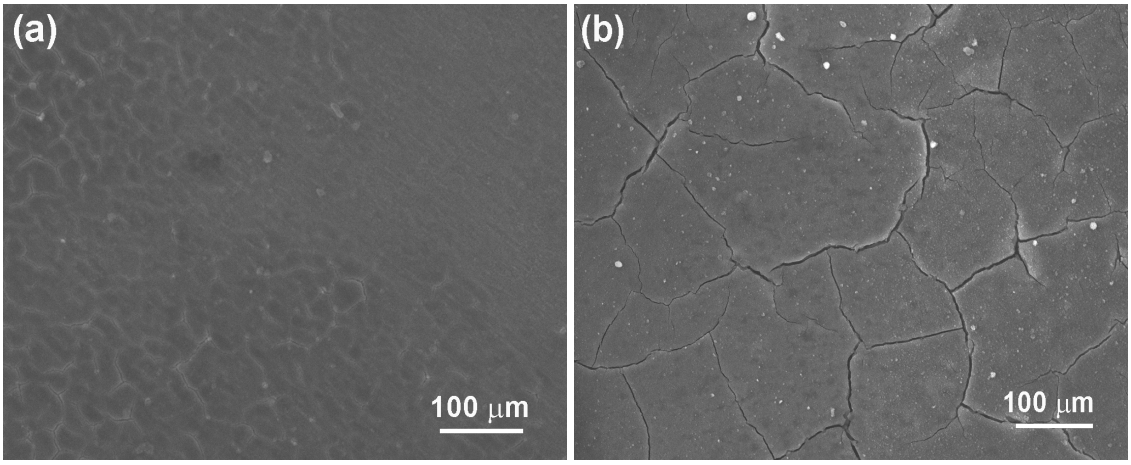

Fig. 7.7 SEM images of electrodes after 100 cycles: (a) Si-PPy (50 wt. % PPy) nanocomposite electrode and (b) nanocrystalline Si electrode.

7.6 Conclusions

PPy was successfully coated onto nanocrystalline Si by *in situ* oxidative chemical polymerization method. The Si-based nanocomposite with 50 wt. % PPy electrode effectively buffers the great volume changes during the cycling process. In the meanwhile, it acts as an efficient host matrix to prevent cracking and pulverization of the Si electrode due to phase transitions, thus improving the cyclability of the Si electrode.

CHAPTER 8

LOW TEMPERATURE SYNTHESIS OF POLYPYRROLE COATED LiV_3O_8 COMPOSITE FOR LITHIUM BATTERY CATHODE

8.1 Introduction

Layered lithium trivanadate, LiV_3O_8, has received much attention as a promising cathode material for rechargeable lithium batteries, because of certain attractive properties, such as high specific capacity, easy preparation, and stability in air [Nassau and Murphy 1981; Panero *et al.*, 1983].

However, the electrical conductivity of LiV_3O_8 powders is still very low. Therefore, the use of a conducting network and a binder is necessary in order to overcome the drawbacks. In general, carbon black and PVDF are mixed with LiV_3O_8 to solve the problem, but the addition of materials without electrochemical activity reduces the apparent energy density [Yoneyama *et al.*, 1991; Gemeay *et al.*, 1995].

As mentioned in previous chapter, PPy is the most popular conducting polymer with the ability to store charges at potential ranging 2.0 – 4.0 V vs. Li/Li^+ [Novák *et al.*, 1997], and it also works well as a binder [Chew *et al.*, 2007]. PPy composites with high electrical conductivity and electrochemical activity for use as cathode has been

extensively studied, such as MnO_2-PPy [Yoneyama *et al.*, 1991], $LiMn_2O_4$-PPy [Gemeay *et al.*, 1995], V_2O_5-PPy [Wong *et al.*, 1998], sulphur-PPy [Wang *et al.*, 2006], and $LiFePO_4$-PPy [Wang *et al.*, 2005], and their possibilities in the field of charge storage devices have also been pointed out.

Here, a low temperature route is applied to synthesize highly homogeneous, uniformly dispersed and structurally disordered LiV_3O_8 particles. However, the cycling stability of this material is not satisfactory. Hence, PPy was coated onto the active material. The structural characterization and electrochemical performance of LiV_3O_8-PPy composite, with different PPy contents and coating method are discussed and compared with the bare LiV_3O_8 material.

8.2 Synthesis Method

LiV_3O_8 was prepared by a low temperature rheological phase reaction [Liu *et al.*, 2002]. Two different coating methods, i.e. *in situ* polymerization (chemical) and high speed ball-milling techniques (mechanical) were applied to coat PPy onto LiV_3O_8.

8.3 Electrochemical Measurements

The cathode was prepared by mixing LiV_3O_8 or LiV_3O_8-PPy composites as active materials with 10 wt. % carbon black and 5 wt. % PVDF binder in NMP solvent to form homogeneous slurry, which was then spread onto aluminium foil to form the electrodes. The electrochemical characterizations were carried out using CR2032 coin cells. The electrolyte used was provided by MERCK KgaA, Germany. The cells were galvanostatically charged (Li^+ insertion) and discharged (Li^+ extraction) between 1.50 -

3.85 V vs. Li/Li^+ at a constant current density of 40 mA g^{-1} at room temperature, using a Neware battery tester. The a.c. impedance spectroscopy was obtained by applying a sine wave of 5 mV amplitude over a frequency range of 100.00 kHz to 0.01 Hz using a CHI 660B electrochemical workstation system (CH Instrument, Cordova TN).

8.4 Physical and Structural Characterizations

When LiOH and V_2O_5 were blended in water, part of the V_2O_5 reacted with LiOH as follows:-

$$2LiOH + V_2O_5 \Rightarrow 2LiVO_3 \quad (8.1)$$

$$2LiVO_3 + 2V_2O_5 \Rightarrow 2LiV_3O_8 \quad (8.2)$$

The first reaction happened easily but the second reaction proceeds slowly [Manev *et al.*, 1995]. After citric acid was added slowly to the mixture and the mixture was then heated at 90 ^oC for 12 h in a vacuum oven to evaporate the water, and a dark green precursor was obtained. According to Tsaramyrsi's report (2001), V_2O_5 could act as an oxidant in an acidic system and combine with citric acid to form a $[(VO_2)C_6H_7O_7]^{2-}$ complex.

$$V_2O_5 + 4C_6H_8O_7 \Rightarrow 2[(VO_2)(C_6H_7O_7)_2]^{2-} + 2H^+ + H_2O \quad (8.3)$$

Fig. 8.1 shows the TGA curve of the precursor. The samples were heated from 60 ^oC to 700 ^oC. It can be seen that the weight loss process can be divided into two stages. The first weight loss begins at 120 °C and ends at 230 °C with a weight loss of

18 wt. %, which mainly corresponds to the loss of water and the excess of free citric acid which has not combined with V_2O_5. The second weight loss occurs in the temperature range of 230 - 350 °C and is attributed to the full decomposition of the complexes and the deintercalation of the water from the complexes, which is associated with a weight loss of 50 wt. %. The weight loss stops at 480 °C, and weight remains stable up to 600 °C, indicating that the expected compound could be obtained by heating the precursor at 480 °C.

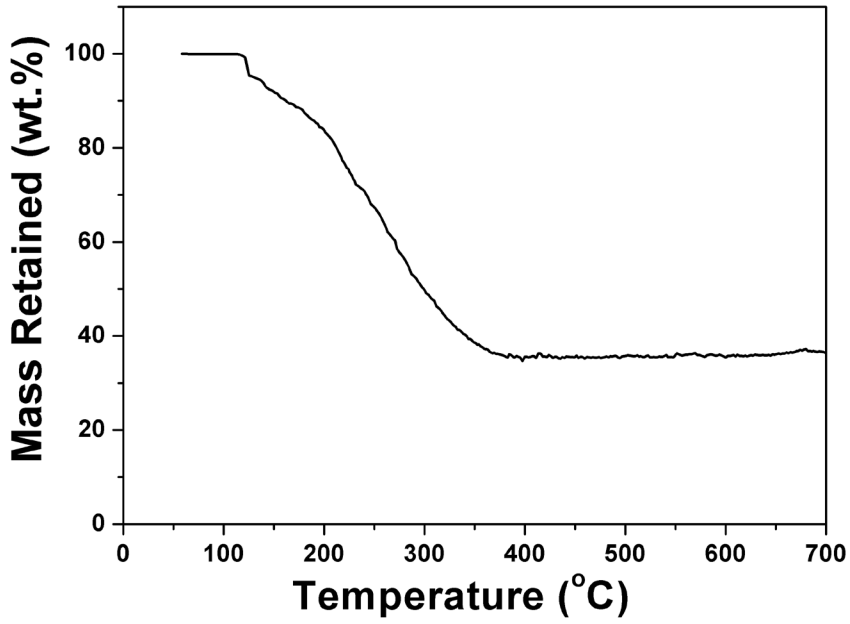

Fig. 8.1 TGA curve of the LiV_3O_8 precursor.

The X-ray diffraction (XRD) pattern of as-prepared LiV_3O_8 was collected between 2-theta angles of 10 ^{o} and 60 ^{o} and the data is plotted in Fig. 8.2. The diffraction peak positions for the sample are consistent with the known layered-type LiV_3O_8 lattice constants given in the literature as a = 6.68 Å, b = 3.60 Å and c = 12.03 Å (JCPDS card no: 72-1193). On the basis of the peak broadening observed in LiV_3O_8, when the Debye-Scherrer equation was applied to the (100) peak, it indicates a

crystallite size of approximately 50 nm. This phenomenon has also been reported in the literatures, which specify that the dimension of the materials is relatively small and fine in nature, with isotropic and strain-free crystallites [West *et al.*, 1987; Pistoia *et al.*, 1990; Kawakita *et al.*, 1999]. The peak at approximately 14 ^{o} is assigned to diffraction at the (100) plane, indicating the layered structure of LiV_3O_8. These layers consist of VO_6 octahedra and VO_5 trigonal bipyramids, which are corner sharing with the octahedra. The Li cations are assumed to be intercalated between such layers [Pistoia *et al.*, 1984; Picciotto *et al.*, 1993].

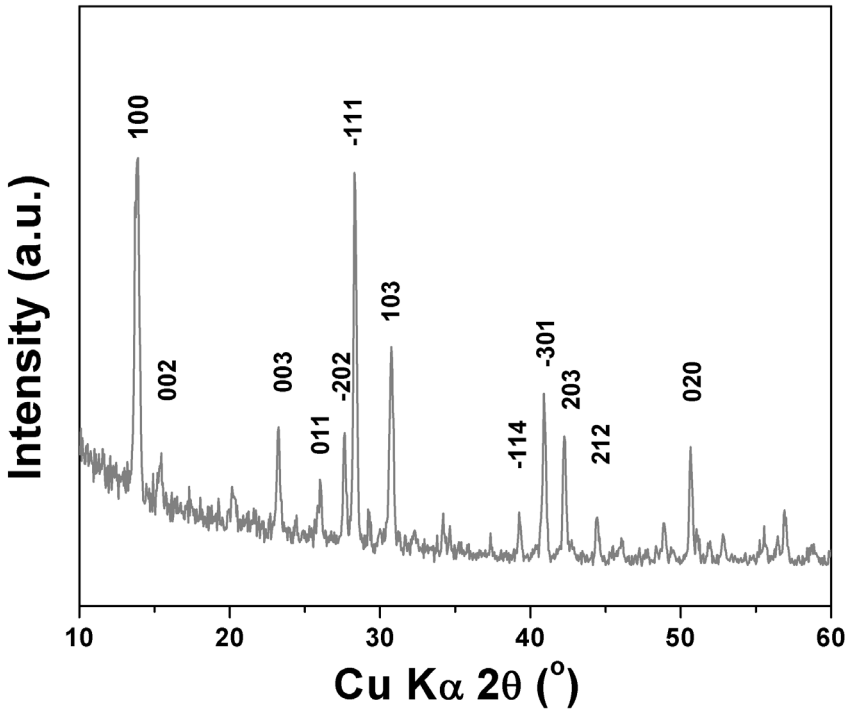

Fig. 8.2 XRD pattern of bare LiV_3O_8.

For *in situ* polymerization method, the amount of PPy in the LiV_3O_8-PPy composite was determined with TGA. Fig. 8.3 shows the TGA analysis of the LiV_3O_8-PPy composite along with those of bare LiV_3O_8 and PPy powders when heated from 60 ^{o}C to 650 ^{o}C. The bare LiV_3O_8 powder maintains a constant weight in the

temperature range used for this experiment. LiV_3O_8-PPy composite shows a single-step weight loss at a temperature of approximately 600 ^oC. Therefore, the change in weight before and after the burning of PPy directly translates into the amount of PPy in the LiV_3O_8-PPy composite. Using this method, it was found that the amounts of PPy in the composite prepared with *in situ* polymerization method are 10 and 24 wt. %, respectively.

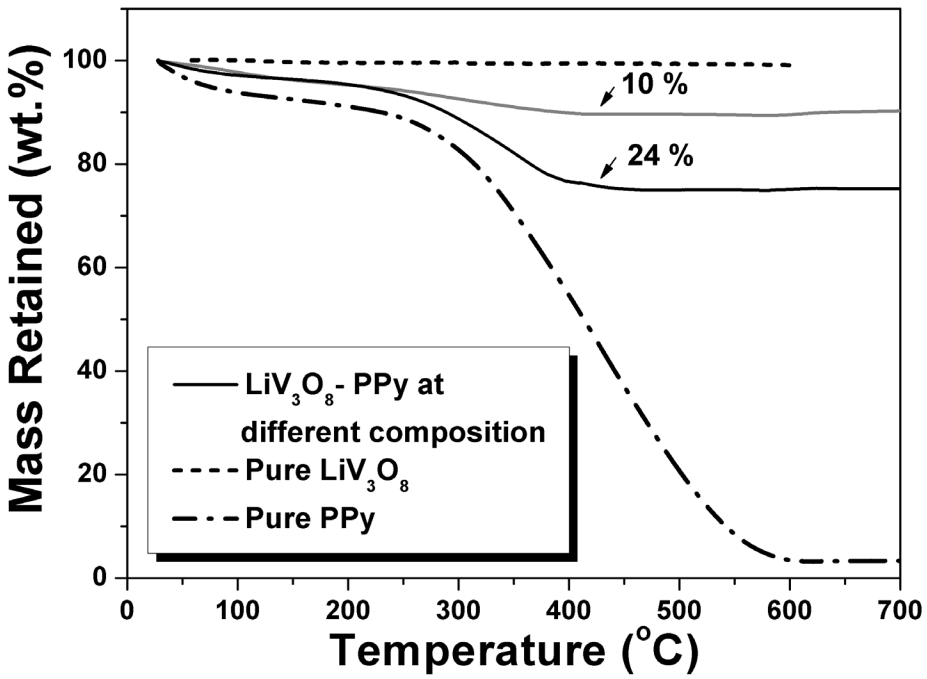

Fig. 8.3 TGA curves of LiV_3O_8-PPy composite.

From SEM images as shown in Fig. 8.4a, it can be observed that the layered host LiV_3O_8 consists of flake-like agglomerates with sharp edges. By comparison, chemically prepared LiV_3O_8-PPy composite presents a distinct contrast in the morphology (Fig. 8.4b-c), which confirms the co-existence of two phases, i.e. amorphous PPy and LiV_3O_8 particles. For 24 wt. % LiV_3O_8-PPy composite, the nano-

sized PPy are well dispersed in the LiV_3O_8 particles. The size of the PPy particles ranges from below 80 to 200 nm (Fig. 8.4d).

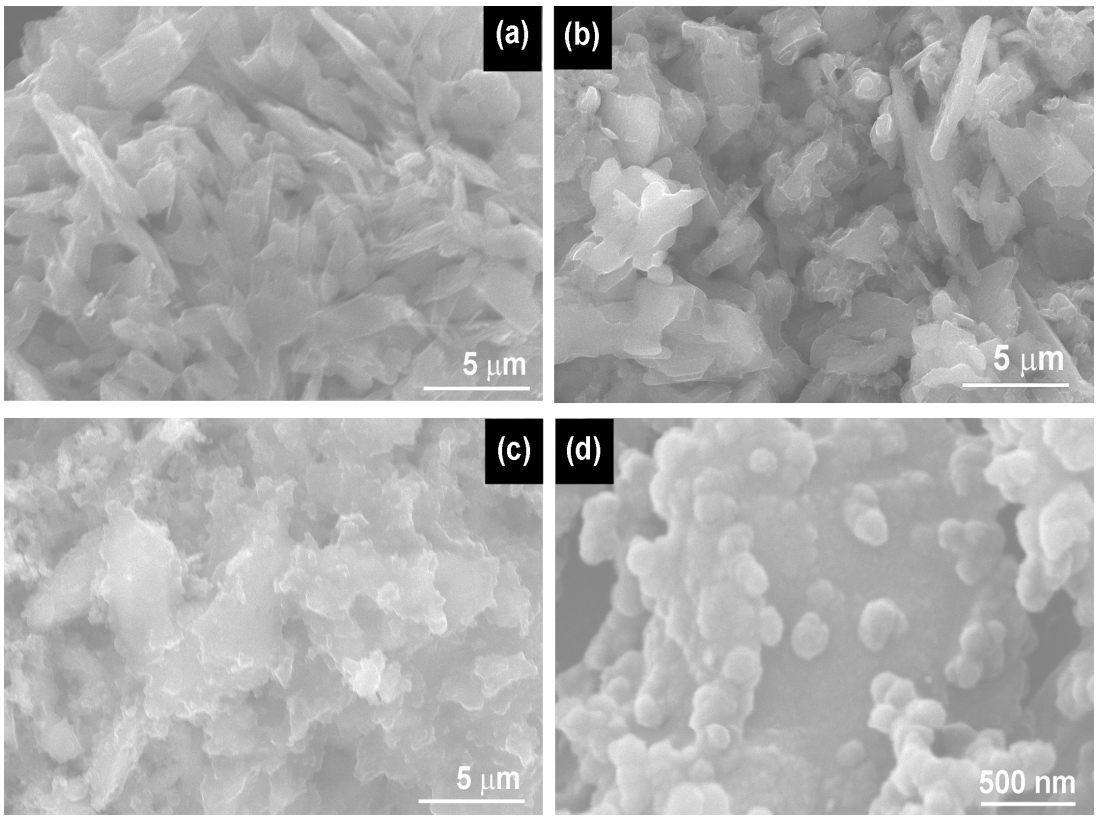

Fig. 8.4 SEM images of (a) pure LiV_3O_8, (b) 10 wt. % LiV_3O_8-PPy composite, and (c) 24 wt. % LiV_3O_8-PPy composite, and (d) higher magnification of image (c).

To verify the homogeneity of PPy distribution in the LiV_3O_8 particles, SEM Energy Dispersive X-ray (EDX) mapping of different elements was conducted for 24 wt. % PPy of the composite (Fig. 8.5). The bright spots shown in Fig 8.5(b) to (d) correspond to the presence of the elements vanadium (V), nitrogen (N), and carbon (C), respectively, in which the N and C are elements of PPy. The results show that N and C are distributed homogeneously throughout the V element, indicating a uniformly coating of nano-PPy within the LiV_3O_8 particles. The homogeneity of the

nanocomposite, for 24 wt. % PPy the case here, plays a fundamental role in terms of cyclability and rate capability [Chabagno *et al.*, 1984].

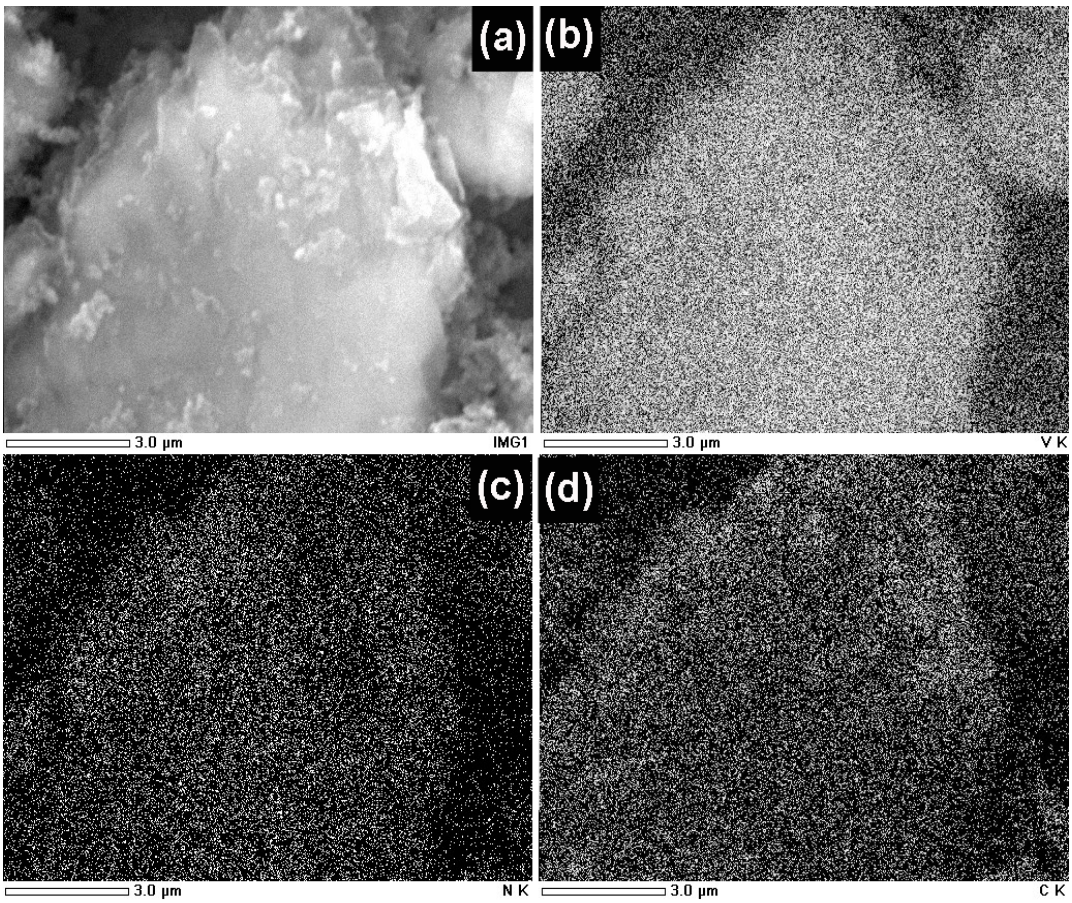

Fig. 8.5 SEM EDX mapping of LiV_3O_8-PPy composite (a) original image (b) V mapping, (c) N mapping, and (d) C mapping.

8.5 Electrochemical Performance

The specific charge as a function of cycle number for bare LiV_3O_8 and LiV_3O_8-PPy composites is compared in Fig. 8.6. The cycle stability is the best when the content of PPy is approximately 24 wt. % for chemically prepared LiV_3O_8–PPy composite electrodes. No further effort was continued to coat more PPy onto the LiV_3O_8 particles since the low specific charge storage of PPy, which is approximately 80 mAh g^{-1} would

reduce the total specific charge of the cells. Hence, the electrochemical properties of LiV_3O_8-based composites with 24 wt. % PPy electrode, which is the optimum content here, was chosen for systematically electrochemical investigation.

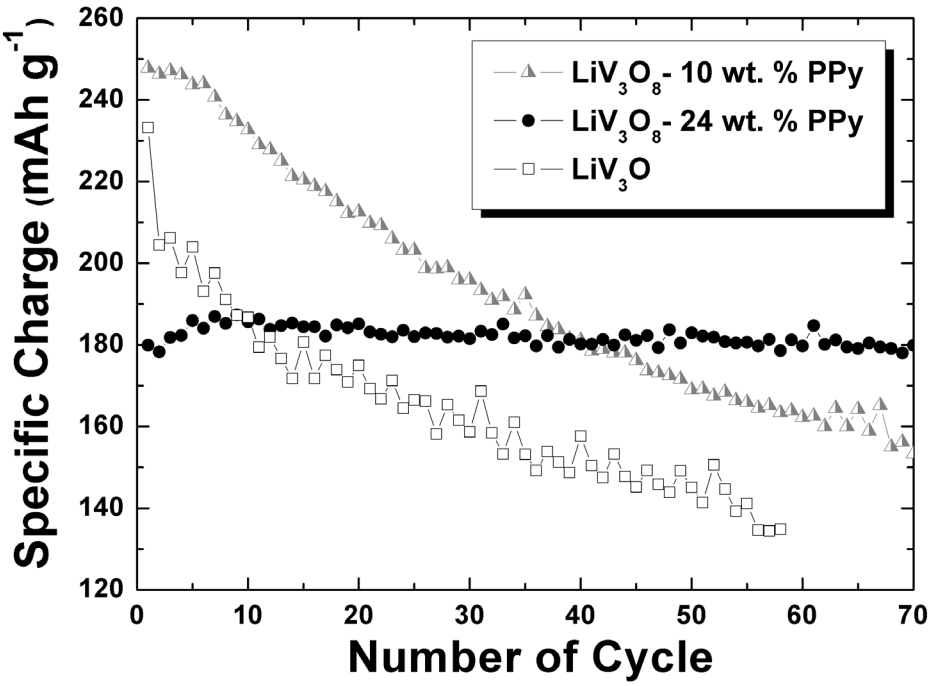

Fig. 8.6 Cycle life of bare LiV_3O_8 and LiV_3O_8-PPy composites.

Fig. 8.7 summarizes the 10th, 50th, and 100th Li^+ insertion and extraction curves for LiV_3O_8 and LiV_3O_8-PPy composite electrodes. The calculated charge storage for both materials was solely based on the LiV_3O_8 and LiV_3O_8–PPy composite material in the electrode. Even though the specific charge for Li^+ insertion of the bare LiV_3O_8 electrode (Fig. 8.7a) at the 10th cycle was 182 mAh g^{-1}, further cycling led to a rapid fading of 120 mAh g^{-1} (at the 100th cycle). Whereas, the cycling performance of the LiV_3O_8-PPy composite electrode is enhanced, with a reversible specific charge of 185 mAh g^{-1} after the 100th cycle (Fig. 8.7b).

There are several plateaus correspond to the Li^+ intercalation and deintercalation of the LiV_3O_8 and the LiV_3O_8-PPy composite electrode as observed in Fig. 8.7. These

plateaus correspond to reduction and oxidation peaks, and were interpreted to the differential charge storage curves shown as insets in Fig 8.7 (a) – (b) and Fig 8.8. The profiles of the differential curves for both electrodes are nearly identical.

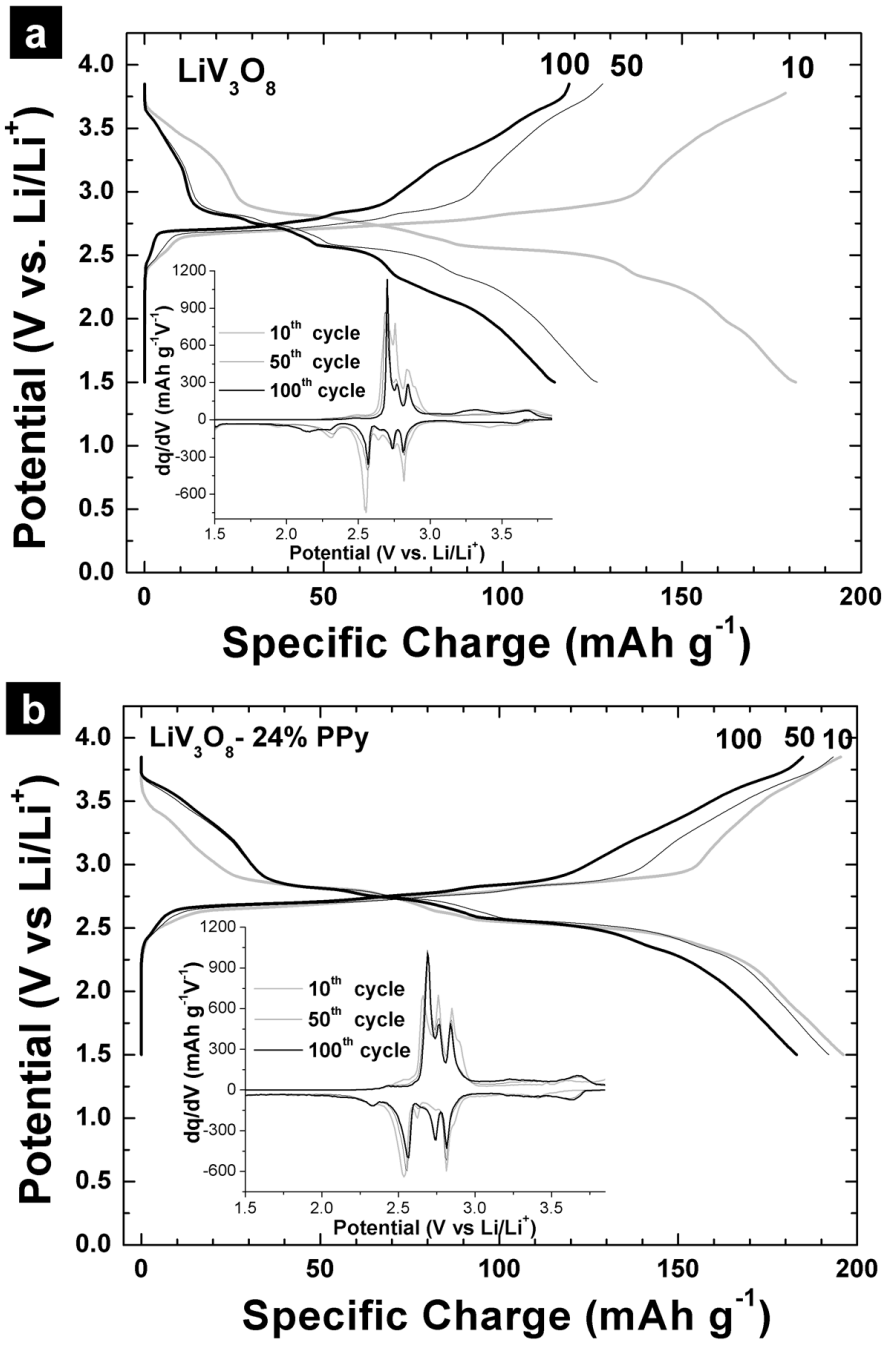

Fig. 8.7 The 10^{th} , 50^{th}, and 100^{th} Li^+ insertion/extraction curves of (a) the LiV_3O_8 electrode and (b) the LiV_3O_8-PPy composite electrode (with the number indicating the cycle number). The insets show the corresponding differential charge storage.

The main reduction peaks appear at a potential of about 2.5 - 2.8 V vs. Li/Li^+, which is related to the insertion of Li^+ into LiV_3O_8. And the oxidation peaks are located at 2.7 - 2.8 V vs. Li/Li^+, which indicates the removal of Li^+ from LiV_3O_8.

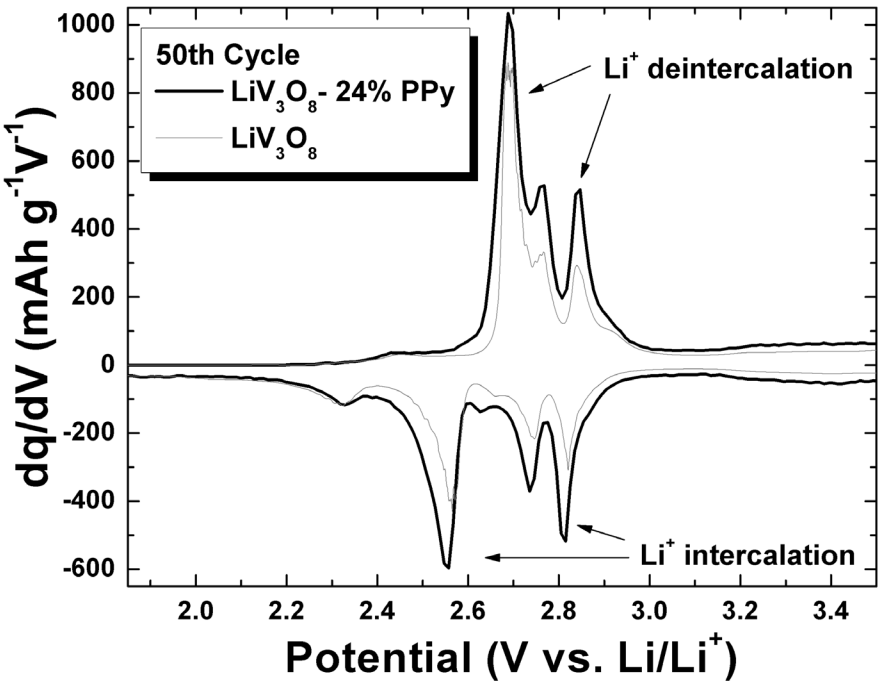

Fig. 8.8 Differential charge storage plots for LiV_3O_8 and LiV_3O_8-PPy composite at the 50^{th} cycle.

It can be seen that the intensity of these peaks in the bare LiV_3O_8 electrode decreases upon cycling (inset in Fig 8.7a), indicating poor cycle stability, whereas the peak intensity for the LiV_3O_8-PPy composite electrode remains stable (Fig. 8.7b) upon cycling. As shown in Fig. 8.8, at the 50^{th} cycle, the LiV_3O_8-PPy composite electrode shows higher peak intensity than the LiV_3O_8 electrode, suggesting higher specific charge and faster kinetics rate for Li^+ intercalation/deintercalation in the LiV_3O_8-PPy composite electrode.

The cycle stability of LiV_3O_8-PPy composite electrode is best proven by the charge retention curve as shown in Fig. 8.9. The specific charge for the bare LiV_3O_8

electrode after 50 cycles is relatively poor. In contrast, the LiV_3O_8-PPy composite electrode exhibits stable retention of nearly 100 %.

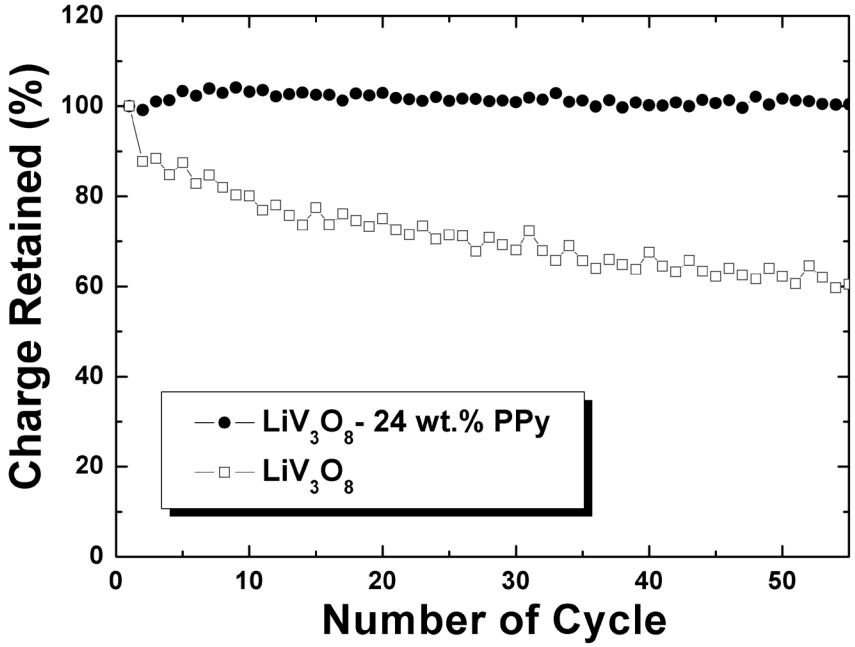

Fig. 8.9 Capacity retention versus cycle number of bare LiV_3O_8 and LiV_3O_8-PPy composite.

The electrochemical performance of PPy coated LiV_3O_8 composite prepared with the *in situ* polymerization method is also compared with mechanical ball-milling method. Fig. 8.10 illustrates the various C-rates of the samples versus number of cycle. Apparently, mechanically prepared LiV_3O_8-PPy composite shows strong fading although the specific charge is the highest at the early stage of cycle life. It appears to have the similar trend line as observed for chemically prepared 10 wt. % PPy coated onto the LiV_3O_8 composite, as shown in Fig. 8.6. In another word, chemical method is more favorable compared to mechanical method, since less PPy is required for the coating in order to achieve similar effect. Moreover, as the C-rate increases, the mechanically prepared LiV_3O_8-PPy composite shows sharp decrease in the

performance. This is especially apparent when C-rate is over C/1.5. On the other hand, LiV_3O_8-PPy composite electrode prepared with the *in situ* polymerization method exhibits stable charge retention even at higher C-rates.

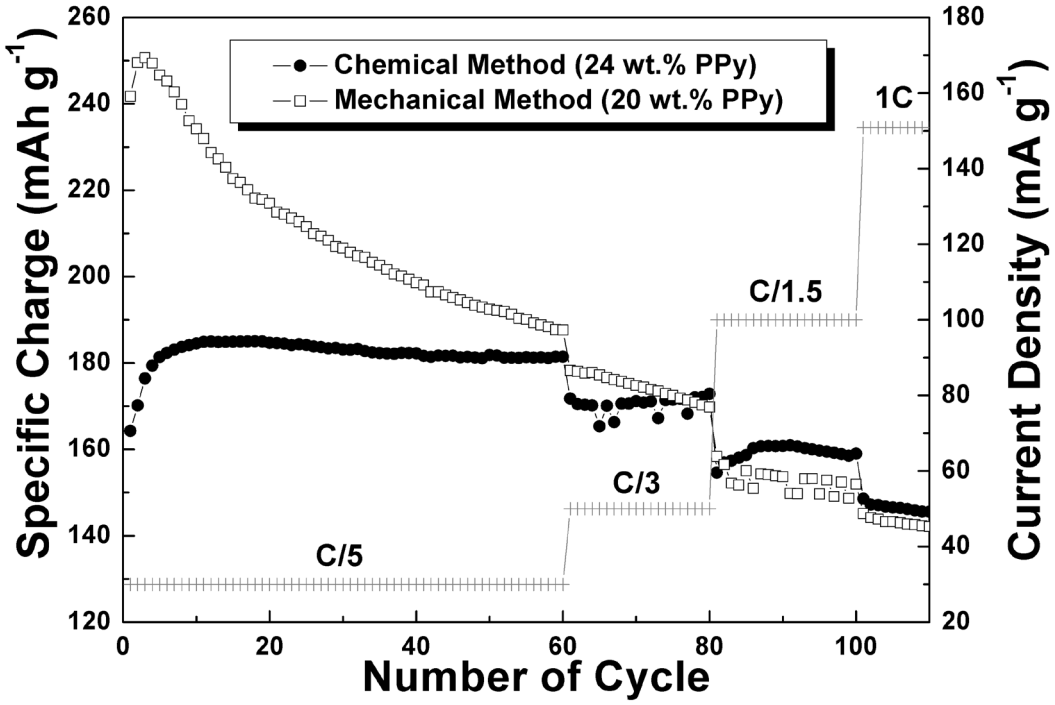

Fig. 8.10 Various C-rates of LiV_3O_8-PPy composite prepared with chemical and mechanical method. A 1 C-rate is assumed for using current density of 150 mA g^{-1}.

During cycling, the specific charge of the chemically prepared LiV_3O_8-PPy composite is first increased, reached a maximum at the 10^{th} cycle and maintained a stable cycle life of approximately 185 mAh g^{-1}. The increase in the specific charge of the LiV_3O_8-PPy composite at the first 10 cycles is attributed to the increase in the intercalation of Li^+ into the composite [Dai *et al.*, 1998; Kuwabata *et al.*, 2005; Huang *et al.*, 2006]. It is believed that PPy particles are uniformly coated onto the surface of LiV_3O_8 powders, which resulted in low diffusivity or intercalation of Li^+ at the initial stage. After a few cycles, some minor defects were found on PPy particles where more

diffusion paths are accessible for Li^+ to intercalate with LiV_3O_8 particles and thus, an increase in charge storage is observed.

To verify this concept, ac impedance measurements were conducted. The Nyquist plots obtained for LiV_3O_8-PPy composite electrode before cycle and after 10 cycles in the fully charge state are compared in Fig. 8.11. The thickness of the electrodes was controlled at 50 μm with the coated area of 1 cm^2. The diameter of the semicircle for LiV_3O_8-PPy composite electrode is 135 Ohm at the 5 cycles and 95 Ohm at the 10 cycles. The diameters of both semicircles are much smaller compared with LiV_3O_8-PPy composite electrode before cycle (425 Ohm). The diameter of the semi-circle represents the inter-particle contact resistance [Fan and Fedkiw, 1998]. Therefore, it can be assumed that the inter-particle resistance was suppressed with the present of PPy. The high accessibility of Li^+ coupled with the high electronic conductivity of the PPy, a good cycling performance of the LiV_3O_8-PPy composite electrode is achieved.

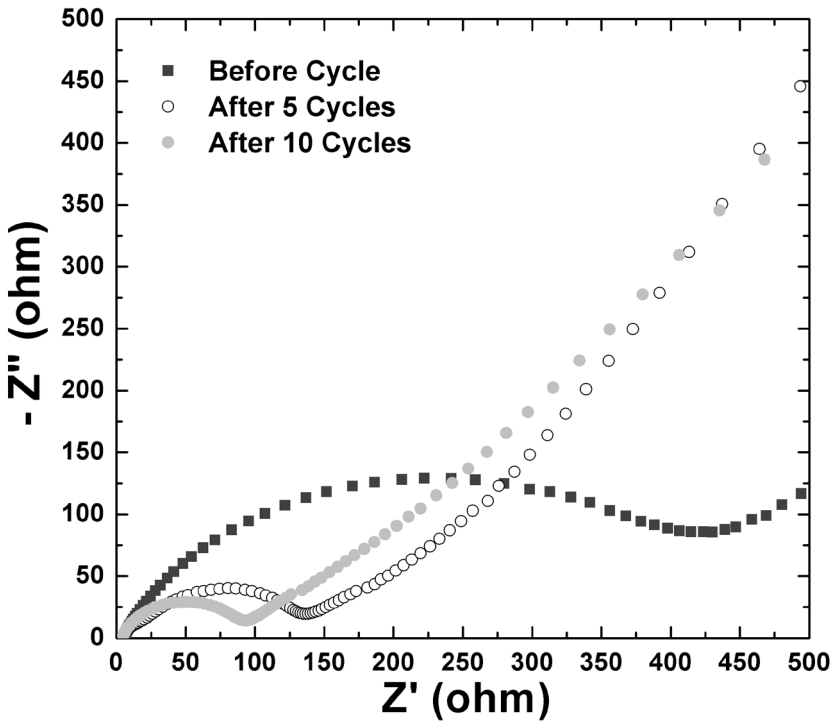

Fig. 8.11 Impedance plots for the LiV_3O_8-PPy composite electrode.

The improved cyclability of the LiV_3O_8-PPy composite electrode is verified by analyzing the surface morphology of the electrode after cycling. Fig. 8.12 shows SEM images of both electrodes after 100 cycles. Larger cracks can be clearly observed in the bare LiV_3O_8 electrode compared with the LiV_3O_8-PPy composite electrode.

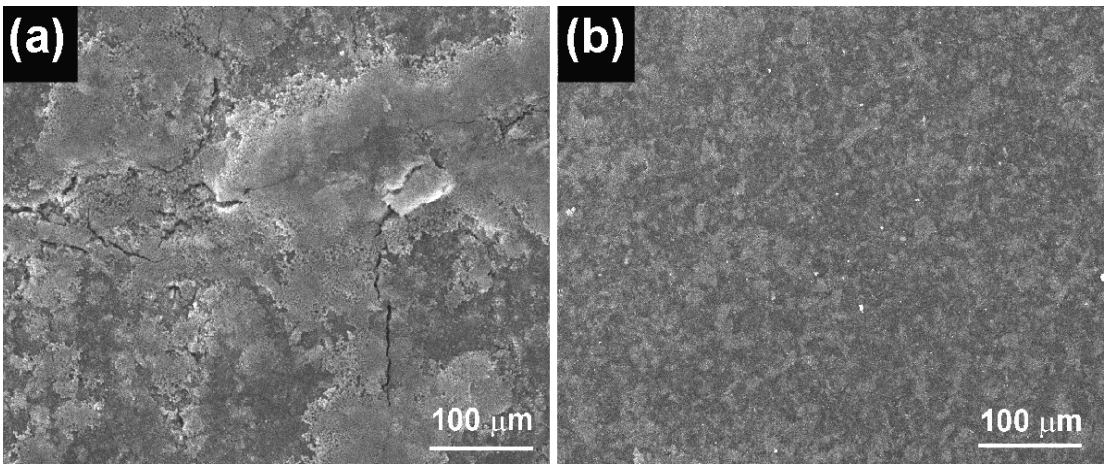

Fig. 8.12 SEM images of electrodes after 100 cycles: (a) LiV_3O_8 electrode and (b) LiV_3O_8-PPy composite electrode.

8.6 Conclusions

Enhanced electrochemical performance is achieved when 24 wt. % PPy coated LiV_3O_8 composite was prepared by a low temperature solution route followed by an *in situ* polymerization method. The resulting composites exhibit excellent cyclability and high coulombic efficiency. The investigations on PPy composite with different oxides have suggested that PPy works well as both conducting matrix and binder.

CHAPTER 9

LITHIUM POLYMER BATTERY BASED ON AN IONIC LIQUID-POLYMER ELECTROLYTE COMPOSITE FOR ROOM TEMPERATURE APPLICATION

9.1 Introduction

Room temperature ionic liquid (RTIL) has been extensively investigated due to their unique properties such as negligible vapor pressure, nonflammability, high ionic conductivity and good thermal and electrochemical stability. Different polymer electrolytes containing RTIL are also studied in the film form, especially for solid lithium-polymer battery [Sakaebe and Matsumoto, 2003; Nakagawa *et al.*, 2003; Shin *et al.*, 2005; MacFarlane *et al.*, 2007] for further improvement of energy density and the enhanced versatility in battery design.

In the present study, experimental results of ionic liquid – polymer electrolyte (IL-PE) composite membrane containing RTIL of *N*-methyl-*N*-propyl pyrrolidinium bis(trifluoromethanesulfonyl) amide (P_{13}TFSA), lithium trifluoromethanesulfonyl (LiTFSA) and 1-butylimidazolium-3-n-butanesulfonate **(**ZW) in polyethylene oxide (PEO) and polyvinylidene fluoride (PVDF) as polymer host is evaluated. This solid polymer electrolyte has relatively high electrical conductivity with good mechanical

properties. Based on previous work [Byrne *et al.*, 2005], a mixture of LiTFSA, P_{13}TFSA and ZW exhibited good electrochemical properties as an electrolyte for lithium battery application. Besides, the ZW has also been used in gel polymer electrolytes to enhance disassociation of the ionic component, and thereby increase the conductivity of the electrolytes [Tiyapiboonchaiya *et al.*, 2004; Sun *et al.*, 2006].

For the application in LPB, the solid IL-PE composite membrane has a relatively narrow potential window, hence 3 V/ lithium materials is chosen to avoid the electrolyte degradation and cathodic decomposition during the cycling. Here, a chemically prepared LiV_3O_8-PPy (24 wt. %) composite was chosen because it represents a better fit with the polymer system and this composite exhibited the highest stability among the materials that we have investigated so far; no significant decrease when the material is galvanostatic charged for 100 cycles in the standard aprotic electrolyte.

9.2 Materials Preparation

The detail synthesis conditions of the chemically prepared LiV_3O_8-PPy composite have already been described in Chapter 8. The IL-PE composite membrane was prepared by a well-known solvent casting technique [Singh and Sekhon, 2005], using PEO and PVDF as the polymer host to improve the mechanical strength of the film. LiTFSA was used as the electrolyte salt. The ratio of LiTFSA, P_{13}TFSA, and ZW is based on the previous work [Byrne *et al.*, 2005]. All the synthesis methods are written in experimental section.

9.3 Electrochemical Measurements

The cathode was prepared by mixing LiV_3O_8-PPy composites as active materials with 10 wt. % carbon black and 5 wt. % PVDF binder in NMP solvent to form a homogeneous slurry, which was then spread onto aluminium foil to form the electrode. The thickness of the electrodes was controlled at 50 μm and the mass loading of the electrode was about 2.20 mg.

The electrode and the as-prepared IL-PE composite membrane were compressed in air and then dried in vacuum oven at 50 ^oC for 12 h to enhance the adhesion of IL-PE | cathode interfaces before transferring into the glove box. To aid in wetting of the electrode surfaces, a small amount of 1 M $LiPF_6$ in a 50:50 (w/w) mixture of EC and DMC electrolyte solution was dropped onto lithium anode and the excess liquid was thoroughly wiped off prior to use. Each LPB cell was assembled by sandwiching the solid polymer electrolyte between a lithium anode and LiV_3O_8-PPy cathode with CR 2032 coin cell.

The LPB cells were charged and discharged galvanostatically in the range of 1.50 - 3.85 V vs. Li/Li^+ at a constant current density of 40 mA g^{-1} at room temperature, using a Neware battery tester. The a.c. impedance measurements were performed for Li | IL-PE | LiV_3O_8-PPy cell using CHI 660C electrochemical workstation system (CH Instrument, Cordova, TN) with a sine wave of 10 mV amplitude over a frequency range of 100 kHz to 0.1 Hz.

9.4 Physical and Structural Characterizations

The conductance measurements were carried out in a locally designed multi-sample conductance cell with the collaboration of Monash University. Ionic conductivity as a function of temperature for the solid IL-PE composite membrane is presented in Fig. 9.1. The conductivity data for the solution of P_{13}TFSA-LiTFSA-ZW is also plotted for comparison purpose. It can be seen from Fig. 9.1 that the conductivity of the solid composite membrane is close to 10^{-4} S cm^{-1} at room temperature. The formation of the solid composite membrane has only diminished the conductivity of the RTIL slightly, which has also been observed previously with liquid plasticized polymer electrolyte materials [Forsyth *et al.*, 1995].

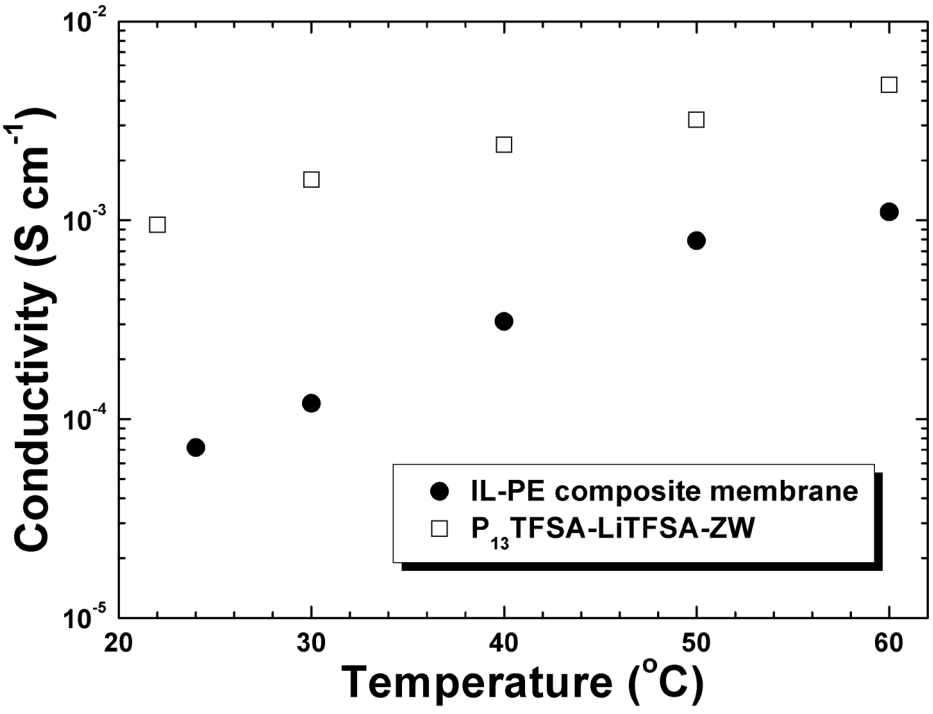

Fig. 9.1 Conductivity as a function of temperature for the IL-PE composite membrane, with conductivity data of the P_{13}TFSA-LiTFSA-ZW solution is included for comparison.

9.5 Electrochemical Performance

The lithium polymer cells were tested at room temperature, which composed of a metallic lithium anode, a solid polymer electrolyte based on an IL-PE composite membrane and a LiV_3O_8-PPy cathode. The electrochemical properties of the assembled LPB cells were systematically investigated. In comparison, LiV_3O_8-PPy composite cell with standard aprotic electrolyte, i.e., 1M $LiPF_6$ in EC and DMC electrolyte solution from MERCK KgaA, Germany is presented.

The calculated charge storage for both cells is solely based on the active material in the electrode. As shown in Fig. 9.2, the specific charge for the Li | IL-PE | LiV_3O_8-PPy cell is close to 190 mAh g^{-1} in the first cycle. The charge is increased during the first 10-15 cycles, perhaps as a result of generation of improved penetration and contact of the P_{13}TFSA component from the electrolyte into the electrode material. The same cathode material in a standard aprotic electrolyte shows similar behavior but much less pronounced.

During cycling, the solid IL-PE composite membrane has higher specific charge than the liquid electrolyte. This may reflect better overall compatibility of the IL-PE based solid electrolyte as compared to the aprotic solvent based electrolyte. LiV_3O_8 particles are known to dissolve in aprotic liquid electrolytes to form an organic-inorganic layer at the surface of the grain [Dubarry *et al.*, 2006; Patey *et al.*, 2008]. The use of the solid polymer electrolyte in this system may avoid the problem by limiting the dissolution and thus allowing a higher specific charge to be exhibited by the material. Nonetheless, the fading after prolonged cycling is observed for the solid IL-PE composite membrane and details will be further discussed in Fig 9.5.

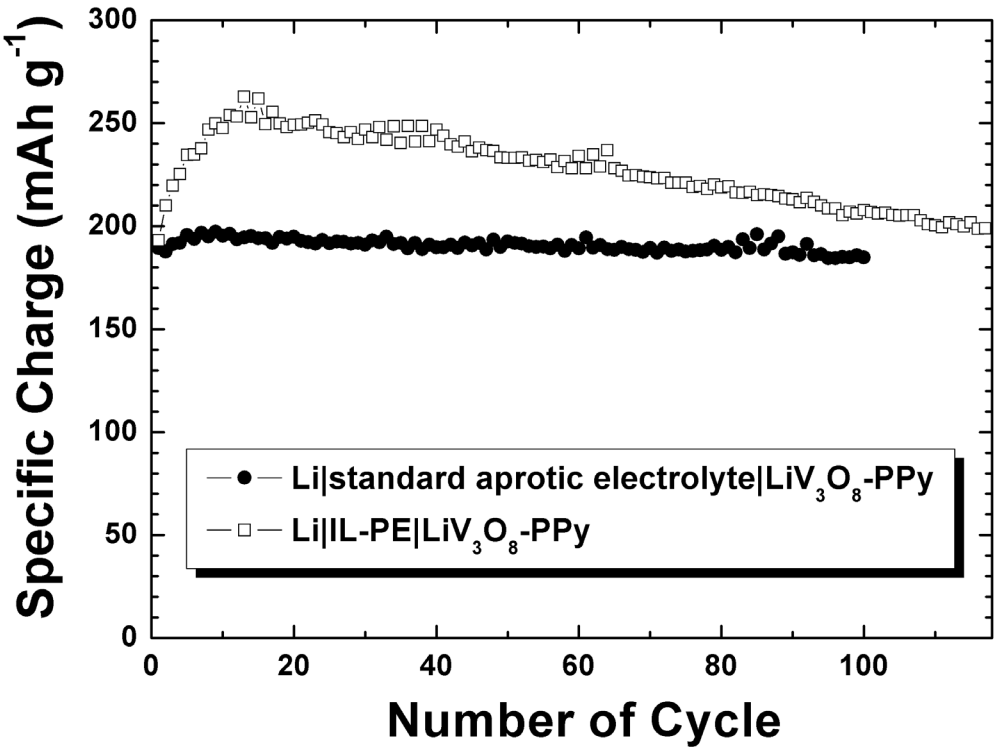

Fig. 9.2 Specific charge as a function of cycle number for Li | Electrolyte | LiV_3O_8-PPy cells assembled with standard aprotic electrolyte (data from previous chapter) and solid IL-PE composite membrane.

A.c. impedance spectra of LiV_3O_8-PPy composite cells before and after 100 cycles were also tested. As shown in Fig. 9.3, the total interfacial resistance for both electrolytes reduced after 100 cycles. However, solid IL-PE composite membrane shows an interfacial resistance about 3 times higher than the normal electrolyte. This difference is not sufficient to impact upon the capacity as measured, however would limit high rate capability. The impedance measurement is the overall characteristics of anode, cathode, and their interfaces. It is certainly expected that a significant solid electrolyte interface (SEI) layer is generated on the Li metal anode in an ionic liquid electrolyte [Howlett et al., 2004; Howlett et al., 2006]. This SEI layer is understood to be the source of the stability exhibited by Li | RTIL interface and it has already been

confirmed by impedance spectroscopy and other methods [Howlett et al., 2006]. On this basis, it is believed that the interfacial impedance detected in the present case is related to the SEI layer of Li | IL-PE interface.

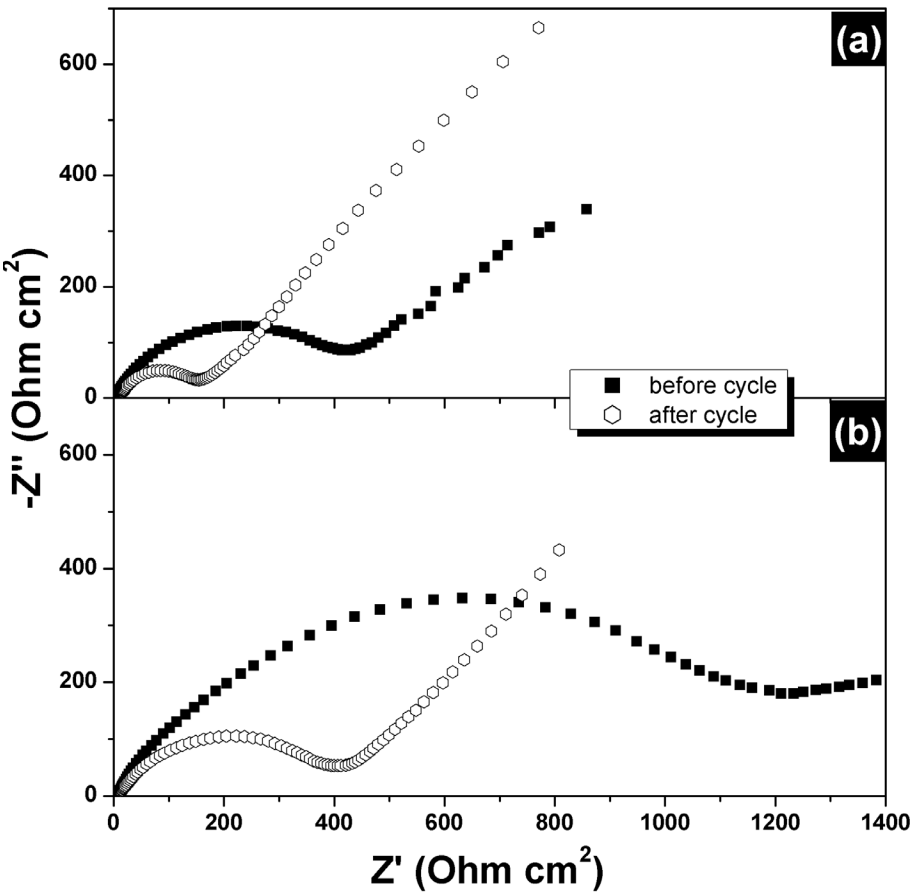

Fig. 9.3 Impedance plots for (a) Li | standard aprotic electrolyte | LiV_3O_8-PPy and (b) Li | IL-PE | LiV_3O_8-PPy electrodes before and after 100 cycles.

Li^+ insertion and extraction curves at 2^{nd}, 5^{th}, 10^{th}, 50^{th} and 100^{th} cycle have been measured with solid IL-PE composite membrane, and the data are plotted in Fig. 9.4. There are several plateaus in the potential region which are relatively typical for the LiV_3O_8 cathode. LiV_3O_8 intercalates Li^+ at 2.3 – 3.0 V vs. Li/Li^+ and deintercalates at 2.5 – 3.0 V vs. Li/Li^+. The specific charge and columbic efficiency of the cell at the 2^{nd}

cycle was 210 mAh g^{-1} and 95 %; at the 5th cycle, they were 235 mAh g^{-1} and 94 %, respectively. After 100th cycle, the columbic efficiency of the cell remained stable at approximately 95% with the reversible capacity of 208 mAh g^{-1}.

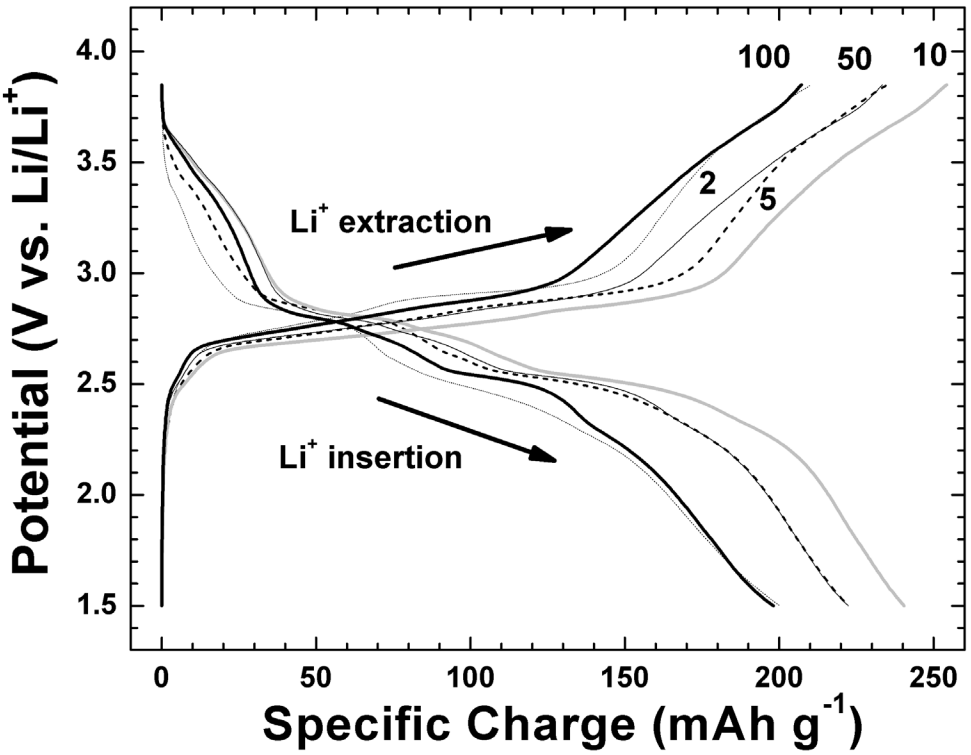

Fig. 9.4 Charge and discharge curves at 2nd, 5th, 10th, 50th and 100th cycle for Li | IL-PE | LiV_3O_8-PPy.

The cycle stability of the LPB cell can be further explored by calculating the "differential charge storage (dq/dV)" from the potential variation as shown in Fig. 9.5. Generally, there are five pairs of peaks in the differential capacity plots at ~ 3.5 (very weak), ~ 2.8, ~ 2.75, ~ 2.6 and ~ 2.35 V vs. Li/Li^+ respectively, which correspond to the plateaus in the Li^+ insertion and extraction curves [Chew *et al.*, 2007]. The sharp peaks indicate that the lithium intercalation/deintercalation proceeds through a few multi-phase regions until the limit for reversible lithium uptake is reached. The intensity of the

cathodic peak of the Li | IL-PE | LiV_3O_8-PPy electrode is becoming poorer and the peaks are shifted upon cycling, indicating a lower charge retention of LiV_3O_8-PPy electrode in solid polymer electrolyte.

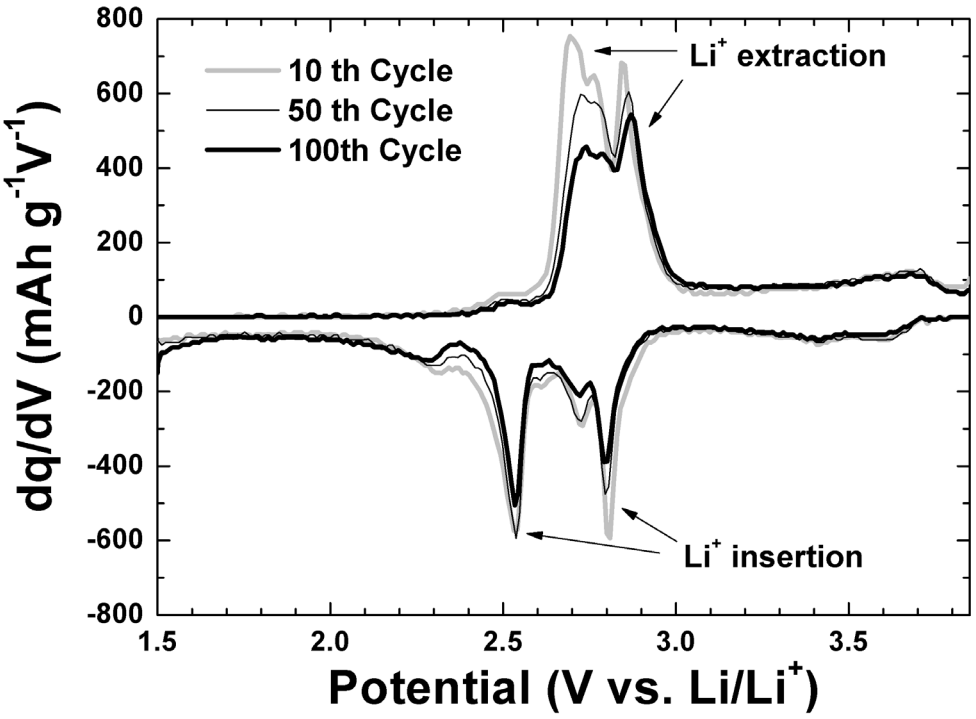

Fig. 9.5 Differential charge vs. potential plots for the Li | IL-PE | LiV_3O_8-PPy at 10^{th}, 50^{th} and 100^{th} cycle.

Two possibilities for the specific charge fading observed in this work are suggested below;

1. Reducing of the RTIL amount in the electrolyte due to the absorption of some RTIL component into the porous electrode, or
2. Swelling of the cathode composite due to the RTIL absorption leading to the loss of electronic conductivity in this system.

To improve the cycle stability of the LPB, the cell should be cycled above room temperature in order to increase the ionic conductivity and the mobility of the Li-ion.

9.6 Conclusions

The cells assembled with solid IL-PE composite membrane, cycled at room temperature show higher specific charge compared with standard aprotic electrolyte. It is believed that the use of the solid polymer electrolyte solves the dissolution problem of vanadium particles by creating a synergist effect at the initial cycling stage. In term of cell performance at practical utility (especially at room temperature), this novel solid polymer electrolyte is a promising candidate for a safe, nonflammable and leak-free lithium polymer battery.

CHAPTER 10

CONCLUSIONS AND OUTLOOK

10.1 General Conclusions

The goal of this doctoral thesis was to study novel electro-active materials and potential polymer electrolytes for use in Li-ion batteries, by means of physical, structural, and electrochemical characterization techniques. The work has been focused on searching for new electro-active materials with high power and energy densities, long term cycling stability, and enhanced safety features provided by polymer electrolyte.

10.1.1 Lithium Insertion Materials for Negative Electrodes

In this study, three popular anode materials based on worldwide scientific research, free-standing carbon nanotube (CNT) electrodes, tin glycolate electrodes, and silicon-polypyrrole composite electrodes were systematically analyzed and reviewed.

Free-standing CNT electrodes have several advantages over the conventional slurry-pasted Cu-based electrodes, since they are lightweight, flexible, have good conductivity, and can be fabricated easily. A comparative study based on three different types of commercial carbon nanotubes (CNTs), i.e., single-wall, double-wall, and multi-

wall was carried out. The conductive CNT electrodes were prepared by a vacuum filtration technique. These films have been characterized as free-standing model anodes for lithium-ion batteries, without the influence of binder (PVDF) and current collector (Cu foil). The experiments revealed that films based on multi-wall CNTs are much better than single-wall and double-wall CNT films in terms of their electrochemical performance, with stable capacity of 300 mAh g^{-1} after 40 cycles. The multi-wall CNT electrode exhibited a reversible, sharp, and intense peak at approximately 0.15 V vs. Li/Li^+ during the Li^+ de-intercalation process, which is similar to what occurs with graphitic material. FE-SEM images revealed that a thin SEI layer was deposited on the surfaces of the multi-wall CNTs after prolonged cycling. It is believed that the structure and the physico-chemical properties of the CNTs play an important role in the reversibility, stability, and cycle life of the free-standing CNT electrodes. Undoubtedly, only multi-wall CNTs have the capability for significant Li^+ ion intercalation/de-intercalation.

For tin-based electro-active materials, this is the first time that mass synthesis of tin glycolate particles has been reported without any additional heat treatment or growth-directing agent, with the tin glycolate particles applied as an anode material for use in Li-ion rechargeable batteries. The tin glycolate particles were prepared by a simple, one-step, polyol-mediated synthesis in air, with tin oxalate as precursor. Hexagonal-shaped, micron-sized tin glycolate particles were formed when the solution had cooled. Further heat treatment on the as-synthesized tin glycolate particles, carried out in air at 600 – 800 ^oC for 2 hrs, produced a series of tin oxides. From the SEM images, it was revealed that the micron-sized, hexagonal-shaped tin glycolate consisted of nanosized tin-based particles (80 – 120 nm), encapsulated within tin glycolate shells. XRD, TGA, and FT-IR measurements were conducted to confirm the three-dimensional

growth of the tin glycolate particles. When applied as an anode material for Li-ion batteries, the as-synthesized tin glycolate particles showed good electrochemical reactivity in Li-ion insertion/extraction, retaining a specific charge of 416 mAh g^{-1} beyond 50 cycles. This performance was significantly better than those of all the other tin oxide nanoparticles (< 160 mAh g^{-1}) that were obtained after heat treatment in air. It is strongly believed that the buffering of the volume expansion by the glycolate upon Li-Sn alloying was the main factor for a much improved cycling of the electrode.

A novel silicon-polypyrrole (Si-PPy) nanocomposite, suitable for lithium-ion battery anodes, was prepared by the *in situ* chemical polymerization method to coat PPy onto the Si surface. The cycling stability of Si-PPy nanocomposite electrodes was significantly improved compared to that of the pure Si anodes. The electrochemical performance of the Si-PPy nanocomposite electrodes was also comparable to that of Si-disordered carbon electrode prepared by spray pyrolysis. It is believed that the vast network of the PPy matrix is a suitable environment to increase the electrical conductivity, buffer the volume change during cycling, and prevent cracking and pulverization of the Si, thus improving the electrochemical performance of the Si-PPy nanocomposite.

10.1.2 Transition Metal Oxide Materials For Positive Electrodes

Two major cathode materials have been reviewed and analyzed in detail, i.e., nanostructured lithium manganese spinel oxide ($LiMn_2O_4$) thin film electrode and lithium trivanadate polypyrrole (LiV_3O_8-PPy) composite electrode.

A new approach has been developed to rapidly synthesize nanostructured $LiMn_2O_4$ thin films by flame spray deposition (FSD) and *in situ* annealing. A precursor

solution of lithium acetylacetonate and manganese acetylacetonate in an organic solution was supplied through a flame spray pyrolysis (FSP) reactor. The liquid solution spray was ignited and stabilized by a premixed methane/oxygen flame ring surrounding the FSP nozzle. Thus, $LiMn_2O_4$ nanoparticles were formed by combustion and deposited onto a current collector followed by *in situ* annealing. Two different types of current collectors, i.e. stainless steel and aluminum coated primer were tested. The prepared thin films were characterized by XRD and FE-SEM. The electrochemical properties of the thin films were evaluated by CV and galvanostatic cycling. The $LiMn_2O_4$ films exhibited good cyclability. Films that underwent sintering and crystal growth during *in situ* annealing developed more robust film structures on the current collector surface and exhibited better electrochemical performance than poorly adhering films. The present studies indicate that spinel $LiMn_2O_4$ thin films can be prepared by the fast and efficient FSD and *in situ* annealing method.

A novel composite, LiV_3O_8-PPy, was synthesized by a low-temperature solution route followed by an *in situ* polymerization method. The PPy acts as a conducting matrix, a binder, and an active material, as well as a volume change buffering agent, which holds the LiV_3O_8 particles in place during charge/discharge cycling. The new material was characterized by SEM. It was found that the PPy nanoparticles were uniformly distributed among the LiV_3O_8 powders, which could significantly enhance the electrical conductivity and stability of the composite electrode. The composite containing 25 wt % PPy exhibits good reversibility, higher coulombic efficiency, and better cycle life than the bare LiV_3O_8 electrode, with a specific charge of 183 mAh g^{-1} retained after 100 cycles.

10.1.3 Polymer Electrolyte

A lithium polymer battery is described based on an ionic liquid-polymer electrolyte (IL-PE) composite membrane operating at room temperature. A solution casting method was used to prepare the IL-PE composite membrane, with PVDF and PEO as the polymer host to improve the mechanical strength of the film, LiTFSA as the electrolyte salt, P_{13}TFSA as a room temperature ionic liquid, and 1-butylimidazolium-3-(n-butanesulfonate) as a zwitterionic compound. Utilizing a LiV_3O_8-PPy composite cathode prepared by *in situ* polymerization, the cell delivered approximately 200 mAh g^{-1} with respect to the mass of the cathode material tested at room temperature. The specific charge is slightly higher than those observed in standard aprotic electrolytes ($LiPF_6$ in EC:DMC solution) and shows slight decay after prolonged cycling. It is believed that the use of the IL-PE composite membrane in this system could solve the dissolution problem of vanadium particles that occurs in normal electrolyte by creating a synergistic effect at the initial cycling stage. There are two possibilities for the capacity fading observed in this work: drying of the gel electrolyte or swelling of the cathode composite, both are due to the IL absorption into the porous electrode, leading to the loss of electronic conductivity in this system.

10.2 Recommendations for Future Work

All topics discussed in this thesis can be further extended, as every new finding opened the door for additional scientific questions and technical improvements. Collected here are some recommendations to be considered as starting ideas for future development.

For the free-standing CNT electrode, a reduction in cost could be implemented by partially replacing the multi-walled CNT content with other electro-active materials, i.e., silicon or tin-based nanomaterials. With homogeneous blending, new free-standing nanocomposite electrode with improved electrochemical performance can be obtained, while retaining the excellent mechanical properties of the flexible electrode. It is also important to calculate the actual specific charge of the free-standing electrode for the total mass of the system and compare it to a classical electrode, including the Cu foil mass. Another possible route to improve the specific charge of the free-standing electrode would be to replace the CNTs with other similar structures of electro-active nanomaterials, i.e., nanobelt, nanowire, and nanosaw structures of silicon or tin-based materials that can be entangled easily by using vacuum filtration. Of course, the prepared film should have sufficient conductivity to be tested as anode. One of the major advantages of this free-standing electrode is to apply it as a model electrode to study the electrochemical interface reaction between the electrode and electrolyte without the influence of the binder, conductive agent, or current collector.

The results based on polyol-mediated tin glycolate make it clear that the charge storage of the anodes was significantly enhanced by an optimized microstructure. A similar effect was also found for Si-PPy nanocomposite, where PPy acts as a conducting matrix and binder to absorb the big volume changes caused by the nanomaterials during Li-ion insertion/extraction processes. Many efforts have been made to ameliorate the volume changes by adding buffering agent to form composite electrodes. Based on previous experience, an alternative solution is suggested here: coating the particles with a thin layer of protective film similar to solid electrolyte interphase (SEI), i.e., an organic compound which can homogeneously cover the surface of the electro-active materials. This protective film could act as the shells of tin glycolate do in the present

samples, to prevent cracking and pulverization of the electro-active materials. Moreover, the irreversible specific charge of the materials may be reduced since the protective layer could function in the same way as the SEI. The suggested method to deposit the film homogeneously onto the surfaces of the all the particles is by electrodeposition. The thickness and composition of the film can be controlled easily with different solution concentrations and deposition times. Of course, a trial and error approach is required to find the right remedy to improve the cycle stability of the electro-active materials.

As for the $LiMn_2O_4$ thin film area, subsequent research work should focus on finding the optimum operating parameters of the flame spray deposition and *in situ* annealing method, and on reducing the deposition time and height above the burner. Experimenting with other good conductive current collectors, such as glassy carbon or highly doped Si substrate is also suggested to improve the adhesion between the $LiMn_2O_4$ nanoparticles and the current collector. If the stainless steel is still to be applied, different thicknesses of the foil are suggested for the testing in order to deposit more active materials onto the current collectors. Moreover, further electrochemical testing can be conducted to study the electrode/electrolyte interface of the thin film. Detailed information on the amount of lithium in the $LiMn_2O_4$ thin film should also be collected by using Rutherford backscattering spectrometry (RBS) and elastic recoil detection analysis (ERDA). Finally, applying lithium spinel thin film as a cathode material would require a targeted specific charge for easy comparison and reference to other relevant research work in the thin film area.

For the LiV_3O_8-PPy composite electrode, the specific charge retained is still not satisfactory. Since PPy is a stable electro-active material to use as cathode, further experimental work should focus on finding novel cathode nanomaterials with high

energy density but low cycle stability, i.e., $Li(Ni_{1/3}Mn_{1/3}Co_{1/3})O_2$, $LiMn_2O_4$, and $LiFePO_4$, which can then be coated with PPy to improve cycle stability while retaining the high energy density. The method of deposition is also important to control the thickness and the homogeneity of the PPy. A thin layer is always preferred, since a high PPy loading level will sacrifice the total energy density of the composite material. This is because PPy only contributes a specific charge of 80 mAh g^{-1}. Of course, detailed study based on the PPy itself is recommended to find the best precursor and the optimum experimental set-up parameters, and hence, to improve the actual specific charge of the material.

The cycle stability at room temperature of cells with IL-PE composite membrane needs to be improved. Some wetting agent may need to be incorporated into the system. Moreover, the cell should also be cycled above room temperature to increase the ionic conductivity and the mobility of the Li^+ cations in the solid polymer electrolyte, and hence improve the cycling performance of the cell. The thickness of the IL-PE composite membrane should be reduced to a minimum, while retaining the mechanical properties of the electrolyte. Further work can also focus on the aging and temperature effects of the solid polymer electrolyte in the system.

Given the appropriate investment in research, the improvement in material and cell design may generate significant improvements in energy density with good safety features. Of equal importance is a better understanding of the electrode-electrolyte interface via *in situ* analytical tools, to facilitate the design of new electro-chemistry and interfaces. With a well defined goal, as proven in this thesis, the future for the next generation of Li-ion batteries is likely to be brighter ahead.

REFERENCES

Adamson AW. A Textbook of Physical Chemistry, New York: Academic Press **1973**.

Amatucci GG, Pereira N, Zheng T, Tarascon JM. Failure mechanism and improvement of the elevated temperature cycling of $LiMn_2O_4$ compounds through the use of the $LiAl_xMn_{2-x}O_{4-z}F_z$ solid solution. J Electrochem Soc **2001**; 148: A171-82.

Armand M. The history of polymer electrolytes. Solid State Ionics **1994**; 69: 309-19.

Aurbach D, Markovsky B, Weissman I, Levi E, Ein-Eli Y. On the correlation between surface chemistry and performance of graphite negative electrodes for Li ion batteries. Electrochim Acta **1999**; 45: 67-86.

Aurbach D, Nimberger A, Markovsky B, Levi E, Sominski E, Gedanken A. Nanoparticles of SnO produced by sonochemistry as anode materials for rechargeable lithium batteries. Chem Mater **2002**; 14: 4155-63.

Ba J, Polleux J, Antonietti M, Niederberger M. Non-aqueous synthesis of tin oxide nanocrystals and their assembly into ordered porous mesostructures. Adv Mater **2005**; 17: 2509-12.

Bach S, Henry M, Baffier N, Livage J. Sol-gel synthesis of manganese oxides. J Solid State Chem **1990**; 88: 325-333.

Baughman RH, Zakhidov AA, de Heer WA. Carbon nanotubes - the route toward applications. Science **2002**; 297: 787-92.

Belin F, Epron F. Characterization methods of carbon nanotubes: A review. Mater Sci Eng B **2005**; 119: 105-18.

Besenhard JO, Fritz HP. The electrochemistry of black carbon. Angew Chem Int Edit Engl **1983**; 22: 950-75.

Besenhard JO, Schöllhorn R. The discharge reaction mechanism of the MoO_3 electrode in organic electrolytes. J Power Sources **1976**; 1: 267-76.

Besenhard JO, Winter M, Yang J, Biberacher W. Filming mechanism of lithium-carbon anodes in organic and inorganic electrolytes. J. Power Sources **1995**; 54: 228-31.

Bragg WH, Bragg WL. The Reflection of X-rays by Crystals (I). Proceedings of the Royal Society of London Series A – Containing Papers of a Mathematical and Physical Character **1913**; 88: 428-438.

Brett CMA, Brett AMO. Electrochemistry: Principles, methods, and Applications. Oxford: Oxford University Press **1993**.

Brodd RJ, Bullock KR, Leising RA, Middaugh RL, Miller JR, Takeuchi E. Batteries, 1977 to 2002. J Electrochem Soc **2004**; 151: K1-11.

Brousse T, Retoux R, Herterich H, Schleich DM. Thin-film crystalline SnO_2-lithium electrodes. J Electrochem Soc **1998**; 145: 1-4.

Buzzeo MC, Evans RG, Compton RG. Non-haloaluminate room-temperature ionic liquids in electrochemistry – A review. Chem Phys Chem **2004**; 5: 1106-20.

Byrne N, Howlett PC, MacFarlane DR, Forsyth M. The Zwitterion effect in ionic liquids: Towards practical rechargeable lithium-metal batteries. Adv Mater **2005**; 17: 2497-501.

Cao A, Xu C, Liang J, Wu D, Wei B. X-ray diffraction characterization on the alignment degree of carbon nanotubes. Chem Phys Lett **2001**; 344: 13-7.

Chabagno JM, Deroo D, Dalard F, Merienne JL. Theoretical study of intercalation in constant current cycling. Solid State Ionics **1984**; 13: 45-52.

Chaloner-Gill B, Shackle DR, Andersen TN. A Vanadium-based cathode for lithium-ion batteries. J Electrochem Soc **2000**; 147: 3375-8.

Chen CH, Kelder EM, Schoonman J. Electrode and solid electrolyte thin films for secondary lithium-ion batteries. J Power Sources **1997**; 68: 377-80.

Chen CH, Schoonman J. Thin-film techniques for advanced energy conversion and storage systems. J Ind Eng Chem **2004**; 10: 1114-25.

Chew SY, Feng C, Ng SH, Wang JZ, Guo ZP, Liu HK. Low-temperature synthesis of polypyrrole-coated LiV_3O_8 composite with enhanced electrochemical properties. J Electrochem Soc **2007**; 154: A633-7.

Chew SY, Guo ZP, Wang JZ, Chen J, Munroe P, Ng SH, Zhao L, Liu HK. Novel nano-silicon/polypyrrole composites for lithium storage. Electrochem Commun **2007**; 9: 941-6.

Chouvin J, Branci C, Sarradin J, Olivier-Fourcade J, Jumas JC, Simon B, Biensan Ph. Lithium intercalation in tin oxide. J Power Sources **1999**; 81-82: 277-81.

Chung SY, Bloking JT, Chiang YM. Electronically conductive phospho-olivines as lithium storage electrodes. Nat Mater **2002**; 1: 123-8.

Claye AS, Fischer JE, Huffman CB, Rinzler AG, Smalley RE. Solid-state electrochemistry of Li single wall carbon nanotube system. J Electrochem Soc **2000**; 147(8): 2845-52.

Coluccia M. Synthesis, optimization and characterization of layered electroactive materials for lithium-ion batteries. Switzerland: Paul Scherrer Institute PhD Thesis **2000**.

Courtney IA, Dahn JR. Electrochemical and *in situ* X-ray diffraction studies of the reaction of lithium with tin oxide composite. J Electrochem Soc **1997a**; 144: 2045-52.

Courtney IA, Dahn JR. Key factors controlling the reversibility of the reaction of lithium with SnO_2 and Sn_2BPO_6 Glass. J Electrochem Soc **1997b**; 144: 2943-8.

Dahn JR. Phase diagram of Li_xC_6. Phys Rev B **1991**; 44: 9170-7.

Dahn JR, Courtney IA, Mao O. Short-range Sn ordering and crystal structure of $Li_{4.4}Sn$ prepared by ambient temperature electrochemical methods. Solid State Ionics **1998**; 111: 289-94.

Dai J, Li SFY, Gao Z, Siow KS. Low-temperature synthesized LiV_3O_8 as a cathode material for rechargeable lithum batteries. J Electrochem Soc **1998**; 145: 3057-62.

Dell RM. Batteries fifty years of materials development. Solid State Ionics **2000**; 134: 139-58.

Dimov N, Kugino S, Yoshio M. Carbon-coated silicon as anode material for lithium ion batteries: advantages and limitations. Electrochim Acta **2003**; 48: 1579-87.

Duan J, Yang S, Liu H, Gong J, Huang H, Zhao X, Zhang R, Du Y. Single crystal SnO_2 zigzag nanobelts. J Am Chem Soc **2005**; 127: 6180-1.

Dubarry M, Gaubicher J, Guyomard D, Steunou N, Livage J. $Li_{1+\alpha}V_3O_8$ gel and xerogel: a new insight. Chem Mater **2004**; 16: 4867-9.

Dubarry M, Gaubicher J, Moreau P, Guyomard D. Formation of $Li_{1+n}V_3O_8/\beta$-$Li_{1/3}V_2O_5$/C nanocomposites by carboreduction and the resulting improvement in Li capacity retention. J Electrochem Soc **2006**; 153: A295-300.

Dubpernell G. Electrodeposition of chromium from chromic acid solutions. New York: Pergamon Press **1977**.

Endo M, Nakamura J, Sasabe Y, Takahashi T, Inagaki M. Lithium secondary battery using vapour grown carbon fibers as a negative electrode and analysis of the electrode mechanism by TEM observation. Trans IEE Jpn A **1995**; 115: 349-56.

Eom JY, Park JW, Kwon HS, Rajendran S. Electrochemical insertion of lithium into multiwalled carbon nanotube/silicon composites produced by ballmilling. J Electrochem Soc **2006**; 153: A1678-84.

Ernst FO, Kammler HK, Roessler A, Pratsinis SE, Stark WJ, Ufheil J, Novák P. Electrochemically active flame-made nanosized spinels: $LiMn_2O_4$, $Li_4Ti_5O_{12}$ and $LiFe_5O_8$. Mater Chem Phys **2007**; 101: 372-8.

Fan J, Fedkiw PS. Electrochemical impedance spectra of full cells: Relation to capacity and capacity-rate of rechargeable Li cells using $LiCoO_2$, $LiMn_2O_4$, and $LiNiO_2$ cathodes. J Power Sources **1998**; 72: 165-73.

Fong F, Sacken K, Dahn JR. Studies of lithium intercalation into carbons using nonaqueous electrochemical cells. J Electrochem Soc **1990**; 137(7): 2009-13.

Forsyth M, Meakin P, Macfarlane DR, Hill AJ. Free volume and conductivity of plasticized polyether-urethane solid polymer electrolytes. J Phys Condensed Matter **1995**; 7: 7601-17.

Frackowiak E, Béguin F. Electrochemical storage of energy in carbon nanotubes and nanostructured carbons. Carbon **2002**; 40(10): 1775-87.

Fragnaud P, Nagarajan R, Schleich DM, Vujic D. Thin-film cathodes for secondary lithium batteries. J Power Sources **1995**; 54: 362-6.

Galiński M, Lewandowski A, Stępniak I. Ionic liquids as electrolytes. Electrochim Acta **2006**; 51: 5567-80.

Gao B, Sinha S, Fleming L, Zhou O. Alloy formation in nanostructured silicon. Adv Mater **2001**; 13: 816-9.

Gemeay AH, Nishiyama H, Kuwabata S, Yoneyama H. Chemical preparation of manganese dioxide/polypyrrole composites and their use as cathode active

materials for rechargeable lithium batteries. J Electrochem Soc **1995**; 142: 4190-5.

Giacovazzo C. Fundamentals of crystallography. Oxford: Oxford University Press **2002**.

Goers D, Buqa H, Hardwick L, Wuersig A, Novák P. Raman spectroscopic and structural studies of heat-treated graphites for lithium-ion batteries. Ionics **2003**; 9: 258-65.

Gritzner G, Kreysa G. Nomenclature, symbols and definitions in electrochemical engineering. Pure & Appl Chem **1993**; 65: 1009-20.

Guo C, Cao M, Hu C. A novel and low-temperature hydrothermal synthesis of SnO_2 nanorods. Inorg Chem Commun **2004**; 7: 929-31.

Guo ZP, Ahn JH, Liu HK, Dou SX. Characterization of nanoparticles of $LiMn_2O_4$ synthesized by a one-step intermediate temperature solid-state reaction. J Nanosci Nanotechnol **2004**; 4: 162-6.

Guo ZP, Milin E, Wang JZ, Chen J, Liu HK. Silicon/disordered carbon nanocomposites for lithium-ion battery anodes. J Electrochem Soc **2005a**; 152: A2211-6.

Guo ZP, Wang JZ, Liu HK, Dou SX. Study of silicon/polypyrrole composite as anode materials for Li-ion batteries. J Power Source **2005b**; 146: 448-51.

Han S, Jang B, Kim T, Oh SM, Hyeon T. Simple synthesis of hollow tin dioxide microspheres and their application to lithium-ion battery anodes. Adv Funct Mater **2005**; 15: 1845-50.

Hardwick LJ, Holzapfel M, Novák P, Dupont L, Baudrin E. Electrochemical lithium insertion into anatase-type TiO_2: An in situ Raman microscopy investigation. Electrochim Acta **2007**; 52: 5357-67.

Howlett PC, Brack N, Hollenkamp AF, Forsyth M, MacFarlane DR. Characterization of the lithium surface in *N*-methyl-*N*-alkylpyrrolidinium

bis(trifluoromethanesulfonyl)amide room-temperature ionic liquid electrolytes. J Electrochem Soc **2006**; 153: A595-606.

Howlett PC, MacFarlane DR, Hollenkamp AF. High lithium metal cycling efficiency in a room-temperature ionic liquid. Electrochem Solid-State Lett **2004**; 7: A97-101.

Huang H, Yin SC, Nazar LF. Approaching theoretical capacity of $LiFePO_4$ at room temperature at high rates. Electrochem Solid State Lett **2001**; 4: A170-2.

Huang Y, Park K, Goodenough JB. Improving lithium batteries by tethering carbon-coated $LiFePO_4$ to polypyrrole. J Electrochem Soc **2006**; 153: A2282-6.

Huggins RA. Lithium alloy negative electrodes formed from convertible oxides. Solid State Ionics **1998**; 113-115: 57-67.

Idota Y, Kubota T, Matsufuji A, Maekawa Y, Miyasaka T. Tin-based amorphous oxide: A high-capacity lithium-ion-storage material. Science **1997**; 276: 1395-7.

Jiang X, Wang Y, Herricks T, Xia Y. Ethylene glycol-mediated synthesis of metal oxide nanowires. J Mater Chem **2004**; 14: 695-703.

Kawakita J, Miura T, Kishi T. Lithium insertion into $Li_4V_3O_8$. Solid State Ionics **1999**; 120: 109-116.

Kim IS, Blomgren GE, Kumta PN. Nanostructured Si/TiB_2 composite anodes for Li-ion batteries. Electrochem Solid-State Lett **2003**; 6: A157-61.

Kim IS, Kumta PN, Blomgren GE. Si/TiN nanocomposites novel anode materials for Li-ion batteries. Electrochem Solid-State Lett **2000**; 3: 493-6.

Kim JM, Chung HT. The first cycle characteristics of $Li[Ni_{1/3}Co_{1/3}Mn_{1/3}]O_2$ charged up to 4.7 V. Electrochimica Acta **2004**; 49: 937-44.

Kim KW, Kim MR, Lee SW, Han KS, Woo SI. The characterization of $LiMn_2O_4$ thin film cathode for lithium rechargeable microbattery prepared by liquid source misted chemical deposition. Chem Vapor Depos **2003**; 9: 187-92.

Kim YA, Kojima M, Muramatsu H, Umemoto S, Watanabe T, Yoshida K, et al. *In situ* Raman study on single- and double-walled carbon nanotubes as a function of lithium insertion. Small **2006**; 2(5): 667-76.

Kumagai N, Yu A. Ultrasonically treated LiV_3O_8 as a cathode material for secondary lithium batteries. J Electrochem Soc **1997**; 144: 830-4.

Kuwabata S, Masui S, Tomiyori H, Yoneyama H. Charge–discharge properties of chemically prepared composites of V_2O_5 and polypyrrole as positive electrode materials in rechargeable Li batteries. Electrochim Acta **2000**; 46: 91-7.

La Mantia F. Characterization of electrodes for Li-ion batteries through electrochemical impedance spectroscopy and mass spectrometry. Switzerland: Paul Scherrer Institute PhD Thesis **2008**.

Lanz M, Kormann C, Steininger H, Heil G, Haas O, Novák P. Large-agglomerate-size lithium manganese oxide spinel with high rate capability for lithium-ion batteries. J Electrochem Soc **2000**; 147: 3997-4000.

Larcher D, Mudalige C, George AE, Poter V, Gharghouri M, Dahn JR. Si-containing disordered carbons prepared by pyrolysis of pitch/polysilane blends: Effect of oxygen and sulfur. Solid State Ionics **1999**; 122**:** 71-83.

Li H, Balaya P, Maier J. Li-storage via heterogeneous reaction in selected binary metal fluorides and oxides. J Electrochem Soc **2004**; 151: A1878-85.

Li H, Shi L, Lu W, Huang X, Chen L. Studies on capacity loss and capacity fading of nanosized SnSb alloy anode for Li-ion batteries. J Electrochem Soc **2001**; 148: A915-22.

Lin K, Xu Y, He G, Wang X. The kinetic and thermodynamic analysis of Li ion in multi-walled carbon nanotubes. Mater Chem Phys **2006**; 99(2-3): 190-6.

Linden D, Reddy T. Handbook of batteries 3rd Edition. New York: McGraw-Hill **2002**.

Lindsay MJ. Data analysis and anode materials for lithium ion batteries. Australia: University of Wollongong PhD Thesis **2004**.

Liu GQ, Zeng CL, Yang K. Study on the synthesis and properties of LiV_3O_8 rechargeable lithium batteries cathode. Electrochim Acta **2002**; 47: 3239-43.

Liu W, Huang X, Wang Z, Li H, Chen L. Studies of stannic oxide as an anode material for lithium-ion batteries. J Electrochem Soc **1998**; 145: 59-62.

Liu W, Farrington GC, Chaput F, Dunn B. Synthesis and electrochemical studies of spinel phase $LiMn_2O_4$ cathode materials prepared by the Pechini process. J Electrochem Soc **1996**; 143: 879-84.

Liu Y, Liu M. Growth of aligned square-shaped SnO_2 tube arrays. Adv Funct Mater **2005**; 15: 57-62.

Liu YC, Hwang BJ, Jian WJ, Santhanan R. *In situ* cyclic voltammetry-surface-enhanced Raman spectroscopy: Studies on the doping–undoping of polypyrrole film. Thin Solid Films **2000**; 374: 85-91.

Lu W, Chung DDL. Anodic performance of vapor-derived carbon filaments in lithium-ion secondary battery. Carbon **2001**; 39(4): 493-6.

MacFarlane DR, Forsyth M, Howlett PC, Pringle JM, Sun J, Annat G, Nell W, Izgorodina EI. Ionic liquids in electrochemical devices and processes: Managing interfacial electrochemistry. Acc Chem Res **2007**; 40: 1165-73.

Mädler L, Roessler A, Pratsinis SE, Sahmb T, Gurlo A, Barsan N, Weimar U. Direct formation of highly porous gas-sensing films by in situ thermophoretic deposition of flame-made Pt/SnO2 nanoparticles. Sens Actuator B-Chem **2006**; 114: 283-295.

Manev V, Momchilov A, Nassalevska A, Pistoia G, Pasquali M. A new approach to the improvement of $Li_{1+x}V_3O_8$ performance in rechargeable lithium batteries. J Power Sources **1995**; 54: 501-7.

Manuel Stephan A, Nahm KS. Review on composite polymer electrolytes for lithium batteries. Polymer **2006**; 47: 5952-64.

Meyer WH. Polymer electrolytes for lithium-ion batteries. Adv Mater **1998**; 10: 439-48.

Miyaki Y. U.S. Patent Application **2005**; 0181276.

Mohamedi M, Lee SJ, Takahashi D, Nishizawa M, Itoh T, Uchida I. Amorphous tin oxide films: Preparation and characterization as an anode active material for lithium ion batteries. Electrochim Acta **2001**; 46: 1161-8.

Murphy DW, Christian PA, Disalvo FJ, Carides JN. Vanadium oxide cathode materials for secondary lithium cells. J Electrochem Soc **1979**; 126: 497-9.

Nakagawa H, Izuchi S, Kuwana K, Nukuda T, Aihara Y. Liquid and polymer gel electrolytes for lithium batteries composed of room-temperature molten salt doped by lithium salt J. Electrochem Soc **2003**; 150: A695-700.

Nakai I, Nakagome T. *In Situ* transmission X-ray absorption fine structure analysis of the Li deintercalation process in $Li(Ni_{0.5}Co_{0.5})O_2$. Electrochem Solid State Lett **1998**; 1: 259-61.

Nassau K, Murphy DW. The quenching and electrochemical behavior of Li_2O-V_2O_5 glasses. J Non-Cryst Solids **1981**; 44: 297-304.

Nissan AH, Batten GLJ. The link between the molecular and structural theories of paper elasticity. Tappi J **1997**; 80: 153-8.

Ng SH, Santos DI, Chew SY, Wexler D, Wang J, Dou SX, Liu HK. Polyol-mediated synthesis of ultrafine tin oxide nanoparticles for reversible Li-ion storage. Electrochem Commun **2007**; 9: 915-9.

Ng SH, Tran N, Bramnik KG, Hibst H, Novák P. A feasibility study on the use of $Li_4V_3O_8$ as a high capacity cathode material for lithium-ion batteries. Chem Eur J **2008**; 14: 11141-8.

Ng SH, Wang JZ, Guo ZP, Chen J, Wang GX, Liu HK. Single wall carbon nanotube paper as anode for lithium-ion battery. Electrochimica Acta **2005**; 51: 23-8.

Ng SH, Wang JZ, Wexler D, Konstantinov K, Guo ZP, Liu HK. Highly reversible lithium storage in spheroidal carbon-coated silicon nanocomposites as anodes for lithium-ion batteries. Angew Chem Int Ed **2006**; 45: 6896-9.

Novák P. Electrochemistry seminar: Lithium-ion batteries as electrochemical energy storages for portability usage. Switzerland: Paul Scherrer Institute **2008**.

Novák P, Müller K, Santhanam KSV, Haas O. Electrochemically active polymers for rechargeable batteries. Chem Rev **1997**; 97: 207-82.

Novák P, Scheifele W, Joho F, Haas O. Electrochemical Insertion of Magnesium into Hydrated Vanadium Bronzes. J Electrochem Soc **1995**; 142(8): 2544-50.

Notten PHL, Roozeboom F, Niessen RAH, Baggetto L. 3-D integrated all-solid-state rechargeable batteries. Adv Mater **2007**; 19: 4564-7.

Ohgi H, Maeda T, Hosono E, Fujihara S, Imai H. Evolution of nanoscale SnO_2 grains, flakes, and plates into versatile particles and films through crystal growth in aqueous solutions. Cryst Growth Des **2005**; 5: 1079-83.

Ohzuku T, Brodd RJ. An overview of positive-electrode materials for advanced lithium-ion batteries. J Power Sources **2007**; 174: 449-56.

Ohzuku T, Makimura Y. Layered lithium insertion material of $LiCo_{1/3}Ni_{1/3}Mn_{1/3}O_2$ for lithium-ion batteries. Chemistry Letters **2001**; 30: 642-3.

Ohzuku T, Ueda A, Yamamoto N. Zero-strain insertion material of $Li[Li_{1/3}Ti_{5/3}]O_4$ for rechargeable lithium cells. J Electrochem Soc **1995**; 142: 1431-5.

Owen JR. Rechargeable lithium batteries. Chem Soc Rev **1997**; 26: 259-67.

Ozawa K. Lithium-ion rechargeable batteries with $LiCoO_2$ and carbon electrodes: the $LiCoO_2$/C system. Solid State Ionics **1994**; 69: 212-21.

Padhi AK, Nanjundaswamy KS, Goodenough JB. Phospho-olivines as positive-electrode materials for rechargeable lithium batteries. J Electrochem Soc **1997**; 144: 1188-94.

Panero S, Pasquali M, Pistoia G. Rechargeable Li/$Li_{1+x}V_3O_8$ Cells. J Electrochem Soc **1983**; 130: 1225-7.

Paulsen JM, Thomas CL, Dahn JR. Layered Li-Mn-oxide with the O_2 structure: A cathode material for Li-ion cells which does not convert to spinel. J Electrochem Soc **1999**; 146: 3560-5.

Park MS, Kang YM, Kim JH, Wang GX, Dou SX, Liu HK. Effects of low-temperature carbon encapsulation on the electrochemical performance of SnO_2 nanopowders. Carbon **2008**; 46: 35-40.

Park MS, Wang GX, Kang YM, Wexler D, Liu HK, Dou SX. Preparation and electrochemical properties of SnO_2 nanowires for application in lithium-ion batteries. Angew Chem Int Ed **2007**; 46: 750-3.

Patey TJ, Ng SH, Büchel R, Tran N, Krumeich F, Wang JZ, Liu HK, Novák P. Electrochemistry of LiV_3O_8 made by flame spray pyrolysis. Electrochem Solid-State Lett **2008**; 11: A46-50.

Peled E. The electrochemical behaviour of alkali and alkaline earth metals in non-aqueous battery systems – the solid electrolyte interphase model. J Electrochem Soc **1979**; 126**:** 2047-51.

Pereira N, Balasubramanian M, Dupont L, McBreen J, Klein LC, Amatucci GG. The electrochemistry of germanium nitride with lithium. J Electrochem Soc **2003**; 150: A1118-28.

Pereira-Ramos JP. Electrochemical properties of cathodic materials synthesized by low-temperature techniques. J Power Sources **1995**; 54: 120-6.

Picciotto LA, Adendorff KT, Liles DC, Thackeray MM. Structural characterization of $Li_{1+x}V_3O_8$ insertion electrodes by single-crystal X-ray diffraction. Solid State Ionics **1993**; 62: 297-307.

Pinna N, Neri G, Antonietti M, Niederberger M. Nonaqueous synthesis of nanocrystalline semiconducting metal oxides for gas sensing. Angew Chem Int Ed **2004**; 43: 4345-9.

Pistoia G, Panero S, Tocci M, Moshtev RV, Manev V. Solid solutions $Li_{1+x}V_3O_8$ as cathodes for high rate secondary Li batteries. Solid State Ionics **1984**; 13: 311-8.

Pistoia G, Pasquali M, Wang G, Li L. $Li/Li_{1+x}V_3O_8$ secondary batteries: synthesis and characterization of an amorphous form of the cathode. J Electrochem Soc **1990**; 137: 2365-70.

Pletcher D. A First Course in Electrode Processes. Alresford Hants: The Electrochem Consultancy **1991**.

Poizot P, Laruelle S, Grugeon S, Dupont L, Tarascon J-M. Nano-sized transition-metal oxides as negative-electrode materials for lithium-ion batteries. Nature **2000**; 407: 496-9.

Ren W, Li F, Chen J, Bai S, Cheng HM. Morphology, diameter distribution and Raman scattering measurements of double-walled carbon nanotubes synthesized by catalytic decomposition of methane. Chem Phys Lett **2002**; 359:196-202.

Saadoune I, Delmas C. On the $Li_xNi_{0.8}Co_{0.2}O_2$System. J Solid State Chem **1998**; 136: 8-15.

Sakaebe H, Matsumoto H. *N*-methyl-*N*-propylpiperidinium bis(trifluoromethanesulfonyl)imide (PP13–TFSI) – novel electrolyte base for Li battery. Electrochem Commun **2003**; 5: 594-8.

Samar B, Somerset NJ. Rechargeable Battery. USPTO **1981**; US4304825.

Singh B, Sekhon SS. Polymer electrolytes based on room temperature ionic liquid: 2,3-dimethyl-1-octylimidazolium triflate. J Phys Chem B **2005**; 109: 16539-43.

Singh D, Houriet R, Giovannini R, Hofmann H, Craciun V, Singh RK. Challenges in making of thin films for $Li_xMn_yO_4$ rechargeable lithium batteries for MEMS. J Power Sources **2001**; 97: 826-31.

Scott RWJ, Coombs N, Ozin GA. Non-aqueous synthesis of mesostructured tin dioxide. J Mater Chem **2003**; 13: 969-74.

Scrosati B. Challenge of portable power. Nature **1995**; 372: 557-8.

Shimoda H, Gao B, Tang XP, Kleinhammes A, Fleming L, Wu Y, et al. Lithium intercalation into opened single-wall carbon nanotubes: storage capacity and electronic properties. Phys Rev Lett **2002**; 88(1): 015502.

Shin JH, Henderson WA, Passerini S. PEO-based polymer electrolytes with ionic liquids and their use in lithium metal-polymer electrolyte batteries. J Electrochem Soc **2005**; 152: A978-83.

Shoyama M, Hashimoto N. Effect of polyethylene glycol addition on the microstructure and sensor characteristics of SnO_2 thin films prepared by sol–gel method. Sens Actuators B **2003**; 93: 585-9.

Simmen F, Lippert T, Novák P, Neuenschwander B, Döbeli M, Mallepell M, Wokaun A. The influence of lithium excess in the target on the properties and

compositions of $Li_{1+X}Mn_2O_{4-\delta}$ thin films prepared by PLD. Appl Phys A **2008**; 93: 711-6.

Spahr ME, Palladino T, Wihelm H, Würsig A, Goers D, Buqa H, et al. Exfoliation of graphite during electrochemical lithium insertion in ethylene carbonate-containing electrolytes. J Electrochem Soc **2004**; 151: A1383-95.

Stark WJ, Pratsinis SE. Aerosol flame reactors for manufacture of nanoparticles. Powder Technol **2002**; 126: 103-8.

Striebel KA, Rougier A, Horne CR, Reade RP, Cairns EJ. Electrochemical studies of substituted spinel thin films. J Electrochem Soc **1999**; 146: 4339-47.

Strobel P, LeCras F, Anne M. Composition–valence diagrams: A new representation of topotactic reactions in ternary transition metal oxide systems. Application to lithium intercalation. J Solid State Chem **1996**; 124: 83-94.

Sudant G, Baudrin E, Dunn B, Tarascon JM. Synthesis and electrochemical properties of vanadium oxide aerogels prepared by a freeze-drying process. J Electrochem Soc **2004**; 151: A666-71.

Sun J, MacFarlane DR, Byrne N, Forsyth M. Zwitterion effect in polyelectrolyte gels based on lithium methacrylate-*N*,*N*-dimethyl acrylamide copolymer. Electrochim Acta **2006**; 51: 4033-8.

Sun X, Liu J, Li Y. Oxides@C core−shell nanostructures: One-pot synthesis, rational conversion, and Li storage property. Chem Mater **2006**; 18: 3486-94.

Tarascon JM, Armand M. Building better batteries. Nature **2001**; 404: 359-67.

Tarascon JM, Gozdz AS, Schmutz C, Shokoohi F, Warren PC. Performance of Bellcore's plastic rechargeable Li-ion batteries. Solid State Ionics **1996**; 86-88: 49-54.

Tarascon JM, Guyomard D. The $Li_{1+X}Mn_2O_4$/C rocking chair system: a review. Electrochim Acta **1993**; 38: 1221-31.

Tarascon JM, Wang E, Shokoohi FK, McKinnon WR, Colson S. The spinel phase of $LiMn_2O_4$ as a cathode in secondary lithium cells. J Electrochem Soc **1991**; 138: 2859-64.

Thackeray MM, David WIF, Bruce PG, Goodenough JB. Lithium insertion into manganese spinels. Mat Res Bull **1983**; 18:461-72.

Thackeray MM. Spinel electrodes for lithium batteries. J American Ceramic Soc **1999**; 82: 3347-54.

Tiyapiboonchaiya C, Pringle JM, Sun J, Byrne N, Howlett PC, MacFarlane DR, Forsyth M. The zwitterion effect in high-conductivity polyelectrolyte materials. Nature Materials **2004**; 3: 29-32.

Tricoli A, Graf M, Mayer F, Kühne S, Hierlemann A, Pratsinis SE, Micropatterning layers by flame aerosol deposition-annealing. Adv Mater **2008**; 16: 3005-10.

Tsaramyrsi M, Kavousanaki D, Raptopoulou CP, Terzis A, Salifoglou A. Systematic synthesis, structural characterization, and reactivity studies of vanadium(V)–citrate anions $[VO_2(C_6H_6O_7)]_2^{2-}$, isolated from aqueous solutions in the presence of different cations. Inorganica Chimica Acta **2001**; 320: 47-59.

Tsumura T, Shimizu A, Inagaki M. Synthesis of $LiMn_2O_4$ spinel via tartrates. J Mater Chem **1993**; 3: 995-6.

Vinod MP, Bahnemann D. Materials for all-solid-state thin-film rechargeable lithium batteries by sol-gel processing. J Solid State Electrochem **2002**; 6: 498-501.

Wang GX, Yang L, Chen Y, Wang JZ, Bewlay S, Liu HK. An investigation of polypyrrole-$LiFePO_4$ composite cathode materials for lithium-ion batteries. Electrochimica Acta 2005; 50: 4649-54.

Wang J, Chen J, Konstantinov K, Zhao L, Ng SH, Wang GX, Guo ZP, Liu HK. Sulphur-polypyrrole composite positive electrode materials for rechargeable lithium batteries. Electrochimica Acta 2006; 51: 4634-8.

Wang Y, Jiang X, Xia Y. A solution-phase, precursor route to polycrystalline SnO_2 nanowires that can be used for gas sensing under ambient conditions. J Am Chem Soc **2003**; 125: 16176-7.

West K, Zachau-Christiansen B, Østergård MJL, Jacobsen T. Vanadium oxide as electrode materials for rechargeable lithium cells. J Power Sources **1987**; 20: 165-72.

Whitten PG, Spinks GM, Wallace GG. Mechanical properties of carbon nanotube paper in ionic liquid and aqueous electrolytes. Carbon **2005**; 43: 1891-6.

Whittingam MS. Electrical energy storage and intercalation chemistry. Science **1976a**; 192: 1126-7.

Whittingham MS. The role of ternary phases in cathode reactions. J Electrochem Soc **1976b**; 123: 315-20.

Whittingam MS. Lithium batteries and cathode materials. Chem Rev **2004**; 104**:** 4271-301.

Whittingham MS, Song Y, Lutta S, Zavalij PY, Chernova NA. Some transition metal (oxy)phosphates and vanadium oxides for lithium batteries. J Mater Chem **2005**; 15: 3362-79.

Wilson M, Dahn JR. Lithium Insertion in Carbons Containing Nanodispersed Silicon J Electrochem Soc **1995**; 142: 326-32.

Winter M, Besenhard JO. Electrochemical lithiation of tin and tin-based intermetallics and composites. Electrochim Acta **1999**; 45: 31-50.

Winter M, Besenhard JO, Albering JH, Yang J, Wachtler M. Prog Batteries Battery Mater **1998**; 17: 208-13.

Winter M, Besenhard JO, Spahr ME, Novák P. Insertion electrode materials for lithium batteries. Adv Mater **1998b**; 10: 738-47.

Winter M, Brodd RJ. What are batteries, fuel cells, and supercapacitors? Chemical Reviews **2004**; 104: 4245-69.

Winter M, Novák P, Monnier A. Graphite for lithium-ion cells: The correlation of the first-cycle charge loss with the Brunauer-Emmett-Teller surface area. J Electrochem Soc **1998**; 145: 428-36.

Wong HP, Dave BC, Leroux F, Harreld J, Dunn B, Nazar LF. Synthesis and characterization of polypyrrole/vanadium pentoxide nanocomposite aerogels. J Mater Chem **1998**; 8: 1019-27.

Wright PV. Polymer electrolytes - the early days. Electrochim Acta **1998**; 43: 1137-43.

Wu GT, Wang CS, Zhang XB, Yang HS, Qi ZF, He PM, et al. Structure and lithium insertion properties of carbon nanotubes. J Electrochem Soc **1999**; 146: 1696-701.

Würsig A, Buqa H, Holzapfel M, Krumeich F, Novák P. Film formation at positive electrodes in lithium ion batteries. Electrochem Solid-State Lett **2005**; 8: A34-7.

Xia Y, Sakai T, Fujieda T, Yang XQ, Sun X, Ma ZF, McBreen J, Yoshio M. Correlating capacity fading and structural changes in $Li_{1+y}Mn_{2-y}O_{4-\sigma}$ spinel cathode materials: A systematic study on the effects of Li/Mn ratio and oxygen deficiency. J Electrochem Soc **2001**; 148: A723-9.

Xie J, Tanaka T, Imanishi N, Matsumura T, Hirano A, Takeda Y, Yamamoto O. Li-ion transport kinetics in $LiMn_2O_4$ thin films prepared by radio frequency magnetron sputtering. J Power Sources **2008**; 180: 576-81.

Xu HY, Wang H, Song ZQ, Wang YW, Yan H, Yoshimura M. Novel chemical method for synthesis of LiV_3O_8 nanorods as cathode materials for lithium ion batteries. Electrochim Acta **2004**; 49: 349-53.

Xu K. Nonaqueous liquid electrolytes for lithium-based rechargeable batteries. Chem Rev **2004**; 104: 4303-417.

Yamada A, Chung SC, Hinokuma K. Optimized $LiFePO_4$ for lithium battery cathodes J Electrochem Soc **2001**; 148: A224-9.

Yang G, Wang G, Hou W. Microwave solid-state synthesis of LiV_3O_8 as cathode material for lithium batteries. J Phys Chem B **2005**; 109: 11186-96.

Yang HG, Zeng HC. Self-Construction of hollow SnO_2 octahedra based on two-dimensional aggregation of nanocrystallites. Angew Chem Int Ed **2004**; 43: 5930-3.

Yoneyama H, Kishimoto A, Kuwabata S. Charge–discharge properties of polypyrrole films containing manganese dioxide particles. J Chem Soc Chem Commun **1991**; 986-7.

Yoshizawa H, Ohzuku T. An application of lithium cobalt nickel manganese oxide to high-power and high-energy density lithium-ion batteries. J Power Sources **2007**; 174: 813-7.

Yuan L, Guo ZP, Konstantinov K, Liu HK, Dou SX. Nano-structured spherical porous SnO_2 anodes for lithium-ion batteries. J Power Sources **2006**; 159: 345-8.

Zhao Q, Zhao Z, Dong T, Xie Y. Facile synthesis and catalytic property of porous tin dioxide nanostructures. J Phys Chem B **2006**; 110: 15152-6.

Zhu J, Lu Z, Aruna ST, Aurbach D, Gedanken A. Sonochemical synthesis of SnO_2 nanoparticles and their preliminary study as Li insertion electrodes. Chem Mater **2000**; 12: 2557-66.

APPENDIX A

LIST OF PUBLICATIONS

Refereed Journal Papers:

(1) ***S.Y. Chew***, C. Feng, S.H. Ng, J. Wang, Z. Guo and H. Liu, "Low-temperature synthesis of polypyrrole-coated LiV_3O_8 composite with enhanced electrochemical properties", *Journal of the Electrochemical Society* **154,** 7, (2007) A633-A637.

(2) ***S.Y. Chew***, Z.P. Guo, J.Z. Wang, J. Chen, P. Munroe, S.H. Ng, L. Zhao and H.K. Liu, "Novel nano-silicon/polypyrrole composites for lithium storage", *Electrochemistry Communications* **9,** 5, (2007) 941-946.

(3) S.H. Ng, D.I. dos Santos, ***S.Y. Chew***, D. Wexler, J. Wang, S.X. Dou and H.K. Liu, "Polyol-mediated synthesis of ultrafine tin oxide nanoparticles for reversible Li-ion storage", *Electrochemistry Communications* **9,** 5, (2007) 915-919.

(4) J. Wang, ***S.Y. Chew***, D. Wexler, G.X. Wang, S.H. Ng, S. Zhong and H.K. Liu, "Nanostructured nickel sulfide synthesized via a polyol route as a cathode material for the rechargeable lithium battery", *Electrochemistry Communications*, **9,** 8, (2007) 1877-1880.

(5) J. Wang, S.H. Ng, ***S.Y. Chew***, D. Wexler, G.X. Wang and H.K. Liu, "Characterization of nanosize molybdenum trisulfide for lithium batteries and MoS_3 structure confirmation via electrochemistry", *Electrochemical and Solid-State Letters,* **10,** 9, (2007), A204-207.

(6) S.H. Ng, J. Wang, D. Wexler, ***S.Y. Chew*** and H.K. Liu, "Amorphous carbon-coated silicon nanocomposites: A low temperature synthesis via spray pyrolysis, and their application as high capacity anodes for Li-ion batteries", *The Journal of Physical Chemistry C,* **111**, 29, (2007), 11131-11138.

(7) S.H. Ng, ***S.Y. Chew***, J. Wang, D. Wexler, Y. Tournayre, K. Konstantinov and H.K. Liu, "Synthesis and electrochemical properties of V_2O_5 nanostructures prepared via a precipitation process for lithium-ion battery cathodes", *Journal of Power Sources,* **174,** 2, (2007), 1032-1035.

(8) S.H. Ng, J. Wang, K. Konstantinov, D. Wexler, ***S.Y. Chew***, Z.P. Guo and H.K. Liu, "Spray-pyrolyzed silicon/disordered carbon nanocomposites for lithium-ion battery anodes", *Journal of Power Sources,* **174**, 2 (2007), 823-827.

(9) L. Yuan, J. Wang, ***S.Y. Chew***, J. Chen, Z.P. Guo, L. Zhao, K. Konstantinov and H.K. Liu, "Synthesis and characterization of SnO_2–polypyrrole composite for lithium-ion battery", *Journal of Power Sources*, **174,** 2, (2007), 1183-1187.

(10) C.Q. Feng, ***S.Y. Chew***, Z.P. Guo, J.Z. Wang and H.K. Liu, "An investigation of polypyrrole–LiV_3O_8 composite cathode materials for lithium-ion batteries", *Journal of Power Sources*, **174,** 2, (2007), 1095-1099.

(11) J. Wang, ***S.Y. Chew***, Z.W. Zhao, S. Ashraf, D. Wexler, J. Chen, S.H. Ng, and H.K. Liu, "Sulfur-Mesoporous Carbon Composites in Conjunction with a Novel Ionic Liquid Electrolyte for Lithium Rechargeable Batteries", *Carbon*, **46**, 2 (2008) 229-235.

(12) See-How Ng, ***Sau-Yen Chew***, Dayse I. dos Santos, Jun Chen, Jia-Zhao Wang, Shi-Xue Dou and Hua-Kun Liu, "Hexagonal-shaped tin glycolate particles: A preliminary study of their suitability as Li-ion insertion electrodes", *Chemistry An Asian Journal*, **3,** 5, (2008), 854-861.

(13) ***S. Y. Chew*,** J. Sun, J. Wang, H. Liu, M. Forsyth, and D. R. MacFarlane, "Lithium polymer battery based on an ionic liquid-polymer electrolyte composite for room temperature applications", *Electrochimica Acta*, **53,** 22 (2008), 6460-6463.

(14) Shu-Lei Chou, Jia-Zhao Wang, ***Sau-Yen Chew***, Hua-Kun Liu, and Shi-Xue Dou, "Electrodeposition of MnO_2 Nanowires on Carbon Nanotube Paper as Free-standing, Flexible Electrode for Supercapacitors", *Electrochemistry Communications,* **10**, 11, (2008), 1724-1727.

(15) Jia-Zhao Wang, Shu-Lei Chou, ***Sau-Yen Chew***, Jia-Zeng Sun, Maria Forsyth, Douglas R. MacFarlane, Hua-Kun Liu, "Nickel Sulfide Cathode in Combination

with an Ionic Liquid-Based Electrolyte for Rechargeable Lithium Batteries", *Solid State Ionics* **179**, 40, (2008), 2379-2382.

(16) Jia-Zhao Wang, Shu-Lei Chou, Jun Chen, ***Sau-Yen Chew***, Guo-Xiu Wang, Konstantin Konstantinov, Jian Wu , Shi-Xue Dou and Hua-Kun Liu, "Paper-Like Free-Standing Polypyrrole and Polypyrrole-$LiFePO_4$ Composite films for Flexible and Bendable Rechargeable Batteries", *Electrochemistry Communications,* **10**, 11, (2008), 1781-1784.

(17) See How Ng, ***Sau Yen Chew***, Jiazhao Wang, Jun Chen, ShiXue Dou, and HuaKun Liu, "Foam-like, microstructural SnO2-carbon composite thin films synthesized via a polyol-assisted thermal decomposition method", *Dalton Transactions*, 4, (2009), 723-729.

Accepted Paper:

(18) ***S.Y. Chew***, T. J. Patey, R. Büchel, Frank Krumeich, J. Wang, H. K. Liu, S.E. Pratsinis, and P. Novák, "$LiMn_2O_4$ thin films synthesized via an *In situ* annealing-assisted flame spray deposition Method", *Journal of Power Sources* (*In press* Dec 2008).

Submitted Paper:

(19) ***Sau Yen Chew***, See How Ng, Petr Novák, Jiazhao Wang, Frank Krumeich, Jun Chen, Shulei Chou, and Hua Kun Liu, "Free-standing Carbon Nanotubes Film as Anode for Lithium Ion Battery", *Carbon* (submitted Feb 2009).